

Springer Proceedings in Physics 141

Martin Oberlack
Joachim Peinke
Alessandro Talamelli
Luciano Castillo
Michael Hölling *Editors*

Progress in Turbulence and Wind Energy IV

Proceedings of the iTi Conference
in Turbulence 2010

 Springer

Editors

Martin Oberlack · Joachim Peinke ·
Alessandro Talamelli · Luciano Castillo ·
Michael Hölling

Progress in Turbulence and Wind Energy IV

Proceedings of the iTi Conference
in Turbulence 2010

Editors

Prof. Dr. Martin Oberlack
Department of Mechanical
Engineering
Technische Universität Darmstadt
Darmstadt
Germany

Prof. Dr. Luciano Castillo
Mechanical, Aerospace & Nuclear
Engineering Department
Rensselaer Polytechnic Institute
Troy
USA

Prof. Dr. Joachim Peinke
Institute of Physics & ForWind
University Oldenburg
Oldenburg
Germany

Dr. Michael Hölling
Institute of Physics & ForWind
University of Oldenburg
Oldenburg
Germany

Prof. Dr. Alessandro Talamelli
II Facoltà di Ingegneria
Universita di Bologna
Forli
Italy

ISSN 0930-8989

e-ISSN 1867-4941

ISBN 978-3-642-28967-5

e-ISBN 978-3-642-28968-2

DOI 10.1007/978-3-642-28968-2

Springer Heidelberg New York Dordrecht London

Library of Congress Control Number: 2012934378

© Springer-Verlag Berlin Heidelberg 2012

This work is subject to copyright. All rights are reserved by the Publisher, whether the whole or part of the material is concerned, specifically the rights of translation, reprinting, reuse of illustrations, recitation, broadcasting, reproduction on microfilms or in any other physical way, and transmission or information storage and retrieval, electronic adaptation, computer software, or by similar or dissimilar methodology now known or hereafter developed. Exempted from this legal reservation are brief excerpts in connection with reviews or scholarly analysis or material supplied specifically for the purpose of being entered and executed on a computer system, for exclusive use by the purchaser of the work. Duplication of this publication or parts thereof is permitted only under the provisions of the Copyright Law of the Publisher's location, in its current version, and permission for use must always be obtained from Springer. Permissions for use may be obtained through RightsLink at the Copyright Clearance Center. Violations are liable to prosecution under the respective Copyright Law.

The use of general descriptive names, registered names, trademarks, service marks, etc. in this publication does not imply, even in the absence of a specific statement, that such names are exempt from the relevant protective laws and regulations and therefore free for general use.

While the advice and information in this book are believed to be true and accurate at the date of publication, neither the authors nor the editors nor the publisher can accept any legal responsibility for any errors or omissions that may be made. The publisher makes no warranty, express or implied, with respect to the material contained herein.

Printed on acid-free paper

Springer is part of Springer Science+Business Media (www.springer.com)



“Allora è l’uomo in pace, quando per morte è uscito delle turbolenze di questo mondo, e venuto alla salute eterna.”

Prima definizione di “Turbolenza” - Vocabolario Accademia della Crusca, Venezia (1612)

“And man shall be at peace when death removes him from the turbulence of this world and he comes to know eternal wellbeing”

First definition of the word “turbolenza” from the Accademia della Crusca Dictionary, Venice, Italy (1612)

To our colleague and friend Tim (1966–2010)

Preface 2011

With the 4th ITI conference in the beautiful ancient town of Bertinoro, North Italy, 2010, the tradition of the interdisciplinary turbulence initiative (ITI) has been continued. About 100 researchers from about 20 different countries gathered in the hospitable centre of the University of Bologna to present the latest contributions in turbulence research. After an external peer review process the present 63 papers were collected for this forth issue on “progress in turbulence” dedicated to the memory of Prof. Tim Nickels. Shortly after giving an invited lecture at the 4th ITI conference, the turbulence community lost a world-class scientist, a friend and devoted family man.

Basic as well as applied research is driven by the rather notorious difficult and essentially unsolved problem of turbulence. In this collection of contributions clear progress can be seen in different aspects, ranging from new quality of numerical simulations to new concepts of experimental investigations and new theoretical developments. The importance of turbulence is shown for a wide range of applications including: combustion, energy, flow control, urban flows, are few examples found in this volume. A motivation this year was to bring fundamentals of turbulence in connection with renewable energy. This lead us to add a special topic relevant to the impact of turbulence on the wind energy conversion.

Beside all progress we have to realize that a general fundamental understanding of turbulence is still missing, even though new approaches are discovered and investigated. These new approaches often lead to new methods, which result in being very useful for other disciplines. Thus turbulence research has been a source of new scientific fields over the last decades. Nonlinear dynamics, chaos research, fractals and complexity may be taken as examples.

This span of research from pure mathematical analysis over turbulence physics to applied turbulence research has lead in the last decades to a broad diversification of turbulence research where contact between different sub-communities has sometimes been lost. It was in particular the latter drifting apart in the community that has

been the stimulation of the interdisciplinary turbulence initiative, which started in 1999 as cooperation between physicists and engineers working in turbulence funded by the German science foundation DFG. Based on the successful previous conferences, we will continue with this initiative for subsequent years with the 5th ITI Conference planned for September 2012.

The structure of the present book is as such that contributions have been bundled according to covering topics i.e. I Basic Turbulence Aspects, II Particle Laden Flows, III Modeling and Simulations, IV, Experimental Methods, V Special Flows, VI Atmospheric Boundary Layer, VII Boundary Layer, VIII Wind Energy and IX Convection.

At this point we would like to thank all authors for their contributions to this proceedings and the referees giving critical comments to the contributions and there with considerably raising the scientific quality. We would like to thank Thomas Ditzinger from Springer for his patience during the production of the book. Finally we gratefully acknowledge the staff of the University of Bologna and Olga Kelbin, George Khujadze, Andreas Rosteck for helping us to carry out this conference.

Martin Oberlack

Joachim Peinke

Alessandro Talamelli

Luciano Castillo

Michael Hölling

(Darmstadt, Oldenburg, Forli and Texas, 2012)

Contents

Session 1: Basic Turbulence Aspects

Scale-Energy Fluxes in Wall-Turbulent Flows	3
<i>A. Cimarelli, E. De Angelis, C.M. Casciola</i>	
Conservation Laws of Helically Symmetric Flows and Their Importance for Turbulence Theory	7
<i>O. Kelbin, A.F. Cheviakov, M. Oberlack</i>	
Velocity/Pressure-Gradient Correlation Modelling for Improved Prediction of Reattachment and Relaxation	11
<i>C. Lo, I. Vallet, B.A. Younis</i>	
Turbulence without Richardson-Kolmogorov Cascade	17
<i>J.C. Vassilicos, N. Mazellier</i>	
New Statistical Symmetries of the Two-Point Correlation Equations for Turbulent Flows	21
<i>Andreas M. Rosteck, Martin Oberlack</i>	
Cumulant Corrections in Turbulence: Quasinormal Approximation, Direct Interaction Approximation, and Non-Gaussian Properties of Turbulence	25
<i>Robert Rubinstein, Wouter J.T. Bos</i>	
Decaying Turbulence and Anomalous Dissipation	31
<i>M. Salewski, W.D. McComb, A. Berera, S. Yoffe</i>	
Secondary Splitting of Zero Gradient Points in Turbulent Scalar Fields	35
<i>Philip Schaefer, Markus Gampert, Norbert Peters</i>	

Multi-scale Analysis of Turbulence in CFD-Simulations	41
<i>Bernhard Stoevesandt, Robert Stresing, Andrei Shishkin, Claus Wagner, Joachim Peinke</i>	
A Note on Spatial Zero Crossings of Fluctuating Velocity Field in Wall Bounded Turbulent Flows	45
<i>Tardu Sedat</i>	
Non-equilibrium Statistical Mechanics of Fluid Turbulence	49
<i>Tomomasa Tatsumi</i>	
Two-Point Enstrophy Statistics of Fully Developed Turbulence	57
<i>Michael Wilczek, Rudolf Friedrich</i>	
Session 2: Particle Laden Flows / Lagrangian Turbulence	
Inertial Particles in a Turbulent Premixed Bunsen Flame	63
<i>F. Battista, F. Picano, G. Troiani, C.M. Casciola</i>	
Lagrangian Acceleration Statistics in 2D and 3D Turbulence	67
<i>Oliver Kamps, Michael Wilczek, Rudolf Friedrich</i>	
Transport of Inertial Particles in Turbulent Jets	71
<i>Francesco Picano, Gaetano Sardina, Paolo Gualtieri, Carlo Massimo Casciola</i>	
Probability Density Functions of Reacting Species Concentrations in Turbulent Wall-Jet	75
<i>Zeinab Pouransari, Geert Brethouwer, Arne V. Johansson</i>	
Session 3: Modeling and Simulation	
Characterisation of Synthetic Turbulence Methods for Large-Eddy Simulation of Supersonic Boundary Layers	81
<i>Guillaume Aubard, Xavier Gloerfelt, J.-C. Robinet</i>	
A Uniformly Valid Theory of Turbulent Separation	85
<i>Bernhard Scheichl, Alfred Kluwick, Frank T. Smith, Jon Paton</i>	
Application and Comparison of Two Different DNS Algorithms for Simulating Transition to Turbulence in Taylor-Green Vortex Flow	91
<i>İlyas Yılmaz, Lars Davidson, Fırat O. Edis, Hasan Saygın</i>	
Session 4: Experimental Methods	
Optimization of a Digital In-line Holography Setup Used with a High-Speed Camera	97
<i>Gerd Gülker, Christoph Hindriksen, Tim Homeyer, Joachim Peinke</i>	

Development of Highly Resolving Drag Based Anemometers	101
<i>Hendrik Heißelmann, Jaroslaw Puczyłowski, Michael Hölling, Joachim Peinke</i>	

Stability and Dynamics of Flow in a Turbulent Boundary Layer Separation Region	105
<i>Vaclav Uruba</i>	

Session 5: Special Flows

Reynolds Stress Modeling for Hypersonic Flows	111
<i>A. Bosco, B. Reinartz, S. Müller, L. Brown, R. Boyce</i>	

Forced Magneto-hydrodynamic Turbulence in Large Eddy Simulation of Compressible Fluid	115
<i>A.A. Chernyshov, K.V. Karelsky, A.S. Petrosyan</i>	

Investigations of Cavity Noise Generation on a Cylinder	119
<i>Tim Homeyer, Gerd Gülker, Christopher Haut, Nils Kirrkamm, Volker Mellert, Manfred Schultz-von Glahn, Joachim Peinke</i>	

Aerodynamic Sound Generation by Turbulence in Shear Flows	123
<i>G. Khujadze, G. Chagelishvili, M. Oberlack, A. Tevzadze, G. Bodo</i>	

Exact Coherent State with Travelling Hairpin Vortex in Plane Couette Flow	129
<i>K. Deguchi, M. Nagata</i>	

Travelling Wave Solutions in Square Duct Flow	135
<i>Shinya Okino, Masato Nagata, Håkan Wedin, Alessandro Bottaro</i>	

Main Instabilities of Coaxial Jets	139
<i>A. Segalini, A. Talamelli</i>	

Set-Up of Anisotropy in a Spanwise Rotating Channel	143
<i>S. Tardu, J. Baerenzung</i>	

Streamwise and Radial Decomposition of a Turbulent Axisymmetric Jet	147
<i>Maja Wänström, William K. George, K.E. Meyer</i>	

The Turbulent Flow in the Close-Up Region of Fractal Grids	151
<i>Stefan Weitemeyer, Robert Stresing, Michael Hölling, Joachim Peinke</i>	

Session 6: Atmospheric Boundary Layer

Statistical Characteristics of a 3×3 Neutrally Stratified Wind Turbine Array Boundary Layer	157
<i>Raúl Bayoán Cal, Max Gibson</i>	

Enhancing the Simulation of Turbulent Kinetic Energy in the Marine Atmospheric Boundary Layer	163
<i>Richard J. Foreman, Stefan Emeis</i>	
Numerical Modeling of a WECs Power Performance under the Influence of Atmospheric and Synthetic Wind Fields	167
<i>Tanja Mücke, Matthias Wächter, Patick Milan, Joachim Peinke</i>	
ABL-Flow over Hills: A Review of Theory and Wind Tunnel Studies ...	171
<i>Graciana Petersen, Bernd Leitl, Michael Schatzmann</i>	
Application of Meteorological Data in Computational Modelling of Wind over Real Terrain Topography	175
<i>K. Wędołowski, K. Bajer</i>	
Session 7: Boundary Layer	
A New Way to Determine the Wall Position and Friction Velocity in Wall-Bounded Turbulent Flows	181
<i>P.H. Alfredsson, R. Örlü</i>	
DNS of Turbulent Boundary Layers Subjected to Adverse Pressure Gradients	187
<i>Guillermo Araya, Luciano Castillo</i>	
Do Flexible Surface-Hairs Manipulate Near-Wall Turbulence?	191
<i>Christoph Brücker</i>	
Analysis of Development of Vortical Structures in a Turbulent Boundary Layer under Adverse Pressure Gradient Based on VITA Method	197
<i>Artur Drozd, Witold Elsner, Stanislaw Drobnik</i>	
New Insights into Adverse Pressure Gradient Boundary Layers	201
<i>W.K. George, M. Stanislas, J.-P. Laval</i>	
Flat Plate Boundary Layer By-Pass Transition by Joint Action of Surface Roughness and External Turbulence	205
<i>O. Hladík, P. Jonáš, O. Mazur, V. Uruba</i>	
Low Speed Streaks Instability of Turbulent Boundary Layer Flows with Adverse Pressure Gradient	209
<i>J.-P. Laval, M. Marquillie, U. Ehrenstein</i>	
Turbulent Boundary-Layer Flow: Comparing Experiments with DNS	213
<i>R. Örlü, P. Schlatter</i>	

Identifying an Artificial Turbulent Spot in the Boundary Layer	217
<i>B. Rehill, E.J. Walsh, L. Brandt, P. Schlatter, T.A. Zaki</i>	
Session 8: Wind Energy	
Comparison between Wind Tunnel and Field Experiments on Wind Turbine Wake Meandering	223
<i>S. Aubrun, T.F. Tchouaké, G. España, G. Larsen, J. Mann, F. Bingöl</i>	
Is the Actuator Disc Concept Sufficient to Model the Far-Wake of a Wind Turbine?	227
<i>S. Aubrun, G. España, S. Loyer, P. Hayden, P. Hancock</i>	
Turbulent Wind Turbine Wakes in a Wind Farm	231
<i>Arno J. Brand, Jan Willem Wagenaar</i>	
Characterization and Stochastic Modeling of Wind Speed Sequences . . .	235
<i>Calif, Emilion</i>	
Wind Turbines in ABL-Flow: A Review on Wind Tunnel Studies	239
<i>F. Cuzzola, B. Leiti, M. Schatzmann</i>	
Intermittent Fingerprints in Wind-Turbine Interactions	243
<i>Emil Hedevang, Klaus Bif, Jochen Cleve, Martin Greiner</i>	
The Relevance of Turbulence for Wind Energy Related Research	247
<i>M. Hölling, A. Morales, J. Schneemann, T. Mücke, M. Wächter, J. Peinke</i>	
The Influence of Turbulence and Vertical Wind Profile in Wind Turbine Power Curve	251
<i>A. Honrubia, A. Viguera-Rodríguez, E. Gómez-Lázaro</i>	
DNS of Actuator Disk Arrays in Ekman Boundary Layers: Preliminary Results	255
<i>R. Johnstone, P.R. Spalart, G.N. Coleman</i>	
An Attempt to Characterize the Structure of Wake Turbulence Using a Combined Experimental and Numerical Approach	259
<i>Gunner C. Larsen, K.S. Hansen, Niels Troldborg, Jakob Mann, Karen Enevoldsen, Ferhat Bingöl</i>	
Lidar Turbulence Measurements for Wind Energy	263
<i>Jakob Mann, Ameya Sathe, Julia Gottschall, Mike Courtney</i>	
Statistical Characteristics of Gusty Wind Conditionally Sampled with an Array of Ultrasonic Anemometers	271
<i>K. Taniwaki, K. Sassa, T. Hayashi, Y. Hono, K. Adachi</i>	

Free-Stream Turbulence Effects on the Flow around an S809 Wind Turbine Airfoil	275
<i>Sheilla Torres-Nieves, Víctor Maldonado, José Lebrón, Hyung-Suk Kang, Charles Meneveau, Luciano Castillo</i>	
Session 9: Convection	
3-d Measurements of the Velocity in the Boundary Layer of Turbulent Convection	283
<i>L. Li, R. du Puits</i>	
Experimental Study of the Near Wall Region of a Natural Convection Driven Flow Next to a Vertical Cylinder	287
<i>Abolfazl Shiri, William K. George</i>	
Direct Numerical Simulations of Indoor Ventilation	293
<i>Olga Shishkina, Claus Wagner</i>	
Application of 3D Particle Tracking Velocimetry in Convection	297
<i>A. Wegfrass, E. Lobutova, C. Resagk</i>	
Author Index	301

Session 1

Basic Turbulence Aspects

Scale-Energy Fluxes in Wall-Turbulent Flows

A. Cimarelli, E. De Angelis, and C.M. Casciola

Abstract. According to the Kolmogorov theory, the most important feature of high Reynolds number turbulent flows is the energy transfer from large to small scales. This energy cascade is believed to universally occur in a certain interval of scales, known as inertial range. This phenomenology has been shown to occur in a wide range of flows but not in wall-turbulence where a reverse cascade in the near-wall region is observed [1]. In order to analyse this new scenario, in the present work a study of a generalized Komogorov equation is performed. The results reveal an energy fluxes loop in the space of scales where the reverse cascade plays a central role. At the base of this phenomena it is found the anisotropic energy injection due to the action of the turbulent structures involved in the near-wall cycle. The data used for the analysis are obtained with a pseudo-spectral code in a channel at $Re_\tau = 550$. The computational domain is $8\pi h \times 2h \times 4\pi h$ with a resolution in the homogeneous directions of $\Delta x^+ = 13.5$ and $\Delta z^+ = 6.7$.

1 The Energy Transfer in Wall-Turbulence

The most important contribution to the description of the energy transfer mechanisms in turbulence is the Kolmogorov theory. Under the assumption of a statistical isotropic condition, this theory is an exact quantitative result obtained by the balance of the second order structure function, $\langle \delta u^2 \rangle$, where $\delta u_i = u_i(x_s + r_s) - u_i(x_s)$ is the fluctuating velocity increment and $\langle \cdot \rangle$ denotes ensemble average. Although this is a well known result it is useful to go back

A. Cimarelli · E. De Angelis

DIEM, Università di Bologna, Viale Risorgimento, 40136 Bologna, Italy

e-mail: andrea.cimarelli2@unibo.it, e.deangelis@unibo.it

C.M. Casciola

DIMA, Università di Roma "La Sapienza" Via Eudossiana 18, 00184 Roma, Italy

e-mail: carlomassimo.casciola@uniroma1.it

over its assumptions. The balance of $\langle \delta u^2 \rangle$, for small scales but sufficiently large so that the viscous diffusion processes may be neglected, reduces to the 4/5 law,

$$\langle \delta u_{||}^3 \rangle = -\frac{4}{5} \langle \epsilon \rangle r \quad (1)$$

where $||$ denotes longitudinal velocity increments and $\epsilon = \nu (\partial u_i \partial x_j) (\partial u_i \partial x_j)$ is the pseudo-dissipation. This relation establishes that the turbulent energy is transferred through the inertial range from large to small scales independently on the scale under consideration and with a constant rate proportional to the energy input/dissipation, $\langle \epsilon \rangle$. There is no direct energy injection and no direct energy extraction. This picture is believed to universally occur independently of the large-scale processes which feeds the turbulence, but fails in wall-turbulence where the interaction between anisotropic production and inhomogeneous spatial fluxes strongly modifies the energy cascade up to a reverse cascade in the near-wall region [1].

Wall-bounded turbulence is characterized by several processes which maybe thought as belonging to two different classes: phenomena which occur in physical space and phenomena which take place in the space of scales. The most significant aspect of the former is the spatial flux of turbulent kinetic energy and of the latter is the energy transfer among scales due to the coupling between eddies of different size. As a consequence, a full understanding of these phenomena requires a detailed description of the processes occurring simultaneously in physical and scale space. A tool for the study of these phenomena is the generalized form of the Kolmogorov equation [2]. This equation, specialized for a channel flow with a longitudinal mean velocity $U(y)$, reads,

$$\begin{aligned} \frac{\partial \langle \delta u^2 \delta u_i \rangle}{\partial r_i} + \frac{\partial \langle \delta u^2 \delta U \rangle}{\partial r_x} + 2 \langle \delta u \delta v \rangle \left(\frac{dU}{dy} \right)^* + \frac{\partial \langle v^* \delta u^2 \rangle}{\partial Y_c} = \\ - 4 \langle \epsilon^* \rangle + 2\nu \frac{\partial^2 \langle \delta u^2 \rangle}{\partial r_i \partial r_i} - \frac{2}{\rho} \frac{\partial \langle \delta p \delta v \rangle}{\partial Y_c} + \frac{\nu}{2} \frac{\partial^2 \langle \delta u^2 \rangle}{\partial Y_c^2} \end{aligned} \quad (2)$$

where $*$ denotes a mid-point average, i.e. $u_i^* = (u_i(x'_s) + u_i(x_s))/2$ and $\langle \cdot \rangle$ denotes now average in the homogeneous directions. Equation [2] is written in a four dimensional space, (r_x, r_y, r_z, Y_c) , and involves a four dimensional energy fluxes vector field $\Phi = (\Phi_{r_x}, \Phi_{r_y}, \Phi_{r_z}, \Phi_c)$,

$$\nabla \cdot \Phi(\mathbf{r}, Y_c) = \xi(\mathbf{r}, Y_c) \quad (3)$$

where $\nabla \cdot$ is a four dimensional divergence, $\Phi_r = (\Phi_{r_x}, \Phi_{r_y}, \Phi_{r_z}) = \langle \delta u^2 \delta \mathbf{u} \rangle - 2\nu \nabla_r \langle \delta u^2 \rangle$, $\Phi_c = \langle v^* \delta u^2 \rangle + 2 \langle \delta p \delta v \rangle / \rho - \nu d \langle \delta u^2 \rangle / 2dY_c$ and $\xi = 2 \langle \delta u \delta v \rangle (dU/dy)^* - 4 \langle \epsilon^* \rangle$. This form allows us to appreciate the two scale-energy fluxes occurring in wall-flows, namely Φ_r through the scales of motion and Φ_c in physical space. These fluxes assembled in the vector Φ balance with a source term ξ which accounts for the energy production and dissipation.

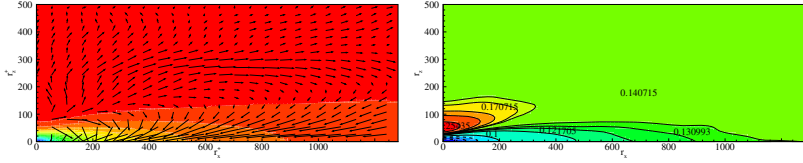


Fig. 1 Scale-space behaviour at $Y_c^+ = 20$ of the energy fluxes vector (Φ_{r_x}, Φ_{r_z}) with contour levels of $\langle \delta u^2 \rangle$ (left) and contour levels of $\xi(r_x, r_z, |Y_c)$ (right).

When this term reaches a positive value, $\xi(\mathbf{r}, Y_c) > 0$, the energy injection via turbulent production exceeds the rate of energy dissipation. Therefore, the regions of the (\mathbf{r}, Y_c) -space where $\xi > 0$ can be thought as characterized by a scale-energy excess.

The phenomena of scale-energy excess is a peculiar aspect which characterizes wall-turbulent flows with respect to homogenous flows where the source term satisfies the constrain $\xi_{hom}(\mathbf{r}) \leq 0$. In homogeneous flows an excess of scale-energy cannot be observed. The energy transfer is initialized at the largest scales by production whose amount equals the energy dissipation, $\xi_{hom}(\mathbf{r}) = 0$ for $r \rightarrow \infty$. Then, out of the limit of large scales, the source term becomes negative, $\xi_{hom}(\mathbf{r}) < 0$, due to the monotonic decrease of the production moving to small scales, see Casciola et al. [3]. Whereas, in wall-turbulence there is not a balance between energy injection and dissipation due to the presence of the inhomogeneous spatial fluxes. Indeed, it is well known that turbulent production exceeds dissipation in the buffer layer leading to an excess of scale-energy $\xi(\mathbf{r}, Y_c) > 0$ at least for larger scales. This is a very important phenomena which strongly modifies the energy fluxes pattern of wall-turbulence from those usually observed in homogeneous flows. Equation 3 describes a vector field $\Phi(\mathbf{r}, Y_c)$ where are present both energy source ($\xi(\mathbf{r}, Y_c) < 0$) and sink ($\xi(\mathbf{r}, Y_c) > 0$) regions in the (\mathbf{r}, Y_c) -space. As shown in figure 1, the energy fluxes follow a sort of loop in the space of scales. The fluxes first diverge from the energy source region feeding longer and wider turbulent fluctuations through a reverse cascade. Then, the fluxes converge to a classical forward cascade reaching the region of energy sink at the smallest dissipative scales. The energy source region and, therefore, the peak of energy production, take place deep inside the spectrum of scales, see figure 1. The energy is not introduced at the top of the spectrum and, therefore, there is not an isotropic recovery as expected in the Kolmogorov theory. The energy transfer is initialized at small scales and, diverging, leads to a strong reverse cascade. The location of the energy source region appears closely related to the action of the coherent structures involved in the near-wall cycle 4. In particular the spacing of this region suggest that this is presumably the imprint of the quasi-streamwise vortices. Indeed, most of the turbulent production of wall-turbulence is commonly associated to their action, see figure 2. Since the region of energy source is related to the streamwise vortices, the

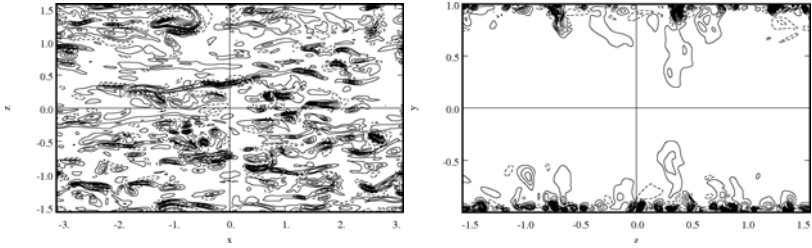


Fig. 2 Isocontour of the instantaneous turbulent production occurring in a xz -plane at $Y_c^+ = 20$ (left) and in a yz -plane (right). The production pattern appears to be the imprint of the structures involved in the near-wall cycle.

generation of the streamwise velocity streaks is a result of the reverse energy cascade. In an energetic point of view, the whole near-wall cycle corresponds to an energy fluxes loop in the space of scales.

2 Conclusions

The present work has been devoted to the assessment of the energy fluxes in the space of scales of wall-turbulent flows. The analysis has shown an unexpected loop in the space of scales of the energy fluxes where a strong reverse cascade occurs. At the base of this phenomena has been found the presence of a peak of energy production in a small-scale region of the buffer layer which causes the divergence of the energy fluxes. This energy source region appears closely related to the dynamics of the quasi-streamwise vortices belonging to the near-wall cycle.

Acknowledgements. This work has been supported by the supercomputing center C.A.S.P.U.R. with a grant of computer time.

References

1. Marati, N., Casciola, C.M., Piva, R.: Energy cascade and spatial fluxes in wall turbulence. *J. Fluid Mech.* 521 (2004)
2. Hill, R.J.: Exact second-order structure-function relationships. *J. Fluid Mech.* 468 (2002)
3. Casciola, C.M., Gualtieri, P., Benzi, R., Piva, R.: Scale-by-scale budget and similarity laws for shear turbulence. *J. Fluid Mech.* 476 (2003)
4. Jiménez, J., Pinelli, A.: The autonomous cycle of near-wall turbulence. *J. Fluid Mech.* 389 (1999)

Conservation Laws of Helically Symmetric Flows and Their Importance for Turbulence Theory

O. Kelbin, A.F. Cheviakov, and M. Oberlack

Abstract. Our present understanding of statistical 3D turbulence dynamics in the large wave number limit (or small scales) largely relies on the dissipation of turbulent kinetic energy a quantity which is invariant under all symmetry groups of Navier-Stokes equations except the scaling groups. In turn, this implies Kolmogorov's sub-range theory and to a large part our understanding of energy transfer. On the other hand in 2D turbulence, which is translational invariant in one direction, the transfer mechanism among scales is rather different since the vortex stretching mechanism is non-existing. Instead, the scale determining key invariant is enstrophy: an area integral of the vorticity squared which is one of the infinite many integral invariants (Casimirs) of 2D inviscid fluid mechanics. Hence the basic transfer mechanisms between 2D and 3D turbulence are very different. To close this gap we consider flows with a helical symmetry which is a twist of translational and rotational symmetry. The resulting equations are " $2\frac{1}{2}D$ " which means they have three independent velocity components though only two independent spatial variables. We presently show that in the inviscid limit the helically symmetric equations of motion admit a finite number of new non-trivial conservation laws comprising

- vorticity - though the basic vortex stretching mechanism is still active for helical flows and
- stream function even in a non-linear form clearly stating a non-local conservation laws since the stream-function is a line integral.

O. Kelbin · M. Oberlack

Chair of Fluid Dynamics, TU Darmstadt, Petersenstr. 30, 64287 Darmstadt, Germany

A.F. Cheviakov

Department of Mathematics and Statistics, University of Saskatchewan, Saskatoon, Canada

M. Oberlack

Center of Smart Interfaces, TU Darmstadt, Petersenstr. 32, 64287 Darmstadt, Germany

M. Oberlack

GS Computational Engineering, TU Darmstadt, Dolivostr. 15, 64293 Darmstadt, Germany

It is to be expected that the new conservation laws may give some deeper insight into turbulence dynamics and hence bridging 2D and 3D turbulence.

1 Mathematical Formulation of Helical Flows

We start with cylindrical coordinates (r, ϕ, z) and introduce helical coordinates (r, η, ξ) defined by $\eta = a\phi - bz/r^2$, $\xi = az + b\phi$, $a, b \in \mathbb{R}$, $a^2 + b^2 > 0$.

A sketch of the coordinate system is depicted in figure 1. Here h the pitch of the helix i.e for $a = 1$ we get $b = -h/(2\pi)$.

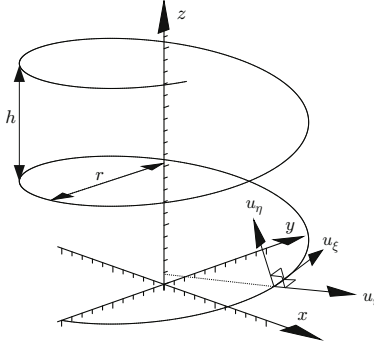


Fig. 1 Helical coordinates with a line $\xi = \text{const.}$, $\eta = \text{const.}$ lines are orthogonal to the ξ -lines.

Considering a helically symmetry implies the key assumption that the velocity vector and pressure respectively write $\mathbf{u} = u_r(t, r, \xi)\mathbf{e}_r + u_\eta(t, r, \xi)\mathbf{e}_\eta + u_\xi(t, r, \xi)\mathbf{e}_\xi$ and $p = p(t, r, \xi)$ i.e. they are all independent of η .

The Euler equations in this helical notation become:

$$\frac{u_r}{r} + \frac{\partial u_r}{\partial r} + \frac{1}{B(r)} \frac{\partial u_\xi}{\partial \xi} = 0, \quad (1a)$$

$$\frac{\partial u_r}{\partial t} + u_r \frac{\partial u_r}{\partial r} + \frac{1}{B(r)} u_\xi \frac{\partial u_r}{\partial \xi} - \frac{B^2(r)}{r} \left(\frac{b}{r} u_\xi + a u_\eta \right)^2 + \frac{\partial p}{\partial r} = 0, \quad (1b)$$

$$\frac{\partial u_\eta}{\partial t} + u_r \frac{\partial u_\eta}{\partial r} + \frac{1}{B(r)} u_\xi \frac{\partial u_\eta}{\partial \xi} + \frac{a^2 B^2(r)}{r} u_r u_\eta = 0, \quad (1c)$$

$$\frac{\partial u_\xi}{\partial t} + u_r \frac{\partial u_\xi}{\partial r} + \frac{u_\xi}{B(r)} \frac{\partial u_\xi}{\partial \xi} + \frac{2abB^2(r)}{r^2} u_r u_\eta + \frac{b^2 B^2(r)}{r^3} u_r u_\xi + \frac{1}{B(r)} \frac{\partial p}{\partial \xi} = 0, \quad (1d)$$

with the metric term $B(r) = \frac{r}{\sqrt{a^2 r^2 + b^2}}$.

The latter equations, presented in primitive variables, may be written in two another formulations i.e. stream function formulation and vorticity variables. Due to

lake of space we do not specify the equations and limit ourselves to the description of the procedure how to obtain these equations. At first we introduce a stream function $\Psi = \Psi(t, r, \xi)$ such that

$$u_r = -\frac{1}{r} \frac{\partial \Psi}{\partial \xi}, \quad u_\xi = \frac{B(r)}{r} \frac{\partial \Psi}{\partial r} \quad (2a)$$

which solves (1a) and in a second step we eliminate the pressure p via cross-differentiation and summation of (1b) and (1d). With this we obtain a PDE system of two equations for Ψ and u_η .

In case of vorticity formulation we apply a curl operator $\omega = \nabla \times \mathbf{u}$ to the momentum equations in (1), which eliminates the pressure p and we obtain 3 transport equations for the vorticity ω . The definition of vorticity components is the following:

$$\omega_r = -\frac{1}{B(r)} \frac{\partial u_\eta}{\partial \xi}, \quad \omega_\xi = \frac{\partial u_\eta}{\partial r} + \frac{a^2 B^2(r)}{r} u_\eta \quad (3a)$$

$$\omega_\eta = -\frac{\partial u_\xi}{\partial r} - \frac{u_\xi}{r} + \frac{1}{B(r)} \frac{\partial u_r}{\partial \xi} + \frac{a^2 B^2(r)}{r} u_\xi - \frac{2abB^2(r)}{r^2} u_\eta. \quad (3b)$$

2 Conservation Laws

We seek for local conservation laws using the *direct method*. The idea behind it is that each equation of the system under investigation will be multiplied with a multiplier depending on all independent and dependent variables including their derivatives up to a given order. The Euler operator will be applied to this system which in turn determines the multipliers and hence leads to local conservation laws in divergence form (see (11))

$$\frac{\partial \Phi_t}{\partial t} + \frac{\partial \Phi_r}{\partial r} + \frac{\partial \Phi_\xi}{\partial \xi} = 0. \quad (4)$$

It can further be proven (see also (11)) that this is a necessary and sufficient condition for conservation laws. For brevity we subsequently only give the densities Φ_t for the three different systems and omit the fluxes:

- Primitive variables:

$$\Phi_t^{(1)} = \frac{1}{2} r \left(u_r^2 + u_\eta^2 + u_\xi^2 \right), \quad \Phi_t^{(2)} = \frac{r}{a} B \left(-\frac{b}{r} u_\eta + a u_\xi \right), \quad (5a)$$

$$\Phi_t^{(3)} = rF \left(\sqrt{a^2 r^2 + b^2} u_\eta \right), \quad \Phi_t^{(4)} = 0, \quad (5b)$$

which include energy, momentum in z -direction, an arbitrary function of momentum in η -direction and, of course, conservation of mass which contains no time derivative.

- Stream function formulation:

$$\Phi_t^{(1)} = \frac{r}{2}u_\eta^2 + \frac{a^2r^2 - b^2}{2(a^2r^2 + b^2)^2}\Psi\Psi_r - \frac{B^2}{2r}\Psi\Psi_{rr} - \frac{1}{2r}\Psi\Psi_{\xi\xi}, \quad (6a)$$

$$\Phi_t^{(2)} = -\frac{2bB}{a}u_\eta - \frac{4b^2B^2}{r^3}\Psi - r\Psi_{\xi\xi}, \quad \Phi_t^{(3)} = -\frac{G(t)}{r}\Psi_{\xi\xi}. \quad (6b)$$

- Vorticity formulation:

$$\Phi_t^{(1)} = \frac{b^2B(r)^4}{r^2}\xi\omega_r - \frac{ar^2B(r)}{2b}\omega_\eta, \quad \Phi_t^{(2)} = 0, \quad \Phi_t^{(3)} = H(t, r)\omega_r, \quad (7a)$$

$$\Phi_t^{(4)} = (a^2r^2 + 2b^2)B(r)^4\xi\omega_r + \frac{bB(r)r^2}{2a}\omega_\eta, \quad (7b)$$

$$\Phi_t^{(5)} = \frac{2abB(r)^4I(t)}{r^2}\xi\omega_r + B(r)I(t)\omega_\eta, \quad (7c)$$

$$\Phi_t^{(6)} = \left(-\frac{a^2B(r)^2}{r}J(t, r, \xi) + J(t, r, \xi)_r \right) B(r)\omega_r + J(t, r, \xi)_\xi\omega_\xi \quad (7d)$$

All the latter conserved quantities do not trivially relate to the classical conservation laws and may need special interpretation.

The analysis of the Navier-Stokes equations for all three formulations did not reveal new conservation laws. In case of primitive variables we obtain same fluxes as in (5) except $\Phi_t^{(1)}$, i. e. conserved quantities for Navier-Stokes equations are momentum in z -direction, an arbitrary function of momentum in η -direction and mass. The energy does not stay preserved. The conserved quantities for streamfunction and vorticity formulations also form a subset of the conserved quantities for Euler equations as is to be expected.

Reference

1. Bluman, G.W., Cheviakov, A.F., Anco, S.C.: Applications of Symmetry Methods to Partial Differential Equations. Springer, Applied Mathematical Sciences, Vol. 168 (2010)

Velocity/Pressure-Gradient Correlation Modelling for Improved Prediction of Reattachment and Relaxation

C. Lo, I. Vallet, and B.A. Younis

Abstract. The computation of complex flows with large separation is one of the numerous instances where second-moment closures outperform two-equations models. Previous studies with the Reynolds-stress model developed by Gerolymos-Vallet [3] (GV RSM) indicate that separation is quite accurately predicted, but also that there is room for improvement in the reattachment and relaxation region. Extensive testing suggests that the modelling of the pressure terms in the Reynolds-stress transport equations has the greatest impact on the prediction of both separation and reattachment. We propose a second-moment closure including a pressure-velocity gradient model with an additional term in the basis of the slow-part redistribution tensor proposed by Lumley [7] and a closure for the pressure-diffusion tensor which model directly the divergence of the pressure-velocity correlation. The present Reynolds-stress model is validated against a shock-wave/turbulent-boundary-layer interaction on a compression ramp and compared with two second-moment closures and the linear two-equations model of Launder-Sharma [5] ($LS\ k - \epsilon$).

1 Introduction

The purpose of the present paper is to develop a second-moment closure, separately modelling the anisotropy of dissipation and redistribution (Eq. 1), maintaining the

C. Lo, Research Assistant
UPMC, case 161, 4 place Jussieu, 75005 Paris France
e-mail: celine.lo@upmc.fr

I. Vallet, Assistant Professor
UPMC, case 161, 4 place Jussieu, 75005 Paris France
e-mail: isabelle.vallet@upmc.fr

B. A. Younis, Professor
Dept. of Civil and Environmental Engineering, University of California,
Davis CA 95616, USA
e-mail: bayounis@ucdavis.edu

satisfactory prediction of separation of the GV RSM [3] and with a specific model for pressure diffusion term $d_{ij}^{(p)}$ (Eq. 2), which was shown in previous studies [8, 9] to improve the prediction of reattachment and relaxation.

The flow is modelled by the Favre-Reynolds-averaged Navier-Stokes equations [3, 10], coupled with the appropriate modelled turbulence-transport equations. The exact transport equations for the Favre-Reynolds-averaged Reynolds-stresses are

$$\begin{aligned}
 \underbrace{\frac{\partial \bar{\rho} \widetilde{u_i'' u_j''}}{\partial t} + \frac{\partial (\bar{\rho} \widetilde{u_i'' u_j''} \tilde{u}_\ell)}{\partial x_\ell}}_{\text{convection } C_{ij}} &= \underbrace{\frac{\partial}{\partial x_\ell} (-\bar{\rho} \widetilde{u_i'' u_j'' u_\ell''} - \overline{p' u_j''} \delta_{i\ell} - \overline{p' u_i''} \delta_{j\ell} + \overline{u_i'' \tau_{j\ell}} + \overline{u_j'' \tau_{i\ell}})}_{\text{diffusion } d_{ij} = d_{ij}^u + d_{ij}^p} \\
 \underbrace{\left(-\bar{\rho} \widetilde{u_i'' u_\ell''} \frac{\partial \tilde{u}_j}{\partial x_\ell} - \bar{\rho} \widetilde{u_j'' u_\ell''} \frac{\partial \tilde{u}_i}{\partial x_\ell} \right)}_{\text{production } P_{ij}} &+ \underbrace{p' \left(\frac{\partial u_i''}{\partial x_j} + \frac{\partial u_j''}{\partial x_i} - \frac{2}{3} \frac{\partial u_k''}{\partial x_k} \delta_{ij} \right)}_{\text{redistribution } \phi_{ij}} + \underbrace{\frac{2}{3} \overline{p' \frac{\partial u_k''}{\partial x_k}} \delta_{ij}}_{\phi_p \cong 0} \\
 - \underbrace{\left(\tau_{j\ell}' \frac{\partial u_i''}{\partial x_\ell} + \tau_{i\ell}' \frac{\partial u_j''}{\partial x_\ell} \right)}_{\text{dissipation } \bar{\rho} \varepsilon_{ij}} &+ \underbrace{\left(-\overline{u_i''} \frac{\partial \bar{p}}{\partial x_j} - \overline{u_j''} \frac{\partial \bar{p}}{\partial x_i} + \overline{u_i''} \frac{\partial \tau_{j\ell}}{\partial x_\ell} + \overline{u_j''} \frac{\partial \tau_{i\ell}}{\partial x_\ell} \right)}_{\text{density fluctuation effects } K_{ij} \cong 0} \quad (1)
 \end{aligned}$$

where the symbol $\check{(\cdot)}$ is used to denote a function of average quantities that is neither a Reynolds-averaged $\overline{(\cdot)}$ nor a Favre-average $\widetilde{(\cdot)}$, $(\cdot)''$ are Favre-fluctuations and $(\cdot)'$ are nonweighted-fluctuations [3]. Convection and production are exact terms whereas the diffusion due to turbulent transport $d_{ij}^u = d_{ij}^{(u)}$ and molecular viscosity d_{ij}^p , the pressure-strain correlation ϕ_{ij} and the dissipation $\bar{\rho} \varepsilon_{ij}$ terms require modelling. The turbulent-length scale was determined by solving the Launder-Sharma [5] modified dissipation-rate $\varepsilon^* = \varepsilon - 2\check{\nabla}(\text{grad}\sqrt{k})^2$ transport-equation, where $k = \overline{u_i'' u_i''} / 2$ is the turbulent-kinetic energy and $\varepsilon = \varepsilon_{ii} / 2$ its dissipation-rate. x_ℓ are the Cartesian space coordinates, u_i are the velocity components, ρ is the density, p is the pressure, τ_{ij} is the viscous stress tensor, and δ_{ij} is the Kronecker symbol.

2 Present Reynolds-Stress Model

We maintain, in the modelling approach the splitting of the velocity/pressure-gradient tensor $\Pi_{ij} = \phi_{ij} + d_{ij}^{(p)}$ into the pressure-diffusion term $d_{ij}^{(p)} = \partial_{x_\ell} (-\overline{u_i' p'} \delta_{j\ell} - \overline{u_j' p'} \delta_{i\ell})$ where $\overline{p' u_j'}$ is the pressure-velocity correlation, the redistribution term ϕ_{ij} and the pressure-dilation correlation ϕ_p which is neglected. In the present closure, the pressure-diffusion model $d_{ij}^{(p)}$ contains a Lumley-type [7] slow quasi-homogeneous term, with a slow and a rapid inhomogeneous terms containing $\text{grad } \varepsilon^* \otimes \text{grad } \varepsilon^*$ and $\text{grad } k \otimes \text{grad } k$ respectively

$$\frac{d_{ij}^{(p)}}{\bar{\rho}} = C^{\text{SP1}} \frac{k^3}{\varepsilon^3} \frac{\partial \varepsilon^*}{\partial x_i} \frac{\partial \varepsilon^*}{\partial x_j} + C^{\text{SP2}} \frac{\partial (u''_m \widetilde{u''_m u''_j} \delta_{i\ell} + u''_m \widetilde{u''_m u''_i} \delta_{j\ell})}{\partial x_\ell} + C^{\text{RP}} \frac{k^2}{\varepsilon^2} \check{S}_{k\ell} a_{\ell k} \frac{\partial k}{\partial x_i} \frac{\partial k}{\partial x_j}$$

$$C^{\text{SP1}} = C^{\text{RP}} = -0.005; C^{\text{SP2}} = -0.022; a_{ij} = \frac{\widetilde{u''_i u''_j}}{k} - \frac{2}{3} \delta_{ij}; \check{S}_{ij} = \frac{1}{2} \left(\frac{\partial \widetilde{u''_i}}{\partial x_j} + \frac{\partial \widetilde{u''_j}}{\partial x_i} \right) \quad (2)$$

The redistribution term ϕ_{ij} , which is zero in $k - \varepsilon$ models ($\phi_{\ell\ell} = 0$), is the most important term in second-moment closures. We propose, a formulation where ϕ_{ij} is modelled separately from the dissipation term $\bar{\rho} \varepsilon_{ij}$

$$\begin{aligned} \phi_{ij} = & -C_\phi^{\text{SH1}} \bar{\rho} \varepsilon^* a_{ij} + C_\phi^{\text{SI1}} \frac{\varepsilon^*}{k} \left[\bar{\rho} \widetilde{u''_m u''_m e''_n e''_m} \delta_{ij} - \frac{3}{2} \bar{\rho} \widetilde{u''_m u''_i e''_n e''_j} - \frac{3}{2} \bar{\rho} \widetilde{u''_m u''_j e''_n e''_i} \right] \\ & - C_\phi^{\text{SH2}} \bar{\rho} \frac{k}{\varepsilon} \frac{\partial k}{\partial x_\ell} \left[a_{ik} \frac{\partial \widetilde{u''_k u''_j}}{\partial x_\ell} + a_{jk} \frac{\partial \widetilde{u''_k u''_i}}{\partial x_\ell} - \frac{2}{3} \delta_{ij} a_{mk} \frac{\partial \widetilde{u''_k u''_m}}{\partial x_\ell} \right] \\ & + C_\phi^{\text{SI2}} \left[\phi_{nm}^{\text{SH2}} e''_n e''_m \delta_{ij} - \frac{3}{2} \phi_{in}^{\text{SH2}} e''_n e''_j - \frac{3}{2} \phi_{jn}^{\text{SH2}} e''_n e''_i \right] \\ & - C_\phi^{\text{RH}} \left(P_{ij} - \frac{1}{3} \delta_{ij} P_{mm} \right) + C_\phi^{\text{RI}} \left[\phi_{nm}^{\text{RH}} e''_n e''_m \delta_{ij} - \frac{3}{2} \phi_{in}^{\text{RH}} e''_n e''_j - \frac{3}{2} \phi_{jn}^{\text{RH}} e''_n e''_i \right] \quad (3) \end{aligned}$$

where the first term of slow-part $\phi_{ij}^{\text{SH1}} + \phi_{ij}^{\text{SI1}}$ is function of the modified dissipation-rate ε^* to reach easily the correct zero-value of the velocity/pressure-gradient tensor Π_{ij} at the wall. The coefficients C_ϕ^{SI1} , C_ϕ^{SI2} and C_ϕ^{RI} which mimic distance from the wall effects but without the use of any wall-topology-related parameters (such as geometric distance from the wall), were calibrated on the DNS basis of Gerolymos-Senechal-Vallet [2] in a fully developed turbulent plane channel flow ($Re_\tau = 180$). The unit-vector \mathbf{e}^1 which points in the the direction of inhomogeneity of the turbulent field was introduced [3] to replace the geometric normal to the wall. The rapid-part closure $\phi_{ij}^{\text{RH}} + \phi_{ij}^{\text{RI}}$ developed by Gerolymos-Vallet [3] was not modified in the present study.

3 Models Comparison on a Supersonic Compression Ramp

The present closure was assessed by comparison with available experimental data on the compression-ramp configuration (Fig. 1) studied by Ardonneau [1]. The computational method used to solve the compressible Navier-Stokes equations with the turbulence closure is described in [4]. The inflow conditions as well as the computational grid details are given in [10]. A second-moment closure, which corresponds to the GV RSM [3] with the homogeneous-rapid-redistribution coefficient C_ϕ^{RH} proposed by Launder-Shima [6] (hereafter GV-LS RSM), was developed to analyse the redistribution-tensor ϕ_{ij} influence. The linear LS $k - \varepsilon$ closure and the GV-LS RSM are not able to predict the separation zone and as a consequence seem to give the best result in the reattachment region. On the contrary, the present closure and the GV RSM, which use the C_ϕ^{RH} developed by Gerolymos-Vallet [3], are in good agreement with experimental data. However the present RSM, which closes

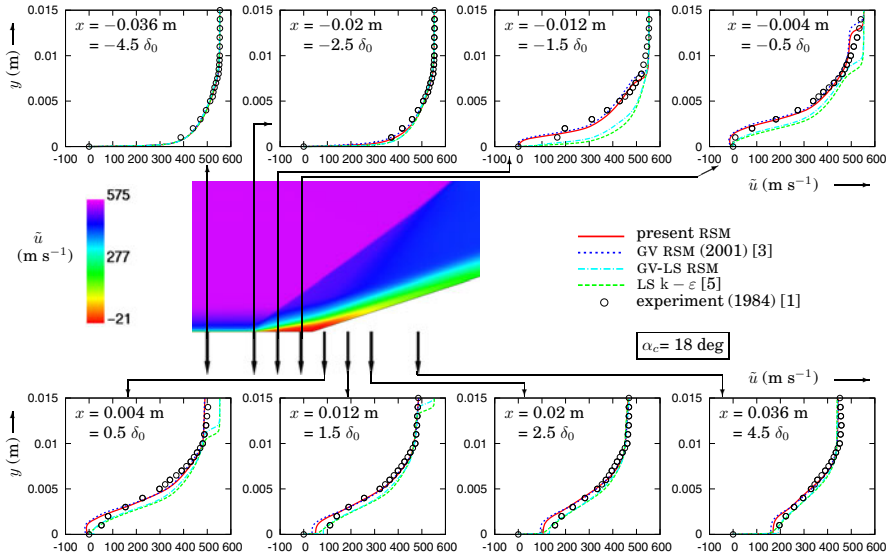


Fig. 1 Comparison of grid-converged computations with measurements [1] of x-wise mean velocity at various axial stations, for the Ardonceau $\alpha = 18$ deg compression-ramp interaction ($M_\infty = 2.25$, $Re_0 = 7 \times 10^3$).

the pressure-diffusion tensor, is slightly better after the corner ($x > 0$), especially in the relaxation region ($x \geq 2.5\delta_0$).

4 Conclusions

A new second-moment closure was assessed on a shock-wave/turbulent-boundary-layer interaction and compared with two other RSMs and a two-equations closure focusing on the prediction of the detachment and reattachment points. The predicting capability of full (differential) RSMs over a classical linear eddy-viscosity model is observed, confirming the study of Yakinthos [11] for attached flow in a 90-deg duct. The importance of the redistribution tensor to predict separation point is clearly identified while the pressure-diffusion closure slightly improve the prediction of the reattachment zone.

References

1. Ardonceau, P.L.: The structure of turbulence in a supersonic shock-wave/boundary-layer interaction. *AIAA J.* 22(9), 1254–1262 (1984)
2. Gerolymos, G.A., Sénéchal, D., Vallet, I.: Performance of very-high-order upwind schemes for DNS of compressible wall-turbulence. *Int. J. Num. Meth. Fluids* 63, 769–810 (2010)

3. Gerolymos, G.A., Vallet, I.: Wall-normal-free near-wall Reynolds-stress closure for 3-D compressible separated flows. *AIAA J.* 39(10), 1833–1842 (2001)
4. Gerolymos, G.A., Vallet, I.: Mean-flow-multigrid for implicit Reynolds-stress-model computations. *AIAA J.* 43(9), 1887–1898 (2005)
5. Launder, B.E., Sharma, B.I.: Application of the energy dissipation model of turbulence to the calculation of flows near a spinning disk. *Lett. Heat Mass Transf.* 1, 131–138 (1974)
6. Launder, B.E., Shima, N.: 2-moment closure for the near-wall sublayer: Development and application. *AIAA J.* 27(10), 1319–1325 (1989)
7. Lumley, J.L.: Computational modeling of turbulent flows. *Adv. Appl. Mech.* 18, 123–176 (1978)
8. Sauret, E., Vallet, I.: Near-wall turbulent pressure diffusion modelling and influence in 3-D secondary flows. *ASME J. Fluids Eng.* 129(5), 634–642 (2007)
9. Vallet, I.: Reynolds-stress modelling of 3-D secondary flows with emphasis on turbulent diffusion closure. *ASME J. Appl. Mech.* 74(6), 1142–1156 (2007)
10. Vallet, I.: Reynolds-stress modelling of $M = 2.25$ shock-wave/turbulent-boundary-layer interaction. *Int. J. Num. Meth. Fluids* 56(5), 525–555 (2008)
11. Yakinthos, K., Vlahostergios, Z., Goulas, A.: Modeling the flow in a 90° rectangular duct using one Reynolds-stress and two eddy-viscosity models. *Int. J. of Heat and Fluid Flow* 29, 35–47 (2008)

Turbulence without Richardson-Kolmogorov Cascade

J.C. Vassilicos and N. Mazellier

Abstract. We study turbulence generated by low-blockage space-filling fractal square grids [5]. This device creates a multiscale excitation of the fluid flow. Such devices have been proposed as alternative and complementary tools for the investigation of turbulence fundamentals, modelling and applications [3, 5, 6]. New insights on the fundamentals of homogeneous turbulence have been found, showing in particular that the small scales are not universal beyond small corrections caused by intermittency, finite Reynolds number and anisotropy. The unprecedented possibilities offered by these devices also open new attractive perspectives in applications involving mixing, combustion and flow management and control.

1 Introduction

A close approximation of homogeneous and isotropic turbulence can be achieved by means of grid-generated turbulence (see e.g. [1]). Even though its relevance to the study of turbulence fundamentals is clear, grid-generated turbulence produced by standard devices is often restricted to low Reynolds numbers. Deeper insights and understanding of turbulence physics (regarding, for instance, the mechanisms of interscale energy transfers) require new experimental approaches. Turbulence generated by multiscale/fractal grids is one such new approach [2]. Multiscale/fractal grids are new devices made from the superposition of a given pattern reproduced and multiplied at smaller scales (see Figure 1). Such a device is expected to excite a

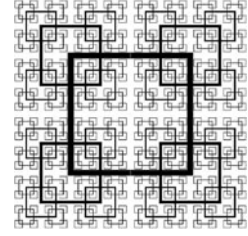
J.C. Vassilicos

Turbulence, Mixing and Flow Control Group, Department of Aeronautics
Institute for Mathematical Sciences
Imperial College London, London, SW7 2BY, UK
e-mail: j.c.vassilicos@imperial.ac.uk

N. Mazellier

Institut PRISME, Université d'Orléans, 45072 Orléans, France
e-mail: nicolas.mazellier@univ-orleans.fr

Fig. 1 Typical example of a square multiscale/fractal grid. In this particular example, the grid has $N = 5$ fractal iterations.



broad range of turbulent scales, unlike standard regular grids. The turbulence generated by some such devices has already led to results which have shed serious doubt on the universality of the small-scale turbulence [3]. An attempt to account for some of these results has recently been made in terms of a single length-scale theory [7]. Here we report new insights on turbulence generated by space-filling fractal square grids and we discuss how the single-scale theory proposed in [7] accounts for our results.

2 Results

The streamwise evolution of the turbulence intensity measured along the centerline downstream of several fractal square grids is plotted in Figure 2. As reported in [2], we observe a protracted region closer to the grid where the turbulence builds-up until it reaches a maximum at $x = x_{peak}$ and then decays.

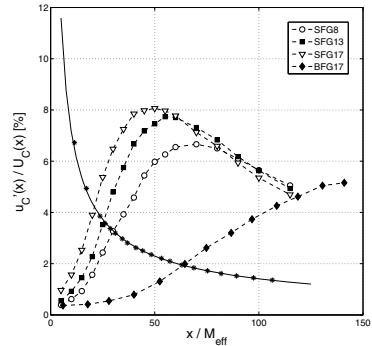


Fig. 2 Turbulence intensity vs streamwise distance for four different fractal grids. See [4] for captions. The symbols (*) represent a standard regular grid.

The location of the turbulence peak is determined by the large-scale geometry of the fractal grids, but the observed fact that the turbulence is approximately homogeneous and isotropic shortly beyond x_{peak} is determined by the multiple scales of the grid (see [4] for more details). It is worth noting that the turbulence levels achieved by means of fractal square grids are much higher than with standard regular grids (* symbols in Figure 2) and comparable to those reported for active grids [6].

A deeper investigation of the turbulent flow has been performed by studying the turbulent length-scales, in particular the integral length-scale L_u (characteristic of the energy containing eddies) and the Taylor micro-scale λ (characteristic of the smallest turbulent eddies). The ratio L_u/λ computed for various inlet velocities U_∞ in the decaying region (i.e. $x > x_{peak}$) of fractal square grid turbulence is plotted in Figure 3 as a function of the Taylor-based Reynolds number Re_λ . It turns out that the ratio L_u/λ is independent of Re_λ for a given U_∞ . This is a huge departure from the usual relationship found in standard fully developed turbulence, i.e. $L_u/\lambda \sim Re_\lambda$. This result seriously calls into question the statement that the dissipation constant and the interscale dynamics of small-scale turbulence are universal for large Re_λ .

Our results may be accounted for by means of a single length-scale self-preserving theory [7]. Starting from the spectral energy equation

$$\frac{\partial}{\partial t} E(k, t) = T(k, t) - 2\nu k^2 E(k, t), \quad (1)$$

and considering solutions of the form

$$E(k, t) = E_s(t, U_\infty, Re_0, *) f(kl(t), Re_0, *), \quad (2)$$

$$T(k, t) = T_s(t, U_\infty, Re_0, *) g(kl(t), Re_0, *), \quad (3)$$

where $Re_0 \equiv \frac{U_\infty l_0}{\nu}$ is the global Reynolds number based on the lateral thickness of the thickest bars on the fractal grid, $l(t) = l(t, Re_0, *)$ is the postulated unique characteristic length-scale of the turbulence, the argument $*$ represents any dependence on the initial/boundary conditions and the functions f and g are dimensionless. Combining Equations (1), (2) and (3) and extrapolating in a way explained in [4] (including an assumption of a $-5/3$ exponent at high Reynolds number) yields

$$E_u(k_x, x) = u'^2(x) L_0 (k_x L_0)^{-5/3} H_u(k_x L_0 Re_0^{-3/4}), \quad (4)$$

$$\varepsilon \approx 1.5 u'^2 U_\infty / x_{peak}, \quad (5)$$

for asymptotically high values of Re_0 , where L_0 is the length of the longest bars on the grid. Our experimental results lend support to the single scale scaling of the energy spectrum as shown in Figure 4.

Fig. 3 Turbulent length-scale ratio vs the Taylor-based Reynolds number. The dashed line represents values computed for standard fully developed turbulence, see [4].

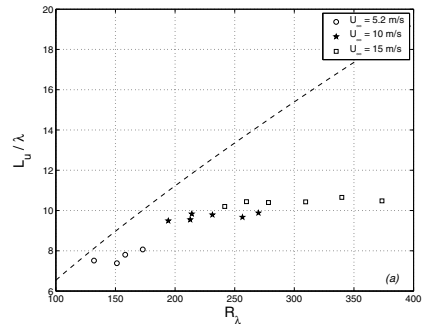
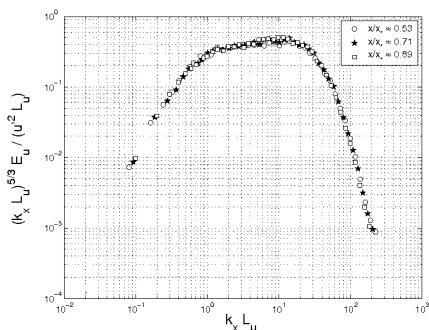


Fig. 4 Compensated 1D Energy spectrum computed at various distances from the grid in the decay region. Large-scale quantities are used for the normalization.



3 Conclusion

We have found new insights on turbulence generated by means of fractal square grids, including an understanding of profiles such as shown in Figure 2. A single length-scale self-preserving theory can account for the departure from a commonly accepted cornerstone assumption of fully-developed turbulence, i.e. that the dissipation constant is universal for high enough Reynolds number. Our study suggests that the turbulence generated by fractal grids is incompatible with the so-called Richardson-Kolmogorov cascade.

References

1. Comte-Bellot, G., Corrsin, S.: The use of a contraction to improve the isotropy of grid-generated turbulence. *J. Fluid Mech.* 25, pt. 4, 657 (1966)
2. Hurst, D., Vassilicos, J.C.: Scalings and decay of fractal-generated turbulence. *Phys. Fluids* 19, 035013 (2007)
3. Seoud, R.E., Vassilicos, J.C.: Dissipation and decay of fractal-generated turbulence. *Phys. Fluids* 19, 105–108 (2007)
4. Mazellier, N., Vassilicos, J.C.: Turbulence without Richardson-Kolmogorov cascade. *Phys. Fluids* 22, 075101 (2010)
5. Mazellier, N., Vassilicos, J.C.: The turbulence dissipation constant is not universal because of its universal dependence on large-scale flow topology. *Phys. Fluids* 20, 015101 (2008)
6. Mydlarski, L., Warhaft, Z.: On the onset of high-Reynolds-number grid-generated wind tunnel turbulence. *J. Fluid Mech.* 320, 331 (1996)
7. George, W.K., Wang, H.: The exponential decay of homogeneous turbulence. *Phys. Fluids* 21, 025108 (2009)

New Statistical Symmetries of the Two-Point Correlation Equations for Turbulent Flows

Andreas M. Rosteck and Martin Oberlack

Abstract. We briefly introduce the two-point correlation equations based on the Navier-Stokes equations for an incompressible fluid. For this special case we determine the set of Lie symmetries, which can be calculated from the classical symmetries of the Navier-Stokes equations and further we present new symmetries, so called statistical symmetries. Finally we give examples where these symmetries can be used, e.g. for wall bounded turbulence and decaying turbulence scaling laws.

1 Two-Point Correlation Equations

The starting point of the entire analysis is based on the Navier-Stokes equations under the assumption of a Newtonian material with constant density ρ and viscosity ν . Using the Reynolds decomposition we gain the averaged Navier-Stokes equations for the mean velocity \bar{U} and pressure \bar{P}

$$\frac{\partial \bar{U}_k}{\partial x_k} = 0, \quad \frac{\partial \bar{U}_i}{\partial t} + \bar{U}_k \frac{\partial \bar{U}_i}{\partial x_k} = -\frac{\partial \bar{P}}{\partial x_i} + \nu \frac{\partial^2 \bar{U}_i}{\partial x_k \partial x_k} - \frac{\partial \overline{u_i u_k}}{\partial x_k}, \quad i = 1, 2, 3, \quad (1)$$

where the pressure P was already normalized with the density and the unknown Reynolds stress tensor $\overline{u_i u_k}$ has appeared. Therein u is the fluctuating velocity and p is the fluctuating pressure to be used below. Instead of the Reynolds stress tensor transport equation approach which contains additional four unclosed tensors we adopt the multi-point correlation approach.

Andreas M. Rosteck · Martin Oberlack

Chair of Fluid Dynamics, Department of Mechanical Engineering,

TU Darmstadt, Petersenstr. 30

64287 Darmstadt, Germany

Martin Oberlack

Center of Smart Interfaces, TU Darmstadt, Petersenstr. 32, 64287 Darmstadt, Germany

Martin Oberlack

GS Computational Engineering, TU Darmstadt, Dolivostr. 15, 64293 Darmstadt, Germany

e-mail: rosteck@fdy.tu-darmstadt.de, oberlack@fdy.tu-darmstadt.de

The idea of two- and multi-point correlation equations in turbulence was presumably first established by Friedmann and Keller [3]. In our previous work [6] we considered the full infinite set of MPC equations in order to gain the general symmetries. However, therein the analysis was based on instantaneous values U and P and correlations based thereon.

In the following we will focus on a lowest order correlations, the two-point correlation (TPC) which is entirely based on the fluctuating quantities u and p . The TPC tensor for the velocity is defined by

$$R_{ij}(x, y) = \overline{u_i(x)u_j(y)} \quad (2)$$

and apparently we may deduce the limiting relation $\lim_{y \rightarrow x} R_{ij}(x, y) = \overline{u_i u_j}(x)$.

The governing equations for the TPC are defined

$$\begin{aligned} & \frac{\partial R_{ij}(x, y)}{\partial t} + \bar{U}_k(x) \frac{\partial R_{ij}(x, y)}{\partial x_k} + \bar{U}_k(y) \frac{\partial R_{ij}(x, y)}{\partial y_k} + R_{ik}(x, y) \frac{\partial \bar{U}_j(y)}{\partial y_k} \\ & + R_{kj}(x, y) \frac{\partial \bar{U}_i(x)}{\partial x_k} + \frac{\partial P_{i[2]}(x, y)}{\partial y_j} + \frac{\partial P_{j[1]}(x, y)}{\partial x_i} - \nu \frac{\partial^2 R_{ij}(x, y)}{\partial x_k \partial x_k} \\ & - \nu \frac{\partial^2 R_{ij}(x, y)}{\partial y_k \partial y_k} - \bar{U}_j(y) \frac{\partial R_{ik}(x, x)}{\partial x_k} - \bar{U}_i(x) \frac{\partial R_{kj}(y, y)}{\partial y_k} + \frac{\partial R_{ijk}(x, y, x)}{\partial x_k} \\ & + \frac{\partial R_{ijk}(x, y, y)}{\partial y_k} = 0, \quad 1 \leq i, j \leq 3, \end{aligned} \quad (3)$$

where $P_{i[1]}(x, y) = \overline{p(x)u_i(y)}$, $P_{i[2]}(x, y) = \overline{p(y)u_i(x)}$ and $R_{ijk}(x, y, z) = \overline{u_i(x)u_j(y)u_k(z)}$. Furthermore, all tensors have to obey continuity equations.

2 Symmetries of the Two-Point Correlation Equations

We show that the Lie symmetries of (3) extended by the continuity equations have two different origins. The first set originates from the Navier-Stokes, respectively the Euler equations, from which those symmetries transfer to the TPC (see [5]). We primarily limit ourselves to the global form of the symmetries and assume the limit of very high Reynolds' numbers so that we will only deal with the corresponding Euler symmetries. Hence, the first set of symmetries has the form

$$\begin{aligned} \bar{T}_l : t^* &= t + a_1, \quad x^* = x, \quad y^* = y, \quad \bar{U}_i^* = \bar{U}_i, \quad \bar{P}^* = \bar{P}, \\ R_{ij}^* &= R_{ij}, \quad R_{ijk}^* = R_{ijk}, \quad P_{i[l]}^* = P_{i[l]}, \\ \bar{T}_{s1} : t^* &= t, \quad x^* = e^{a_2} x, \quad y^* = e^{a_2} y, \quad \bar{U}_i^* = e^{a_2} \bar{U}_i, \quad \bar{P}^* = e^{2a_2} \bar{P}, \\ R_{ij}^* &= e^{2a_2} R_{ij}, \quad R_{ijk}^* = e^{3a_2} R_{ijk}, \quad P_{i[l]}^* = e^{3a_2} P_{i[l]}, \\ \bar{T}_{s2} : t^* &= e^{a_3} t, \quad x^* = x, \quad y^* = y, \quad \bar{U}_i^* = e^{-a_3} \bar{U}_i, \quad \bar{P}^* = e^{-2a_3} \bar{P}, \\ R_{ij}^* &= e^{-2a_3} R_{ij}, \quad P_{i[l]}^* = e^{-3a_3} P_{i[l]}, \end{aligned}$$

$$\begin{aligned}
\bar{T}_4 - \bar{T}_6 : t^* &= t, \quad x^* = \mathbf{a} \cdot x, \quad r_{(l)}^* = \mathbf{a} \cdot r_{(l)}, \quad \bar{U}^* = \mathbf{a} \cdot \bar{U}, \quad \bar{P}^* = \bar{P}, \\
R_{ij}^* &= \mathbf{A}_{\{2\}} \otimes R_{ij}, \quad P_{i[l]}^* = \mathbf{A}_{\{1\}} \otimes P_{i[l]}, \\
\bar{T}_{g,\alpha} : t^* &= t, \quad x_i^* = x_i + f_\alpha(t) \delta_{\alpha,i}, \quad y_i^* = y_i + f_\alpha(t) \delta_{\alpha,i}, \quad \bar{U}_i^* = \bar{U}_i + f'_\alpha(t) \delta_{\alpha,i} \\
\bar{P}^* &= \bar{P} - x_\alpha f''_\alpha(t), \quad R_{ij}^* = R_{ij}, \quad R_{ijk}^* = R_{ijk}, \quad P_{i[l]}^* = P_{i[l]}, \\
\bar{T}_p : t^* &= t, \quad x^* = x, \quad y^* = y, \quad \bar{U}^* = \bar{U}, \quad \bar{P}^* = \bar{P} + f_4(t), \\
R_{ij}^* &= R_{ij}, \quad R_{ijk}^* = R_{ijk}, \quad P_{i[l]}^* = P_{i[l]}
\end{aligned} \tag{4}$$

with $1 \leq \alpha, i, j \leq 3, 1 \leq l \leq 2$ and $f_1(t) - f_4(t)$ arbitrary but smooth functions. $\bar{T}_4 - \bar{T}_6$ represent the rotation symmetries since \mathbf{A} is a concatenation of rotation matrices as $A_{i(0)j(0)i(1)j(1)\dots i(n)j(n)} = a_{i(0)j(0)} a_{i(1)j(1)} \dots a_{i(n)j(n)}$.

The second set of symmetries is taken from [6] where they were derived. It is important to mention that they have no corresponding symmetries in the Navier-Stokes or Euler equations.

The first one is a scaling of all velocity and pressure tensors,

$$\begin{aligned}
\bar{T}_{sn} : t^* &= t, \quad x^* = x, \quad y^* = y, \quad \bar{U}_i^* = e^{as} \bar{U}_i, \quad \bar{P}^* = e^{as} \bar{P}, \\
R_{ij}^* &= e^{as} [R_{ij} + (1 - e^{as}) \bar{U}_i \bar{U}_j], \quad P_{i[l]}^* = e^{as} [P_{i[l]} + (1 - e^{as}) \bar{U}_i \bar{P}], \\
R_{ijk}^* &= R_{ijk} + e^{as} (1 - e^{as}) [\bar{U}_i R_{jk} + \bar{U}_j R_{ik} + \bar{U}_k R_{ij}] \\
&\quad + e^{as} (1 + 3e^{as} - 2e^{2as}) \bar{U}_i \bar{U}_j \bar{U}_k.
\end{aligned} \tag{5}$$

A second type of symmetries of a rather different kind refer to translation symmetries of the mean velocity and the correlation tensors

$$\begin{aligned}
\bar{T}_{H\alpha} : t^* &= t, \quad x^* = x, \quad y^* = y, \quad \bar{U}_i^* = \bar{U}_i + \delta_{\alpha,i} C_\alpha, \quad \bar{P}^* = \bar{P}, \quad P_{i[l]}^* = P_{i[l]} - \delta_{\alpha,i} C_\alpha P_{i[l]}, \\
R_{ij}^* &= R_{ij} - C_\alpha (\delta_{j,\alpha} \bar{U}_i + \delta_{i,\alpha} \bar{U}_j) - C_\alpha^2 \delta_{i,\alpha} \delta_{j,\alpha} \\
R_{ijk}^* &= R_{ijk} + 2C_\alpha^3 \delta_{i,\alpha} \delta_{j,\alpha} \delta_{k,\alpha} + 2C_\alpha^2 (\bar{U}_i \delta_{j,\alpha} \delta_{k,\alpha} + \bar{U}_j \delta_{i,\alpha} \delta_{k,\alpha} + \bar{U}_k \delta_{i,\alpha} \delta_{j,\alpha}) \\
&\quad - C_\alpha (R_{ij} \delta_{k,\alpha} + R_{ik} \delta_{j,\alpha} + R_{jk} \delta_{i,\alpha} - \bar{U}_i \bar{U}_j \delta_{k,\alpha} - \bar{U}_i \bar{U}_k \delta_{j,\alpha} - \bar{U}_j \bar{U}_k \delta_{i,\alpha}) \\
\bar{T}_{H\alpha,\beta} : t^* &= t, \quad x^* = x, \quad y^* = y, \quad \bar{U}_i^* = \bar{U}_i, \quad \bar{P}^* = \bar{P}, \quad P_{i[l]}^* = P_{i[l]}, \\
R_{ij}^* &= R_{ij} + \delta_{\alpha\beta,ij} C_{\alpha,\beta}, \quad R_{ijk}^* = R_{ijk} - (\delta_{\alpha\beta,ij} \bar{U}_k + \delta_{\alpha\beta,ik} \bar{U}_j + \delta_{\alpha\beta,jk} \bar{U}_i) C_{\alpha,\beta}, \\
\bar{T}_{H\alpha,\beta,\gamma} : t^* &= t, \quad x^* = x, \quad y^* = y, \quad \bar{U}_i^* = \bar{U}_i, \quad \bar{P}^* = \bar{P}, \quad P_{i[l]}^* = P_{i[l]}, \\
R_{ij}^* &= R_{ij}, \quad R_{ijk}^* = R_{ijk} + \delta_{\alpha\beta\gamma,ijk} C_{\alpha,\beta,\gamma}
\end{aligned} \tag{6}$$

with $1 \leq \alpha, \beta, \gamma \leq 3$, which also have a correspondence for the pressure tensors

$$\begin{aligned}
\bar{T}_l : t^* &= t, \quad x^* = x, \quad y^* = y, \quad \bar{U}_i^* = \bar{U}_i, \quad \bar{P}^* = \bar{P} + D, \\
R_{ij}^* &= R_{ij}, \quad R_{ijk}^* = R_{ijk}, \quad P_{i[l]}^* = P_{i[l]} - D \bar{U}_i \\
\bar{T}_{l\alpha,q} : t^* &= t, \quad x^* = x, \quad y^* = y, \quad \bar{U}_i^* = \bar{U}_i, \quad R_{ij}^* = R_{ij}, \quad R_{ijk}^* = R_{ijk}, \\
\bar{P}^* &= \bar{P}, \quad P_{i[l]}^* = P_{i[l]} + D_{\alpha,q} \delta_{\alpha,i} \delta_{q,l} \quad \text{with } 1 \leq \alpha \leq 3, \quad q \in [1, 2].
\end{aligned} \tag{7}$$

3 Applications and Outlook

The calculated symmetries can be used to derive invariant solutions, in the turbulence usually called turbulent scaling laws. In fact, the Lie symmetries theory is the basis for this process.

Considering a wall-bounded shear flow, the symmetries can be used to verify the logarithmic law of the wall [6]. Apart from the classical symmetries \bar{T}_{s1} , \bar{T}_{s2} , \bar{T}_2 the statistical symmetries \bar{T}_{sn} , $\bar{T}_{H\alpha}$ and $\bar{T}_{H\alpha,\beta}$ are needed to derive the logarithmic wall law and the corresponding scaling laws for the TPC tensors. Let x_2 be the distance from the wall of the first point x , and r the distance between both points x and y , then the scaling laws for the TPCs are given by

$$\begin{aligned} R_{ij} &= (x_2 + a)^{-\gamma} \bar{R}_{ij}(\tilde{r}) + b_{ij} \quad \text{for } ij \neq 11 \\ R_{11} &= f(\tilde{r})(x_2 + a)^{-\gamma} - (Cd \ln(\tilde{r}_2 + 1) + C^2 - b_{11}) \\ &\quad - (2dC + d^2 \ln(\tilde{r}_2 + 1)) \ln(x_2 + a) - d^2 \ln^2(x_2 + a), \end{aligned} \quad (8)$$

with a , b_{ij} , C , d and γ are constant, $\tilde{r}_k = \frac{r_k}{x_2 + a}$ and $f(t)$ an arbitrary but smooth function.

A second application of the newly derived symmetries is decaying homogeneous and isotropic turbulence. Applying the classical symmetries \bar{T}_t , \bar{T}_{s1} , \bar{T}_{s2} we gain the well-known power law decay $k \sim (t + t_0)^{-m}$ with the kinetic energy k . This is in conformance with the classical theories in decaying turbulence. A new exponential decay scaling law of the form $k \sim e^{-t/t_0}$ has first been generated in [1] and experimentally observed in a fractal grid experiment [2, 7]. Also this behaviour can be explained by the given symmetries (see [4, 6]), where the set of classical symmetries \bar{T}_t , \bar{T}_{s1} , \bar{T}_{s2} is extended by \bar{T}_{sn} .

The next step in our analysis will be to derive all symmetries of the multi-point equations in order to derive a considerably extended set of turbulent scaling laws.

References

1. George, W.K., Wang, H.: The exponential decay of homogeneous turbulence. *Phys. Fluids* 21, 025108 (2009)
2. Hurst, D., Vassilicos, J.C.: Scalings and decay of fractal-generated turbulence. *Phys. Fluids* 19, 035103 (2007)
3. Keller, L., Friedmann, A.: Differentialgleichungen für die turbulente Bewegung einer kompressiblen Flüssigkeit. In: *Proc. First. Int. Congr. Appl. Mech.*, pp. 395–405 (1924)
4. Khujadze, G., Oberlack, M.: DNS and scaling laws from new symmetry groups of ZPG turbulent boundary layer flow. *Theoret. Comput. Fluid Dyn.* 18, 391–411 (2004)
5. Oberlack, M.: Symmetrie, Invarianz und Selbstähnlichkeit in der Turbulenz. Habilitation thesis. RWTH Aachen (2000)
6. Oberlack, M., Rosteck, A.: New statistical symmetries of the multi-point equations and its importance for turbulent scaling laws. *Discrete Contin. Dyn. Syst., Ser. S* 3, 451–471 (2010)
7. Seoud, R.E., Vassilicos, J.C.: Dissipation and decay of fractal-generated turbulence. *Phys. Fluids* 19, 105–108 (2007)

Cumulant Corrections in Turbulence

Quasinormal Approximation, Direct Interaction Approximation, and Non-Gaussian Properties of Turbulence

Robert Rubinstein and Wouter J.T. Bos

Abstract. The calculation of fourth-order cumulants by Kraichnan's direct interaction approximation is reviewed and applied to the Batchelor-Howells-Townsend spectrum in low Prandtl number scalar convection.

1 Introduction

Taylor's *statistical theory of turbulence* formulated the basic problem of computing the correlation tensor $U_{ij}(\mathbf{k}; t, t') = \langle u_i(\mathbf{k}, t) u_j(-\mathbf{k}, t') \rangle$ in homogeneous turbulence. But the Navier-Stokes equations only provide a relation between this correlation and the third-order moments $\langle u_m(\mathbf{p}, t) u_n(\mathbf{q}, t) u_j(-\mathbf{k}, t') \rangle$, where the wavenumbers $\mathbf{k}, \mathbf{p}, \mathbf{q}$ satisfy the *triad condition* $\mathbf{k} = \mathbf{p} + \mathbf{q}$, not a determinate equation. This impasse shows that a statistical theory of turbulence cannot follow from the Navier-Stokes equations alone; some statistical hypothesis is needed.

The first systematic attempt to provide such a hypothesis was the *quasinormal theory* [1], which we briefly outline. By inverting the linear viscous operator, the Navier-Stokes equations can be written as

$$u_m(\mathbf{p}, t) = \int_0^t ds G_{QN}(\mathbf{p}; t, s) P_{mrs}(\mathbf{p}) \int_{\mathbf{p}' + \mathbf{p}'' = \mathbf{p}} d\mathbf{p}' d\mathbf{p}'' u_r(\mathbf{p}', s) u_s(\mathbf{p}'', s) \quad (1)$$

where $G_{QN}(\mathbf{p}; t, s) = \exp[-\nu p^2(t - s)]H(t - s)$ and $P_{mrs} = \frac{1}{2}i(p_r P_{ms} + p_s P_{mr})$ with $P_{ij} = \delta_{ij} - p^{-2} p_i p_j$. Substituting in the third order correlation gives

Robert Rubinstein
Newport News, VA USA

Wouter J.T. Bos
CNRS-LMFA, Ecole Centrale de Lyon, Université de Lyon, Ecully, France
e-mail: wouter.bos@ec-lyon.fr

$$\int_0^t ds G_{QN}(\mathbf{p}; t, s) P_{mrs}(\mathbf{p}) \int_{\mathbf{p}'+\mathbf{p}''=\mathbf{p}} \langle u_r(\mathbf{p}', s) u_s(\mathbf{p}'', s) u_n(\mathbf{q}, t) u_j(-\mathbf{k}, t') \rangle + \dots \quad (2)$$

where the dots indicate two additional terms found by operating similarly on $u_n(\mathbf{q}, t)$ and $u_j(-\mathbf{k}, t')$. This expression for a third-order moment in terms of fourth-order moments couples the triad $(\mathbf{k}, \mathbf{p}, \mathbf{q})$ to all triads $(\mathbf{p}, \mathbf{p}', \mathbf{p}'')$. The *quasnormality hypothesis* consists in expressing the fourth order correlation in Eq. (2) in terms of second order correlations as if the random field u were Gaussian. The crucial property of a Gaussian random field is that the uncorrelated Fourier amplitudes are also statistically independent. Then the only contributions are from $\mathbf{p}' + \mathbf{q} = 0$ and $\mathbf{p}'' - \mathbf{k} = 0$ and from the symmetric combinations $\mathbf{p}'' + \mathbf{q} = 0$ and $\mathbf{p}' - \mathbf{k} = 0$. Hence

$$G_{QN}(p)P(p) \int \langle u(p')u(p'')u(q)u(-k) \rangle = 2G_{QN}(p)P(p)U(q)U(k) \quad (3)$$

Here, we have introduced a symbolic notation in the interest of simplicity, suppressing tensor indices, vector notation, and time arguments. This hypothesis ‘closes’ the third-order moment $\langle u(p)u(q)u(-k) \rangle$ in terms of statistical properties evaluated at the wavevectors $\mathbf{k}, \mathbf{p}, \mathbf{q}$ alone.

Kraichnan’s [2] *direct interaction approximation* (DIA) introduced two new ideas into the statistical theory: (i) Abandoning the plausible hope that turbulence theory might be closed in terms of the correlation function alone, Kraichnan replaced the viscous propagator G_{QN} by the *linear response function* G_{DIA} , a new statistical quantity. (ii) To close the fourth-order correlations in Eq. (2), Kraichnan proposed the *direct interaction hypothesis*: the dominant contributions to the fourth order correlation come from the original triad $\mathbf{k}, \mathbf{p}, \mathbf{q}$. Then

$$\begin{aligned} G_{DIA}(p)P(p) \int \langle u(p')u(p'')u(q)u(-k) \rangle \\ \approx 2G_{DIA}(p)P(p) \langle u(-q)u(k)u(q)u(-k) \rangle \end{aligned}$$

Finally, Kraichnan argued, on the basis of a ‘weak dependence property’ ([2] section 2.2) that $\langle u(-q)u(k)u(q)u(-k) \rangle = U(q)U(k)$. The result is

$$G_{DIA}(p)P(p) \int \langle u(p')u(p'')u(q)u(-k) \rangle = 2G_{DIA}(p)P(p)U(q)U(k) \quad (4)$$

Formally, it is the same as Eq. (3), but with G_{DIA} replacing G_{QN} . From this viewpoint, the main difference between quasnormality and DIA lies in the treatment of *two-time* properties of turbulence by the functions G_{QN} and G_{DIA} .

This strong formal resemblance perhaps motivated Proudman’s comments [3] on Kraichnan’s then recently proposed theory at the 1961 Marseille meeting:

In other words, the zero-fourth-cumulant theory implies that the triple moment is non-zero only on account of interaction between its own three wavenumbers. Such a theory may be termed a “direct interaction theory.” Kraichnan’s theory is of this kind, and down at this conceptual level, therefore, it is closely related to zero-fourth-cumulant

theories. Indeed both theories tend to have the same very general properties and to stand or fall by similar criteria.

Recall that a *cumulant* is the difference between a correlation of any order and its value assuming the statistical independence of its factors. Kraichnan replied that *DIA does not assume the vanishing of fourth-order cumulants*, but this statement was substantiated only much later [4], by showing explicitly how *cumulant corrections* to fourth-order moments are computed using DIA. The existence of nonzero cumulants points to *statistical dependence* among the uncorrelated Fourier amplitudes, a possibility which is inconsistent with an assumption of strict Gaussianity. To illustrate this computation, consider the correlation

$$\langle u(p)u(q)u(-p')u(-q') \rangle$$

where $p + q = p' + q' = k$. There are two triads: (k, p, q) and (k, p', q') . The Gaussian value, found by assuming that the Fourier amplitudes are independent, contains nonzero contributions only when $p = p'$ and $q = q'$ or when $p = q'$ and $q = p'$; thus, the Gaussian contribution is

$$\langle u(p)u(q)u(-p')u(-q') \rangle_G = 2U(p)U(q)$$

DIA cumulant corrections are found as follows: using Eq. (II), but with G_{DIA} instead of G_{QN} , replace $u(p)$ by $G_{DIA}(p)P(p)u(r)u(s)$ and operate similarly on $u(p')$, to obtain

$$G_{DIA}(p)P(p)G_{DIA}(p')P(-p')\langle u(r)u(s)u(q)u(-r')u(-s')u(-q') \rangle \quad (5)$$

The *direct interaction hypothesis* restricts interactions to the original triads (k, p, q) and (k, p', q') . It forces $r = r' = k$, $s = -q$, $s' = -q'$, giving the cumulant correction $G(p)P(p)G(p')P(-p')U(k)U(q)U(-q')$. Another structure for a cumulant correction is found from $u(p) \rightarrow G_{DIA}(p)P(p)u(r)u(s)$ and $u(r) \rightarrow G_{DIA}(r)P(r)u(r')u(r'')$. The result is $G_{DIA}(p)P(p)G_{DIA}(k)P(k)U(q)U(p')U(q')$. Without insisting on details, we note that the two response functions imply two time integrations leading to factors which we abbreviate symbolically as Θ . Then formally, the cumulant correction is

$$\begin{aligned} & \langle u(p)u(q)u(-p')u(-q') \rangle_C \\ & = -\Theta^2 P(p)P(p')U(k)U(q)U(q') + \Theta^2 P(k)P(p)U(q)U(p')U(q') \end{aligned} \quad (6)$$

The opposite signs are linked to an important consistency property of DIA cumulant corrections: they vanish in a (Gaussian) thermal equilibrium ensemble with $U(k)$ constant. This conclusion is nontrivial, because thermal equilibrium provides a special condition in which the Fourier amplitudes actually are independent; yet in DIA, there is no consideration of the multipoint velocity pdf's, only of the second order correlation. Indeed, if we could prove that *all* DIA cumulant corrections vanish in equipartition then DIA would imply that the equipartition state is Gaussian.

(The consistency of DIA with equipartition distinguishes it from elementary closures like the Heisenberg and Kovznay models).

But we stress that a proof that the DIA cumulant corrections vanish in equipartition depends crucially on the *geometric factors*, the combinations of projection operators P_{ij} , that enter the exact expression corresponding to Eq. (6). Indeed, properties of these factors imply that some fourth order cumulant corrections vanish (4): these include the corrections to the moments $\langle u(x+r)^2 u(x)^2 \rangle$ and the pressure correlation $\langle p(x+r)p(x) \rangle$.

Can cumulant corrections be computed similarly by quasinormality? We might just say that the fourth order cumulant is zero, and that there is nothing more to add. Or we might consider a kind of ‘extended quasinormality’ by following the steps leading to Eq. (5) then approximating the sixth-order correlation as if u were Gaussian. The result differs sharply from DIA, because many more wavevectors are involved: by either procedure, DIA and quasinormality lead to a completely different result. Whereas (3) proposed assimilating direct interaction to quasinormality, we see that the difference between them is very considerable.

2 The Batchelor-Howells-Townsend Spectrum

We briefly consider a problem in which fourth order cumulants have been ignored: the Batchelor-Howells-Townsend (BHT) spectrum in low Prandtl number convection.

If scalar fluctuations are damped at a wavenumber much smaller than the Kolmogorov scale for velocity fluctuations, then the scalar fluctuations can exhibit a *Batchelor-Howells-Townsend* (BHT) spectrum, a power-law dissipation range of the form (6)

$$E_\theta(k) = C\varepsilon_\theta \frac{\varepsilon^{2/3}}{\kappa^3} k^{-17/3} \quad (7)$$

where θ is a passive scalar, $E_\theta(k)$ is the spectrum of fluctuations of θ (so that $\langle \theta^2 \rangle = \int_0^\infty dk E_\theta(k)$), κ is the molecular diffusivity of θ , and $\varepsilon_\theta = \kappa \langle |\nabla \theta|^2 \rangle$ is the rate of destruction of fluctuations of θ by molecular diffusion. The BHT spectrum is believed to apply if $\kappa \gg \nu$, at scales smaller than the diffusive cutoff scale, but larger than the Kolmogorov scale, so that

$$\left(\frac{\varepsilon}{\kappa^3} \right)^{1/4} \ll k \ll \left(\frac{\varepsilon}{\nu^3} \right)^{1/4}. \quad (8)$$

The condition $\kappa \gg \nu$ insures the existence of such a range of scales.

The BHT spectrum can be obtained (6) by observing that the first inequality in Eq. (8) can be rewritten as

$$\varepsilon^{1/3} k^{2/3} \ll \kappa k^2 \quad (9)$$

This inequality suggests that the time derivative in the scalar evolution equation can be ignored, and that a statistical balance can therefore exist between advection by

the velocity field \mathbf{u} and viscous diffusion. Then equate the advection term to the dissipation term, square both sides of this equation, and take averages to obtain

$$\langle (\mathbf{u} \cdot \nabla \theta)^2 \rangle = \kappa^2 \langle (\nabla^2 \theta)^2 \rangle. \quad (10)$$

(details are found in [6]). Assuming this balance at every scale in the range of interest gives

$$\int_{\mathbf{k}=\mathbf{p}+\mathbf{q}} d\mathbf{p}d\mathbf{q} \int_{\mathbf{k}=-\mathbf{p}'-\mathbf{q}'} d\mathbf{p}'d\mathbf{q}' \langle \mathbf{k} \cdot \mathbf{u}(\mathbf{p}) \mathbf{k} \cdot \mathbf{u}(\mathbf{p}') \theta(\mathbf{q}) \theta(\mathbf{q}') \rangle = \kappa^2 k^4 U_\theta(\mathbf{k}) \quad (11)$$

where $U_\theta(\mathbf{k}) = \langle \theta(\mathbf{k}) \theta(-\mathbf{k}) \rangle$ is the modal intensity of θ fluctuations (for isotropy, $E_\theta(k) = 4\pi k^2 U_\theta(k)$). Applying quasnormality to the integral on the left in Eq. (11) (note that $\langle u_i \theta \rangle = 0$ in the isotropic case) and using incompressibility to replace \mathbf{k} by \mathbf{q} , the left side of Eq. (11) becomes

$$\int_{\mathbf{k}=\mathbf{p}+\mathbf{q}} d\mathbf{p}d\mathbf{q} U_{mn}(\mathbf{p}) q_m q_n U_\theta(\mathbf{q}) \quad (12)$$

where we have reverted to index notation in the interest of clarity. In Eq. (12), $U_{mn}(\mathbf{p}) = \langle u_m(\mathbf{p}) u_n(-\mathbf{p}) \rangle$ is the velocity correlation tensor. The BHT regime applies to wavenumbers k such that all of the scalar dissipation has occurred at scales much larger than k : then $q/k \approx 0$ and $p/k \approx 1$ and the last integral can be approximated by $U(k) P_{mn}(\mathbf{k}) \int d\mathbf{q} q_m q_n U_\theta(\mathbf{q})$ where isotropy implies $U_{mn}(\mathbf{k}) = U(k) P_{mn}(\mathbf{k})$ ($P_{mn}(\mathbf{k})$ is the solenoidal projection defined earlier.) Substituting the last integral in the left side of Eq. (11) and integrating both sides over the spherical shell $|\mathbf{k}| = k$ gives

$$E(k) \frac{\varepsilon_\theta}{\kappa} = \frac{2}{3} \kappa^2 k^4 E_\theta(k) \quad (13)$$

where we have used $\int d\mathbf{q} q^2 U_\theta(\mathbf{q}) = \varepsilon_\theta / \kappa$. Eq. (7) follows by substituting a Kolmogorov spectrum for $E(k)$.

Although arguments were given in [6] supporting this particular application of quasnormality, the fact remains that without any theory to even suggest an estimate for the cumulant, the quasnormality approximation to the fourth-order moment on the left side of Eq. (11) remains completely uncontrolled. It is therefore of some interest to compute this cumulant by DIA, since there is, at least to our knowledge, no other analytical way to assess the importance of cumulants in this computation.

Cumulants are found by substituting $\theta \rightarrow G_\theta k u \theta$ or $u \rightarrow G P u u$; however, cumulants evaluated by the second substitution vanish if the velocity field is isotropic. One DIA cumulant correction scales as

$$k^4 \int_{\mathbf{k}=\mathbf{p}+\mathbf{q}} d\mathbf{p}d\mathbf{q} \int_{\mathbf{k}=-\mathbf{p}'-\mathbf{q}'} d\mathbf{p}'d\mathbf{q}' U(p) U(p') U_\theta(k) \Theta(p, k, q) \Theta(p', k, q') \quad (14)$$

The factors Θ depend on time integrals of DIA descriptors of the two-time properties of turbulence; a preliminary assessment of their effect is found by assuming a simple

form, for example $\Theta(p, k, q) \sim 1/(\varepsilon^{1/3} p^{2/3} + \kappa k^2 + \varepsilon^{1/3} q^{2/3})$. In the limit in which the BHT spectrum is expected, $\Theta(p, k, q) \approx \Theta(k, k, 0)$. Consideration of the signs shows that the cumulant correction alters the BHT balance so that instead of Eq. (7), we have

$$E(k) \frac{\varepsilon_\theta}{\kappa} - \eta(k)^2 E_\theta(k) = \kappa^2 k^4 E_\theta(k) \quad (15)$$

where, for scaling,

$$\eta(k) \sim \frac{k^3 E(k)}{\varepsilon^{1/3} k^{2/3} + \kappa k^2} \sim \varepsilon^{1/3} k^{2/3} \frac{\varepsilon^{1/3} k^{2/3}}{\varepsilon^{1/3} k^{2/3} + \kappa k^2} \quad (16)$$

where a Kolmogorov spectrum has been substituted for $E(k)$. Under the condition of Eq. (9), the cumulant contribution to Eq. (15), the second term on the left side, can be neglected since η contains the factor $\varepsilon^{1/3} k^{2/3} / \kappa k^2$. Then the BHT balance remains correct to leading order. This conclusion agrees with the analysis of [5].

3 Conclusions

Fourth-order cumulants can be computed by DIA. Consequently, some non-Gaussian fourth-order properties of turbulence are accessible to closure. Nonzero cumulant corrections are found for the Batchelor-Howells-Townsend range of a passive scalar; however, they do not invalidate the basic scaling argument found by assuming quasi-normality. It is often correctly observed that passive scalar advection is an especially ‘intermittent’ phenomenon; however, this does not preclude the possibility of evaluating low-order non-Gaussian properties of this phenomenon by closure considerations.

Acknowledgements. We would like to thank Yukio Kaneda and Toshiyuki Gotoh for numerous discussions of Kraichnan’s work on cumulant corrections.

References

1. Tatsumi, T.: Proc. Roy. Soc. A239, 16–45 (1957)
2. Kraichnan, R.H.: J. Fluid Mech. 5, 497–543 (1959)
3. Proudman, I.: The mechanics of turbulence, p. 107. Gordon and Breach, New York (1961)
4. Chen, S., Herring, J., Kerr, R., Kraichnan, R.H.: Phys. Fluids A 1, 1844 (1989)
5. Kraichnan, R.H.: Phys. Fluids 11, 945–953 (1968)
6. Batchelor, G.K., Howells, I.D., Townsend, A.A.: J. Fluid Mech. 5, 134–139 (1959)

Decaying Turbulence and Anomalous Dissipation

M. Salewski, W.D. McComb, A. Berera, and S. Yoffe

Abstract. In this contribution, we present results from an investigation of the normalised dissipation rate in decaying homogeneous isotropic turbulence. Due to the time-dependence of this system, it is necessary to find a time that indicates an evolved state of turbulent decay. We establish criteria for determining such times and use these to make measurements on our system. It is found that these criteria give results which are compatible with those of the current literature.

1 Introduction and Motivation

Dissipation is fundamental to turbulence and it is important to understand the mechanism by which dissipation is amplified in a turbulent system. It is equally important to understand how dissipation, given by the normalised dissipation rate,

$$C_\varepsilon \equiv \frac{\varepsilon L}{U^3} \quad (1)$$

scales with the Reynolds number, R as this would allow prediction of the dissipation rate for various systems.

Following on from this, it is curious to note that the dissipation rate tends toward a constant when the Reynolds number is increased asymptotically. This is surprising since one would expect the dissipation rate to tend toward zero when the viscosity, which is the sole source of dissipation, becomes vanishingly small,

$$\lim_{R \rightarrow \infty} C_\varepsilon = C_{\varepsilon, \infty}. \quad (2)$$

It is this phenomenon that is called the *anomalous dissipation*.

Matthew Salewski

Fachbereich Physik, Philipps-Universität Marburg, D-35032 Marburg, DE

e-mail: matthew.salewski@physik.uni-marburg.de

W. David McComb · Arjun Berera · Sam Yoffe

School of Physics and Astronomy, University of Edinburgh, Edinburgh EH9 3JZ, UK

e-mail: wdm@ph.ed.ac.uk

There is much experimental and numerical evidence to support such a claim. Sreenivasan collected results from wind-tunnel experiments of 1940-1980 [10] which show a result $C_\varepsilon \sim 1$ for decaying experiments. A more recent publication of Pearson *et al* [8] shows a collection of experimental results for forced turbulence in wind-tunnels and other shear flows for Taylor-Reynolds numbers $R_\lambda \sim 1200$. Similarly, Kaneda *et al* [3], compiled results of various DNS studies to compare with their own which show $R_\lambda \sim 1100$. Lastly, a numerical investigation by Bos *et al* [2] compares forced and decaying systems. Upon inspection, these results collectively show that the dissipation rate is finite for the largest observed R , and that the asymptotic values are $C_\varepsilon \sim 0.5$ and $C_\varepsilon \sim 1$ for forced and decaying systems respectively.

The purpose of this investigation is to look into the mechanisms that are behind this so-called anomaly, and to understand the difference in decaying and forced turbulence data. To study these topics, we simulate freely-decaying homogeneous isotropic turbulence. As the system is continuously evolving in time, there is a need to specify when such a measurement can be made. Here we look to intrinsic dynamics to establish criteria for these times.

2 Results and Discussion

For our present purposes, we wish to compute the dissipation rate,

$$\varepsilon(t) = \int_0^\infty 2\nu k^2 E(k,t) dk \quad (3)$$

and the maximum of the spectral energy flux,

$$\Pi_{\max}(t) = \int_{\kappa_0}^\infty T(k,t) dk, \quad (4)$$

where the wavenumber κ_0 is defined such that $T(\kappa_0, t) = 0$. The latter quantity gives some measure of the energy flowing into the dissipative scales, effectively controlling the rate of dissipation. Normalising both quantities by $U(t)^3/L(t)$, we find C_ε and C_Π , respectively.

For forced turbulence, one can take the time-averaged steady-state values of these quantities; however, in decaying turbulence no such state exists. Measurements taken too early risk that the system is not sufficiently developed, and if the measurement is too late then the decay is entirely viscous [11]. One then requires a time that is indicative of turbulence; the dynamical criteria that we employ are the maximum dissipation and the largest spread of energy in wavenumber space. To characterise the former, we look for a peak in the dissipation rate; for the latter we estimate this as a peak in the energy of the Kolmogorov wavenumber, $k_D \equiv (\varepsilon/\nu^3)^{1/4}$.

As these times roughly give the onset of developed decaying turbulence, they are possibly too early. To adjust for this, so-called eddy-turnover times, $L(t)/U(t)$ are added. This gives a set of measurement times: t_m , $t_m + L(t_m)/U(t_m)$, and $t_m + 2L(t_m)/U(t_m)$. For the peak dissipation time, the label is $t_{\Pi|\varepsilon}$ and for the peak of the

Kolmogorov wavenumber, t_D . The dissipation peak time requires additional care for low R , where it does not exist; in such cases the temporal maximum of the flux $\Pi_{\max}(t_{\Pi})$ is used (see [9] for details).

To investigate these issues, we have employed both a closure and DNS. The closure used here is the Local Energy Transfer (LET) theory of McComb (see [6] and references therein). The DNS is a pseudo-spectral code of 128^3 and 256^3 gridpoints. For the values of Reynolds number concerned here, the comparison between the closure and the DNS is quite agreeable. Using the closure allows a more computationally efficient means of obtaining turbulent statistics than that achieved with our current DNS capabilities. This allows the computations to run for longer times, to determine the effect of the measurement times on the quantities of interest.

The computations are run from two different initial spectra, the specifications for which can be found in [4]. The results of Fig. 1 show that the dissipation and flux are separated by a finite amount; this is a consequence of decaying turbulence as noted in [5]. However, the value for C_ε is lower than the values given in the current literature. It is possible then that the measurement time is too early. The plots of Fig. 2 show that as later measurements are taken the value of the dissipation increases giving some values closer to those mentioned above.

It is additionally worth noting that the value of the dissipation rate does seem to converge for these later times. Longer computations are needed to confirm this and determine its significance. In contrast, the normalised flux converges quite rapidly to a value near to that of C_ε for forced turbulence.

We have investigated the normalised dissipation rate for decaying homogeneous isotropic turbulence. In doing so, we have developed criteria for taking measurements on freely-decaying systems. Using these criteria, we find results that are compatible with those given in the current literature.

It is not known whether the criteria used to find the measurement times are valid for all systems. For example, the peak in the dissipation rate does not always occur and additional criteria are needed to account for this [9]. Future investigations are

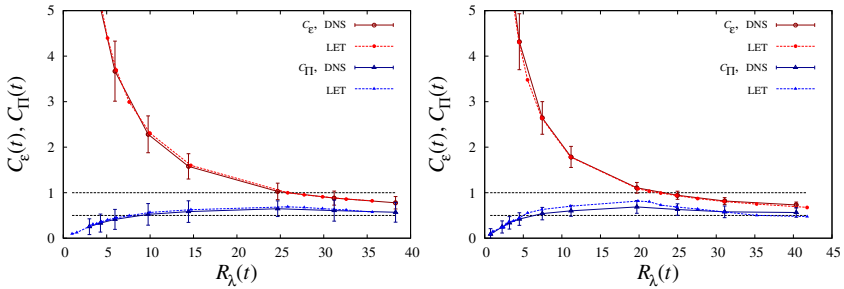


Fig. 1 Comparison of DNS and LET results for C_ε and C_{Π} . Our current DNS capabilities only allow the earliest time, $t_{\Pi|\varepsilon}$, for measurement. The results on the left use an initial k^2 spectrum whereas those on the right use an initial k^4 spectrum.

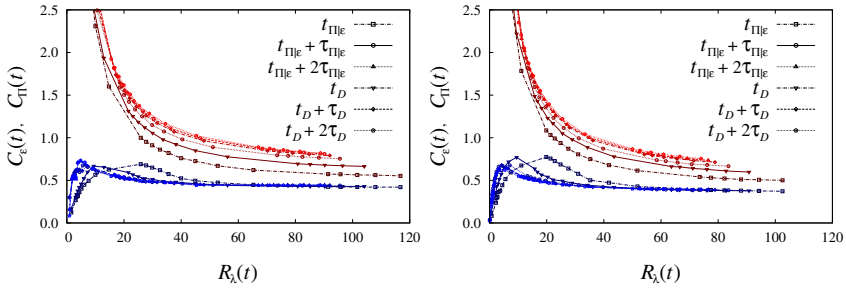


Fig. 2 Plots of LET results for C_ϵ and C_Π using different measurement times. The results are arranged as in the previous figure.

needed to determine the validity of these times and the systems they are used to measure.

References

1. Batchelor, G.K.: The theory of homogeneous turbulence, 2nd edn. Cambridge University Press, Cambridge (1971)
2. Bos, W.J.T., Shao, L., Bertoglio, J.-P.: Phys. Fluids 19, 045101 (2007)
3. Kaneda, Y., Ishihara, T., Yokokawa, M., Itakura, K., Uno, A.: Phys. Fluids 15, L21 (2003)
4. McComb, W.D.: The Physics of Fluid Turbulence. Oxford University Press (1990)
5. McComb, W.D.: arXiv:0909.4951 (2009)
6. McComb, W.D., Kiyani, K.: Phys. Rev. E 72, 016309 (2005)
7. McComb, W.D., Berera, A., Salewski, M., Yoffe, S.: Phys. Fluids 22, 061704 (2010)
8. Pearson, B.R., Krogstad, P.-Å., van de Water, W.: Phys. Fluids 14, 1288 (2002)
9. Salewski, M.: PhD thesis. University of Edinburgh (2010)
10. Sreenivasan, K.R.: Phys.Fluids 27, 1048 (1984)

Secondary Splitting of Zero Gradient Points in Turbulent Scalar Fields

Philip Schaefer, Markus Gampert, and Norbert Peters

Abstract. The mechanisms related to the secondary splitting of zero gradient points of scalar fields are analyzed using the two dimensional case of a scalar extreme point lying in a region of local strain. The velocity field is assumed to resemble a stagnation point flow, cf. Gibson [1], which is approximated using a Taylor expansion up to third order. It is found that the splitting can only be explained when the third order terms of the Taylor expansion of the flow field are included. The non-dimensional splitting time turns out to depend on three parameters, namely the local Péclet number Pe_δ based on the initial size of the extreme point δ and two parameters which are measures of the rate of change of the local strain. For the limiting case $Pe_\delta \rightarrow 0$, the splitting time is found to be finite but Péclet number independent, while for the case of $Pe_\delta \rightarrow \infty$ it increases logarithmically with the Péclet number.

1 Introduction

Gibson [1] analyzed the behaviour at the smallest scales of turbulent scalar fields in terms of the properties of zero gradient points and minimal gradient surfaces. He concluded that these regions of the field are of physical importance to the problem of turbulent mixing. Among other findings, Gibson identified two physical mechanisms which lead to the creation of new zero gradient points: while initially zero gradient points must be created from regions of uniform scalar gradient, he concludes that the majority of such points results from the combined action of strain and diffusion on existing zero gradient points, which leads to their splitting into new extreme points. This effect is called secondary splitting. In recent works by Peters et al. [2, 3, 4], extreme points of turbulent scalar fields have again received attention in the context of dissipation element theory. The temporal evolution of dissipation elements is inherently connected to the evolution of their ending points.

Philip Schaefer · Markus Gampert · Norbert Peters
Institut für Technische Verbrennung RWTH Aachen University
e-mail: pschaefer@itv.rwth-aachen.de

In the present study we will consider the splitting to take place in a two-dimensional environment to extract the relevant physical mechanisms and their interplay. In a coordinate system moving with the extremum the flow field relative to the extreme point can be described as a stagnation point flow. Mathematically, the problem is described by the transport equation for the passive scalar ϕ , which reads

$$\frac{\partial \phi}{\partial t} + u \frac{\partial \phi}{\partial x} + v \frac{\partial \phi}{\partial y} = D \left(\frac{\partial^2 \phi}{\partial x^2} + \frac{\partial^2 \phi}{\partial y^2} \right). \quad (1)$$

In Eq. [1](#) ϕ denotes the two-dimensional scalar field, and u and v are the velocity components of the velocity field relative to the extreme point in x - and y -direction. D denotes the constant diffusivity of the scalar. We restrict the analysis to a symmetric problem for the scalar as well as the velocity field. An extreme point of finite size can be described locally by a Gaussian bell-shaped-curve of the form $\phi(x, y, t_0) = \phi_0 \exp((x^2 + y^2)/\delta^2)$, where the sign of ϕ_0 determines the type of the extreme point while δ determines its characteristic size. The stagnation point flow around the extreme point will be expanded in a Taylor series up to third order. We introduce

$$\alpha = \left. \frac{\partial u}{\partial x} \right|_{x_0, y_0} = - \left. \frac{\partial v}{\partial y} \right|_{x_0, y_0}, \beta_x = \left. \frac{\partial^3 u}{\partial x^3} \right|_{x_0, y_0}, \beta_y = \left. \frac{\partial^3 v}{\partial y^3} \right|_{x_0, y_0}, \quad (2)$$

and non-dimensionalize the problem using the variables $\tilde{\phi} = \phi/\phi_0$, $\tilde{t} = \alpha t$, $\tilde{x} = x/\delta$ and $\tilde{y} = y/\delta$. Dropping the tildes for simplicity, the problem reads

$$\begin{aligned} \frac{\partial \phi}{\partial t} + \left(x + \frac{1}{6} B_x x^3 - \frac{1}{2} B_y x y^2 \right) \frac{\partial \phi}{\partial x} + \\ \left(-y + \frac{1}{6} B_y y^3 - \frac{1}{2} B_x x^2 y \right) \frac{\partial \phi}{\partial y} &= \frac{1}{Pe_\delta} \left(\frac{\partial^2 \phi}{\partial x^2} + \frac{\partial^2 \phi}{\partial y^2} \right), \\ \phi(x, y, t_0) &= \exp(-(x^2 + y^2)), \end{aligned} \quad (3)$$

with the non-dimensional parameters $Pe_\delta = (\alpha \delta^2)/D$, $B_x = (\delta^2 \beta_x)/\alpha$ and $B_y = (\delta^2 \beta_y)/\alpha$. While the first of these is a Péclet number based on the characteristic size δ of the extreme point, the latter two are measures for the rate of change of the local strain in x - and y -direction.

2 Analysis and Validation

As the problem stated in Eq. [3](#) is entirely symmetric, one can argue that the splitting will take place at the symmetry-point, which can be shifted to the origin without loss of generality. The splitting time is then characterized by the time at which the second derivative of the scalar field at the origin changes its sign. As an analytical solution of Eq. [3](#) is not readily available, we seek a solution by expanding ϕ in terms of a series of the form

$$\phi(x, y, t) = \sum_{n=1}^{\infty} \phi_n(x, y, t), \quad (4)$$

in which n corresponds to the order of the Taylor expansion terms of the flow field included in Eq. 3. For the symmetric case considered here n assumes only odd numbers. An approximate solution of Eq. 3 in the vicinity of the origin can be written as $\phi(x, y, t) \approx \phi_1(x, y, t) + \phi_3(x, y, t)$, if terms up to order three are included. The splitting time t_s follows from

$$\frac{\partial^2(\phi_1 + \phi_3)}{\partial x^2} \Big|_{x=0, y=0, t_s} = 0 \rightarrow t_s = f(Pe_\delta, B_x, B_y). \quad (5)$$

Introducing Eq. 4 in 3 and collecting terms of same order, the first-order problem reads

$$\frac{\partial \phi_1}{\partial t} + x \frac{\partial \phi_1}{\partial x} - y \frac{\partial \phi_1}{\partial y} = \frac{1}{Pe_\delta} \left(\frac{\partial^2 \phi_1}{\partial x^2} + \frac{\partial^2 \phi_1}{\partial y^2} \right), \quad (6)$$

$$\phi_1(x, y, t_0) = \exp(-(x^2 + y^2)), \quad (7)$$

which can be solved analytically, cf. Bernard 5 for a related treatment, and its contribution to Eq. 5 yields

$$\frac{\partial^2 \phi_1}{\partial x^2} \Big|_{x=0, y=0, t} = - \frac{2e^{-2t}}{1 + \frac{2}{Pe_\delta}(1 - e^{-2t})}. \quad (8)$$

As this expression asymptotically tends to zero for large times, the first-order solution does not account for the splitting, so that the next higher-order correction must be considered. Reintroducing Eq. 4 into Eq. 3 the equation for the third-order expansion term ϕ_3 reads

$$\frac{\partial \phi_3}{\partial t} + x \frac{\partial \phi_3}{\partial x} - y \frac{\partial \phi_3}{\partial y} = \frac{1}{Pe_\delta} \left(\frac{\partial^2 \phi_3}{\partial x^2} + \frac{\partial^2 \phi_3}{\partial y^2} \right) - \underbrace{\left(\frac{1}{6} B_x x^3 - \frac{1}{2} B_y x y^2 \right) \frac{\partial \phi_1}{\partial x} - \left(\frac{1}{6} y^3 B_y - \frac{1}{2} x^2 y B_x \right) \frac{\partial \phi_1}{\partial y}}_P, \quad (9)$$

$$\phi_3(x, y, t_0) = 0. \quad (10)$$

In Eq. 9 a time-dependant source term labeled P appears, which is due to the higher-order velocity terms in the Taylor expansion. Eq. 9 is an inhomogenous equation which can be solved using Green's function G (which for the present case can be given analytically), so that the second derivative of ϕ_3 can be evaluated and the third order contribution to Eq. 5 follows.

An analytical expression of the splitting time is not attainable for $Pe_\delta \rightarrow 0$, but one can show that the influence of the Péclet number vanishes as it approaches zero, while the splitting time remains finite, so that only a dependance on the parameters B_x and B_y remains. Contrary to the case of vanishing Péclet numbers an analytical

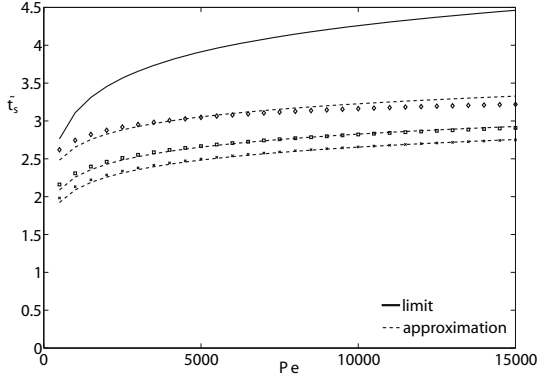


Fig. 1 Comparison of the analytically derived splitting time with the numerical solution of the Taylor-Green vortex; \diamond , $B_x = -0.1$; \square , $B_x = -0.5$; \times , $B_x = -1.0$

expression for the splitting time can be derived in the limit of large Péclet numbers and for a maximal splitting time of $t_{s,max.} \ll 1/2 \ln(Pe_\delta/2 + 1)$. The expression for t_s reads for $\mathcal{O}(B_x) = \mathcal{O}(B_y)$

$$t_s = \frac{1}{4} \ln \left(\frac{4Pe_\delta}{-B_x} \right) + \frac{B_x - B_y}{2B_x} \sqrt{\frac{-B_x}{4Pe_\delta}}. \quad (11)$$

Different calculations of a two-dimensional steady Taylor-Green vortex (where $B_x = -B_y$) with Péclet numbers up to 15.000 for three different values of B_x were performed. Fig. 1 shows the obtained non-dimensional splitting time over the Péclet number together with the analytical approximation, cf. Eq. 11 which are in good agreement.

3 Concluding Discussion

A comparison of the terms proportional to B_x and B_y respectively in the expression for the splitting time t_s reveals that those proportional to B_y are small compared to the ones proportional to B_x . This is especially true for the limiting case of large Péclet numbers. It turns out that a finite splitting time only exists for negative values of B_x , which for positive values of α corresponds to a decelerating rate of strain in the x -direction. This is the essence of the physical mechanisms leading to a splitting of the extreme point. First, the inward convection in y -direction leads to an accumulation of scalar in the vicinity of the main axis of strain, until the counteracting diffusion balances this transport. At the same time the flow convects the scalar away from the stagnation point along the main axis of strain, in which diffusive transport is negligibly small. Whether a splitting occurs or not, depends on the sign of B_x . While for positive values of B_x , which physically corresponds to an acceleration of the velocity in x -direction, no splitting occurs, it does occur for negative

values of B_x , which corresponds to a deceleration of the velocity in x -direction. This can be explained by looking at the balance of the different transport phenomena in the vicinity of the stagnation point before the splitting occurs: while diffusion and convection balance each other in y -direction, the convective transport in x -direction dominates diffusion and removes scalar from the stagnation point. For a linear stagnation point flow the rate of removal is constant along the x -axis and no splitting can occur. For positive values of B_x , the convection is smallest at the origin and then increases along the x -axis which can again not lead to a splitting. The situation is different for negative values of B_x which corresponds to a larger removal of scalar at the origin than in its vicinity, so that the scalar which is removed at the origin accumulates on both sides of the origin, leading to the formation of two new extreme points while the old one splits.

Acknowledgements. This work has been funded by the Deutsche Forschungsgemeinschaft under grant Pe 241/36-1.

References

1. Gibson, C.H.: Fine Structure of Scalar Fields Mixed by Turbulence I. Zero Gradient Points and Minimal Gradient Surfaces. *Phys. Fluids* 11, 2305–2315 (1968)
2. Wang, L., Peters, N.: The length scale distribution function of the distance between extremal points in passive scalar turbulence. *J. Fluid Mech.* 554, 457–475 (2006)
3. Wang, L., Peters, N.: Length scale distribution functions and conditional means for various fields in turbulence. *J. Fluid Mech.* 608, 113–138 (2008)
4. Schaefer, P., Gampert, M., Goebbert, J.H., Wang, L., Peters, N.: Testing of Model Equations for the Mean Dissipation using Kolmogorov Flows. *Flow, Turbulence and Combustion* 85, 225 (2010)
5. Bernard, P.S.: Convective diffusion in two-dimensional incompressible linear flow. *SIAM Rev.* 32, 660–666 (1990)

Multi-scale Analysis of Turbulence in CFD-Simulations

Bernhard Stoevesandt, Robert Stresing, Andrei Shishkin, Claus Wagner, and Joachim Peinke

Abstract. We performed a 3D DNS simulation using spectral/hp method on an fx79-w151a airfoil at a Reynolds number of $Re=5000$ at an angle of attack of $\alpha = 12^\circ$. Due to a separating flow, an inhomogeneous turbulent field evolved in the wake above the trailing edge. Within this field time series of the flow properties have been gathered at selected points. The data of the time series at one point have been analyzed on the back ground of a multipoint correlation method. From statistics of velocity increments Kramers-Moyal coefficients have been estimated.

The resulting stochastic process given by the Kramers-Moyal coefficients have been used to reconstruct a time series of the flow velocity increments at a differing point in space within the flow field. Even though the short dataset enabled just a first impression of the method, the results showed a surprisingly good agreement.

1 The Simulation

Using the spectral finite element code $\mathcal{N}\epsilon\kappa\mathcal{T}\alpha r$ [2] a direct numerical simulation (DNS) has been done for the flow around an fx79w-151a airfoil with an angle of attack $\alpha = 12^\circ$ at a Reynolds number of $Re=5000$. Here we used an incompressible version of the Navier-Stokes solver using spectral elements in streamwise and crossflow direction with a 2D grid and a Fourier expansion for the discretisation of the spanwise direction. The time step had to be reduced to $\Delta t \approx 10^{-5}$ making the computations rather expensive. Validations of this version of the code have been undertaken for a cylinder flow by Ma and Dong [3, 4].

Bernhard Stoevesandt · Robert Stresing · Joachim Peinke
ForWind - University of Oldenburg, Marie-Curie-Str. 1, 26129 Oldenburg
e-mail: bernhard.stoevesandt@forwind.de

Andrei Shishkin · Claus Wagner
DLR Göttingen, Bunserstr. 12, 37073 Göttingen
e-mail: claus.wagner@dlr.de

Fig. 1 The magnitude of the velocity rms showing the increased turbulent kinetic energy starting from above the trailing edge in the wake.

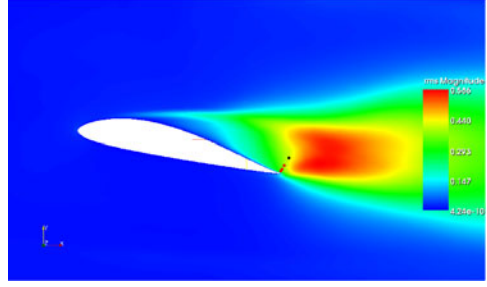


Fig. 1 shows the distribution of the rms magnitude of the flow. At chosen observation points in the region of the turbulent flow, the characteristic fields of the flow have been recorded over a period of $t=27$ resulting in a dataset of 11166 recordings. This data has been used for the statistical flow analysis and the stochastic reconstruction.

2 Increment Statistics

To investigate the flow field velocity $U_k(x_k, t)$ we consider the increments

$$u(\gamma) = U(\zeta) - U(\zeta - \gamma) \quad (1)$$

with ζ being x_k or t , γ being a scale, and u being an increment of the velocity U for any component k at scale γ . With the approach described by Renner et. al. [5] we analyze if Markov properties exist. This means

$$p(u_i(\gamma_i) | u_{i+1}(\gamma_{i+1}), \dots, u_n(\gamma_n)) = p(u_i(\gamma_i) | u_{i+1}(\gamma_{i+1})). \quad (2)$$

holds for the corresponding PDFs. If this is valid, the joint PDF reduces to

$$p(u(\gamma_1), u(\gamma_2), \dots, u(\gamma_n)) = p(u(\gamma_1) | u(\gamma_2)) \dots p(u(\gamma_{n-1}) | u(\gamma_n)) \cdot p(u(\gamma_n)) \quad (3)$$

As shown by Renner et. al. [5] such PDFs can be reconstructed using a Kramers-Moyal expansion with $D^{(k)}$ denoting the Kramers-Moyal coefficients which can be estimated from a given dataset. If $D^{(4)} = 0$ the Kramers-Moyal expansion reduces to the Fokker-Planck equation [6].

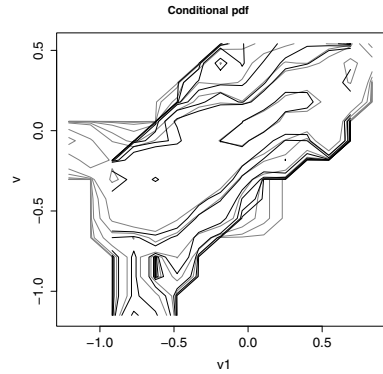
The method has been under investigation for time and spatial scales [5, 7]. Here we used it for an analysis of a flow field generated by the simulation.

3 Markov Analysis and Reconstruction of the Time Series

The velocity field at a single base point within the described turbulent region above the trailing edge has been analysed. To validate the estimation of Markov properties in time for the velocity-increment, we have to proof that (2) holds for the time steps

$\tau = \gamma$, for $\lambda_M \leq \tau \leq L$, with λ_M being the Markov and L the integral length scale. Here we use $\tau = 0.1375$, $\tau_1 = 2\tau$ and $\tau_2 = 3\tau$. For the evaluation the PDFs have been binned. As the dataset consisted of only slightly more than 10000 data points, only 15 bins were used for the comparison. Fig. 2 shows the contour plots of the single and double conditioned PDFs of equation (2) for the v (cross flow) velocity component. For brevity we refrain here from presenting the similar results for u and w . The contours show rather good agreement. Deviances can be explained by the lack of data. Thus we accept the assumption of Markov properties in this area of the flow.

Fig. 2 The figures show the contour plot of the PDF of $p(u(\tau)|u_1(\tau_1))$ (gray) and $p(u(\tau)|u_1(\tau_1), u_2(\tau_2))$ (black) for $\tau = 0.1375$ for v -increments.



Assuming Markov properties we can proceed in estimating the Kramers-Moyal expansion from the data for different τ . As we find that $D^{(4)} \ll D^{(2)}$ we proceeded with the reconstruction of the time series using the Langevin equation, which can be following Itô a reformulation of the the Fokker-Planck equation. Here we use a discretized version

$$u_{i+1} = u_i + \tau D^{(1)}(u, \tau) + \sqrt{\tau D^{(2)}(u, \tau)} \Gamma(\tau). \quad (4)$$

where $\Gamma(\gamma)$ is Gaussian distributed white noise, with the given τ and an initial u_0 from the original time series. In Fig. 3 the increment statistics of the original time series of v is plotted against the reconstructed one. Apart from some small deviances, which are most likely due to the limited data set, the reconstructed curve agrees rather good with the data.

Additionally the resulting Kramers-Moyal coefficients have been used with equation (4) to interpolate increments from the original point in space to a different point using instead of τ for time increments $r = x1_k - x2_k$ for spacial increments. First results in fig. 4 match surprisingly good.

Fig. 3 Plot of the non conditioned PDFs $p(u_k, \tau)$ (line) and $p(u_{k,rec}, \tau)$ dots at $\tau = 0.1375$.

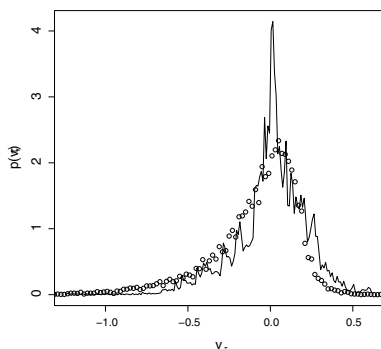
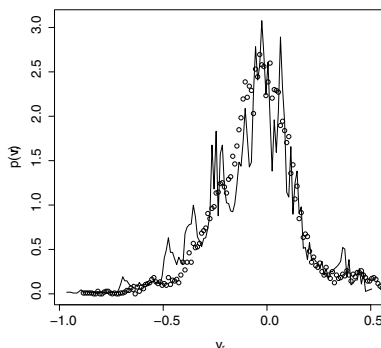


Fig. 4 Plot of the non conditioned PDFs $p(u_k, r)$ (line) and $p(u_{k,rec}, r)$ dots at $r = 0.088$.



References

1. Nawroth, A.P., Peinke, J.: Multiscale reconstruction of time series. *Physics Letters A* 360, 234–237 (2006)
2. Kirby, R.M., Warburton, T., Sherwin, S.J., Beskok, A., Karniadakis, G.E.: Dynamic Simulations without Remeshing. In: *Proceedings of the ASME*, vol. 397 (1999)
3. Ma, X., Karamanos, G.S., Karniadakis, G.E.: Dynamics and low-dimensionality of a turbulent near wake. *J. of Fluid Mech.* 410, 29–65 (2000)
4. Dong, S., Karniadakis, G.E., Ekmekci, A., Rockwell, D.: A combined direct numerical simulation - particle image velocimetry study of the turbulent near wake. *J. of Fluid Mech.* 569, 185–207 (2006)
5. Renner, C., Peinke, J., Friedrich, R.: Markov properties of small scale turbulence. *J. Fluid Mech.* 433, 383–409 (2001)
6. Risken, H.: *The Fokker-Planck Equation*. Springer (1996)
7. Stresing, R., Tutkun, M., Peinke, J.: Spatial Multi-Point Correlations in Inhomogeneous Turbulence. In: Peinke, J., Oberlack, M., Talamelli, A. (eds.) *Progress in Turbulence III*. Springer Proceedings in Physics, vol. 131, pp. 33–36. Springer, Heidelberg (2009)

A Note on Spatial Zero Crossings of Fluctuating Velocity Field in Wall Bounded Turbulent Flows

Tardu Sedat

Abstract. Spatial zero-crossings of fluctuating velocity and shear stress fields are investigated in a turbulent channel flow, through direct numerical simulations. It is confirmed that the Liepmann and Taylor scales resulting from spatial zero crossings coincide more or less as in experimental time-series. A simple relationship is provided for the zero-crossing frequency of shear stress signals. It is further shown that the spanwise zero-crossings of the local wall normal velocity contributes up to 80% to the dissipation near the wall.

1 Introduction

Zero-crossings of fluctuating velocity time series provide a simple way to access to Taylor scales in wall-bounded flows (see [1],[2] and references within). Experiments have shown that the time scale related to the velocity zero-crossings is roughly equal to the Taylor scale in wall-bounded flows. We revisit the problem here by considering the zero-crossings of fluctuating velocity fields in space, at a given time. Direct numerical simulations (DNS) at low Reynolds number (180 based on the half channel width h and shear velocity) are used for this purpose. The computational domain extends to $4\pi h \times 2h \times 4/3\pi h$ in the streamwise, wall normal and spanwise directions and the number of computational modes are respectively $256 \times 128 \times 256$.

2 Results

Define by $f_{0,ij}$ the spatial cross zero crossings of the velocity component $u_i(x_i, t)$ at a fixed time in the x_j direction. By cross-zero crossings we mean that the velocity changes sign while it goes through zero, i.e. the tangential zero crossings are not

Tardu Sedat
LEGI, B.P. 53 X, 38041 Grenoble, Cedex 9, France
e-mail: Sedat.Tardu@hmg.inpg.fr

taken into account. The Liepmann scale associated with $f_{0,ij}$ is $\Lambda_{ij} = \frac{1}{\pi f_{0,ij}}$. For a Gaussian signal the Liepmann scale is exactly equal to

$$\Lambda_{ij} = \lambda_{ij} = \sqrt{\frac{\overline{u_i^2}}{(\partial u_i / \partial x_j)^2}} \quad (1)$$

where λ_{ij} is defined as the associated Taylor scale [1]. The spatial coordinates are denoted by $x(j=1)$, $y(j=2)$ and $z(j=3)$ in respectively the streamwise, wall normal and spanwise directions. The subscript $i=1, 2$ and 3 corresponds respectively to the x, y and z components of the fluctuating velocity field that are also denoted by u, v and w . It is well known for a while that the time series of fluctuating wall normal v and streamwise velocity u fluctuations in the wall bounded turbulent flows follow quite closely this relationship, despite the strongly non-Gaussian character of the instantaneous flow field [1]. Our own experimental results (not discussed here) are also in close agreement with these findings. We checked the validity of the relation (1), for the spatial zero crossings of the u, v and w , in the x and z directions at homogeneous y planes through DNS data. Globally, the Liepmann scales based on the spatial zero-crossings follow more or less well the equation (1), with a maximum deviation of $\pm 15\%$. Fig. 1 shows the ratio Λ/λ for the streamwise and spanwise zero-crossings of the wall normal fluctuating velocity field, versus the distance to the wall in inner variables y^+ where $()^+$ denotes quantities scaled by the viscosity and the shear velocity. It is seen that the Liepmann scale is close to the Taylor scale in the whole wall layer, despite a systematic increase and decrease of Λ/λ respectively in the low-buffer and log layers. Fig. 2 shows the Taylor scales of u and v in the spanwise direction ($j=3$, and $i=1$ or 2 in the equation 1). It is seen that λ_{uz}^+ is constant in the low buffer layer and increases in the log-layer. The linear increase of λ_{vz}^+ from the wall to the centerline is remarkable. One of the questions that arise from previous investigations is the zero-crossing frequency of the shear stress signals such as uv (see [1]). Consider for simplicity the time series $uv(t)$ (the results may easily be generalized to spatial zero-crossings). The cross-crossings frequency f_{0uv} of the signal uv through zero is simply

$$f_{0uv} = f_{0u} + f_{0v} - f_{0u \wedge v} \quad (2)$$

where the simultaneous zero-crossing frequency $f_{0u \wedge v}$ of u and v is subtracted since, otherwise they are doubly accounted. Now, at simultaneous zero-crossing points one has $\partial(uv)/\partial t = 0$, and these points are tangential zero-crossings that are not taken into account. Therefore $f_{0u \wedge v} = 0$, and

$$\frac{\Lambda_{uv}}{\Lambda_u} = \frac{1}{1 + (\Lambda_u/\Lambda_v)} \quad (3)$$

Our experimental and numerical data and the measurements reported in [1] are in perfect agreement with this relationship.

It has been argued for a while that the zero-crossings of fluctuating velocity signals should largely contribute to the dissipation in, at least, isotropic turbulence.

That the zero-crossing frequency of u is related to $(\partial u / \partial x)^2$, does obviously not imply that the dissipation is locally important during the zero-crossings, and this point has not been entirely elucidated. The wall flow on the other hand can be considered locally isotropic only far away from the wall, say near the centerline of a channel, or the edge of a boundary layer. Using a suitably defined Dirac function at the zero-crossings points, it can be rigorously shown that the ensemble-averaged dissipation at the zero-crossing points of the component $u_i(x_i, t)$ in the direction x_j is:

$$\varepsilon_{zcij} = \frac{E(\varepsilon | u_{i,j} | | u_i = 0)}{E(|u_{i,j}| | u_i = 0)} \quad (4)$$

where $|u_{i,j}(x_j)|$ is the absolute value of the derivative $\partial u_i / \partial x_j$, E stands for the expected value and $\varepsilon = \nu u_{i,j}(u_{i,j} + u_{j,i})$ is the local dissipation. Namely the mean dissipation at the zero-crossing points is the normalized mean of the dissipation times the absolute velocity derivative and not simply the ensemble averaged dissipation when the zero-crossings occur. The latter represents correctly the contribution to the dissipation at zero-crossing points, with:

$$\varepsilon_{zcij} = E(\varepsilon | u_i = 0) \quad (5)$$

only when ε and $u_{i,j}$ are independent, which obviously is not the case here. The contribution C_ε , defined as the ratio of dissipation occurring at zero-crossings to the total dissipation, can then easily be obtained from (4) while the pseudo contribution $C_{P\varepsilon}$ is related to (5). We determined C_ε and $C_{P\varepsilon}$ for the three components of fluctuating velocity in the x and z directions at a given distance from the wall. Contrarily to what has been suggested before, the zero crossings of the wall normal velocity v in the spanwise direction z contribute mostly to the dissipation (Fig. 3) instead of longitudinal x crossings of u (or any other combination, not shown here). The contribution to the dissipation at v zero-crossings is larger than 40% at $y^+ > 20$, reaching 80% near the wall, as it is clearly seen in Fig. 3. In the logarithmic region all contributions decrease to about 30%.

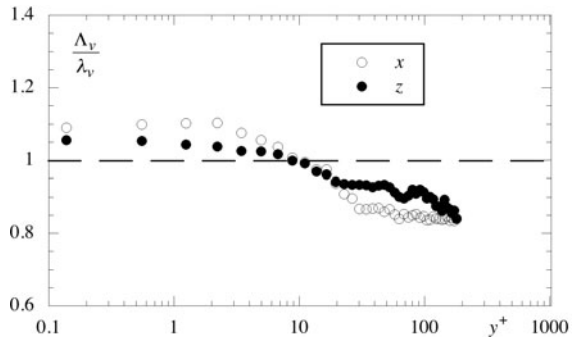


Fig. 1 Ratio of Liepmann to Taylor scales of the wall normal velocity fluctuations in the streamwise and spanwise directions

Fig. 2 Spanwise Taylor scales in wall units related to streamwise and spanwise velocity fluctuations.

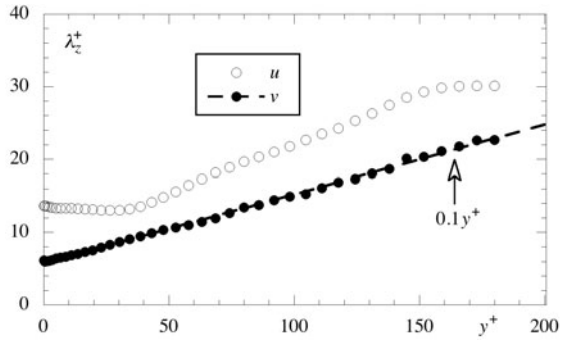
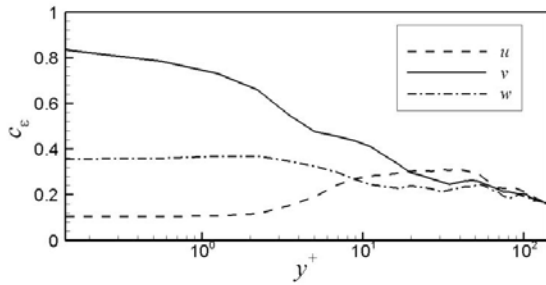


Fig. 3 Contribution of spanwise zero crossings of the fluctuating velocity field to the total dissipation.



3 Conclusion

Results analyzed in this paper suggest that the small-scale structure of the turbulence close to the wall up to the buffer layer is locally dominated by the wall normal velocity fluctuations and their spanwise zero-crossings. The dissipation largely occurs at the core of small-scale coherent streamwise vortices wherein the wall normal velocity crosses zero by changing its sign. The situation is less clear in the high buffer and log layers wherein it is difficult to relate the dissipation to the spatial zero-crossings of the velocity field.

References

1. Kailasnath, P., Sreenivasan, K.R.: Zero crossings of velocity fluctuations in turbulent boundary layers. *Phys. Fluids* A5(11), 2879–2885 (1993)
2. Sreenivasan, K.R., Bershadskii, A.: Clustering properties in turbulent signals. *J. Statistical Physics* 125, 1145–1157 (2006)

Non-equilibrium Statistical Mechanics of Fluid Turbulence

Tomomasa Tatsumi

Abstract. Theory of fluid turbulence based on the non-equilibrium statistical mechanics is formulated using the infinite set of equations for the multi-point velocity distributions given by Lundgren (1967) [2] and Monin (1967) [3] and the *cross-independence closure hypothesis* proposed by Tatsumi (2001) [4]. The present hypothesis is found to give identical closure to the distribution equations and hence the closed equations for the velocity distributions must be exact. This conclusion is confirmed by the fact that the moment-expansion of the distribution equations presents the equations for the mean velocity-products of various orders which are completely identical with the known equations derived from the Navier-Stokes equation directly. Another interesting result is that the energy-dissipation rate ε is expressed as an integral of the velocity-difference distribution which is mostly contributed from small-scale turbulence, making close analogy with the 'fluctuation-dissipation theorem' of non-equilibrium statistical mechanics.

1 Closure Problem of Turbulence

The complete statistical description of fluid turbulence is given by Lundgren (1967) [2] and Monin (1967) [3] in terms of the infinite set of equations for the multi-point probability distributions of the turbulent velocity. In practice, we have to deal with only finite subsets of the equations and then encounter the problem of *closure* of these equations since the equation for the n -point distribution includes the $(n + 1)$ -point distribution as a new unknown. In order to overcome this difficulty, a *closure hypothesis* has to be introduced to the unclosed equations.

Tomomasa Tatsumi

Kyoto University, Professor Emeritus, 26-6 Chikuzendai, Momoyama, Fushimi,
Kyoto 612-8032 Japan

e-mail: tatsumi@skyblue.ocn.ne.jp

1.1 Cross-Independence Closure

The probability distributions of the velocities $\mathbf{u}_i(t) = \mathbf{u}(\mathbf{x}_i, t)$ ($i = 1, 2$) are defined as

$$\begin{aligned} f(\mathbf{v}_1, \mathbf{x}_1, t) &= \langle \delta(\mathbf{u}_1(t) - \mathbf{v}_1) \rangle, \\ f^{(2)}(\mathbf{v}_1, \mathbf{v}_2; \mathbf{x}_1, \mathbf{x}_2; t) &= \langle \delta(\mathbf{u}_1(t) - \mathbf{v}_1) \delta(\mathbf{u}_2(t) - \mathbf{v}_2) \rangle, \end{aligned} \quad (1)$$

where δ denotes the three-dimensional delta function, $\langle \rangle$ the mean of the random variable with respect to its probability distribution, and \mathbf{v}_i the probability variable for the random velocity $\mathbf{u}_i(t)$.

In general, the distributions f and $f^{(2)}$ are not correlated, but if they are related in some case, this relation may be used as a closure hypothesis. The simplest one for this purpose may be the *independence* relation,

$$f^{(2)}(\mathbf{v}_1, \mathbf{v}_2; \mathbf{x}_1, \mathbf{x}_2; t) = f(\mathbf{v}_1, \mathbf{x}_1, t) f(\mathbf{v}_2, \mathbf{x}_2, t). \quad (2)$$

which is valid if $f(\mathbf{v}_1)$ and $f(\mathbf{v}_2)$ are both normal, so that it is called the *quasi-normal approximation*. This relation is generally valid for large distances $r = |\mathbf{x}_2 - \mathbf{x}_1| \rightarrow \infty$ according to the asymptotic independence in this limit, but usually not valid otherwise.

On the other hand, if we consider the sum and difference of the velocities \mathbf{u}_1 and \mathbf{u}_2 as

$$\mathbf{u}_+(t) = (\mathbf{u}_1(t) + \mathbf{u}_2(t))/2, \quad \mathbf{u}_-(t) = (\mathbf{u}_2(t) - \mathbf{u}_1(t))/2, \quad (3)$$

and define the distributions of the *cross-velocities* \mathbf{u}_+ and \mathbf{u}_- as

$$\begin{aligned} g_{\pm}(\mathbf{v}_{\pm}; \mathbf{x}_1, \mathbf{x}_2; t) &= \langle \delta(\mathbf{u}_{\pm}(t) - \mathbf{v}_{\pm}) \rangle, \\ g^{(2)}(\mathbf{v}_+, \mathbf{v}_-; \mathbf{x}_1, \mathbf{x}_2; t) &= \langle \delta(\mathbf{u}_+(t) - \mathbf{v}_+) \delta(\mathbf{u}_-(t) - \mathbf{v}_-) \rangle, \end{aligned} \quad (4)$$

\mathbf{v}_{\pm} denoting the probability variables for the random velocities \mathbf{u}_{\pm} , we can assume the following relation for the distributions $g^{(2)}$ and g_{\pm} :

$$g^{(2)}(\mathbf{v}_+, \mathbf{v}_-; \mathbf{x}_1, \mathbf{x}_2; t) = g_+(\mathbf{v}_+; \mathbf{x}_1, \mathbf{x}_2; t) g_-(\mathbf{v}_-; \mathbf{x}_1, \mathbf{x}_2; t), \quad (5)$$

which may be called the *cross-independence* relation.

Using the identity between the distributions $f^{(2)}$ and $g^{(2)}$,

$$f^{(2)}(\mathbf{v}_1, \mathbf{v}_2; \mathbf{x}_1, \mathbf{x}_2; t) d\mathbf{v}_1 d\mathbf{v}_2 = g^{(2)}(\mathbf{v}_+, \mathbf{v}_-; \mathbf{x}_1, \mathbf{x}_2; t) d\mathbf{v}_+ d\mathbf{v}_-, \quad (6)$$

the *cross-independence* relation (5) can be taken as another closure hypothesis for the distribution $f^{(2)}$,

$$\begin{aligned} f^{(2)}(\mathbf{v}_1, \mathbf{v}_2; \mathbf{x}_1, \mathbf{x}_2; t) &= 2^{-3} g^{(2)}(\mathbf{v}_+, \mathbf{v}_-; \mathbf{x}_1, \mathbf{x}_2; t) \\ &= 2^{-3} g_+(\mathbf{v}_+; \mathbf{x}_1, \mathbf{x}_2; t) g_-(\mathbf{v}_-; \mathbf{x}_1, \mathbf{x}_2; t). \end{aligned} \quad (7)$$

where the coefficient is due to the Jacobian $\partial(d\mathbf{v}_+, d\mathbf{v}_-) / \partial(d\mathbf{v}_1, d\mathbf{v}_2) = 2^{-3}$.

1.2 Complete Closure

Unlike the *independence* relation (2), the *cross-independence* relation (7) is shown to be valid for small values of r in addition to large values. It generally follows as the coincidence conditions of the the velocity distributions for $r = |\mathbf{x}_2 - \mathbf{x}_1| \rightarrow 0$ that

$$\begin{aligned} \lim_{|\mathbf{x}_2 - \mathbf{x}_1| \rightarrow 0} f^{(2)}(\mathbf{v}_1, \mathbf{v}_2; \mathbf{x}_1, \mathbf{x}_2; t) &= f(\mathbf{v}_1, \mathbf{x}_1, t) \delta(\mathbf{v}_2 - \mathbf{v}_1), \\ \lim_{|\mathbf{x}_2 - \mathbf{x}_1| \rightarrow 0} g_+(\mathbf{v}_+; \mathbf{x}_1, \mathbf{x}_2; t) &= f(\mathbf{v}_1, \mathbf{x}_1, t), \\ \lim_{|\mathbf{x}_2 - \mathbf{x}_1| \rightarrow 0} g_-(\mathbf{v}_-; \mathbf{x}_1, \mathbf{x}_2; t) &= \delta(\mathbf{v}_-) = 2^3 \delta(\mathbf{v}_2 - \mathbf{v}_1). \end{aligned} \quad (8)$$

That is,

$$\lim_{|\mathbf{x}_2 - \mathbf{x}_1| \rightarrow 0} f^{(2)}(\mathbf{v}_1, \mathbf{v}_2; \mathbf{x}_1, \mathbf{x}_2; t) = \lim_{|\mathbf{x}_2 - \mathbf{x}_1| \rightarrow 0} 2^{-3} g_+(\mathbf{v}_+; \mathbf{x}_1, \mathbf{x}_2; t) g_-(\mathbf{v}_-; \mathbf{x}_1, \mathbf{x}_2; t), \quad (9)$$

which shows the *completeness* of the *cross-independence closure* (7) for small values of $r \rightarrow 0$.

2 Closure of One-Point Equation

2.1 Closed One-Point Equation

The Lundgren-Monin equation for the one-point velocity distribution f is expressed for general inhomogeneous turbulence as follows:

$$\begin{aligned} \left[\frac{\partial}{\partial t} + \mathbf{v}_1 \cdot \frac{\partial}{\partial \mathbf{x}_1} \right] f(\mathbf{v}_1, \mathbf{x}_1, t) &= -v \lim_{|\mathbf{x}_2 - \mathbf{x}_1| \rightarrow 0} \left| \frac{\partial}{\partial \mathbf{x}_2} \right|^2 \frac{\partial}{\partial \mathbf{v}_1} \cdot \int \mathbf{v}_2 f^{(2)}(\mathbf{v}_1, \mathbf{v}_2; \mathbf{x}_1, \mathbf{x}_2; t) d\mathbf{v}_2 \\ &+ \frac{\partial}{\partial \mathbf{v}_1} \cdot \frac{\partial}{\partial \mathbf{x}_1} \frac{1}{4\pi} \int \int |\mathbf{x}_2 - \mathbf{x}_1|^{-1} \left(\mathbf{v}_2 \cdot \frac{\partial}{\partial \mathbf{x}_2} \right)^2 f^{(2)}(\mathbf{v}_1, \mathbf{v}_2; \mathbf{x}_1, \mathbf{x}_2; t) d\mathbf{v}_2 d\mathbf{x}_2, \end{aligned} \quad (10)$$

which includes the higher-order distributions $f^{(2)}$ on the right-hand side.

The closure of this equation by means of the *cross-independence closure hypothesis* (7) is made according to the procedure employed by Tatsumi (2001) (4), and the closed equation for the *one-point velocity distribution* f is obtained as follows:

$$\begin{aligned} \left[\frac{\partial}{\partial t} + \mathbf{v}_1 \cdot \frac{\partial}{\partial \mathbf{x}_1} + v \frac{\partial}{\partial \mathbf{v}_1} \cdot \mathbf{v}_1 \left| \frac{\partial}{\partial \mathbf{x}_1} \right|^2 + \alpha(\mathbf{x}_1, t) \left| \frac{\partial}{\partial \mathbf{v}_1} \right|^2 - \frac{\partial}{\partial \mathbf{v}_1} \cdot \frac{\partial}{\partial \mathbf{x}_1} \beta(\mathbf{v}_1; \mathbf{x}_1, t) \right] \\ \times f(\mathbf{v}_1, \mathbf{x}_1, t) = 0, \end{aligned} \quad (11)$$

where the parameters $\alpha(\mathbf{x}_1, t)$ and $\beta(\mathbf{v}_1, \mathbf{x}_1, t)$ are defined as

$$\alpha(\mathbf{x}_1, t) = \frac{2}{3} \mathbf{v} \lim_{|\mathbf{x}_2 - \mathbf{x}_1| \rightarrow 0} \left| \frac{\partial}{\partial \mathbf{x}_2} \right|^2 \int |\mathbf{v}_-|^2 g_-(\mathbf{v}_-; \mathbf{x}_1, \mathbf{x}_2; t) d\mathbf{v}_-, \quad (12)$$

$$\begin{aligned} \beta(\mathbf{v}_1, \mathbf{x}_1, t) &= \frac{1}{4\pi} \int \int |\mathbf{x}_2 - \mathbf{x}_1|^{-1} \left(\mathbf{v}_2 \cdot \frac{\partial}{\partial \mathbf{x}_2} \right)^2 \left(1 + \mathbf{v}_- \cdot \frac{\partial}{\partial \mathbf{v}_1} \right) \\ &\quad \times g_-(\mathbf{v}_-; \mathbf{x}_1, \mathbf{x}_2; t) d\mathbf{v}_- d\mathbf{x}_2. \end{aligned} \quad (13)$$

The parameter $\alpha(\mathbf{x}_1, t)$ is shown to be equivalent to the *energy dissipation rate* $\varepsilon(\mathbf{x}_1, t)$ as follows:

$$\alpha(\mathbf{x}_1, t) = \frac{1}{3} \mathbf{v} \sum_{i,j=1}^3 \left\langle \left(\frac{\partial u_i(\mathbf{x}_1, t)}{\partial x_{1j}} \right)^2 \right\rangle = \frac{1}{3} \varepsilon(\mathbf{x}_1, t), \quad (14)$$

according to the definition of the energy dissipation rate ε .

Although Eq.(11) provides us with the closed equation for the distribution f , we cannot solve this equation by itself since its parameters α and β depend upon the distribution g_- which is a part of the distribution $f^{(2)}$ according to Eqs.(4) and (6). Thus, in order to solve the equations for the velocity distributions, we have to deal with at least the pair of the equations for the distributions f and $f^{(2)}$.

It is interesting to note that the *energy dissipation rate* $\alpha = \varepsilon/3$, being expressed by Eq.(12) in terms of the *velocity-difference distribution* g_- which is mostly contributed from small turbulent fluctuations, really manifests the "*fluctuation-dissipation theorem*" of non-equilibrium statistical mechanics.

2.2 One-Point Moment Equations

The closed equation (11) for the distribution f has been obtained from the unclosed but exact Lundgren-Monin equation (10) through the *complete closure* (9). Thus the exactness of Eq.(11) for the distribution f seems undoubted. This can be confirmed by comparing the moment equations of Eq.(11) with the known equations for the *mean velocity products*.

Actually, the equations for the *mean velocity* $\bar{\mathbf{u}}(\mathbf{x}, t) = \langle \mathbf{u}(\mathbf{x}, t) \rangle$ and the *mean kinetic energy* $E(x, t) = \langle |\mathbf{u}(\mathbf{x}, t)|^2 / 2 \rangle$ of turbulence are obtained as the first two equations of the moment expansion of Eq.(11), and it is found that these equations are identical with the known equations derived from the Navier-Stokes equation (see for details Tatsumi (2011) [5]). This agreement gives two important consequences. First, it confirms the exactness of the result due to the present complete closure. Secondly, it makes the classical *closure problem* around the mean velocity products needless since they are simultaneously derived from the velocity distributions of concern.

3 Closure of Two-Point Equation

3.1 Closed Two-Point Equation

The Lundgren-Monin equation for the two-point velocity distribution $f^{(2)}$ is expressed as follows:

$$\begin{aligned}
 & \left[\frac{\partial}{\partial t} + \mathbf{v}_1 \cdot \frac{\partial}{\partial \mathbf{x}_1} + \mathbf{v}_2 \cdot \frac{\partial}{\partial \mathbf{x}_2} \right] f^{(2)}(\mathbf{v}_1, \mathbf{v}_2; \mathbf{x}_1, \mathbf{x}_2; t) \\
 &= -\nu \sum_{n=1}^2 \lim_{|\mathbf{x}_3 - \mathbf{x}_n| \rightarrow 0} \left| \frac{\partial}{\partial \mathbf{x}_3} \right|^2 \frac{\partial}{\partial \mathbf{v}_n} \cdot \int \mathbf{v}_3 f^{(3)}(\mathbf{v}_1, \mathbf{v}_2, \mathbf{v}_3; \mathbf{x}_1, \mathbf{x}_2, \mathbf{x}_3; t) d\mathbf{v}_3 \\
 &+ \sum_{n=1}^2 \frac{\partial}{\partial \mathbf{v}_n} \cdot \frac{\partial}{\partial \mathbf{x}_n} \frac{1}{4\pi} \int \int |\mathbf{x}_3 - \mathbf{x}_n|^{-1} \left(\mathbf{v}_3 \cdot \frac{\partial}{\partial \mathbf{x}_3} \right)^2 \\
 &\times f^{(3)}(\mathbf{v}_1, \mathbf{v}_2, \mathbf{v}_3; \mathbf{x}_1, \mathbf{x}_2, \mathbf{x}_3; t) d\mathbf{v}_3 d\mathbf{x}_3. \tag{15}
 \end{aligned}$$

The closure of Eq. (15) is made by applying the *cross-independence closure hypothesis* (7) to the pairs of the velocities $(\mathbf{v}_1, \mathbf{v}_3)$ and $(\mathbf{v}_2, \mathbf{v}_3)$ of the distribution $f^{(3)}$. The result depends upon whether the distance $r = |\mathbf{x}_2 - \mathbf{x}_1|$ belong to the *global* range larger than the distances $r' = |\mathbf{x}_3 - \mathbf{x}_1|$ and $r'' = |\mathbf{x}_3 - \mathbf{x}_2|$ or to the *local* range comparable to r' and r'' .

If the distance r belongs to the *global* range, the closed equation for the *distribution* $f^{(2)}$ is obtained as follows (see for details Tatsumi (2011)[5]):

$$\begin{aligned}
 & \left[\frac{\partial}{\partial t} + \sum_{m=1}^2 \left\{ \mathbf{v}_m \cdot \frac{\partial}{\partial \mathbf{x}_m} + \nu \frac{\partial}{\partial \mathbf{v}_m} \cdot \mathbf{v}_m \left| \frac{\partial}{\partial \mathbf{x}_m} \right|^2 \right\} \right] f^{(2)}(\mathbf{v}_1, \mathbf{v}_2; \mathbf{x}_1, \mathbf{x}_2; t) \\
 &= - \sum_{m=1}^2 \left\{ \alpha(\mathbf{x}_m, t) \left| \frac{\partial}{\partial \mathbf{v}_m} \right|^2 - \frac{\partial}{\partial \mathbf{v}_m} \cdot \frac{\partial}{\partial \mathbf{x}_m} \beta(\mathbf{v}_m, \mathbf{x}_m, t) \right\} f^{(2)}(\mathbf{v}_1, \mathbf{v}_2; \mathbf{x}_1, \mathbf{x}_2; t), \tag{16}
 \end{aligned}$$

where the parameters α and β are defined in the similar manner as $\alpha(\mathbf{x}_1, t)$ and $\beta(\mathbf{v}_1, \mathbf{x}_1, t)$ in §2.2 respectively.

3.2 Two-Point Moment Equation

The equation for the two-point *velocity correlation* $U^{(2)}(\mathbf{x}_1, \mathbf{x}_2; t) = \langle \mathbf{u}(\mathbf{x}_1, t) \cdot \mathbf{u}(\mathbf{x}_2, t) \rangle$ is obtained by taking the double integral moment of Eq. (17) (see for details Tatsumi (2011)[5]). This equation is again in complete agreement with the corresponding equation derived from the Navier-Stokes equation. This agreement gives another confirmation for the exactness of the *cross-independence closure*.

4 Closure of Two-Point Local Equation

4.1 Closed Two-Point Local Equation

For dealing with the velocity distributions in the *local* range, we have to use the local variables normalized by Kolmogorov's length $\eta = (v^3/\varepsilon_0)^{1/4}$ and velocity $v = (v\varepsilon_0)^{1/4}$, ε_0 being an initial value of $\varepsilon(\mathbf{x}, t)$. It is also necessary to transform the velocities $(\mathbf{v}_1, \mathbf{v}_2)$ of the degenerate distributions $f^{(3)}$ in the Lundgren-Monin equation (15) for the distribution $f^{(2)}$ into the cross-velocities $(\mathbf{v}_+, \mathbf{v}_-)$ in order to secure their mutual independence. Then, the closed two-point local equation is obtained following the same procedure as that for deriving the closed two-point equation (17) in §3.1 as follows (see for details Tatsumi (2011) [5]):

$$\begin{aligned} & \left[\frac{\partial}{\partial t^*} + \sum_{m=1}^2 \left\{ \mathbf{v}_m^* \cdot \frac{\partial}{\partial \mathbf{x}_m^*} + \frac{1}{2} \frac{\partial}{\partial \mathbf{v}_m^*} \cdot \mathbf{v}_m^* \left(\left| \frac{\partial}{\partial \mathbf{x}_1^*} \right|^2 + \left| \frac{\partial}{\partial \mathbf{x}_2^*} \right|^2 \right) \right\} \right] f^{(2)}(\mathbf{v}_1^*, \mathbf{v}_2^*; \mathbf{x}_1^*, \mathbf{x}_2^*; t^*) \\ &= - \left[\sum_{\pm} \alpha_{\pm}^*(\mathbf{x}_1^*, \mathbf{x}_2^*; t^*) \left| \frac{\partial}{\partial \mathbf{v}_{\pm}^*} \right|^2 + \sum_{m=1}^2 \frac{\partial}{\partial \mathbf{v}_m^*} \cdot \frac{\partial}{\partial \mathbf{x}_m^*} \beta^*(\mathbf{v}_m^*, \mathbf{x}_m^*, t^*) \right] \\ & \times f^{(2)}(\mathbf{v}_1^*, \mathbf{v}_2^*; \mathbf{x}_1^*, \mathbf{x}_2^*; t^*), \end{aligned} \quad (17)$$

where the parameters $\alpha_{\pm}^*(\mathbf{x}_1^*, \mathbf{x}_2^*; t^*)$ and $\beta^*(\mathbf{v}_m^*, \mathbf{x}_m^*, t^*)$ are defined as

$$\alpha_{\pm}^*(\mathbf{x}_1^*, \mathbf{x}_2^*; t^*) = \frac{2}{3} \lim_{|\mathbf{x}_3^* - \mathbf{x}_1^*| \rightarrow 0} \left| \frac{\partial}{\partial \mathbf{x}_3^*} \right|^2 \int |\mathbf{v}_{\pm}^{*'}|^2 g_{\pm}(\mathbf{v}_{\pm}^{*'}; \mathbf{x}_1^*, \mathbf{x}_2^*, \mathbf{x}_3^*; t^*) d\mathbf{v}_{\pm}^{*'}, \quad (18)$$

$$\begin{aligned} \beta^*(\mathbf{v}_m^*, \mathbf{x}_m^*, t^*) &= \frac{1}{4\pi} \int \int |\mathbf{x}_3^* - \mathbf{x}_m^*|^{-1} \left(\mathbf{v}_3^* \cdot \frac{\partial}{\partial \mathbf{x}_3^*} \right)^2 \left(1 + \mathbf{v}_{-m}^* \cdot \frac{\partial}{\partial \mathbf{v}_m^*} \right) \\ & \times g_{-}(\mathbf{v}_{-}^{*'}; \mathbf{x}_m^*, \mathbf{x}_3^*; t^*) d\mathbf{v}_{-m}^* d\mathbf{x}_3^*, \end{aligned} \quad (19)$$

where $\mathbf{v}_{-m}^* = (\mathbf{v}_3^* - \mathbf{v}_m^*)/2$. The parameters $\alpha_{\pm}^*(\mathbf{x}_1^*, \mathbf{x}_2^*; t^*)$ represent the energy-dissipation rates in the *local* range of r^* corresponding to $\alpha(\mathbf{x}_1, t)$ and $\alpha(\mathbf{x}_2, t)$ for the *global* range of r^* .

4.2 Two-Point Local Moment Equation

The equation for the two-point *velocity correlation* in the *local* range $U^{(2)*}(\mathbf{x}_1^*, \mathbf{x}_2^*; t^*) = \langle \mathbf{u}^*(\mathbf{x}_1^*, t^*) \cdot \mathbf{u}^*(\mathbf{x}_2^*, t^*) \rangle$ is obtained by taking the double integral moment of Eq. (17) (see for details Tatsumi (2010) [5]). This equation does not seem to have been obtained already, but it is completely consistent with the corresponding equation for the *global* range.

5 Concluding Remarks

It has been established that the equations for the one-point velocity distribution f , the two-point velocity distribution $f^{(2)}$ and the two-point local velocity distribution $f^{(2)*}$, which have been closed by making use of the *cross-independence* closure hypothesis, constitute the minimum deterministic set of equations for non-equilibrium statistical mechanics of fluid turbulence.

It is to be noted that the present theory, which is based on the unclosed but exact Lundgren-Monin equation and the identically valid closure hypothesis, provides us with a complete statistical formulation of turbulence. Of course, it can be the case that the physical simplicity of a theory is depreciated by its mathematical complexity, but even in such a case, we can expect to be helped by the simplicity due to the inertial similarity of turbulent flows at large Reynolds numbers.

References

1. Kolmogorov, A.N.: The local structure of turbulence in incompressible viscous fluid for very large Reynolds numbers. Dokl. Akad. Nauk SSSR 30, 301–305 (1941)
2. Lundgren, T.S.: Distribution functions in the statistical theory of turbulence. Phys. Fluids 10, 969–975 (1967)
3. Monin, A.S.: Equations of turbulent motion. PMM J. Appl. Math. Mech. 31, 1057–1068 (1967)
4. Tatsumi, T.: Mathematical Physics of Turbulence. In: Kambe, T., et al. (eds.) Geometry and Statistics of Turbulence, pp. 3–12. Kluwer Academic Publishers, Dordrecht (2001)
5. Tatsumi, T.: Cross-Independence Closure for Statistical Mechanics of Fluid Turbulence. Journal of Fluid Mechanics 670, 364–403 (2011)

Two-Point Enstrophy Statistics of Fully Developed Turbulence

Michael Wilczek and Rudolf Friedrich

Abstract. We study the two-point enstrophy statistics of three-dimensional stationary homogeneous isotropic turbulence in the framework of kinetic equations for the probability density functions. The unclosed terms are estimated from data obtained from direct numerical simulations. The results yield insights into the statistics of enstrophy production and dissipation as well as the interaction of different spatial scales.

1 Introduction

The closure problem of turbulence is a central issue in theoretical turbulence research. A comprehensive way of treating the statistical problem is to study the multi-point probability density functions (PDFs) for velocity or vorticity. When deriving an evolution equation for the N -point PDF, the closure problem shows up in terms of a coupling to the $N + 1$ -point PDF [1, 2, 3]. Alternatively, one may introduce conditional averages entering the PDF equation as unknown functions [4, 5, 6], which then have to be modeled or taken from experiments or numerical simulations. This approach will be followed in the present paper.

While research on the velocity statistics in this framework has been initiated by Lundgren and Monin, Novikov has intensively studied the statistical features of the vorticity field. It turns out that the mathematical structure of the two hierarchies shares many formal similarities, however, the differing topology of the fields leads, for example, to a nearly Gaussian single-point PDF in the case of the velocity and a strongly non-Gaussian PDF for the vorticity. This fact makes the vorticity statistics particularly interesting to study. Furthermore, the more localized nature of the field allows to study the statistics in terms of dynamical processes of enstrophy production and dissipation.

Michael Wilczek · Rudolf Friedrich

Institute for Theoretical Physics, Westfälische Wilhelms-Universität, Wilhelm-Klemm-Str. 9, 48149 Münster, Germany

e-mail: mwilczek@uni-muenster.de, fiddir@uni-muenster.de

2 PDF Equation for Two-Point Enstrophy Statistics

The equation of motion for the enstrophy field is given by

$$\frac{\partial}{\partial t} \frac{\omega^2}{2} + \mathbf{u} \cdot \nabla_{\mathbf{x}} \frac{\omega^2}{2} = \omega \cdot \mathbf{S}\omega + \nu \omega \cdot \Delta_{\mathbf{x}} \omega + \omega \cdot (\nabla_{\mathbf{x}} \times \mathbf{F}), \quad (1)$$

where the left-hand side represents the convective derivative of the enstrophy, which is driven by enstrophy production (involving the rate-of-strain tensor \mathbf{S}), diffusion and the external forcing on the right-hand side. In the following we will consider statistically stationary homogeneous isotropic turbulence. Standard PDF methods [4] and additional application of statistical symmetries [7] now allow to derive evolution equations for PDFs from this equation of motion. Already the single-point equation for $f_1(z_1) = \langle \delta(\frac{1}{2}\omega_1^2(\mathbf{x}_1, t) - z_1) \rangle$ leads to the interesting result that, given a sufficiently high Reynolds number, the conditional enstrophy production balances the dissipative terms in very good approximation [5, 8, 6],

$$\langle \omega_1 \cdot \mathbf{S}_1 \omega_1 | z_1 \rangle + \langle \nu \omega_1 \cdot \Delta_{\mathbf{x}_1} \omega_1 | z_1 \rangle \approx 0, \quad (2)$$

and it has been shown that in this case the conditional average related to the external forcing has a negligible influence. This balance equation studied by Novikov [5, 8] may be regarded as a generalization of the Tennekes-Lumley balance of average enstrophy production and dissipation [9]. Proceeding to the two-point PDF $f_2(z_1, z_2; r)$ the corresponding evolution equation takes the form

$$\begin{aligned} \frac{1}{r^2} \frac{\partial}{\partial r} r^2 [\langle \delta u_l | z_1, z_2, r \rangle f_2] &\approx - \frac{\partial}{\partial z_1} [\langle \omega_1 \cdot \mathbf{S}_1 \omega_1 + \nu \omega_1 \cdot \Delta_{\mathbf{x}_1} \omega_1 | z_1, z_2, r \rangle f_2] \\ &\quad - \frac{\partial}{\partial z_2} [\langle \omega_2 \cdot \mathbf{S}_2 \omega_2 + \nu \omega_2 \cdot \Delta_{\mathbf{x}_2} \omega_2 | z_1, z_2, r \rangle f_2] \end{aligned} \quad (3)$$

involving the conditional enstrophy production and diffusion (related to the dissipation of enstrophy) at the two points \mathbf{x}_1 and \mathbf{x}_2 (separated by \mathbf{r}) as well as a coupling of the PDF in scale due to the conditional longitudinal velocity increment. For the present analysis we have neglected the terms related to the external forcing; the influence of the forcing on the vorticity correlations in the inertial range has been discussed in [10]. It can be shown that for a Gaussian random field both the longitudinal velocity increment as well as the enstrophy production terms vanish, such that not only the *shape* of the two-point PDF f_2 but also the *mathematical structure* of the above equation is closely related to the non-Gaussian features of the vorticity statistics. In the case of statistical independence the two-point PDF factorizes and the single-point conditional balance (2) is recovered. A further observation is that, as the velocity increment has to fulfill the constraint $\langle \delta u_l \rangle = 0$, probability fluxes both up- and downscale for different values of z_1 and z_2 are expected.

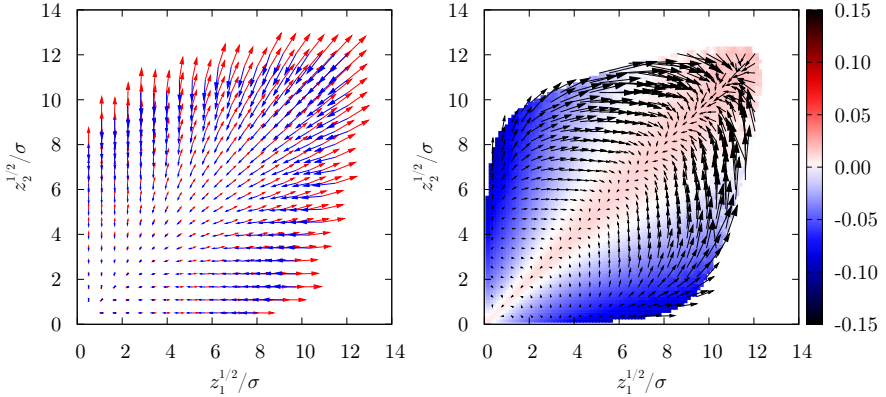


Fig. 1 Left: conditional enstrophy production (red) and enstrophy dissipation (blue). Right: Net vector field in the enstrophy plane and conditional longitudinal velocity increment (color scale) for $r = 2.5\eta$. The enstrophy axes are scaled by $\sigma = (\langle \omega^2 \rangle / 6)^{\frac{1}{2}}$, the color bar for the velocity increment by $\sigma_{\delta u_1, \infty} = \lim_{r \rightarrow \infty} \langle \delta u_1(r)^2 \rangle^{\frac{1}{2}}$. The lengths of the vectors has been adjusted, where the vector field in the right figure is amplified by a factor of ten compared to the vector field in the left figure.

3 DNS Results

The DNS results have been obtained by a standard pseudospectral method in a simulation of statistically stationary turbulence forced on large scales with 512^3 grid points at a Taylor-based Reynolds number of $R_\lambda = 112$. The conditional vector field spanned by the unclosed terms appearing in equation (3) is shown in figure 1 for a spatial distance of $r = 2.5\eta$. The vector field corresponding to the enstrophy production points into the direction of larger values of enstrophy and hence has an amplifying effect. The opposite effect is achieved by the dissipative terms, which produce a vector field pointing inwards. If the two vector fields are summed up, as in the PDF equation (3), they cancel to a good extent, only a small non-vanishing net vector field remains. This shows that enstrophy production and dissipation are strongly localized processes, which already almost balance pointwise in sample space.

The small remaining vector field by and large has an amplifying effect if $z_1 \not\approx z_2$ and a depleting effect if $z_1 \approx z_2$. This means that if, on the statistical average, the enstrophy is not equal in two nearby points, turbulence tends to level this difference. Once the enstrophy has leveled, a decay sets in. For intermediate distances not presented here the forcing term might give additional contributions.

In addition to the evolution in the z_1 - z_2 -plane one has to consider the evolution in scale related to the conditional longitudinal velocity increment also shown in figure 1. Here, the first thing to note is that the velocity increment field changes sign in the z_1 - z_2 -plane taking a negative sign if z_1 strongly differs from z_2 and becoming positive if the two enstrophies are roughly equal. If the conditional velocity increment is non-vanishing, this change of sign has to occur in order to yield $\langle \delta u_1 \rangle = 0$.

This observation adds another aspect to the interpretation of the statistical results. If two nearby enstrophies differ strongly, they tend to be attracted on the statistical average and tend to separate if the two enstrophies are roughly equal. While we observe for small to intermediate spatial separations a local imbalance of enstrophy production and dissipation as well as a probability flux in scale, the single-point balance (2) along with a vanishing conditional velocity increment is recovered for large spatial distances (figures not shown here).

4 Conclusions

We have presented results on the two-point enstrophy statistics in the framework of PDF equations. The unclosed terms have been estimated from DNS allowing for a characterization of the evolution of the two-point enstrophy statistics in the enstrophy plane and across scales. In particular, we find that the enstrophy production and the dissipative terms cancel to a good extent on all scales; a comparably small net vector field, however, remains on small to intermediate scales. This imbalance goes along with a probability flux in scale coupling the statistics of different distances. The results shed light on the connection between basic dynamical features of small-scale turbulence and their statistical implications. The Reynolds number dependence of the statistical quantities as well as an investigation of the influence of the forcing remains future work.

Acknowledgments. We thank Michel Voßkuhle and Anton Daitche for fruitful discussions. Computational resources were granted within the project h0963 at the LRZ Munich.

References

1. Lundgren, T.S.: Distribution Functions in the Statistical Theory of Turbulence. *Physics of Fluids* 10(5), 969 (1967)
2. Monin, A.S.: Equations of turbulent motion. *Prikl. Mat. Mekh.* 31(6), 1057 (1967)
3. Novikov, E.A.: Kinetic equations for a vortex field. *Soviet Physics-Doklady* 12(11), 1006 (1968)
4. Pope, S.B.: *Turbulent Flows*. Cambridge University Press, Cambridge (2000)
5. Novikov, E.A.: A new approach to the problem of turbulence, based on the conditionally averaged Navier-Stokes equations. *Fluid Dynamics Research* 12(2), 107 (1993)
6. Wilczek, M., Friedrich, R.: Dynamical origins for non-Gaussian vorticity distributions in turbulent flows. *Physical Review E* 80(1), 016316 (2009)
7. Wilczek, M., Daitche, A., Friedrich, R.: On the velocity distribution in homogeneous isotropic turbulence: correlations and deviations from Gaussianity. *J. Fluid Mech.* 676, 191 (2011)
8. Novikov, E.A., Dommermuth, D.G.: Conditionally averaged dynamics of turbulence. *Mod. Phys. Lett. B* 8(23), 1395 (1994)
9. Tennekes, H., Lumley, J.L.: *A First Course in Turbulence*. MIT Press, Cambridge (1983)
10. Novikov, E.A.: Statistical Balance of Vorticity and a New Scale for Vortical Structures in Turbulence. *Phys. Rev. Lett.* 71(17), 2718 (1993)

Session 2

Particle Laden Flows / Lagrangian Turbulence

Inertial Particles in a Turbulent Premixed Bunsen Flame

F. Battista, F. Picano, G. Troiani, and C.M. Casciola

1 Introduction

Many fields of engineering and physics are characterized by reacting flows seeded with particles of different inertia and dimensions, e.g. solid-propellant rockets, reciprocating engines where carbon particles form due to combustion, volcano eruptions. Particles are also used as velocity transducers in Particle Image Velocimetry (PIV) of turbulent flames. The effects of combustion on inertial particle dynamics is still poorly understood, despite its relevance for its effects on particle collisions and coalescence, phenomena which have a large influence in soot formation and growth [1]. As a matter of fact, the flame front induces abrupt accelerations of the fluid in a very thin region which particles follow with different lags depending on their inertia. This phenomenon has a large impact on the particle spatial arrangement. The issuing clustering is here analyzed by a DNS of Bunsen turbulent flame coupled with particle Lagrangian tracking with the aim of evaluating the effect of inertia on particle spatial localization in combustion applications. The Eulerian algorithm is based on Low-Mach number expansion of Navier-Stokes equations that allow arbitrary density variations neglecting acoustics waves, for detail see [4].

2 Theoretical Background

In order to define a proper theoretical framework, basic assumptions appropriate for the particle suspensions we are addressing are necessary. We deal with small

F. Battista · F. Picano · C.M. Casciola

Dipartimento di Meccanica e Aeronautica, Università Sapienza, Rome, Italy

e-mail: francesco.battista, francesco.picano@uniroma1.it

carlomassimo.casciola@uniroma1.it

G. Troiani

ENEA C.R. Casaccia, via anguillarese 301, 00123 Roma Italy

e-mail: guido.troiani@enea.it

spherical particles highly diluted to allow neglecting inter-particle collisions and force feedback on the fluid. Gravitational and thermophoretic forces are not considered and the particle mass-density ρ_p is taken to be much larger than the fluid density ρ_f . Under these assumptions the non-dimensional equation of motion for dispersed particles reads [3, 5]:

$$\dot{V} = \frac{U - V}{\tau_p} \quad (1)$$

where U and V are the fluid velocity at the particle position and the particle velocity, respectively, with $\tau_p = (18 d_p^2 \rho_p) / (v \rho_f)$ the particle response time to fluid velocity fluctuations (here d_p is the particle diameter and v the fluid kinematic viscosity). In its motion through the instantaneous flame front, the particle dynamics is controlled by the flamelet Stokes number,

$$St_{fl} = \frac{\tau_p S_{fl} (T_b/T_u - 1)}{\delta_{fl}}, \quad (2)$$

defined as the ratio of the typical time scale of the flame and the particle relaxation time. Actually, in turbulent premixed combustion the strong fluid accelerations across the front determines the relevant flow time scale which is expressed in terms of the characteristics of the laminar flame, $\tau_{fl} = (\delta_{fl}) / (\Delta u_{fl})$, with δ_{fl} the thermal thickness, $\Delta u_{fl} = S_{fl} (T_b/T_u - 1)$ the velocity jump across the front and S_{fl} the laminar flame speed, see [4] for further details and for a short description of computational algorithm and code used for the simulations described below.

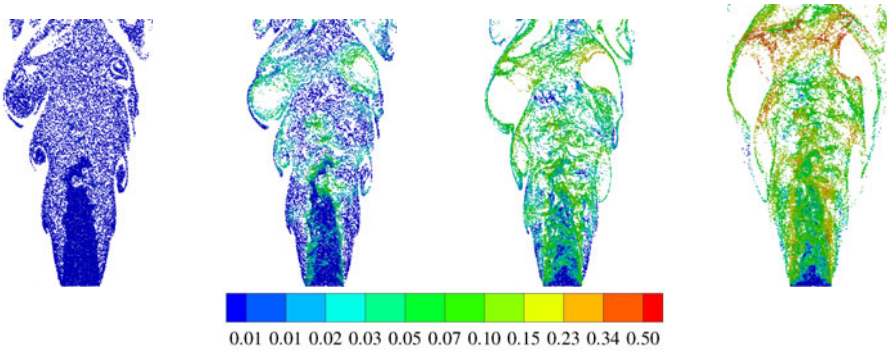


Fig. 1 Thin slice of width $R/20$ in the axial-radial plane of the instantaneous particle configuration for different Stokes time. From left: $St_{fl} = 0.022$, $St_{fl} = 0.54$, $St_{fl} = 2.16$ and $St_{fl} = 8.65$. Colors denote the norm of the difference between particle and fluid velocity: $|V - U|/U_0$.

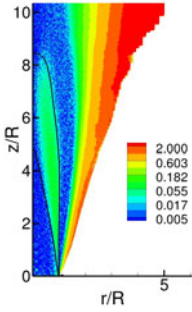


Fig. 2 Cluster Index field of $St_{fl} = 0.022$ particle, contour, computed through the equation (3); solid lines indicates two isolevels of the reactant concentration $Y_R/Y_R^0 = 0.05$ and $Y_R/Y_R^0 = 0.95$

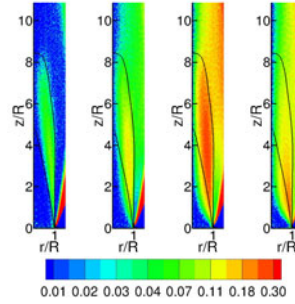


Fig. 3 Contours of the Cluster Index (3) for all particles, from left $St_{fl} = 0.022$, $St_{fl} = 0.54$, $St_{fl} = 2.16$ and $St_{fl} = 8.65$, respectively. The lines indicate two isolevels of the reactant concentration $Y_R/Y_R^0 = 0.05$ and $Y_R/Y_R^0 = 0.95$.

3 Results

Instantaneous configurations of the four particle populations are presented in figure 4 to illustrate the effect of the fluid density variation induced by the heat release on the particles. The different particle concentration between fresh and exhaust gas regions is apparent. The normalized velocity difference $|V - U|/U_0$ increases increasing the flamelet Stokes number St_{fl} , figure 5. While light particles relax to the fluid velocity relatively fast, a non negligible relative slip persists for heavier particles well into the product region. In any case the largest deviation from the local fluid velocity is localized in the flame front, where the abrupt acceleration occurs on the fast time scale set by chemical reactions, typically much shorter than the particle relaxation time, figure 6.

Figure 4 also shows the inertia-induced clustering taking place at smaller and smaller scales as the Stokes number is reduced. For intermediate particles, $St_{fl} = 0.54$ and 2.16 , clusters are particularly apparent in the product region, where voids have dimensions large enough to be clearly detected by the eye. The particles with the smallest inertia, $St_{fl} = 0.022$, due to their negligible inertia, are almost uniformly distributed in the two regions separated by the flame front, and away from the front behave more or less as a pure tracer.

The influence of inertia on the particle spatial distribution is better analyzed by exploiting the Clustering Index CI [2], that quantifies the deviation of the actual distribution from a perfectly random Poissonian arrangement,

$$CI = \frac{\overline{(\delta n)^2}}{\bar{n}} - 1, \quad (3)$$

where \bar{n} and $\overline{(\delta n)^2}$ are the particle average number in a fixed volume ΔV and its variance, respectively. The Clustering Index vanishes for a Poissonian distribution

and attains its absolute minimum, -1 , when the particles are equally spaced. When the particles aggregate in clusters, the clustering index becomes positive, $CI > 0$. In the case of inhomogeneous systems, like those addressed here, the clustering index is a scalar field $CI(\mathbf{x})$, which depends on the position of the volume ΔV used in its definition. For the present simulations, the clustering index field is reported in figure 2 for particles with $St_{fl} = 0.022$ and control volume ΔV corresponding to the computational cell. CI is positive within the flame brush and in the outer jet region. Both these regions are spanned by a fluctuating interface separating two zones with different particle concentration. The particle arrangement originated by such process differs substantially from a purely random homogeneous distribution and gives reason for the observed values of CI . Figure 3 reports the cluster index for all particle populations. Notably, increasing inertia, the departure from Poissonianity is found also in the product region. Nonetheless, the maximum deviation occurs for $St_{fl} = 2.16$ particles, still in the flame brush, since heavier particles are less influenced by the fluid expansion in the flame brush region, thus exhibiting a more uniform field of the clustering index.

4 Final Remarks

In the present paper we have discussed several issues related to particle clustering in turbulent premixed flames, by addressing a prototype Bunsen configuration. The clustering index CI proved useful to quantify clustering by measuring the departure of the particle distribution from a perfectly random arrangement. Maximum clustering is achieved for particles with order one flamelet Stokes number and it occurs within the flame brush, where the fluctuations of the instantaneous flame front couple with the inertial response. It is expected that the strong clustering found in the flame brush and in the outer part of the product region could play a crucial role in the coalescence processes involved in particulate formation and soot growth [1].

References

1. Hu, B., Yang, B., Koynlu, U.O.: Soot measurements at the axis of an ethylene/air non-premixed turbulent jet flame. *Comb. and Flame* 134(1-2), 93–106 (2003)
2. Kostinski, A.B., Shaw, R.A.: Scale-dependent droplet clustering in turbulent clouds. *J. Fluid Mech.* 434(-1), 389–398 (2001)
3. Maxey, M.R., Riley, J.J.: Equation of motion for a small rigid sphere in a nonuniform flow. *Phys. Fluids* 26(4), 883 (1983)
4. Picano, F., Battista, F., Troiani, G., Casciola, C.M.: Dynamics of PIV seeding particles in turbulent premixed flames. *Experiments in Fluids*, 114 (2010)
5. Stella, A., Guj, G., Kompenhans, J., Raffel, M., Richard, H.: Application of particle image velocimetry to combusting flows: design considerations and uncertainty assessment. *Experiments in Fluids* 30, 167–180 (2001)

Lagrangian Acceleration Statistics in 2D and 3D Turbulence

Oliver Kamps, Michael Wilczek, and Rudolf Friedrich

Abstract. In this paper we compare Lagrangian statistical quantities in the direct energy cascade of three-dimensional turbulence and the corresponding observables for the case of the inverse energy cascade in two dimensions. We focus on the acceleration of a tracer particle along its trajectory. Interpreting the acceleration as a stochastic process we show that for both systems the Markov time scale, which is an indicator for the length of the memory of a stochastic process, is in the order of magnitude of the Lagrangian integral time scale.

1 Introduction

It is a well known fact that two- and three-dimensional turbulent flows show some peculiar differences like the opposed direction of energy transfer. Especially the absence of intermittency of the Eulerian increment statistics in the inverse cascade of forced two-dimensional turbulence is a distinguishing feature between both types of flows [1]. Recently it was shown that, despite these pronounced differences in the Eulerian description, in the Lagrangian frame of reference observables like velocity increments or acceleration exhibit similar statistical properties like intermittency or long time correlations [2]. From this perspective it seems to be fruitful to compare the Lagrangian characteristics of two- and three-dimensional turbulence in a systematic way to explore which features of the Lagrangian observables are of a more universal nature and which of them depend more on the structure of the Eulerian flow field.

The basis of our investigation are two numerical pseudospectral simulations of the forced Navier-Stokes equation leading to a statistically stationary, homogeneous

Oliver Kamps
Center for Nonlinear Science, University of Münster
e-mail: okamp@uni-muenster.de

Michael Wilczek · Rudolf Friedrich
Institute for Theoretical Physics, University of Münster

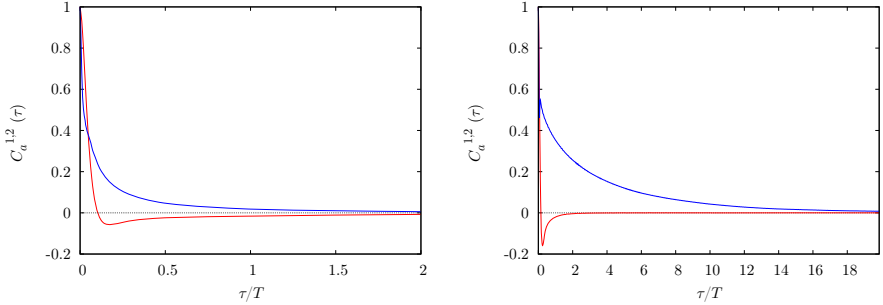


Fig. 1 The correlation functions $C_a^1(\tau)$ (red) and $C_a^2(\tau)$ (blue) for the three-dimensional (left) and the two-dimensional (right) case.

and isotropic flow field. One simulation was performed in two dimensions where the forcing is located at small length scales and a large scale energy sink is introduced to remove the energy flowing to large scales due to the inverse cascade. The other one was conducted on a three-dimensional domain with a forcing located at large scales leading to a direct energy cascade towards small scales. In both cases we use periodic domains with side length 2π and a resolution of 1024 grid points in each direction. To follow the tracer particles, the Eulerian fields are interpolated by a bi- and tri-cubic interpolation scheme, respectively. Further details can be found in [2] and [3].

In the following we will focus on the Cartesian components of the acceleration a_i and velocity v_i . Assuming isotropy we will skip the index and write a and v . By $T = \int_0^\infty d\tau C_v(\tau)$ we define the Lagrangian integral time scale via the autocorrelation $C_v(\tau)$ of the velocity components, which is a very useful quantity to compare time scales between the two systems under investigation.

2 Long Time Correlations and Long Time Memory

A frequently used quantity to characterize the evolution of the acceleration is the autocorrelation function. Here we consider the autocorrelation of the acceleration components $C_a^1(\tau)$ and the squared components $C_a^2(\tau)$. They are defined by

$$C_a^n(\tau) = \frac{\langle a^n(t)a^n(t+\tau) \rangle - \langle a^n(t) \rangle \langle a^n(t+\tau) \rangle}{\langle a^{2n}(t) \rangle - \langle a^n(t) \rangle^2}. \quad (1)$$

Due to the statistical stationarity of the velocity signal the area under the autocorrelation function of the derivative, here the acceleration, has to vanish. For this reason $C_a^1(\tau)$ in Fig. 1 shows the characteristic undershoot. For both cases $C_a^1(\tau)$ decays on a time scale between T and $2T$. For $C_a^2(\tau)$ we see a pronounced difference. In three dimensions $C_a^2(\tau)$ decays on approximately the same time scale as $C_a^1(\tau)$, whereas in the two-dimensional case it decays much slower. This indicates a stronger clustering of acceleration events with a similar amplitude, which might arise due to the

fact that in two dimensions the acceleration amplitude has less directions to decorrelate. Although the correlation describes how much information on past states is carried along with the tracer, it does not describe which information from the past, here denoted as *memory*, is needed to predict the next state. If we want to address this aspect, we have to consider the full statistical description of the acceleration of a tracer particle along its trajectory, which is given by the N -time probability density function (PDF) $f(a_N, \dots, a_1)$, where a_i denotes $a(t_i)$ and the sampling interval is $t_{i+1} - t_i = \Delta t$. In the limit $\Delta t \rightarrow 0$ the information would be complete. However, it is sufficient to choose the sampling interval smaller than the time scale on which the signal is smooth¹. In numerical simulations such a sampling time could be the time step given by the CFL criterion. Nevertheless, a description in terms of a N -time PDF is very complex even when N is countable. In the case that $a(t_i)$ can be described by a Markov process this high dimensional PDF can be decomposed into a product of two-time conditional PDFs

$$f(a_N, \dots, a_1) = p(a_N|a_{N-1}) \times \dots \times p(a_2|a_1)f(a_1). \quad (2)$$

In the case of a stationary process $p(a_i|a_{i-1})$ would be identical for all i , which implies that the whole process can be described by a single two-time conditional PDF. The question is for which time lag $\tau = t_{i+1} - t_i$ this decomposition can be performed. For a pure Markov process we would have $\tau = 0$ by definition, which would imply that even on the time scale of the smallest step Δt the Markov property is fulfilled. For most systems, however, τ is larger than Δt . For instance, in the case of the direct cascade of three-dimensional turbulence it has been shown in [4] that the evolution of the longitudinal velocity increments in scale can be described by a nonstationary Markov process when the step between two increments on different scales is larger than the Taylor-length. A necessary condition to check for the Markov property of the acceleration is the Chapman-Kolmogorov equation

$$p_{CK}(a_i|a_{i-2}) = \int da_{i-1} p(a_i|a_{i-1})p(a_{i-1}|a_{i-2}). \quad (3)$$

When the Markov property is fulfilled, $p_{CK}(a_i|a_{i-2})$ has to be equal to the transition probability $p(a_i|a_{i-2})$ directly estimated from the data. To test for the equality of the two transition probabilities, we use the correlation measure

$$\tilde{M}(a_{i-2}, \tau) = \frac{\int da_i p(a_i|a_{i-2})p_{CK}(a_i|a_{i-2})}{\sqrt{\int da_i p^2(a_i|a_{i-2})} \sqrt{\int da_i p_{CK}^2(a_i|a_{i-2})}}. \quad (4)$$

Additionally, by computing $M(\tau) = N^{-1} \int da_{i-2} \tilde{M}(a_{i-2}, \tau)$ with $N = a_{i-2}^{\max} - a_{i-2}^{\min}$, we average over the condition a_{i-2} . If the Markov assumption is correct, $M(\tau)$ converges to 1. In Fig. 2 the result of this test is depicted. The time for the acceleration to become undistinguishable from a Markov process is $2T$ to $2.5T$ and $1T$ to $1.5T$

¹ This assumption seems to contradict the description in terms of a stochastic process. But as we consider the whole ensemble of tracer particles, a probabilistic theory is meaningful.

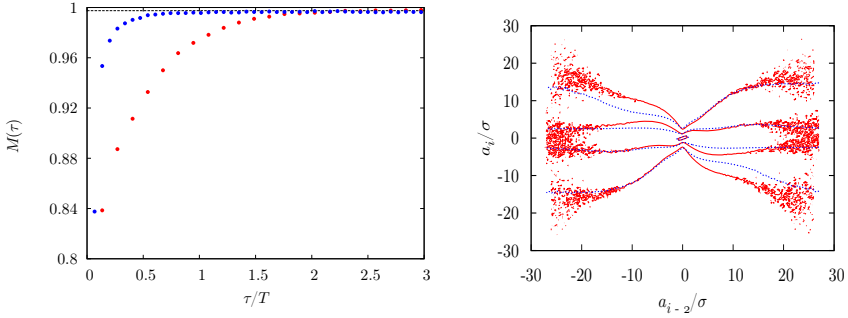


Fig. 2 Left: Correlation measure $M(\tau)$ for 3D (red) and 2D (blue) turbulence. Right: An example for $p(a_i|a_{i-2})$ (red) and $p_{CK}(a_i|a_{i-2})$ (blue) for $\tau \approx 0.13T$.

for three and two dimensions, respectively. Although for two dimensions this time is a little bit shorter, it lies in the order of magnitude of the integral time scale in both cases. This means that over the whole inertial range the acceleration retains its memory.

To conclude, in this paper we have investigated the properties of the acceleration of a Lagrangian particle in two- and three-dimensional homogeneous isotropic turbulence. We have shown that in both flows the acceleration shows long time correlations and, what is more important, in both cases the acceleration can only be described by a Markov process for time lags in the order of magnitude of the integral time scale. This finding not only shows that the acceleration is a very complex quantity with a long time memory. It has also important implications for Lagrangian modeling because in many models the acceleration is assumed to be a Markov process already on the shortest time scale (see e.g. [5]).

References

1. Boffetta, G., Celani, A., Vergassola, M.: Inverse energy cascade in two-dimensional turbulence: Deviations from Gaussian behavior. *Phys. Rev. E* 61, R29–R32 (2000)
2. Kamps, O., Friedrich, R.: Lagrangian statistics in forced two-dimensional turbulence. *Phys. Rev. E* 78, 036321 (2008)
3. Wilczek, M., Friedrich, R.: Dynamical origins for non-Gaussian vorticity distributions in turbulent flows. *Phys. Rev. E* 80, 016316 (2009)
4. Friedrich, R., Peinke, J.: Description of a Turbulent Cascade by a Fokker-Planck Equation. *Phys. Rev. Lett.* 78, 863–866 (1997)
5. Sawford, B.L.: Reynolds number effects in Lagrangian stochastic models of turbulent dispersion. *Physics of Fluids A: Fluid Dynamics* 3, 1577–1586 (1991)

Transport of Inertial Particles in Turbulent Jets

Francesco Picano, Gaetano Sardina, Paolo Gualtieri, and Carlo Massimo Casciola

1 Introduction

Particulate turbulent jets are crucial in several fields of earth science, physics and engineering. In particular turbulent jets are characterized by the entrainment of fresh irrotational air into the turbulent core. The coupling of the particle dynamics with the jet entrainment may affect the dynamics of droplet evaporation/condensation in clouds or in spray injectors.

The dynamics of inertial particles has been addressed in several configurations, homogeneous isotropic/shear flows and wall-bounded flows, discussing certain non-trivial phenomena such as small-scale clustering [8] or turbophoresis [7]. Despite its relevance, transport of inertial particles in free turbulent jets has not been addressed in details so far. A number of papers concerns the inflow-dependent near field or the effects of high particle loading on the jet spreading rate, e.g. [4, 2]. To contribute filling the gap, data of a Direct Numerical Simulation of a free particle-laden turbulent jet are here presented.

2 Numerical Algorithm

The algorithm for the fluid phase is based on an explicit second-order staggered finite-difference scheme using cylindrical coordinates and on a third order Runge-Kutta integration in time, see [5, 6] for details and tests. The jet is generated by a turbulent inflow that uses data from a companion DNS of a fully developed pipe flow with bulk Reynolds number $Re_R = U_0 R / \nu = 2000$, where R is the pipe radius, U_0 the bulk velocity and ν the kinematic viscosity. A typical run involves $784 \times 145 \times 128$ grid points in axial z , radial r , and azimuthal θ directions, respectively.

Francesco Picano · Gaetano Sardina · Paolo Gualtieri · Carlo Massimo Casciola
Dip. di Ingegneria Meccanica e Aerospaziale, Sapienza University of Rome, Italy
e-mail: francesco.picano,gaetano.sardina@uniroma1.it
paolo.gualtieri,carlomassimo.casciola@uniroma1.it

The computational mesh is stretched in the radial and axial direction, to keep a resolution comparable with the Kolmogorov length all through the flow domain [6]. Traction-free conditions are enforced on the side boundary at $r = 28R$, while convective outflow conditions are placed at $z = 83R$. The particles are assumed to be rigid and spherical with a diameter d_p smaller than Kolmogorov scale and with density much larger than the fluid one. Dealing with diluted suspensions, both inter-particle collisions and the force feedback on the carrier fluid are neglected. In such conditions the only significant force acting on the particles is the viscous Stokes drag, and each particle evolves with: $\dot{\mathbf{v}} = (\mathbf{u}|_p - \mathbf{v})/\tau_p$, where \mathbf{v} and $\mathbf{u}|_p$ denote the particle velocity and the fluid velocity at particle position, while $\tau_p = \rho_p d_p^2 / (\rho \nu 18)$ is the particle response time (Stokes time). A mixed linear-quadratic formula based on Lagrange polynomials is used to interpolate the fluid velocity at particle positions, see [5, 6] for details. Temporal discretization for the particle equation uses the same method of the fluid phase. The nominal Stokes number is defined as the ratio of τ_p and a characteristic time scale of the carrier fluid, $St_0 = \tau_p U_0 / R$. Six particle populations are considered differing for the Stokes number in the range $St_0 = 2 \div 64$ (the typical particle Reynolds number is $Re_p = \mathcal{O}(1)$ for $St_0 = 64$). The injection rate is fixed to be 150 particles per R/U_0 time for each population. After that the statistical steady state is reached ($T > 1000R/U_0$), more than 160 time independent fields with temporal separation of $2.5R/U_0$ are used to calculate convergent statistics.

3 Results and Discussion

The behavior of the jet may be grasped observing the instantaneous configuration of a passive scalar transported by the turbulent flow, see the contours in each panel of figure 1. The instantaneous configuration of three particle populations, $St_0 = 2$, $St_0 = 16$ and $St_0 = 64$, is presented in the panels of figure 1 from left to right, respectively. The effect of the inertia is apparent for the smallest particles considered that display small-scale clustering [8]. On the contrary, in the same region heavier particles show an almost even distribution with particles with $St_0 = 16$ particles exhibiting clustering only at the end of computational domain. As it will be discussed in the following, particle transport depends on an axial-dependent Stokes number based on the local flow time scales, see [1, 6].

The left panel of figure 2 provides the axial behavior of the centerline mean particle concentration in comparison with the passive scalar. Particle populations show unexpected concentration peaks that move downstream increasing the particle inertia, i.e. St_0 . The location of these humps is controlled by the large scale local Stokes number St_L based on the time scale given by $T_L = r_{1/2}/U_c$, where $r_{1/2} = S(z - z_0)$ is the jet half-width and $U_c = U_0 B 2R / (z - z_0)$ is the average centerline fluid velocity (in this case $S = 0.089$, $B = 6.77$, $z_0 = -0.8R$). Hence the local Stokes number $St_L = \tau_p / T_L \propto (z - z_0)^{-2}$ decreases quadratically in the downstream evolution. Peaks occur at locations where $St_L = \mathcal{O}(1)$. The particles behave as tracers further downstream where $St_L \ll 1$, showing a centerline concentration similar to that of a passive scalar. These findings should be crucial when the particle concentration

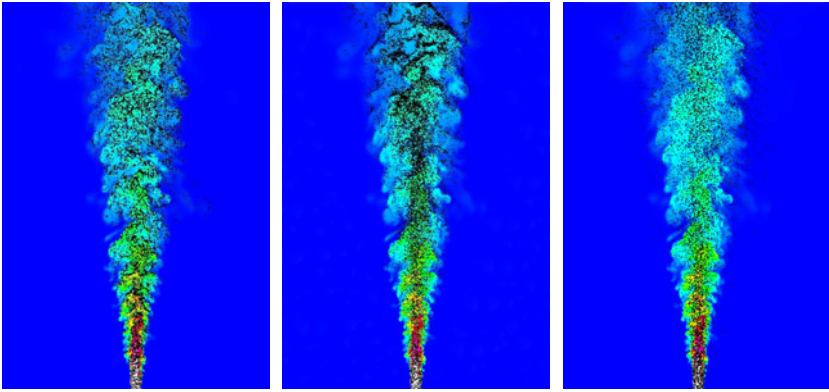


Fig. 1 Instantaneous configuration of a thin axial-radial slice of the turbulent jet: particles and passive scalar (Smidth number 0.7). Left, particles with $St_0 = 2$; middle, particles with $St_0 = 16$; right, particles with $St_0 = 64$.

is larger and the feedback of the particles on the fluid phase becomes relevant influencing the jet-column stability and determining the conditions for the collapse of buoyant two-phase jets, [3]. Since the present work focuses on the one-way coupling regime, the investigation on these aspects is left for future studies.

Another peculiar feature of the particle-laden jet concerns the sampling properties of the Lagrangian phase. Actually since the mass flux transported by the jet increases linearly during the axial development, ambient fluid is captured via entrainment process from the edge. The jet is made up of two parts, the inner turbulent core and the outer irrotational region of ambient fluid that is captured by the turbulent jet core. A tracer, introduced at the jet inflow, will follow a convoluted trajectory that locally remains in the turbulent region and never samples the irrotational part of the flow outside the core. A visual impression of this behavior is provided in figure 11 where the passive scalar is localized only in the jet core. Hence the statistics of the fluid phase as “perceived” by the particles, i.e. conditioned to the particle presence, will differ from the fluid unconditional statistics at least at the edge of

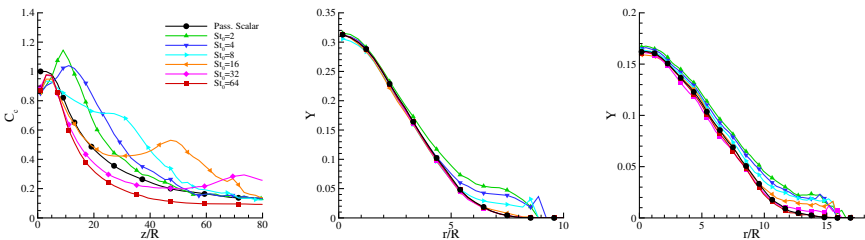


Fig. 2 Left panel: centerline concentration of the passive scalar and particle populations vs z/R . Middle and right panels: mean concentration of the passive scalar sampled by the particle populations vs r/R at two axial stations, $z/R = 30$ and $z/R = 60$ respectively.

the jet. Particles with small inertia, e.g. $St_0 = 2$, behaving almost as tracers present preferential sampling as shown in the middle and right panels of figure 2, where the particle-conditioned average passive scalar concentration is displayed at two axial distances, $z/R = 30$ and $z/R = 60$ respectively. The concentration of the scalar sampled by these very light particles is larger than the unconditioned value near the edge of the jet, figure 2. On the contrary, most massive particles, e.g. $St_0 = 64$, sample more evenly the fluid events and match the unconditioned statistics, figure 2. In fact, due to their large inertia, their trajectories are less correlated from that of tracers and the particles invade also the irrotational outer region, right panel of 1. Also these features are controlled by the local Stokes number $St_L(z)$ with particles displaying sampling bias near the jet edge when $St_L \ll 1$, as understood by comparing the behavior of different particles at different positions of the jet, e.g. $St_0 = 8 - 16$ at $z/R = 30 - 60$ in figure 2. As a final comment, these findings are expected to play a crucial role in the dynamics of sprays, where the droplet evaporation rate depends on the local concentration of the vapour phase sampled by the droplet.

References

1. Casciola, C., Gualtieri, P., Picano, F., Sardina, G., Troiani, G.: Dynamics of inertial particles in free jets. *Physica Scripta T* (2010)
2. Hardalupas, Y., Taylor, A., Whitelaw, J.: Velocity and Particle-Flux Characteristics of Turbulent Particle-Laden Jets. *Proc. R. Soc. London A* 426(1870), 31 (1889)
3. Kaminski, E., Tait, S., Carazzo, G.: Turbulent entrainment in jets with arbitrary buoyancy. *J. Fluid Mech.* 526(-1), 361 (2005)
4. Longmire, E., Eaton, J.: Structure of a particle-laden round jet. *J. Fluid Mech.* 236, 217 (1992)
5. Picano, F., Sardina, G., Casciola, C.: Spatial development of particle-laden turbulent pipe flow. *Phys. Fluids* 21, 093,305 (2009)
6. Picano, F., Sardina, G., Gualtieri, P., Casciola, C.: Anomalous memory effects on transport of inertial particles in turbulent jets. *Phys. Fluids* 22, 051,705 (2010)
7. Reeks, M.: The transport of discrete particles in inhomogeneous turbulence. *J. of Aerosol Science* 14(6), 729 (1983)
8. Toschi, F., Bodenschatz, E.: Lagrangian properties of particles in turbulence. *Ann. Rev. Fl. Mech.* 41, 375 (2009)

Probability Density Functions of Reacting Species Concentrations in Turbulent Wall-Jet

Zeinab Pouransari, Geert Brethouwer, and Arne V. Johansson

Abstract. Direct numerical simulation of a simple reaction between two scalars in a plane turbulent wall jet has been performed. In addition to mean and fluctuation intensities also higher order statistics and the probability density functions of the reacting scalars have been examined. The probability density functions shed light on the behavior of the passive and reacting scalars close to the wall and also to the near-wall characteristics of the reaction.

1 Introduction

The turbulent plane wall-jet has features in close resemblance to a wide range of mixing and combustion applications. During the last decades, both direct numerical simulation (DNS) [1] and [2], and large-eddy simulation (LES) [4], have been used to study the turbulent wall-jet. The first three-dimensional DNS of a reacting turbulent flow was performed by Riley et al. (1986) [5], where they simulated a single reaction of two scalars, without heat release, for a mixing layer. Recently, Gruber et al. (2010), [6], studied the turbulent flame-wall interaction in a channel flow using DNS. In the present study, DNS is used to study a simple reaction in a plane turbulent wall-jet. The flow is isothermal and involves a single step reaction between an oxidizer and a fuel species. It is of importance to investigate the progression of the reaction; with this aim in mind, we study the probability density functions (pdf's) of fuel, oxidizer and a passive scalar at several downstream positions at different distances from the wall.

2 DNS of a Reacting Turbulent Wall-Jet

The numerical code used in the simulations employs a high order compact finite difference scheme and Runge-Kutta method for spatial and temporal integration,

Zeinab Pouransari · Geert Brethouwer · Arne V. Johansson
Linné Flow Centre, KTH Mechanics, SE-100 44 Stockholm, Sweden
e-mail: zeinab@mech.kth.se

respectively, to resolve the fully compressible mass, momentum and energy conservation equations. Details of the numerical method are explained in [11]. The simulation set-up and the flow configuration of the present study is the same as it is described in [3]. The inlet based Reynolds and Mach numbers of the wall-jet are $Re = 2000$ and $M = 0.5$, therefore, the compressibility effects are small [11]. A single-step irreversible reaction is considered where the oxidant species O and the fuel species F react to form a product P , which is described as $aO + bF \rightarrow cP$. Stoichiometric coefficients of one are used for all species and the molecular weights are also assumed to be equal for the reactants. At the inlet, fuel and oxidizer enter the domain separately in a non-premixed manner. To specify the reaction rate a Damköhler number of $Da = hk_r \rho_j / U_j = 3$ is used. The applied Da defines the ratio of the convection to reaction time scale in terms of inlet properties. For the heat fluxes a constant Prandtl number of $Pr = \mu c_p / \lambda = 0.72$ is used. The Schmidt number of the scalars is also constant and equal to the Prandtl number. The reaction is temperature independent and does not release heat. Since the flow is uncoupled from the reaction, the influence of turbulent mixing on the reaction can be studied in the absence of temperature effects. Apart from the reactants, a conserved scalar equation is also solved for comparison.

3 Statistics, PDF's and the Higher Order Moments

The reaction starts immediately after the inlet and mainly occurs in the upper shear layer in thin sheet like structures. However, reactions also take place near the wall. The cross stream profiles of the scalar concentrations and the fluctuation of the reacting scalars are displayed in Figs. 1(a) and (b) respectively: showing that all non-reacting and reacting scalar profiles collapse when using outer scaling.

It can be observed in Figs. 2 that the pdf's of the fuel and the passive scalar are rather similar from the wall up to the vicinity of the half-height of the jet, i.e. $y/y_{1/2} = 1$ plane, but beyond this position the passive scalar pdf still keeps its near-Gaussian shape while the fuel pdf has a large peak at low concentration showing

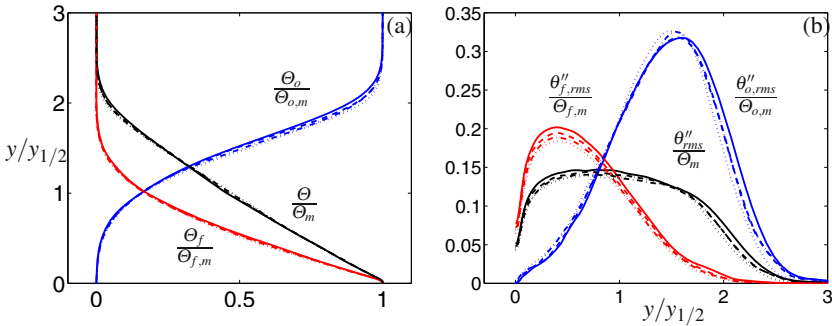


Fig. 1 Statistics of oxidizer (blue), fuel (red) and passive (black) scalars at several downstream positions. Solid: $x/h = 27$, dashed: $x/h = 25$, dash-dotted: $x/h = 23$, dotted: $x/h = 21$ (a) cross-stream profiles of the reacting scalars (b) fluctuation of the reacting scalars.

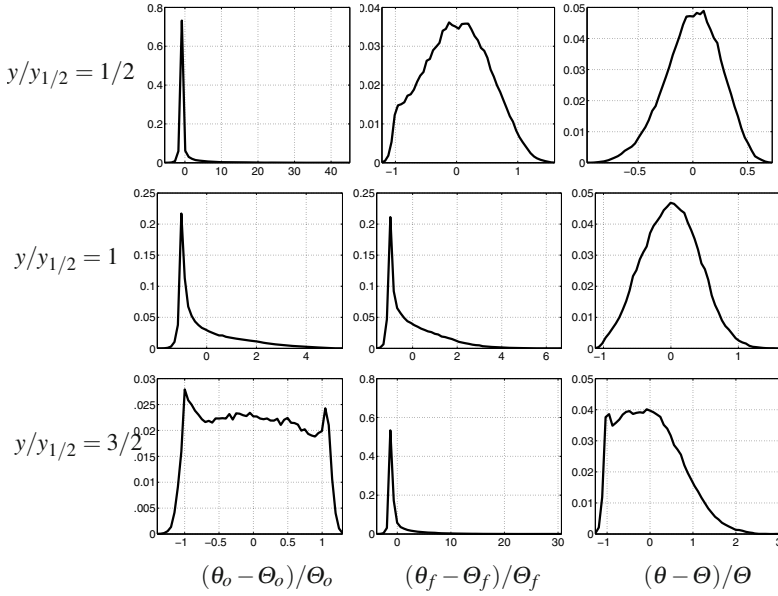


Fig. 2 Probability density functions of different species at $x/h = 20$ in several wall-normal locations. Minimum and maximum concentrations in each plot matches the borders of plot and zero on x-axis points to the mean concentration.

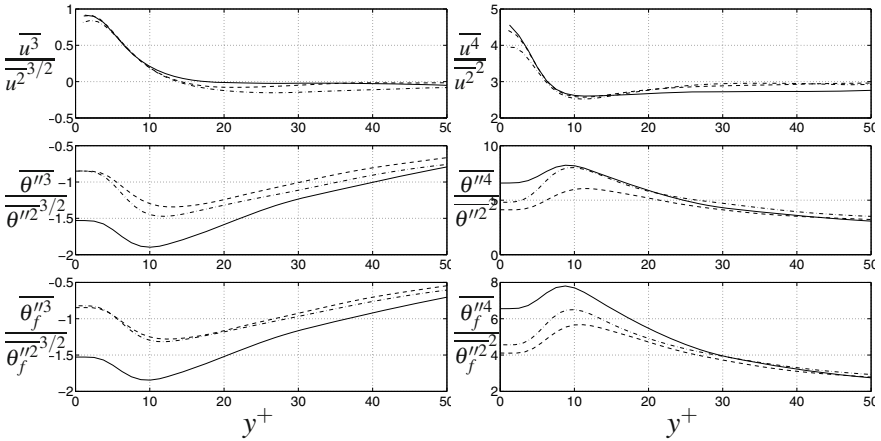


Fig. 3 Distributions of third-order moments (skewness) and the fourth-order moments (flatness) of streamwise velocity u , passive scalar concentration θ and the fuel species concentration θ_f , in a reacting turbulent wall jet. Solid line: $x/h = 15$, dashed line: $x/h = 20$, dot-dashed line: $x/h = 25$. Here y^+ is yu_τ/ν .

that much of the fuel has been consumed. The pdf's of the fuel concentration have long exponential tails in the outer shear layer, which is an evidence for the existence of high intermittency. Worth to notice is that the shape of the fuel and oxidizer pdf curves are most similar at the half-height planes at any particular downstream position. The oxidizer pdf's are close to the minimum concentration values close to the wall which is a reasonable behavior considering the oxidizer concentration profile, see Fig. 1. By moving away from the wall, the pdf profile becomes broader and around $y/y_{1/2} = 1.5$ another peak occurs in the pdf of oxidizer which is close to the maximum concentrations. This implies that the probability of particles with low concentration coming from the wall region or caused by reaction with the fuel and particles with high concentration coming from outer region are both high at this position. Hence, the formation of these two peaks. The peak at the minimum concentration disappears around $y/y_{1/2} = 2$.

In order to investigate the intermittency effects at different wall-normal levels, skewness and flatness of the scalar concentrations and the velocities are shown in Fig. 3. The positive skewness of the streamwise velocity close to the wall points to the intermittent high velocities, and this is a rather universal behavior for all wall-bounded flows. By contrast, the peaks in the skewness and flatness profiles for both passive scalar and the reacting scalar are around $y^+ = 10$. In contrast to the streamwise velocity, which has the sharpest gradient at the wall and consequently the largest skewness and flatness values, the gradients of the passive and reacting scalars are zero at the wall, and therefore, large fluctuations are rare. However, some low concentration packages will splash toward the wall and the intermittent characteristic of this penetration of the lower concentrations into the lower levels results in large skewness and flatness around $y^+ = 10$. Moving away from the wall, the skewness slowly increases and the flatness decreases.

Acknowledgements. Financial supports by Swedish National Research program of Combustion Science and Technology (CECOST) and computer time provided by SNIC are acknowledged.

References

1. Ahlman, D., Brethouwer, G., Johansson, A.V.: Direct numerical simulation of a plane turbulent wall-jet including scalar mixing. *Phys. Fluids* 19, 065102 (2007)
2. Ahlman, D., Velter, G., Brethouwer, G., Johansson, A.V.: Direct numerical simulation of non-isothermal turbulent wall-jets. *Phys. Fluids* 21, 35101 (2009)
3. Pouransari, Z., Brethouwer, G., Johansson, A.V.: Direct Numerical Simulation of a Turbulent Reacting Wall-Jet. In: Kuerten, H., et al. (eds.) *Direct and Large-Eddy Simulation VIII. ERCOFTAC*, vol. 15, pp. 345–350. Springer, Heidelberg (2011)
4. Dejoan, A., Leschziner, M.A.: Large eddy simulation of a plane turbulent wall jet. *Phys. Fluids* 17, 025102 (2005)
5. Riley, J.J., Metcalfe, R.W., Orszag, S.A.: Direct numerical simulation of chemically reacting turbulent mixing layers. *Phys. Fluids* 29, 406–422 (1986)
6. Gruber, A., Sankaran, R., Hawkes, E.R., Chen, J.H.: Turbulent flamework interaction: a direct numerical simulation study. *J. Fluid Mech.* 658, 5–32 (2010)

Session 3

Modeling and Simulation

Characterisation of Synthetic Turbulence Methods for Large-Eddy Simulation of Supersonic Boundary Layers

Guillaume Aubard, Xavier Gloerfelt, and J.-C. Robinet

Abstract. For the simulation of a supersonic turbulent boundary layer, two methods of generating synthetic turbulent inflow data are compared, namely the Random Fourier Modes (RFM), and the Synthetic Eddy Method (SEM). The first one relies on theoretical properties of turbulence, whereas the second one is essentially based on empirical informations. The adaptation distance needed to recover a realistic wall turbulence is smaller than 10 initial boundary layer thicknesses for the SEM inflow, and roughly twice longer for the RFM inflow. A correct prescription of the phase information is seen to be a key element to efficiently generate a sustained wall turbulence.

1 Introduction

The spatial development of fully turbulent flows with wall-resolved large-eddy simulations (LES) is still very expensive, so that synthetic turbulence inflow methods can constitute an efficient alternative to the simulation of the complete transition. Moreover, contrary to recycling methods, the introduction of artificial fluctuations through random sequences does not introduce any periodicity in the flow. However, the difficulty to synthesize realistic fluctuations leads to relatively long adaptation distances. In the present study, two methods for generating synthetic turbulence are compared : the Synthetic Eddy Method (SEM) of Jarrin et al. [3], and the Random Fourier Modes (RFM) introduced by Kraichnan [5]. The fluctuating velocity field from the SEM simply consists in the random superimposition of Gaussian-type spots, with length and time scales depending on the distance from the wall as described in Pamiès et al. [6]. Second-order moments are imposed to the normalized stochastic signal through a Cholesky decomposition of a prescribed Reynolds stress tensor. The RFM procedure is based on theoretical properties of

Guillaume Aubard · Xavier Gloerfelt · J.-C. Robinet
Arts et Métiers ParisTech, DynFluid Laboratory, Paris, France
e-mail: guillaume.aubard@ensam.eu

homogeneous turbulence. The stochastic velocity field consists in the sum of space-time Fourier modes, whose amplitude is deduced from a von Kármán energy spectrum. The field is unfrozen by the prescription of a local convection speed, and of a pulsation ω_n corresponding to the time evolution of the turbulence. The Heisenberg time, $\omega_n = 2\pi u' k_n$, where u' is the *rms* fluctuating velocity and k_n the wavenumber of mode n , has been chosen [1] [2]. The isotropic stochastic turbulent field is then weighted by prescribed vertical profiles of *rms* velocities. Both methods have been adapted to compressible flows through the introduction of density fluctuations using the strong Reynolds analogy.

2 Test Case : Supersonic Turbulent Boundary Layer

The test case is the DNS of Pirozzoli et al. [7] at $Re_\theta = 4260$ and $M_\infty = 2.25$. LES simulations are realized with two meshes, a “coarse” one ($\Delta_x^+ = 39$, $\Delta_{y_{min}}^+ = 2.9$, $\Delta_z^+ = 18$), and a “fine” one ($\Delta_x^+ = 33$, $\Delta_{y_{min}}^+ = 1.7$, $\Delta_z^+ = 13$). The size of the computational box is $Lx \times Ly \times Lz = 15\delta_0 \times 4\delta_0 \times 1.5\delta_0$. Time averaging has been performed over 1000 δ_0/U_∞ non-dimensional time units, which allows good convergence of flow statistics up to second order. The LES methodology combines a finite-difference scheme with good spectral properties with the use of a selective filtering providing the necessary regularization at small scales [2].

Figure 1(a) and (b) shows that the mean flow data and the turbulent intensities compare favorably to the DNS reference data. The friction velocity is underestimated in both cases by about 10% which is customary using LES resolutions.

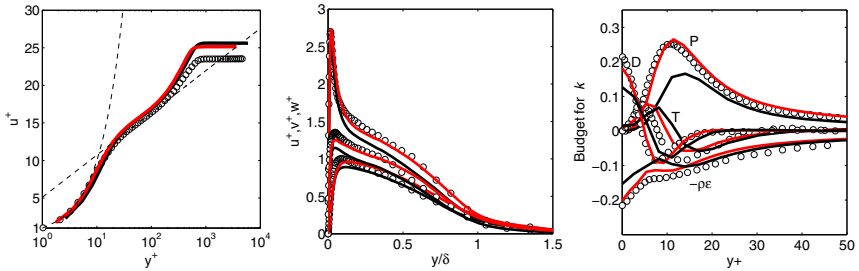


Fig. 1 (a) Van-Driest-transformed mean velocity profiles; (b) *rms* velocity profiles normalized by the friction velocity; (c) Predominant terms in the TKE budget (P : production, D : viscous diffusion, T : turbulent transport, $-\rho\epsilon$: viscous dissipation) : (—), coarse LES; (—), fine LES; (○), DNS of Pirozzoli et al. [7].

Fig. 1(c) shows the predominant terms of the turbulent kinetic energy (TKE) budget. All the terms show good agreement with the DNS, but the production term is underestimated in the coarse case due to an underestimation of the *rms*-velocity profiles.

3 Comparison of the Two Inflow Methods

Figure 2 shows the evolution of the *rms* velocities for different longitudinal locations as a function of boundary layer thickness δ_0 . The RFM case undergoes an initial decay of the turbulent intensities, corresponding to the destruction of the non physical eddies, also illustrated by the large falling down of the friction velocity in Fig. 3. The field starts to rebuilt after about five δ_0 . On the contrary, the SEM case shows Reynolds stresses almost established in a few δ_0 .

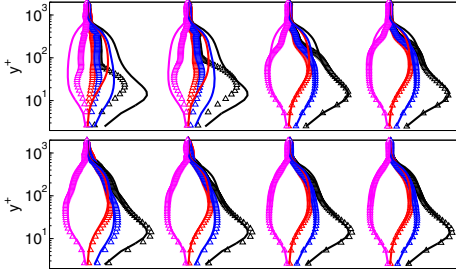


Fig. 2 u_{rms} (Δ), v_{rms} (Δ), w_{rms} (Δ), and uw_{rms} (Δ) for RFM (top) and SEM (bottom), for $x/\delta_0 = 3, 5, 10, 15$ from the left to the right. LES reference : straight lines.

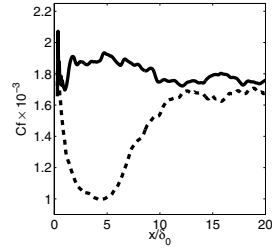


Fig. 3 Longitudinal C_f evolution for RFM (---) and SEM (—) methods.

The energy spectra of the longitudinal and normal velocities for the inflow plane and at a location of $15\delta_0$ are shown in Fig. 4. The inflow spectra are rather realistic in both cases, even if the RFM spectra show a lack of energy in the inertial subrange, so that the coherent eddies are slowly reconstructed by an inverse energy cascade. On the contrary, the inflow and downstream spectra in the SEM case are already very close, so that the reconstruction phase is significantly reduced.

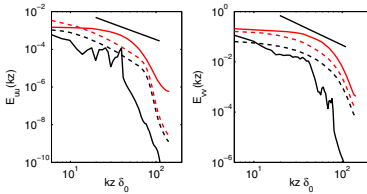


Fig. 4 Power spectra E_{uu} (left) and E_{vv} (right) at $y/\delta_0 = 0.35$: RFM inflow plane (—), RFM for $x/\delta_0 = 15$ (---), SEM inflow plane (—), SEM for $x/\delta_0 = 15$ (---).

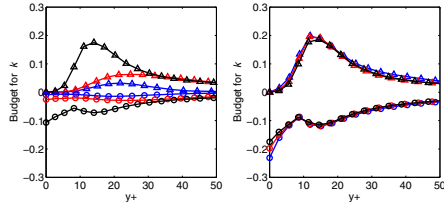


Fig. 5 Normalized production (Δ) and dissipation term (\circ) for RFM (left) and SEM (right), for $x/\delta_0 = 3$ (—), 5 (—), 15 (—).

The longitudinal evolution of the production and dissipation terms in the turbulent kinetic energy budget (Fig. 5) is consistent with the previous results. The production term is easier to match since it depends only on the mean and *rms* velocities, whereas the dissipation term depends on the spectral content of the turbulence and is still not correct at a position of $15\delta_0$ in the RFM case. In the SEM case, the two terms are already correct few δ_0 downstream of the inlet, since the *rms* velocities and the spectral content are already close to the target values.

4 Conclusion

The SEM, applied in a form close to the one proposed by Pamiès et al. [6], has shown to produce realistic wall turbulence in less than 10 initial boundary layer thicknesses. The key improvement, when compared to synthetic methods issued from the RFM, is the prescription of a realistic phase information that gives correct space correlations notably in the direction of inhomogeneity of the flow. This method is particularly promising for the high-Reynolds-number flows of engineering interest even if the parametrization of the method has not been investigated in this range. The performances obtained in this study are very close to those obtained at $Re = 3535$ and $M_\infty = 0.1$ in Pamiès et al. [6], suggesting that there is minimal influence of the Mach number on the adaptation distance.

Acknowledgements. This work was granted access to the HPC resources of IDRIS and CCRT under the allocation 2010-6125 made by GENCI (Grand Equipement National de Calcul Intensif).

References

1. Béchara, W., Bailly, C., Lafon, P., Candel, S.: Stochastic approach to noise modeling for free turbulent flows. *AIAA Journal* 32(3), 455–463 (1994)
2. Gloerfelt, X., Le Garrec, T.: Generation of inflow turbulence for aeroacoustic applications. In: 14th AIAA/CEAS Aero Acoustics Conference, Vancouver, Canada, AIAA Paper 2008-2926, May 5-7 (2008)
3. Jarrin, N., Benhamadouche, S., Laurence, D., Prosser, R.: A synthetic-eddy-method for generating inflow conditions for large-eddy simulation. *International Journal of Heat and Fluid Flow* 27, 585–593 (2006)
4. Keating, A., Piomelli, U., Balaras, E., Kaltenbach, H.: A priori and a posteriori tests of inflow conditions for large-eddy simulation. *Phys. Fluids* 16(12), 4696 (2004)
5. Kraichnan, R.: Diffusion by a random velocity field. *Phys. Fluids* 13(1), 22–31 (1970)
6. Pamiès, M., Weiss, P., Garnier, E., Deck, S., Sagaut, P.: Generation of synthetic turbulent inflow data for large eddy simulation of spatially evolving wall-bounded flows. *Phys. Fluids* 21(4), 045,103–045,118 (2009)
7. Pirozzoli, S., Grasso, F., Gatski, T.: Direct numerical simulation and analysis of a spatially evolving supersonic turbulent boundary layer at $M = 2.25$. *Phys. Fluids* 16(3), 530–545 (2004)

A Uniformly Valid Theory of Turbulent Separation

Bernhard Scheichl, Alfred Kluwick, Frank T. Smith, and Jon Paton

Abstract. The contribution deals with recent theoretical results concerning separation of a turbulent boundary layer from a blunt solid object in a uniform stream, accompanied by a numerical study. The investigation is restricted to incompressible nominally steady two-dimensional flow past an impervious obstacle surface. Then the global Reynolds number represents the only parameter entering the description of the Reynolds-averaged flow. It shall be large enough to ensure that laminar-turbulent transition takes place in a correspondingly small region encompassing the stagnation point. Consequently, the concomitant asymptotic hierarchy starts with the external Helmholtz–Kirchhoff potential flow, which detaches at an initially unknown point \mathcal{D} from the body, driving the turbulent boundary layer. It is found that the separation mechanism is inherently reminiscent of the transition process. The local analysis of separation not only fixes the actual scaling of the entire boundary layer but is also expected to eventually predict the position of \mathcal{D} in a rational way.

1 Non-interactive Global and Boundary Layer Flow

Consider a parallel flow just disturbed by the presence of a bluff body and let the Reynolds number Re formed with the unperturbed free-stream velocity and a

Bernhard Scheichl

AC²T Research GmbH, Viktor Kaplan-Straße 2, A-2700 Wiener Neustadt, Austria

e-mail: bernhard.scheichl@tuwien.ac.at

Bernhard Scheichl · Alfred Kluwick

Institute of Fluid Mechanics and Heat Transfer, Vienna University of Technology, Austria

e-mail: alfred.kluwick@tuwien.ac.at

Frank T. Smith

Department of Mathematics, University College London, UK

e-mail: frank@math.ucl.ac.uk

Jon Paton

TotalSim Ltd, Brackley, Northants, UK

e-mail: jon@totalsim.co.uk

typical body dimension take on arbitrarily large values: what is the actual position of flow separation? This question represents a long-standing but nevertheless central challenge in theoretical hydrodynamics. Matched asymptotic expansions prove the adequate means for a rigorous treatment of this problem. Here we present the essential results of this analysis by starting with the overall flow structure and leaving the technical details to [6] and [7]. In the following all quantities are non-dimensional with the aforementioned reference values and the fluid density. Hence x, y, u denote natural coordinates along and normal to the body surface, with $x = y = 0$ indicating the stagnation point \mathcal{S} , and the velocity component in x -direction, respectively.

Two findings are decisive. Firstly, laminar–turbulent transition near \mathcal{S} generates a boundary layer that is basically characterised by (i) a main layer exhibiting an asymptotically small relative streamwise velocity deficit and (ii) the classical shear stress equilibrium in the viscous wall layer. Together with the required direct match of both flow regions items (i) and (ii) establish the picture of a classical turbulent boundary layer but with an a priori unknown scaling. This reflects the remarkable property that it never attains a fully developed turbulent state, even for arbitrarily large values of Re . Such an “underdeveloped” turbulent boundary layer contrasts with common reasoning but is reliable as viscous–inviscid flow interaction near separation requires the wall layer thickness to vary predominantly algebraically with the boundary layer thickness δ (rather than exponentially as in the classical case).

Secondly, it has become evident from [3] and numerous subsequent related experimental studies that for increasing values of Re the point of gross separation approaches a position a finite distance remote from its rear stagnation point observed in case of fully attached potential flow. This contradicts the conclusion drawn in the first theoretical investigation of this problem that accounts for the global flow structure [2]. A critical review [5] has finally promoted the experimental observation as a starting point for further analysis. This in turn suggests that in the formal limit $Re^{-1} = 0$ the free-stream flow past the body is to be sought in the class of Helmholtz–Kirchhoff flows, parametrised solely by the position of \mathcal{D} where the well-known Brillouin–Villat (BV) singularity is encountered. Then the surface velocity u_s imposed on the attached boundary layer and the stream function F that accounts for the velocity defect satisfy the fundamental asymptotic relationships

$$u_s(x; k) \sim 1 + 2k\sqrt{-s} + O(-s), \quad s = x - x_{\mathcal{D}}(k), \quad s \rightarrow 0_-, \quad (1)$$

$$1 - u/u_s(x; k) \sim \varepsilon \partial_{\eta} F(x, \eta; k) + O(\varepsilon^2), \quad \eta = y/\delta(x; Re), \quad \varepsilon \rightarrow 0. \quad (2)$$

Here the positive parameter k measures the strength of the BV singularity and in turn the position $x_{\mathcal{D}}$ of \mathcal{D} . Determining both the correct value of k and the dependencies of δ and the defect measure ε on Re represents one crucial goal of this research. Notable previous works (e.g. [1], [11]) unfortunately lacked the discussion of the global flow and thus led to different (large-defect) structures of the boundary layer, where the resulting inconsistencies precluded a uniformly valid flow description.

The canonical situation of the flow around the circular unit cylinder (Re formed with the cylinder radius) is tackled numerically. We first approximate the potential flow by choosing $k = 0.45$ or, by exploitation of Levi–Civita’s method,

$x_{\mathcal{D}} \doteq 113.5^\circ$. This seems reliable in view of the experimentally observed separation angles for the largest values of Re available so far ($Re \approx 10^6 - 10^7$) and the basic assumption concerning the asymptotic flow state. Integration of the leading-order small-defect equations subject to $u_s(x; k)$ and supplemented with an (asymptotically consistent) algebraic mixing-length closure starting at stagnation yields the results displayed in Fig. 1. An initially favourable and then adverse pressure gradient (APG) acts on the boundary layer. In contrast to usual reasoning (cf. [8]), it is not in “quasi-equilibrium” as the variation of F with x is fully present. The profiles of $\partial_\eta F$ at various x -stations exhibit the logarithmic near-wall behaviour and admit a wake-type shape near $x = x_{\mathcal{D}}$, well-recognised in other APG turbulent boundary layers (cf. [1], [2], [4]). Furthermore, let $\Delta(x; k)$ denote the appropriately scaled boundary layer thickness. The expansion $[F, \Delta] \sim [(1 - 4k\sqrt{-s})F_{\mathcal{D}}(\eta), (1 - 2k\sqrt{-s})\Delta_{\mathcal{D}}] + O(-s)$, $s \rightarrow 0_-$, derived from (1) and (2) is revealed by the numerical data. However, due to the associated splitting of $\partial_\eta F$ in an infinite series of logarithmic velocity portions as $\eta \rightarrow 0$ a direct match of the small-defect and the wall layer is only accomplished by the introduction of a so-called intermediate layer immediately upstream of \mathcal{D} .

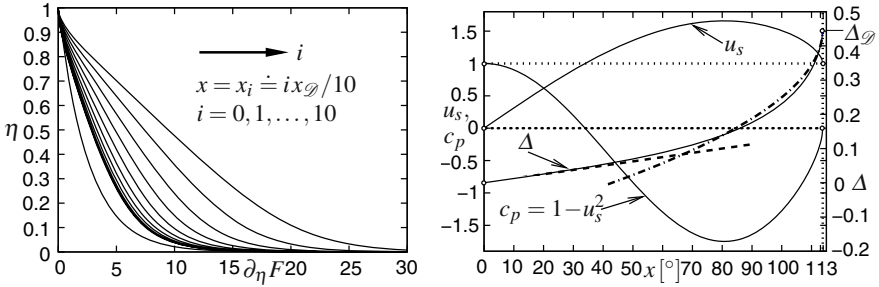


Fig. 1 Defect function $\partial_\eta F$ and key quantities, asymptotes of $\Delta(x; k)$: linear rise in $x = 0$ (dashed), square-root behaviour near $x = x_{\mathcal{D}}$ (dashed-and-dotted)

Detached Eddy Simulation (DES) underlies the snapshot of instantaneous circular-cylinder flow in Fig. 2(a). Here $Re = 10^6$ and $x_{\mathcal{D}} \doteq 95^\circ$, which is also promising.

2 “Inner” and “Outer” Flow Interaction

The separation process is vitally governed by the interplay of two locally strong interaction mechanisms, see Fig. 2(b): an “inner” (viscous–inviscid) one associated with a novel triple-deck structure, and an “outer” (rotational–irrotational) one expressed by a linear problem describing an inviscid vortex flow. The latter is subject to a solvability condition that arises from matching both interactive flow regimes. This is currently expected to finally fix the actual value of k for a given body shape.

In the classical description of the viscous wall layer the shear stress equilibrium is followed by the influence of the pressure and finally the inertia terms on the momentum equation in x -direction. The BV singularity triggers a rather complex

multi-stage breakdown of this asymptotic hierarchy a short distance upstream of \mathcal{D} , initiated by the emergence of the intermediate layer mentioned above. This eventually leads to the formation of a so-called lower deck adjacent to the surface of streamwise extent δ_{TD} , say, where all those contributions except for the turbulent shear stress are in operation at leading order. Hence, separation takes place within a distance of $O(\delta_{\text{TD}})$ from \mathcal{D} as a self-consistent flow description in terms of viscous-inviscid interaction aims at avoiding the occurrence of both the well-known Goldstein and the BV singularity. This mechanism intrinsically renders the wall layer locally a passive main deck: it transfers the flow displacement exerted by the lower deck to an upper deck formed on its top (together with a passive buffer layer). Here the induced potential flow accounts for the pressure feedback in the lower deck. Herewith the interaction loop is closed and the aforementioned triple-deck structure completed. As a result, the BV singularity is resolved in a manner formally identical to that found in the asymptotic theory of laminar break-away separation [10], [9].

This situation is virtually unaffected by the outer small-defect portion of the boundary layer. On the other hand, expansion (2), applicable to the oncoming boundary layer sufficiently far upstream of \mathcal{D} , subject to (1) ceases to be valid in the square region of outer interaction where both s and y are of $O(\delta)$ and which encloses the triple deck. Finally, the triple-deck structure requires that $\delta_{\text{TD}}/\delta = O(\varepsilon)$, with $\varepsilon \propto 1/\ln Re$ (which agrees with the classical boundary layer scaling) and $\delta_{\text{TD}} = Re^{-4/9}$ (which specifies the notion of underdeveloped flow). Activities of current and future research include the aforementioned determination of k and the description of the associated body- and large-scale separated flow.

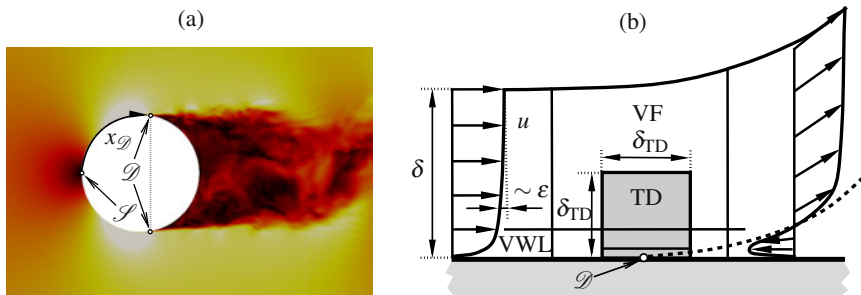


Fig. 2 (a) DES: colours (greytones) distinguish isotachs; (b) sketch of separating flow: viscous wall layer (VWL), triple deck (TD, shaded), vortex-flow region (VF), separating streamline (dashed)

References

1. Melnik, R.E.: Comput. Fluids 17(1)
2. Neish, A., Smith, F.T.: J. Fluid Mech. 241
3. Roshko, A.: J. Fluid Mech. 10(3)

4. Scheichl, B.: Asymptotic Methods in Fluid Mechanics: Survey and Recent Advances. In: Steinrück, H. (ed.) CISM Courses and Lectures, vol. 523, pp. 221–246. Springer, New York (2010)
5. Scheichl, B., Kluwick, A.: *J. Fluids Struct.* 24(8)
6. Scheichl, B., Kluwick, A., Alletto, M.: *Acta Mech.* 201(1-4)
7. Scheichl, B., Kluwick, A., Smith, F.T.: *J. Fluid Mech.* 670 (2011)
8. Schlichting, H., Gersten, K.: *Boundary-layer Theory*, 8th edn. Springer, New York (2003)
9. Smith, F.T.: *Proc. R. Soc. Lond. A* 356 (1687)
10. Sychev, V.V.: *Fluid Dyn.* 7(3)
11. Sychev, V.V.: *Fluid Dyn.* 22(3)

Application and Comparison of Two Different DNS Algorithms for Simulating Transition to Turbulence in Taylor-Green Vortex Flow

İlyas Yılmaz, Lars Davidson, Firat O. Edis, and Hasan Saygın

Abstract. An all-Mach number, fully implicit, non-dissipative DNS algorithm and an incompressible, dissipative DNS algorithm were applied for simulating transition to turbulence in TGV flow to assess their behavior for this flow regime. The all-Mach number solver was developed and parallelized. A method was also adopted to remove oscillating pressure corrections in time. In order to compare the behavior of the algorithms, various flow diagnostics were calculated. The results were also compared to results given in the literature. The development of the flow and the peak structures show some differences due to different dissipative and energy conserving properties of the algorithms. However the physics of TGV flow are well captured by both, even though the grid is not fully resolved.

1 Introduction

Taylor-Green Vortex Flow (TGV) is the simplest fundamental flow that represents vortex stretching and energy cascade processes that lead to turbulence [1]. Initially, it is well-organized and laminar. At later times, the viscous diffusion plays an important role in dynamics and distorted structures are formed. The decay rate of the

İlyas Yılmaz

Energy Inst., Istanbul Tech. Univ., Maslak, Istanbul, Turkey

e-mail: yilmazily@itu.edu.tr

Lars Davidson

Div. of Fluid Dyn., Dept. of Appl. Mech., Chalmers Univ. of Tech., Gothenburg, Sweden

e-mail: lada@chalmers.se

Firat O. Edis

Fac. of Aero. & Astro., Istanbul Tech. Univ., Maslak, Istanbul, Turkey

e-mail: edis@itu.edu.tr

Hasan Saygın

Fac. of Engineering & Architecture, Istanbul Aydın Univ., Florya, Istanbul, Turkey

e-mail: hasansaygin@aydin.edu.tr

kinetic energy reaches its peak after a couple of eddy-turnover time, around $t \approx 9$. Then the flow structures die out due to the viscosity, following approximately the power law spectrum. This transitional behavior is entirely determined by the viscosity. For $Re \geq 1000$, this picture becomes very clear [2]. Numerically, the kinetic energy should be preserved during the inviscid simulations, due to the lack of the viscous effects in the Euler equations.

The aim of this study is to assess the behavior of two different DNS algorithms for simulating transition to turbulence in TGV flow. In Sec. 2, the numerical methods are briefly reviewed. In Sec. 3, the initial setup of TGV flow is given. The results are presented and the comparisons between the algorithms as well as the existing results in the literature are done in Sec. 4. Conclusions are made in Sec. 5.

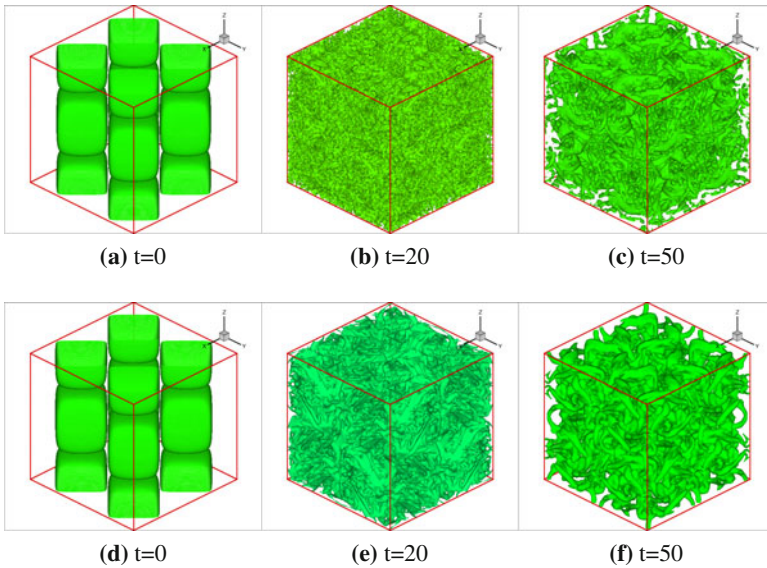


Fig. 1 $Q(=0.019)$ iso-surfaces; the all-Mach (top) and the Incompressible alg. (bottom).

2 Numerical Methods

An all-Mach number, non-dissipative, implicit algorithm which solves the compressible Navier-Stokes equations was initially chosen [3]. A solver based on the algorithm was developed and parallelized. A method was implemented to remove the possible oscillating pressure corrections in time. An implicit, two-step time-advancement algorithm which solves the incompressible Navier-Stokes equations was also chosen to represent pure incompressible, dissipative approach [4]. These are both second-order in space and time.

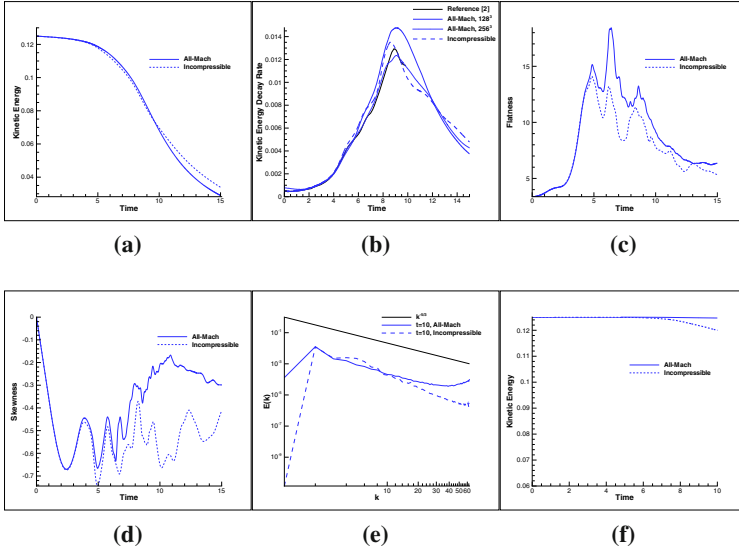


Fig. 2 Evolution and comparison of various flow diagnostics

3 Numerical Setup of Taylor-Green Vortex Flow

Initial velocities are $u_0 = U \sin(kx) \cos(ky) \cos(kz)$, $v_0 = -U \cos(kx) \sin(ky) \cos(kz)$, $w_0 = 0$. Pressure provided by the solution of the Poisson equation for this velocity field is $P_0 = P_\infty + (\rho_0 U^2 / 16) (2 + \cos(2kz)) (\cos(2kx) \cos(2ky))$ where k is the wave number, $\frac{2\pi}{L}$. L is the domain length 2π . Boundaries are triply-periodic. For the all-Mach algorithm, the Mach number is set to 0.084 by adjusting P_∞ and initial density (ρ_0) is given as 1. Since the characteristic velocity is bounded by the unity and the characteristic length is set to 1, the Reynolds number (Re) is defined as the inverse of the kinematic viscosity, $1/\nu$. For the viscous case, it is set to 1500. This also leads to an eddy-turnover time of order unity. The Taylor microscale Re number (Re_λ) can be defined as $\sqrt{2Re}$, giving $\cong 55$ at initial. The viscous and the inviscid ($Re = \infty$) simulations were performed on uniform 128^3 grid.

4 Results

As turbulence develops in time, initially well-organized structures start to break into smaller ones and lose their initial symmetries due to the energy cascade and the vortex stretching for the viscous case. This physics is well captured by the algorithms (Fig. 1). Kinetic energies plotted in Fig. 2a follow a similar path in time up to transition. The incompressible one dissipates the kinetic energy more rapidly at later times. Both give higher dissipation rates than the reference for the same Re number (Fig. 2b). This is due to the unresolved grid for the given Re number as seen from

the result of the all-Mach algorithm on 256^3 grid in the same figure. The transition time is predicted slightly earlier by the incompressible one. The peak structures at transition ($t \approx 9$) are different. Although the calculated values of the velocity structure functions in Fig. 2c and Fig. 2d are within the given range in the literature, a more regular energy cascade by the incompressible algorithm is predicted. Obviously, a much clear inertial range behavior than the one given in Fig. 2e is observed at high-Re numbers [2]. At high wavenumbers, energy is not dissipated efficiently by the all-Mach algorithm due to its non-dissipative nature. This also points out the higher grid resolution requirement of the all-Mach algorithm.

In the absence of the viscosity, the initial kinetic energy was preserved by the all-Mach algorithm during the course of the long-term inviscid simulation. However, a viscous-like decay is observed by the incompressible one at later times in Fig. 2f. The all-Mach algorithm is able to capture the flow dynamics on finite number of cells, due to its non-dissipative behavior.

5 Conclusions

A fully parallel, all-Mach number, non-dissipative, fully implicit DNS solver was developed and applied to transition to turbulence in 3D TGV flow. An implicit, incompressible, dissipative algorithm was also used in the simulations for comparison. The viscous and the inviscid cases were considered. Although there are some differences in the development of the flow and the peak structures at later times, due to their different dissipative and energy conserving properties, the macro-scale physics of TGV flow are well captured by the both.

Acknowledgements. IY thanks to Ist. Tech. Univ. (ITU) and The Sci. and Tech. Res. Council of Turkey (TUBITAK) for supporting his stay in Sweden. The financial support of SNIC (Swedish National Infrastructure for Comp.) for computer time at C3SE (Chalmers Center for Comp. Sci. and Eng.) under the Project SNIC001-10-22 is also gratefully acknowledged.

References

1. Taylor, G.I., Green, A.E.: Mechanism of the production of small eddies from large ones. *Roy. Soc. London Proc. Series A* 158, 499–521 (1937)
2. Brachet, M.E., Meiron, D.I., Orszag, S.A., Nickel, B.G., Morf, R.H., Frisch, U.: Small scale structure of the Taylor-Green vortex. *J. Fluid Mechanics* 130, 411–452 (1983)
3. Hou, Y., Mahesh, K.: A Robust, collocated, implicit algorithm for direct numerical simulation of compressible, turbulent flows. *J. of Comp. Phy.* 205, 205–221 (2005)
4. Davidson, L., Peng, S.-H.: Hybrid LES-RANS: A one-equation SGS model combined with a k-omega model for predicting recirculating flows. *Int. J. Num. Meth. in Fluids* 43, 1003–1018 (2003)

Session 4

Experimental Methods

Optimization of a Digital In-line Holography Setup Used with a High-Speed Camera

Gerd Gülker, Christoph Hindriksen, Tim Homeyer, and Joachim Peinke

Abstract. In order to study Lagrangian properties of turbulent flows a compact digital in-line holography setup in combination with a high-speed camera was used to track time resolved 3D particle positions. First measurements on a vortex flow show reliable trajectories confirming the expected flow field. However, the use of a non-optimised camera and the poor depth resolution of the system lead to problems in tracking particles over long periods in time.

1 Introduction

Recent advances in turbulence research require the determination of fully 3D trajectories of small particles in flows. The motion of such inertial particles is of great interest in studying the Lagrangian properties and the dynamics of turbulent flows. Cloud formation and atmospheric transport as well as mixing processes have been successfully described on the basis of particle trajectories, but problems of fundamental importance remain unresolved. One such issue e.g. is the Heisenberg-Yaglom prediction of fluid particle accelerations, based on the 1941 scaling theory of Kolmogorov. In general the determination of 3D particle trajectories with time resolution better than Kolmogorov time scale is quite difficult and requires rather complex and expensive instrumentation [1]. In our approach 3D particle tracking velocimetry (PTV) based on digital holography combined with a high-speed camera was used. The method convinces by its simplicity, especially the in-line version. Unfortunately, the depth resolution of the particle positions is poor and the use of a camera not optimized for holographic recording lead to additional noise, which makes accurate particle tracking difficult. In this paper first measurements with this method applied to a vortex flow are presented.

Gerd Gülker · Christoph Hindriksen · Tim Homeyer · Joachim Peinke
ForWind - Institute of Physics, University of Oldenburg, D-26111 Oldenburg, Germany
e-mail: {gerd.guelker, christoph.hindriksen,
tim.homeyer, peinke}@uni-oldenburg.de

2 Experiments

In our investigations we used a holographic in-line setup with one single camera, which has several advantages. First of all it is very compact and simple. Since only one camera is used it is very cost-effective and avoids the alignment of multiple cameras, which can be quite elaborate. Additionally, the mainly forward-scattered light is recorded, which means that the laser light is used very economically. This again reduces the complexity and the costs, because high powered lasers are unnecessary. Finally, the method opens the ability to measure particle size and shape, which is also important in some further areas of actual questioning.

In Fig. 1 the experimental setup is shown. The collimated beam of a frequency-doubled cw Nd:YAG laser with 100 *mW* optical output power illuminates the object, which in our experiments is a water filled glass cuvette with dimensions of $5 \times 5 \times 5 \text{ cm}^3$. A magnetic stirrer is used to produce a vortex flow symmetrical to the *y*-direction of the cuvette. The water is seeded with 10 μm mono-disperse polystyrene Polybead microspheres. A neutral density filter can be used to properly adapt the intensity, since less than 50 *mW* is sufficient in this configuration. The laser light scattered by the particles forms the object light, while the unobstructed light acts as the reference light, thus forming a digital hologram on the camera sensor. In our experiments we used an IDT X-Stream HS CMOS camera with 1280x1024 pixels with pixel size of 12 μm x 12 μm . The maximum frame rate at full resolution is 628 frames per second (*fps*) and can be increased up to 40,000 *fps* at reduced resolution. During our measurements series of holograms were recorded at 625 *fps* with exposure time of 8 μs per frame.

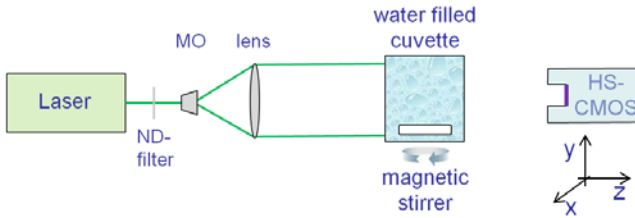


Fig. 1 Digital in-line holography PTV setup with high-speed camera and water filled cuvette. Vortex flow is produced by magnetic stirrer. MO: microscope objective.

3 Hologram Evaluation and Results

The reconstruction of the digital holograms is directly performed in the computer. If a hologram $h(x, y)$ is illuminated with the plane reference wave $R(x, y)$ of wavelength λ the diffraction image $\Gamma(\xi, \eta)$ in the axial distance d is described by the Fresnel-Kirchhoff diffraction integral

$$\Gamma(\xi, \eta) = \frac{i}{\lambda} \int_{-\infty}^{\infty} \int_{-\infty}^{\infty} h(x, y) R(x, y) \frac{\exp(-i\frac{2\pi}{\lambda} \rho)}{\rho} dx dy \quad (1)$$

where ρ is the distance between two points in the hologram and in the reconstruction plane. For reconstruction we used the Fresnel approximation where ρ is approximated by a Taylor expansion. The 3D particle field stored in each hologram is recovered by reconstructing slices of the real object wave of $10 \mu m$ distance, respectively. These slices are composed to obtain the complete particle field. Before reconstructing the recorded volume the digital holograms are preprocessed to improve their quality and the quality of the particle images. Especially the un-diffracted part of the reference beam, as well as stray light lead to disturbing interference patterns, which can completely obscure the diffraction patterns of the particles. This is shown in the left part of Fig. 2, where an unprocessed hologram is shown. To filter out these parasitic patterns different procedures are proposed in literature. Here, a very effective and robust method can be applied. All holograms of one time series are added up point-wise and a mean value is calculated for every image point. This averaged hologram is then subtracted from every single hologram recording before reconstruction. The immense reduction of the noise is clearly visible in Fig. 2 right. The next step in the evaluation process of the reconstructed wave field is the detection of particle positions. Here we used the well known intensity method. In this method bright spots in the reconstructed planes exceeding a certain threshold are identified to get the transversal positions. Their intensity maxima in depth are defined as their longitudinal positions. The reconstructed particle fields of subsequently recorded holograms were then processed using a free particle-tracking algorithm [2]. The resulting traces in all our experiments show physically reasonable trajectories confirming the expectations based on the known vortex flow, which is demonstrated in Fig. 3. Here, the measured traces of 80 particles tracked over 200 reconstructed volumes are shown in a top view (projection in x-z plane). The vortex structure is clearly visible, which impressively confirm the suitability of the method. In this graph the extension in the x direction was limited to $12 mm$. Thus, the center of the concentric traces is not in the middle but can be estimated to be at the bottom of Fig. 3. Unfortunately, in all our experiments we were not able to trace the particles over all the reconstructed frames. That means that we lost the traces from time to time which lead to a lot of gabs in the trajectories. Thus, the PTV algorithm must be optimized and a further reduction of noise is essential.

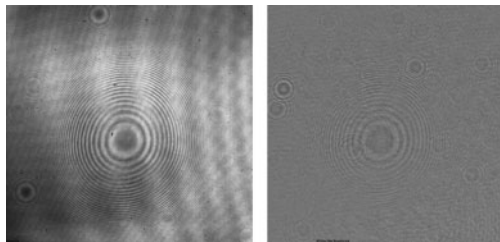


Fig. 2 Hologram recording before (left) and after pre-processing (right).

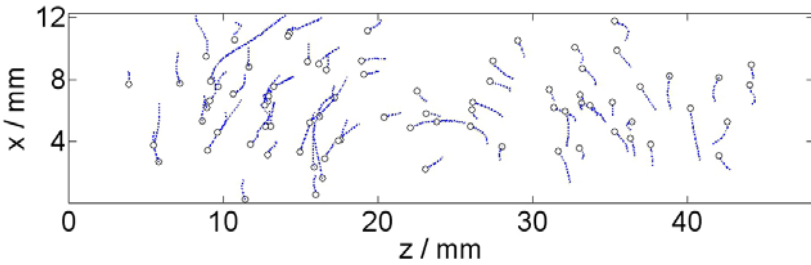


Fig. 3 Trajectories of ~ 80 particles in a top view (x - z projection). Vortex structure centered at the bottom of the graph clearly recognizable.

4 Conclusion

It was shown that 3D trajectories of particles in a vortex flow can be measured by digital in-line holography with high time resolution. In future improvements the PTV algorithm has to be optimized and further noise reduction is necessary in order to avoid gaps in the measured particle traces.

References

1. La Porta, A., Voth, G.A., Crawford, A., Alexander, J., Bodenschatz, E.: Fluid particle accelerations in fully developed turbulence. *Nature* 409, 1017–1019 (2001)
2. Crocker, J.C., Grier, D.G.: Methods of digital video microscopy for colloidal studies. *Journal of Colloid and Interface Science* 179, 298–310 (1996)

Development of Highly Resolving Drag Based Anemometers

Hendrik Heißelmann, Jaroslaw Puczyłowski, Michael Hölling, and Joachim Peinke

Abstract. This contribution presents two new drag based anemometers for highly resolved atmospheric flow measurements. Although both sensors are based on the same measuring principle, they are designed to meet significantly different requirements. The 2D Laser-Cantilever-Anemometer is intended for small scale velocity and direction investigations with frequencies in the order of several kHz. The sphere anemometer is designed to be a robust and higher resolving alternative to commonly used sensors in wind energy such as cup anemometers.

1 Introduction

Wind energy converters (WEC) are operating inside the turbulent atmospheric boundary layer and are exposed to rapid fluctuations of wind speed and direction during their entire life-time. Besides fast changes in the power production, this fluctuating wind field yields in higher aerodynamic loads on the WEC components. Hence highly resolved measurements of atmospheric wind fields are needed for a detailed description of their properties as well as for validation of wind field models. However, currently available anemometers exhibit a variety of problems: X-wire / X-film probes provide a high temporal and spatial resolution for small scale turbulence investigations, but they are extremely fragile and quickly destroyed under atmospheric conditions. More robust anemometers such as cup anemometers or ultrasonic anemometers suffer from a significantly lower resolution and accuracy. Therefore, two new sensor prototypes for atmospheric flow measurements have been developed at the University of Oldenburg. While both anemometers make use of the drag force acting on a flexible structure exposed to the flow, they are designed for different fields of application as described below.

Hendrik Heißelmann · Jaroslaw Puczyłowski · Michael Hölling · Joachim Peinke
ForWind - Institute of Physics, University of Oldenburg, D-26111 Oldenburg, Germany
e-mail: hendrik.heisselmann@uni-oldenburg.de

2 2D Laser Cantilever Anemometer

The 2D Laser Cantilever Anemometer (2D LCA) for atmospheric flows is based on the previously developed 2D LCA for laboratory use as described in [1] [2]. It makes use of the velocity-dependent drag force F acting on a flexible cantilever beam. The cantilever, which is exposed to the flow is bending with the deflection of its tip being related to the flow velocity via calibration. In order to detect this deflection, the light pointer principle known from atomic force microscopy is utilized. As shown in Fig. 2, a laser beam is focussed on the small cantilever at the tip of the anemometer housing. The reflected spot is aimed onto the active area of a two-dimensional position sensitive detector (2D-PSD). Thus, the bending of the cantilever can be tracked.

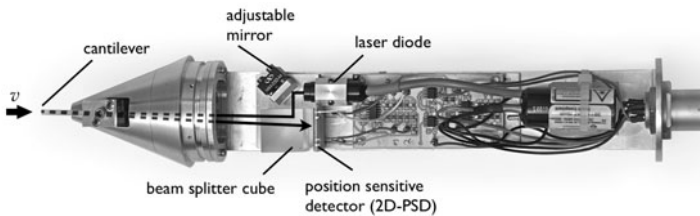
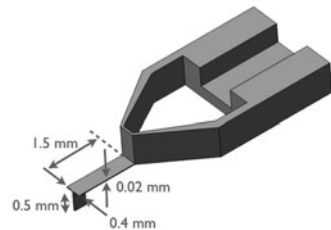


Fig. 1 Picture of the 2D LCA for atmospheric flow measurements with removed housing. The light path of the laser is indicated by the black line.

A special cantilever design was developed in order to match the challenges of atmospheric flow measurements even in off-shore environments. An improved robustness of the cantilever itself was achieved by increasing its dimensions ($1.5 \times 0.4 \times 0.02 \text{ mm}^3$) as sketched in Fig. 2 left. Moreover, the cantilever was

Fig. 2 Sketch of the improved cantilever design with fin and window. The Cantilever design and dimensions were optimized to meet the requirements of outdoor operation.

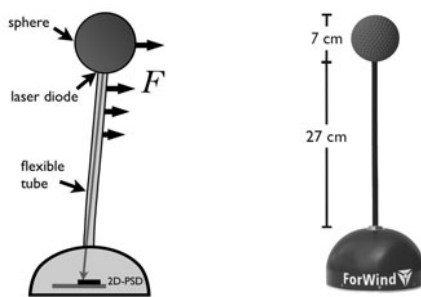


made of stainless steel instead of commonly used silicon. The anemometer's sensitivity to crossflow components was increased by adding a small fin to the cantilever tip. This yields a more pronounced torsion of the cantilever in inclined flow and thus enables directional measurements in the range of $\pm 40^\circ$ around the main flow direction with a temporal resolution of approximately 10 kHz. A comparison of the 2D LCA for laboratory use and a commercially available X-wire probe has been performed in turbulent flow. The results presented in [3] give evidence about the ability of the new anemometer to compete with standard X-wire sensors in terms of accuracy as well as resolution.

3 Sphere Anemometer

While the 2D LCA presented in Sect. 2 is designed to obtain information of small scale atmospheric turbulence, the sphere anemometer is developed for applications in wind energy industry. It consists of a sphere of 7 cm diameter which is mounted on top of a flexible tube as shown in Fig. 3. Once the anemometer is exposed to the flow, the sphere and its support are bending due to the acting drag forces F . A laser diode is attached to the tip of the tube and directly aimed onto the 2D-PSD at the bottom of the anemometer housing to detect the deflection of the tip. The absence of mounts in the vicinity of the sphere-tube combination enables directional measurements for the full 360° range. For a detailed description of the setup see [4].

Fig. 3 *Left:* Sketch of the sphere anemometer setup. A laser diode is mounted inside the sphere and aimed onto a 2D-PSD. The sphere-tube combination is bending due to the drag forces F acting. *Right:* Photography of the sphere anemometer.



In order to link the deflection with the prevailing wind speed and direction, a two-dimensional calibration function was recorded (see. Fig. 4). A system of concentric rings is obtained, and no overlapping nor crossing of calibrations for subsequent angles of attack is observed. Nevertheless, a system of circles would be expected, but a slight increase of the tube's cross-section at $\phi = 90^\circ$ and $\phi = 270^\circ$ causes the small discrepancy from the expectation. The dynamical behavior of the sphere anemometer was characterized in wind tunnel experiments. Fast wind speed fluctuations ($f \approx 1.3$ Hz) were produced with a motor-driven "gust generator". A comparison of the recorded time series with sphere anemometer, cup anemometer and a hot-wire reference is shown in Fig. 5. While the cup anemometer exhibits the effect of over-speeding and cannot resolve the fluctuations, the sphere anemometer data agrees quite well with the hot-wire reference, although small deviations of the peak velocities are observed. These are due to the different sensor dimensions (7 cm vs. 0.5 cm). The comparison of the respective power spectra (cf. [4]) confirms the sphere anemometer's ability to resolve fluctuations up to its natural frequency of approximately 38 Hz.

Fig. 4 2D calibration function of the sphere anemometer, obtained by variation of the angle of attack (AoA) and velocity. The velocity increases with radius and is coded in gray-scales while the AoA increases in counter clockwise direction. Each point in the plot corresponds to the position of the laser spot on the active area of the 2D-PSD.

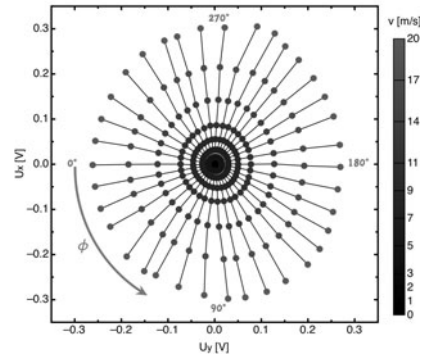
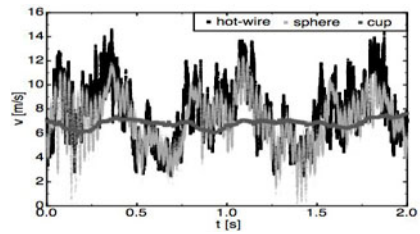


Fig. 5 Excerpts of gust measurements with sphere anemometer (light gray), cup anemometer (dark gray) and hot-wire reference (black). The cup anemometer cannot resolve the fluctuations. Sphere anemometer and hot-wire data agree quite well.



4 Conclusion

Two new drag-based anemometers for wind speed and direction measurements were presented. While the 2D-LCA serves as an alternative to X-wires in small scale atmospheric measurements, the sphere anemometer is designed to fill the gap between cup anemometer and expensive ultrasonic anemometers in wind energy industry. Experimental results could confirm the ability of both new anemometers to compete with commonly used standard sensors in their respective field of application.

References

1. Barth, S., et al.: Laser-Cantilever-Anemometer: A new high resolution sensor for air and liquid flows. *Rev. Sci. Instrum* (2005), doi:10.1063/1.1979467
2. Hölling, M., Peinke, J.: Using the 2D Laser-Cantilever-Anemometer for Two-Dimensional Measurements in Turbulent Flows. In: Peinke, J., Oberlack, M., Talamelli, A. (eds.) *Progress in Turbulence III*. Springer Proceedings in Physics, vol. 131, pp. 61–64. Springer, Heidelberg (2009)
3. Puczylowski, J., Hölling, M., Peinke, J.: Measurements with a 2D Laser-Cantilever-Anemometer compared to an x-wire probe. In: *80th Annual Meeting of the International Association of Applied Mathematics and Mechanics*, pp. 461–462. Wiley, Weinheim (2010)
4. Heißelmann, H., Hölling, M., Peinke, J.: Using the Sphere Anemometer for Wind Speed and Direction Measurements. In: *TORQUE 2010: The Science of Making Torque from Wind*, pp. 13–18 (2010)

Stability and Dynamics of Flow in a Turbulent Boundary Layer Separation Region

Vaclav Uruba

Abstract. Separation of a turbulent boundary layer on a flat plate under adverse pressure gradient was studied experimentally using Time-Resolved PIV technique. The results of spatio-temporal analysis of the flow-field in the separation zone are presented. For this purpose, the Proper Orthogonal Decomposition method is used to perform the dynamical system reduction which is then analyzed using Principal Oscillation Patterns method. The study contributes to understanding mechanisms of a boundary layer separation process. The acquired information could be used to improve strategies of a boundary layer separation control.

1 Introduction

Turbulent boundary layer (BL) separation is under permanent attention of researchers. Above a critical Reynolds number, the flow field is shown to undergo self-sustained 2D low-frequency fluctuations in the upstream region of the separation, evolving into aperiodic vortex shedding further downstream. Low-frequency fluctuations, also called "flapping", have been shown to be a characteristic feature of separated layers in general ([1]). It has been argued that they are due to a global instability manifested in the reattachment region ([3]), triggered by topological flow changes generating secondary recirculation zones ([2]).

In the classical approach the only point is defined, "detachment point", it occurs where the time-averaged wall shearing stress is zero. This model suggests BL separation with the mean back-flow coming from far downstream. The dynamical model suggested by Simpson [5] supposes location of maximal Reynolds stress and turbulence production close to the line of zero mean longitudinal velocity component. The coherent structures rising in this location travel toward the wall impinging it and forming recirculation region with rather complicated instantaneous structure.

Vaclav Uruba

Institute of Thermomechanics AS CR, v.v.i., Praha, Czech Republic

e-mail: uruba@it.cas.cz

2 Approaches

The blow-down aerodynamic rig has been used for the experiment. The test section for adverse pressure gradient generation in channel was employed. Origin of the coordinates is in the beginning of the diffuser, the cross-section here is $100 \times 100 \text{mm}^2$. Downstream of this section, the upper wall is inclined with angle 16deg , the bottom plane wall is used to study the boundary layer separation. To prevent separation from the upper wall, this is permeable and sucked out. The mean flow velocity outside boundary layer at $x = 0$ was 6m/s , the boundary layer was of turbulent nature, about 5mm thick.

Standard configuration of time resolved PIV was used for the measurements, measuring plane was the plane of symmetry of the channel. Two velocity components in this plane were evaluated in the grid 79×18 points, 5108 subsequent complete vector fields were evaluated with frequency 1545Hz representing approx. 3.3s . Details on used measuring techniques are given in ([6]).

To study the dynamics, the main problem is a huge number of the degrees of freedom, which should be reduced substantially. First, reduction of the dynamical system dimension is to be done using the Proper Orthogonal Decomposition (POD) method. Then, the stability of reduced system is analyzed using the Principal Oscillation Patterns (POPs) method.

The POPs is based on modal structures of temporal and spatial linear evolution dynamics. Each mode is characterized by a complex eigenvalue involving information on frequency, phase and growth/decay. The basis of the POPs analysis was formulated by Hasselmann [4] for discrete Markov processes in linearized dynamical systems driven by white noise with application in climatology. The spectral and modal analysis of Green resolvent provides the complex modes characterized with frequency f and so called e-fold time τ_e which gives the delay for the mode amplitude reduction in ratio $1 : e$ (e stands for the natural logarithm base). All evaluated modes are stable as a rule, however the least stable modes are pointed out. The eigenvalues are either complex-conjugate (then only positive imaginary part has physical meaning) or real (those modes are aperiodic - proportionally decaying). Detailed description of this method is given in [8].

3 Results

First, the mean vector field in time was evaluated, see Fig. 1 where zero mean longitudinal velocity component line l_0 and detachment point D are shown. Then, the mean pattern was subtracted from each snap. For the POPs analysis the reduced dynamical system characterized by the 30 most energetic POD modes representing approx. 82% of the total fluctuation energy have been considered.

In Fig. 2 frequencies and e-fold times of the first 10 modes are shown. The modes are ordered according to stability: less stable (i.e. bigger τ_e) first. The modes could be divided into periodical (complex) and aperiodic (imaginary part of eigenvalue

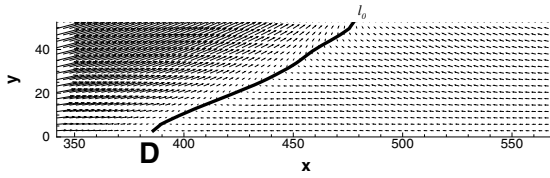


Fig. 1 Mean vector field with zero mean longitudinal component line l_0 and detachment point D

vanish), anyway decaying in time. However, some of nominally periodical modes behaves nearly aperiodically as well because of period much bigger then e-fold time (2,3,4,9,10).

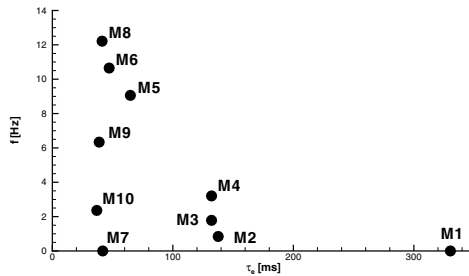


Fig. 2 Modes 1-10 frequencies f and e-fold times τ_e

The mode 1 is aperiodic with e-fold time $330ms$, imaginary part of the mode vanishes, real part is represented by vortical structures over whole separation region, see Fig. 3. The modes 2, 3, 4 are nearly aperiodic as well with the e-fold time about $135ms$ and period order of seconds, the mode 7 is fully aperiodic.

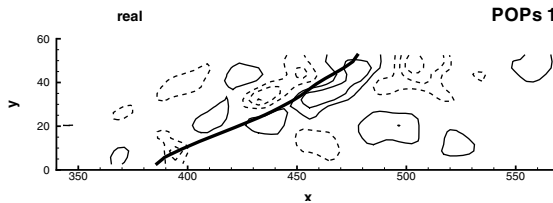


Fig. 3 Real part of POPs mode 1, vorticity contours (dashed negative) and l_0 line

The first really periodic mode is the 5 with e-fold time $65ms$ and frequency $9Hz$, however its periodicity is affected by decaying. The mode represents system of vortex pairs travelling along the l_0 line, this could be seen from the imaginary and real parts in Fig. 4. The same is true about mode 6 and 8.

The phenomenon of flapping in separating BL could be explained either by periodical modes (e.g. 5,6) or by pseudoperiodical appearance of aperiodically decaying modes (e.g. 1,2,7,10).

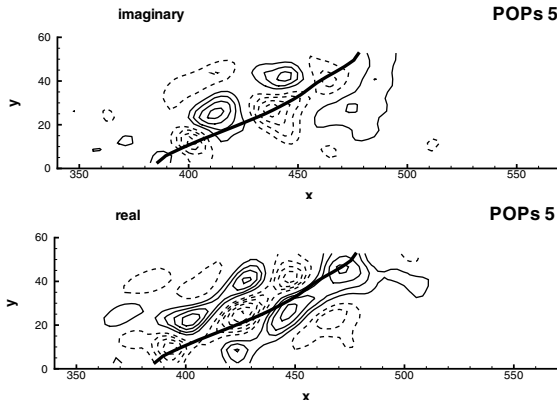


Fig. 4 Imaginary and real parts of POPs mode 5, vorticity contours (dashed negative) and l_0 line

4 Conclusions

The stability modes have been studied on the reduced dynamical model of a BL separation region. The proportionally decaying and traveling structures associated with flapping process have been identified both in shear and in the whole separation regions.

Acknowledgements. The author gratefully acknowledges financial support of the Grant Agency of the Czech Republic, projects No. 101/08/1112 and P101/10/1230.

References

1. Cherry, N.J., Hiller, R., Latoup, M.P.: Unsteady measurements in a separated and reattaching flow. *J. Fluid Mech.* 144, 13–46 (1984)
2. Dallmann, U., Herberg, T., Gebing, H., Su, W.-H., Zhang, H.-Q.: Flow field diagnostics: topological flow changes and spatio-temporal flow structure. *AIAA Paper 95-0791* (1995)
3. Haggmark, C.P., Bakchinov, A.A., Alfredsson, P.H.: Experiments on a two-dimensional laminar separation bubble. *Phil. Trans. R. Soc. Lond. A* 358, 3193–3205 (2000)
4. Hasselmann, K.: Stochastic climate models. *Tellus* 28, 473–485 (1976)
5. Simpson, R.L.: Aspects of turbulent boundary-layer separation. *Prog. Aerospace Sci.* 32, 457–521 (1996)
6. Uruba, V., Knob, M.: Dynamics of Controlled Boundary Layer Separation. In: Jonas, P., Uruba, V. (eds.) *Colloquium Fluid Dynamics 2007, IT AS CR, v.v.i., Praha*, pp. 95–96 (2007)
7. Uruba, V.: Dynamics of a Boundary Layer Separation. In: Vad, J. (ed.) *14th CMFF 2009*, pp. 268–275. University of Technology and Economics, Budapest (2009)
8. Uruba, V.: A New Method for Vector Fields Dynamics Analysis. In: Zolotarev, I. (ed.) *Engineering Mechanics 2010, Svratka* (2010)

Session 5

Special Flows

Reynolds Stress Modeling for Hypersonic Flows

A. Bosco, B. Reinartz, S. Müller, L. Brown, and R. Boyce

Abstract. Despite the enormous increase in computational capabilities and use of computational fluid dynamics as a design tool in the aircraft industry, the correct prediction of complex hypersonic turbulent flows involving shock wave boundary layer interaction (SWBLI) is still a challenge [1]. Well assessed turbulence models that are known to perform properly at lower speed, cannot be used in hypervelocity flows without a proper validation. In this paper the use of a differential Reynolds Stress Model for the prediction of SWBLI on a compression corner is presented and the results are discussed for attached and separated boundary layers.

1 Introduction

A correct prediction of shock wave boundary layer interaction (SWBLI) in turbulent hypersonic flows, particularly separation size, reattachment point and peak heating is mandatory for the development of hypersonic vehicles. The investigation of such flows is currently inaccessible with DNS and LES simulation methods, therefore RANS is the only available numerical tool for academic and engineering research. Currently the most famous and used RANS models are eddy viscosity models that rely on the Boussinesq hypothesis of a proportionality between the Reynolds stress tensor and the strain rate tensor. These models, used in their original formulation, are known to have difficulties to predict interactions between shock waves and boundary layer as well as pressure induced separation [2]. For this reason a Reynolds stress model has been implemented in the well validated code Quadflow and used for studying hypersonic flows. A compression corner at 15 and 40 degrees has been investigated experimentally and numerically and the results are discussed in this paper.

A. Bosco · B. Reinartz · S. Müller
RWTH Aachen, Templergraben 55, 52056 Aachen, Germany
e-mail: bosco@aices.rwth-aachen.de

L. Brown · R. Boyce
University of Queensland, St Lucia QLD 4072, Australia

2 Experiment

The experimental campaign has been conducted in the T4 free-piston tunnel at the University of Queensland. A Mach 6.68 contoured nozzle has been used. Experiments have been performed using air as test gas and a nozzle-supply enthalpy of about 3 MJ/kg that justifies the assumption of perfect gas in the numerical simulations, since under this condition only minimal real gas effect are present. The experimental inflow conditions are also used for the simulations and are as follows: $P_\infty = 9871$ Pa, $\rho_\infty = 0.08642$ kg/m³, $U_\infty = 2516$ m/s, $T_\infty = 390$ K and $M_\infty = 6.35$.

The model design is shown in Figure 1. The flat plate and the ramp are 150 mm and 250 mm long, respectively. The model is 150 mm wide. A boundary layer trip, 45 mm downstream of the leading edge has been used to enhance laminar to turbulent transition. The ramp angle can be set either to 15 or 40 degrees. Fast response thin film gauges have been used to measure heat fluxes along the plate and self made k-type thermocouples along the ramp. Pressure measurements have been taken on a line slightly off-center (23 mm).

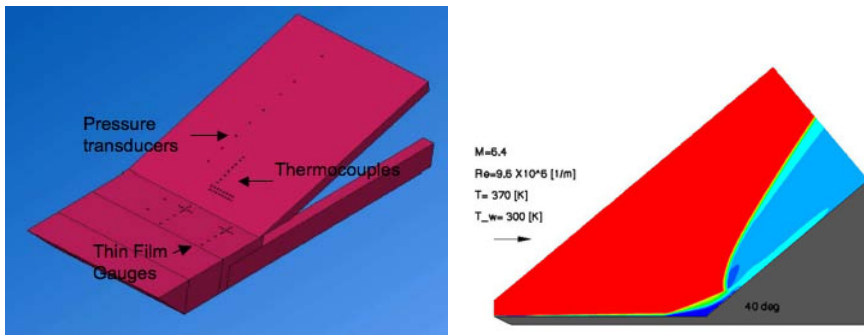


Fig. 1 Schematic sketch of the experimental model (left) and Mach number contour plot obtained using a Reynolds Stress Model (right).

3 Numerical Methods

The numerical simulations are performed using the in house code Quadflow. Quadflow uses a cell-centered finite volume method and block-structured grids [3]. For the convective fluxes the AUSMDV Riemann solver is used, for the viscous fluxes a cell-centered method and for time integration both an explicit Runge-Kutta second order five stage scheme and a first order implicit Euler scheme.

The Reynolds Stress Model (RSM) chosen to be implemented is the SSG/LRR- ω model by Eisfeld et al. [4]. It is a combination of the SSG model [5] in the far

field and the LRR model [6] near the wall. The idea is to extend the applicability of the SSG model to wall-bounded flows in conjunction with an ω -equation. The LRR model chosen is a simplified version by Wilcox who coupled it with his ω -equation as in [7]. The choice of this model near the wall is justified by the desire of having a low-Reynolds number model. As Wilcox shows, the near-wall behaviour of second-order closure models is strongly influenced by the scale-determining equation [7]. Models based on an ω -equation often predict acceptable values of the wall integration constant and are quite easy to integrate through the viscous sublayer with respect to models based on the ε -equation. The ω -equation of Menter has been chosen to provide a turbulent length scale for the present model. The blending function of Menter has been employed to smoothly blend the coefficients of the two models.

4 Results

The results obtained using a 15 degree compression ramp and a boundary layer trip show that the boundary layer is fully turbulent and attached. No significant differences between the turbulence models could be detected and for this reason the results are not presented here.

The comparison is more interesting for a fully turbulent boundary layer with separation as occurs at 40 degrees. Figure 1 shows a Mach contour plot. The grid is two-dimensional and has a resolution of 450x250 cells. The first grid spacing at wall is of 10^{-7} m which allows to have a maximum y^+ of 0.2 at reattachment. The simulations are run using the same computational grid and the grid study has been conducted using the RSM which is assumed to have tighter requirements. Figure 2 shows the measured pressure and heat fluxes distributions compared with the results obtained using different turbulence models. Both quantities show that the eddy viscosity models used here, the SST k - ω model of Menter and the k - ω model of Wilcox, are not able to predict boundary layer separation as clearly detected by the experimental results. On the other hand both the RSM and the EARSM (Explicit Algebraic Reynolds Stress Model) seem to predict the separation size with a satisfactory agreement. Looking at the heat fluxes, the RSM seems to provide better results when compared with the experiment. It is interesting to notice that despite the fact that the EARSM and RSM show similar behaviors, they actually predict two different phenomena. The EARSM captures a weak shock at the reattachment as can be seen in the pressure peak. The much more significant pressure rise at reattachment detected by the RSM can be related to the strong shock captured by this model. The reasons for this difference need to be further investigated.

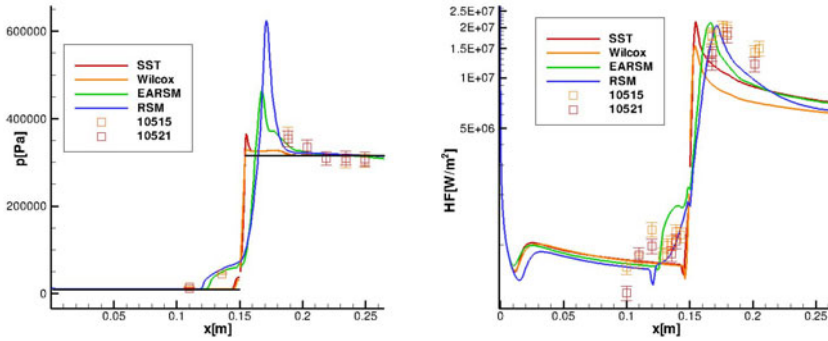


Fig. 2 Pressure and heat fluxes distribution for a fully turbulent flow over a 40 degrees compression corner. Symbols refers to experimental data and lines to computational results.

5 Conclusions

For the prediction of hypersonic turbulent separated flows the use of a differential Reynolds Stress Model can considerably improve the quality of the results and give good values of the separation size and peak heating. Well assessed turbulence models for transonic flows produce unreliable results for this kind of flow while the use of a EARSM provides reasonable results but needs a further analysis.

Acknowledgements. Financial support from the Deutsche Forschungsgemeinschaft (German Research Association) through grant GSC 111 and Research Training Group GRK 1095 is gratefully acknowledged. A big thanks to James Turner for his invaluable help through all the experimental campaign.

References

1. Dolling, D.S.: Fifty Years of Shock-Wave/Boundary-Layer Interaction research: What Next? AIAA J. 39, 1517–1531 (2001)
2. Eisfeld, B.: Implementation of Reynolds stress models into the DLR-FLOWer code. Internal DLR report, IB 124-2004/31 (2004)
3. Bramkamp, F., Lamby, P., Müller, S.: An adaptive multiscale finite volume solver for unsteady and steady flow computations. J. Comp. Physics 197, 460–490 (2004)
4. Eisfeld, B., Brodersen, O.: Advanced Turbulence Modelling and Stress Analysis for the DFG-F5 Configuration. In: 23rd AIAA Applied Aerodynamics Conference, Toronto, June 6-9 (2005)
5. Speziale, C.G., Sarkar, S., Gatski, T.B.: Modelling the pressure-strain correlation of turbulence: an invariant dynamical system approach. J. Fluid Mech. 227, 254–272 (1991)
6. Launder, B.R., Reece, G.J., Rodi, W.: Progress in the development of a Reynolds-stress turbulence closure. J. Fluid Mech. 68, 537–566 (1975)
7. Wilcox, D.C.: Turbulence Modeling for CFD. DCW Industries Inc. (1993)

Forced Magnetohydrodynamic Turbulence in Large Eddy Simulation of Compressible Fluid

A.A. Chernyshov, K.V. Karelsky, and A.S. Petrosyan

Abstract. Large eddy simulation technique for studying forced compressible magnetohydrodynamic turbulence is suggested. In our work, this method is based on a solution of filtered MHD equations by finite-difference methods and on a linear representation of driving forces in the momentum conservation and the magnetic induction equations. The emphasis is made on important and so far uninvestigated questions about ability of the large eddy simulation method to reproduce Kolmogorov and Iroshnikov-Kraichnan scale-invariant spectra in compressible MHD flows.

1 Introduction

Large-eddy simulation (LES) method is an effective instrument for the study of complex turbulent fluid flows. However, validity of LES for studies of physical processes in forced compressible magnetohydrodynamic (MHD) turbulence remains unidentified. The problem is that in the case of compressible MHD turbulence for numerical solutions of equations in LES (as well as in direct numerical simulation (DNS) approach) the finite-difference and finite-volume schemes in physical space are the most proper. The solutions of the basic equations by finite-difference methods allow to investigate inhomogeneous and non-stationary turbulent flows directly. The traditional way of driving force implementation for the compressible MHD flows relies on studies of incompressible turbulent fluid and is based on the spectral representation of external force and a subsequent re-calculation of this force in physical space. In compressible MHD, four types of waves exist: Alfvén, fast magnetosonic, slow magnetosonic and entropy. In this case the interactions between the aforementioned types of waves can lead to the richer picture of the turbulence spectra in the inertial range. The traditional forms of external forces may strongly

A.A. Chernyshov · K.V. Karelsky · A.S. Petrosyan
Theoretical Section, Space Research Institute of the Russian Academy of Sciences,
Profsoyuznaya 84/32, 117997, Moscow, Russia
e-mail: achernyshov@iki.rssi.ru

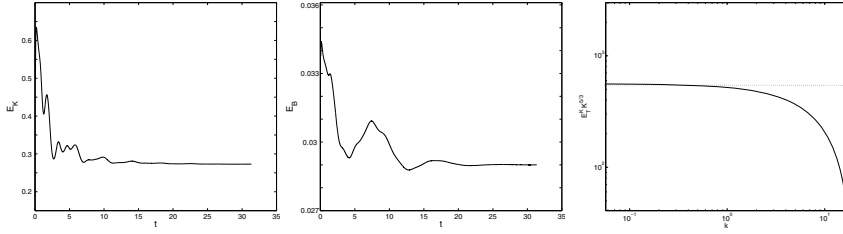


Fig. 1 Time evolution of kinetic energy (left), magnetic energy (middle) and normalized, time-averaged and smoothed spectrum of the total energy, multiplied by $k^{5/3}$ (right) for the first case.

oversimplify the flow pattern in compressible MHD plasma turbulence. Validation of LES requires proving the possibility of reproducing of the scale-similarity spectra rather than comparing the DNS and LES methods as has been done in our previous works [1] [2] [3] [4]. For the study of forced compressible MHD turbulence in the inertial range, we apply the linear driving force in the form recently introduced in hydrodynamics of incompressible fluid by Lundgren [5]. In spite of certain advantages of the linear forcing method, it still has not been widely adopted for the studies of turbulence by the DNS and LES methods. In this work we develop the method of linear forcing for compressible MHD turbulence.

2 Linear Forcing in Compressible MHD Turbulence

In the equation for the fluctuating part of the velocity in a compressible MHD turbulent flow, there is term $\rho \acute{u}_j (\partial U_i / \partial x_j)$ that corresponds to the production term in the turbulent kinetic energy equation [5]. The term $\langle \rho \acute{u}_i \acute{u}_j \rangle \frac{\partial U_i}{\partial x_j}$ is the production of turbulent energy resulting from the interaction between the Reynolds stress and the mean shear. Thus, this term for isotropic homogeneous turbulence is appropriate to force a stationary flow with a driving term proportional to velocity

$$F_i^u = \Theta \rho u_i \quad (1)$$

where Θ is the coefficient which is determined from the balance of kinetic energy for a statistically stationary state: $\Theta = \frac{1}{3 \langle \rho \rangle u_{rms}^2} [\langle u_j \frac{\partial}{\partial x_j} p \delta_{ij} \rangle + \varepsilon + \frac{1}{8\pi} \langle u_j \frac{\partial}{\partial x_j} B^2 \delta_{ij} \rangle]$ where $\varepsilon = -\langle u_j \partial \sigma / \partial x_j \rangle$ is the mean dissipation rate of turbulent energy into heat. The coefficient Θ in (1) can be both constant and recalculated during a simulation.

The determination of the driving force F_i^b in induction equation is similar. In the equation for the fluctuating part of the magnetic field in a compressible MHD turbulence, the term $\acute{B}_j (\partial U_i / \partial x_j)$ corresponds to a production term in the equation of turbulent magnetic energy because the term $\frac{\langle \acute{B}_i \acute{B}_j \rangle}{4\pi} \frac{\partial U_i}{\partial x_j}$ is a source term for the production of the magnetic turbulent energy in a consequence of interaction between magnetic field and mean fluid shear. We suggest that driving force in the magnetic induction equation is proportional to magnetic field and driving force F_j^b is:

$$F_i^b = \Psi B_i \quad (2)$$

where Ψ is the coefficient. Similar the above evaluation of Θ , the coefficient Ψ is determined from the balance of magnetic energy for the statistically stationary state $\Psi = \chi / (3B_{rms}^2)$, where $\chi = \langle \eta B_i (\partial^2 B_i / \partial x_j^2) \rangle$ is resistive dissipation of the turbulent magnetic energy and $B_{rms}^2 = \langle B^2 \rangle / 3$ is the root-mean-square magnetic field.

3 LES of Forced MHD Turbulence. Results and Conclusions

After the use of Favre-filtering procedure for system of MHD equations, the influence of the small-scale turbulence on the filtered part of MHD equations is defined through the subgrid terms: $\tau_{ij}^u = \bar{\rho} (\overline{u_i u_j} - \tilde{u}_i \tilde{u}_j) - \frac{1}{M_a^2} (\overline{B_i B_j} - \tilde{B}_i \tilde{B}_j)$ and $\tau_{ij}^b = (\overline{u_i B_j} - \tilde{u}_i \tilde{B}_j) - (\overline{B_i u_j} - \tilde{B}_i \tilde{u}_j)$. Here, the polytropic gas $p = \rho^\gamma$ is assumed. We use extended Smagorinsky model for compressible MHD case for subgrid-scale closure which showed accurate results in a wide range of similarity numbers [2].

The driving forces F_i^u and F_i^b are in momentum and induction equations respectively. This forces in dimensionless form are defined by means of the theory of linear forcing in (1) and (2):

$$\tilde{F}_i^u = \frac{1}{3\langle \bar{\rho} \rangle \tilde{u}_{rms}^2} \left[\tilde{\epsilon} + \frac{\langle \tilde{u}_j \frac{\partial}{\partial x_j} \bar{\rho}^\gamma \delta_{ij} \rangle}{\gamma M_s^2} + \frac{\langle \tilde{u}_j \frac{\partial}{\partial x_j} \bar{B}^2 \delta_{ij} \rangle}{2M_a^2} \right] \bar{\rho} \tilde{u}_i \quad (3)$$

$$\tilde{F}_i^b = \frac{1}{3\bar{B}_{rms}^2} \left[\left\langle \frac{1}{Re_m} \bar{B}_i \frac{\partial^2 \bar{B}_i}{\partial x_j^2} \right\rangle \right] \bar{B}_i \quad (4)$$

where $\tilde{\epsilon} = -\langle \frac{\tilde{u}_i}{Re} \frac{\partial \tilde{\sigma}}{\partial x_j} \rangle$. Note that additional term associated with subgrid-scale tensor can arise in an energy balance when defining a coefficient in the expression for the driving force. However, we apply a dynamic procedure for definition of model constants in the Smagorinsky model for MHD case. Therefore, their values are self-consistently computed during run time using the dynamic procedure where model constants are chosen to minimize (applying least-squares method) the dependence of turbulent statistics on the filter-width $\tilde{\Delta}$.

For the first numerical case similarity numbers are: $Re = 1500$, $Re_M = 800$, $M_s = 0.89$, $\gamma = 1.7$ and $E_k \gg E_M$, that is, the value of kinetic energy is initially much higher of magnetic energy. The evolution of kinetic energy E_k and magnetic energy E_M is presented for this case in Fig 1. Statistically stationary turbulence arises after an initial time interval when large fluctuations are observed and the values of E_K and E_M practically do not vary with time. It means that balance between dissipation and energy injected in the system is occurred. Note that E_K reaches a stationary regime slightly faster than E_M . Kolmogorov-like spectrum, $-5/3$, is observed, that is, nonlinear interactions are much more considerable than magnetic ones and the fluid is practically neutral hydrodynamic. The normalized and smoothed spectrum of total energy $E_T = E_M + E_K$ is shown in Fig 1(right). The total energy spectrum is derived after time averaging of values in the stationary regime.

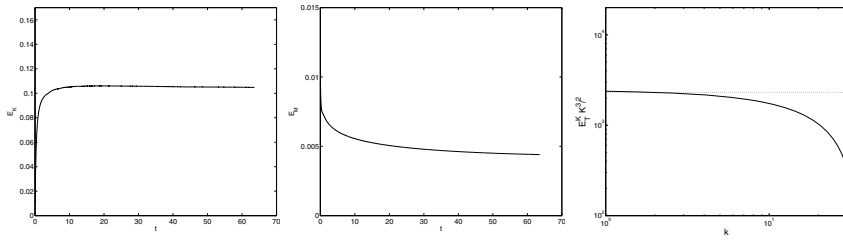


Fig. 2 Time evolution of kinetic energy (left), magnetic energy (middle) and normalized, time-averaged and smoothed spectrum of the total energy, multiplied by $k^{3/2}$ (right) for the second case.

The second case corresponds to the computations when $E_k < E_M$. In Fig. 2 time dynamics of E_k (left) and E_M (middle) respectively is shown. Rapid increase of the E_k takes place while sharp reduction of the magnetic field values is observed. Then, E_k and E_M attain to a stationary regime. The normalized and smoothed spectrum of the total energy is shown in Fig. 2(right). As seen from Fig. 2(right), clearly defined inertial range of MHD turbulence exists and Iroshnikov-Kraichnan spectrum with power exponent $k^{-3/2}$ is observed in agreement with theoretical studies. In this case, fluctuations in the form of Alfvén waves take place in electrically conducting fluid and magnetic interactions play the noticeable role in turbulent energy cascade.

To summarize, in this work LES method for the study of compressible MHD turbulence plasma in the inertial range by means of an external force is suggested. It is supposed that in the linear forcing the driving force is directly proportional to the velocity in the momentum equation and the driving force is proportional to the magnetic field in the induction equation. It is shown that linear forcing is a proper method for modeling forced MHD turbulence in physical space.

Acknowledgements. This work was supported by Grant of President of Russian Federation for supporting young scientists (MK-1349.2011.2) and Russian Foundation for Basic Research. A.Ch. gratefully acknowledges the financial support from Dynasty Foundation.

References

1. Chernyshov, A.A., Karelsky, K.V., Petrosyan, A.S.: Phys. Plasmas 13(3), 032304 (2006)
2. Chernyshov, A.A., Karelsky, K.V., Petrosyan, A.S.: Physics of Fluids 19(5), 055106 (2007)
3. Chernyshov, A.A., Karelsky, K.V., Petrosyan, A.S.: Physics of Fluids 20(8), 085106 (2008)
4. Chernyshov, A.A., Karelsky, K.V., Petrosyan, A.S.: Theor. Comput. Fluid Dyn. 23(6), 451 (2009)
5. Lundgren, T.S.: Center for Turbulence Research Annual Research Briefs, pp. 461–473 (2003)

Investigations of Cavity Noise Generation on a Cylinder

Tim Homeyer, Gerd Gülker, Christopher Haut, Nils Kirrkamm, Volker Mellert, Manfred Schultz-von Glahn, and Joachim Peinke

Abstract. Cavity noise generation is of particular interest for e.g. the aeronautical and automotive industry where a lot of different shaped cavities occur on curved surfaces. In this work the flow over a small rectangular cavity ($L/D \approx 1$) on a cylinder at velocity ramps up to 45 m/s was investigated in an acoustic wind tunnel. Acoustical and PIV measurements indicate a sudden transition of the circulating flow to a turbulent boundary layer at the typical Reynolds number leading to cavity noise. The onset of the acoustic radiation is contemporaneous with this transition and shows a strong hysteresis. Pressure measurements directly on the cylinder surface reveal a hydrodynamics and acoustics coupling point in front of the cavity.

1 Cavity Noise

Cavity noise generation is still a recurrent problem for scientists and engineers. In 1964 Rossiter published his flow experiments on oscillations in rectangular cavities

Tim Homeyer · Gerd Gülker · Nils Kirrkamm · Joachim Peinke

ForWind - Institute of Physics, University of Oldenburg, D-26111 Oldenburg, Germany

e-mail: tim.homeyer@uni-oldenburg.de,

gerd.guelker@uni-oldenburg.de,

nils.kirrkamm@uni-oldenburg.de, peinke@uni-oldenburg.de

Christopher Haut

Acoustics, Institute of Physics, University of Oldenburg, D-26111 Oldenburg, Germany

e-mail: c.haut@uni-oldenburg.de

Volker Mellert

Acoustics Group, Institute of Physics, University of Oldenburg,

D-26111 Oldenburg, Germany

e-mail: volker.mellert@uni-oldenburg.de

Manfred Schultz-von Glahn

ITAP - Institut für Technische und Angewandte Physik GmbH,

D-26111 Oldenburg, Germany

e-mail: schultz@itap.de

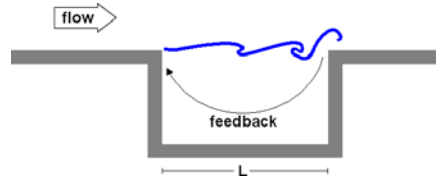
[1]. He found a formula that describes the relation between the inflow velocity U , the length of the cavity L and the radiated frequency

$$f = \frac{U}{L} \frac{m - \gamma}{\frac{1}{K} + M} \quad (1)$$

where M is the Mach number and m the mode ("Rossiter modes"). The constants γ and K (0.25 and 0.61 respectively for cavities which *length/depth* ratios are approximately 1) were found empirically. Nowadays there exists some slightly modified equations with tuned constants, but the basic relation was preserved.

The approved theory depicts, that a feedback loop exists inside the cavity: The flow separates from the leading edge, the oscillations of the shear layer are hitting the trailing edge where the sound generation takes place. The propagating acoustic waves again are amplifying the oscillations of the shear layer at the leading edge. This hydrodynamic-acoustic coupling effect is leading to strong tonal frequencies.

Fig. 1 Sketch of a cavity of length L . A feedback loop inside the cavity leads to a hydrodynamic-acoustic coupling at the leading edge. (modified from [2])



2 Experiments

Today cavity oscillations are of particular interest for e.g. the aeronautical and automotive industry where a lot of different shaped cavities occur on curved surfaces. The goal is to prevent noise generation with passive or even active control mechanisms [2, 3]. For this purpose the particular flow situation has to be analyzed and understood. In this work the flow over a small rectangular cavity (length/depth ≈ 1) milled on a plastic cylinder (Fig. 2) at velocity ramps between 25 m/s to 45 m/s is under investigation in an acoustic wind tunnel. During the ramps the sound pressure level (SPL) was recorded with a directional microphone perpendicular to the cylinder and the flow. In Fig. 3 the measured spectrogram of a downward ramp is shown. Tonal frequencies between 6 – 10 kHz with up to more than 100 dB and their higher

Fig. 2 A cylinder (thick drain pipe out of plastic) of 140 mm diameter with a small milled cavity of 3.55 mm length and 3.2 mm depth, located at 102.5 degrees from the stagnation point.

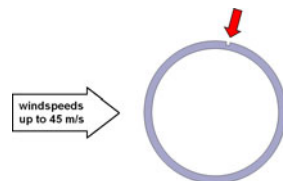


Fig. 3 Spectrogram of the SPL for a wind speed ramp downwards. Tonal frequencies and their higher harmonics are observable. A sudden stop of the acoustic radiation is visible at 37 m/s . The pressure values below 1 kHz are due to background noise.

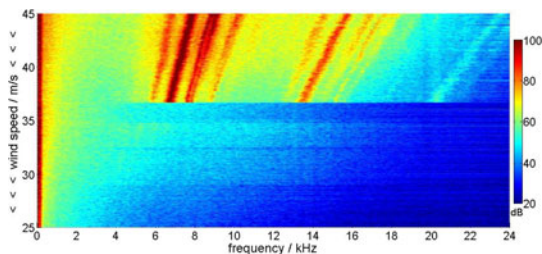
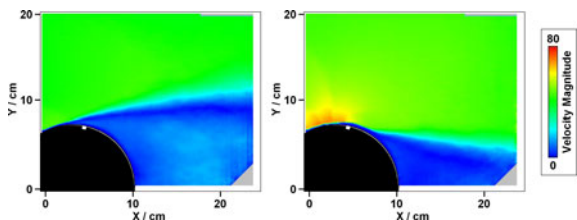


Fig. 4 Averaged PIV recordings at 35 m/s (left) and 36 m/s (right) inflow. The transition to a turbulent boundary layer leads to a separation of the flow *behind* the cavity. A noticeable reduction of the wake is observable.



harmonics are visible. An abrupt stop of the acoustic radiation at a wind speed of 37 m/s and a strong hysteresis of this alteration was cognizable. When upwards ramps were driven the sound radiation suddenly starts at 42 m/s .

2D Particle Image Velocimetry measurements were performed to visualize the flow around the cylinder. A Nd:YAG double pulse laser which has a repetition rate of 10 Hz was used to record 50 double images for different wind speeds respectively. It was observed that about 35 m/s and lower wind speeds the flow separates from the surface *in front of* the cavity. At 36 m/s and above the boundary layer becomes turbulent and attaches back to the surface before separating *behind* the cavity (Fig. 4). Thus the transition to a turbulent boundary layer provides that the cavity is blown with high local wind speeds. The known critical Reynolds number of this transition on a cylinder (tainted with hysteresis) is around $Re = 350000$. For our setup this corresponds to a wind speed around 37 m/s , which is in well agreement with the observation of the transition and the stop of the radiated sound.

The measured frequencies in Fig. 3 do not match with the theoretical frequencies calculated with Rossiter's formula for the given cavity length (see Fig. 5 left). Measurements with piezoresistive pressure transducers (Endevco 8507C-2) on the surface of the cylinder showed, that the dominant frequency can be recovered 5 cm in front of the cavity. Since this frequency is only found at that position, it is assumed, that the hydrodynamic-acoustic coupling takes place here and that this point is the sensitive boundary layer transition point. If we interpret L in Eq. 1 not as the length of the cavity, but as the distance between the sound generation and the coupling point, one can calculate theoretical frequencies with Rossiter's formula which have the appropriate distances towards each other (see Fig. 5 right). This second feedback loop leads to modes that are only excited in the spectral neighborhood of

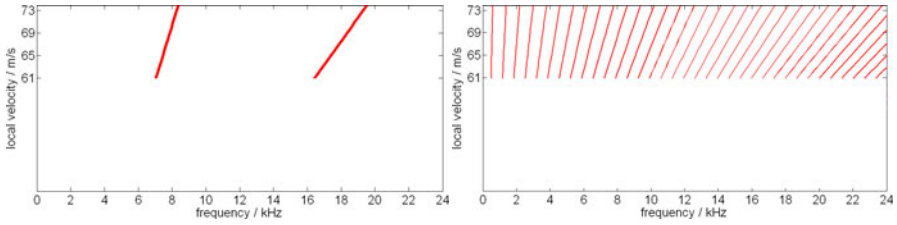


Fig. 5 Frequencies calculated with Rossiter's formula (Eq. (1)) with $U =$ measured local velocities above the cavity, left: modes $m = 1 : 2$ for a cavity of length $L = 3.55$ mm, right: modes $m = 1 : 35$ with $L = 50$ mm as the distance between the sound generation and the coupling point.

the Rossiter modes of the cavity, resulting in a spectrum which is in good agreement to the measured one (Fig. 3). [4]

3 Conclusion

The special flow situation around a small cavity on a cylinder generates tonal frequencies that do not match with the classical Rossiter theory. Pressure measurements indicate a second feedback loop to the boundary layer transition point that might explain the measured frequencies. PIV measurements showed that this transition is clearly responsible for the sudden stop and onset of the acoustic radiation and the included hysteresis. To solve open questions experiments will continue and promising CFD simulation with OpenFoam have already started. The final goal after the understanding of the complex interaction between hydrodynamics and acoustics is to find a passive modification to prevent the noise generation.

References

1. Rossiter, J.E.: Wind-tunnel experiments on the flow over rectangular cavities at subsonic and transonic speeds. Aero. Res. Council. R&M, No. 3438 (1964)
2. Cattafesta, L., Williams, D., Rowley, C., Alvid, F.: Review of active control of flow-induced cavity resonance. AIAA 2003-3567 (2003)
3. Colonius, T.: An Overview of Simulation, Modeling, and Active Control of Flow/Acoustic Resonance in Open Cavities. AIAA 2001-0076 (2001)
4. Added in proof: New measurements revealed Kelvin-Helmholtz instabilities as the source for the observed frequencies. Details will be published in another paper soon

Aerodynamic Sound Generation by Turbulence in Shear Flows

G. Khujadze, G. Chagelishvili, M. Oberlack, A. Tevzadze, and G. Bodo

Abstract. A comparative analysis of linear and nonlinear aerodynamic sound generation in two dimensional (2D) plane inviscid unbounded shear flow with uniform density, pressure and constant shear of velocity is presented. Self-consistent treatment of a linear aerodynamic sound generation and its interpretation are given in terms of modes with linear coupling induced by the non-normality of the flow. Perturbations of potential vorticity is identified as the only source of acoustic waves in the flow within the linear regime. Numerical simulation of a dynamics of the testing turbulent/stochastic perturbation embedded in the flow is presented. It was found that the linear aerodynamic sound dominates (up to large amplitudes of the turbulent perturbations) over the nonlinear one both at moderate and high shear rates.

Dynamics of stochastic/turbulent perturbations. The nonlinear aerodynamic sound generation by turbulence has been long analyzed since the foundation of the theory of aerodynamic sound in pioneering papers by Lighthill [1, 2]. He noted that velocity shear can increase the acoustic wave emission in the aerodynamic situation due to the existence of linear terms in the inhomogeneous part of the analogy equations (second derivative of the Reynolds stress). In the paper [3] by Chagelishvili

G. Khujadze · M. Oberlack
Chair of Fluid Dynamics, TU Darmstadt, Germany

M. Oberlack
Center of Smart Interfaces, TU Darmstadt, Darmstadt, Germany

G. Khujadze · M. Oberlack
GS Computational Engineering, TU Darmstadt, Darmstadt, Germany

G. Chagelishvili
M. Nodia Institute of Geophysics, Tbilisi, Georgia

G. Chagelishvili · A. Tevzadze
E. Kharadze Abastumani Astrophysical Observatory, Tbilisi, Georgia

G. Bodo
Osservatorio Astronomico di Torino, Pino Torinese, Italy

et al. the mechanism of a linear aerodynamic sound generation was disclosed and described. Specifically, it was shown that the linear phenomenon of the vortex mode conversion into the acoustic wave mode induced by the flow non-normality is the only contributor to the acoustic waves of the unbounded shear flow in the linear regime. From the physical point of view *potential vorticity* was identified as the linear source of acoustic waves in shear flows.

We performed comparative analysis of linear and nonlinear aerodynamic sound generation by the turbulent perturbations in constant shear flow and studied numerically the generation of acoustic waves by stochastic/turbulent perturbations embedded in 2D planar unbounded inviscid constant shear flow with uniform background density and pressure ($U_0 = (Ay, 0)$; $A, \rho_0, P_0 = \text{const}$). The governing hydrodynamic equations of the flow under investigation are:

$$\frac{\partial \rho}{\partial t} + \frac{\partial \rho U_i}{\partial x_i} = 0, \quad \left(\frac{\partial}{\partial t} + U_j \frac{\partial}{\partial x_j} \right) U_i = -\frac{1}{\rho} \frac{\partial P}{\partial x_i}, \quad (1)$$

$$\left(\frac{\partial}{\partial t} + U_i \frac{\partial}{\partial x_i} \right) P = -\frac{\gamma P}{\rho} \left(\frac{\partial}{\partial t} + U_j \frac{\partial}{\partial x_j} \right) \rho, \quad i, j = x, y, \quad (2)$$

where γ – adiabatic index, $c_s^2 \equiv \gamma P_0 / \rho_0$ – sound speed. Potential vorticity is defined as: $\mathcal{W} = [\text{curl} \mathbf{U}]_z / \rho$. Only stochastic streamwise and crossstream perturbation velocities are embedded in the flow at $t = 0$: $u_i(x_i, 0) \neq 0$; $\rho'(x, y, 0) = 0$; $P'(x, y, 0) = 0$. They are localized in the crossstream direction and homogeneous in the streamwise direction. $u_i(x_i, 0)$ are defined by the following stream function:

$$\psi(x, y, 0) = B e^{-\frac{y^2}{L_l^2}} \int_{-\infty}^{+\infty} dk_x dk_y \left(\frac{k_x k_y}{k_0^2} \right)^4 e^{-\frac{k_x^4 + k_y^4}{k_0^4}} e^{i(k_x x + k_y y)} \zeta(k_x, k_y), \quad (3)$$

where $\zeta(k_x, k_y)$ is random numbers in the range $[0, 1]$ different for different k_x and k_y ; L_l – the localization scale in the crossstream direction; k_0 – the peak center in the streamwise wavenumber (K_x) axis. The half-width of the spectrum of the initial perturbations satisfy the condition $\Delta k_0 \ll k_0$, that allows to discriminate linearly and nonlinearly generated acoustic waves and, thus, to carry out comparative analysis of linear and nonlinear aerodynamic sound generation by turbulent perturbations. The perturbations are inserted in the flow in the physical plane at the parameters $B = 0.5 \times 10^4$, $L_l = 3$, $k_0 = 10$, $c_s = 1$, $A = 4$ at $t = 0$ (see Fig. 1). Simulations were performed using the hydrodynamics module of the PLUTO code [4]. The domain and the grid were $-10 \leq x, y \leq 10$ and 1024×1024 respectively. Finer grid (2048×2048) was used to test the results of the simulations. Dissipative effects are only those related to the use of a mesh of finite width when the Euler equations are solved using the PLUTO code.

A fault of acoustic analogy treatment in the identification of the true linear sources of aerodynamic sound. The results of the acoustic analogy approach strongly depends on the form of the analogy equation as well as on the aero-acoustic

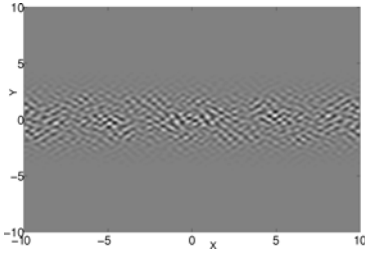


Fig. 1 Potential vorticity $\mathcal{W}(x, y, 0)$ in the physical plane at $t = 0$.

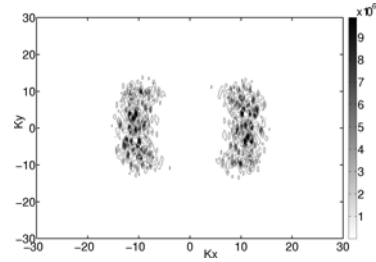


Fig. 2 Linear source $S^{(l)}(k_x, k_y, 0)$ at $t = 0$ in the wavenumber plane.

variable chosen to analyze the process. This is even more essential when the convective terms are important and the model should take into account the background flow. Hence, the acoustic analogy equation has been the subject to various approximations in order to correctly take into account the effect of the background inhomogeneous flow. However, identification of the true sources of aerodynamic sound remains relevant. Discussing the true linear sources of aerodynamic sound, we compare the linear acoustic wave production in the unbounded shear flows induced by the non-normality of the flow (described in the paper [3]) with the linear part of the acoustic analogy source. The linear part of the acoustic analogy source can be defined as:

$$S^{(l)} = 2 \frac{\partial^2}{\partial x^2} (\rho_0 A y u_x) + 2 \frac{\partial^2}{\partial x \partial y} (\rho_0 A y u_y). \quad (4)$$

The spectrum of the source ($S^{(l)}(k_x, k_y)$) in our case at $t = 0$ is presented in Fig. 2 which shows that the acoustic analogy linear source is distributed in all quadrants of the wavenumber plane, i.e. the linear source also generates acoustic field with $k_x k_y < 0$. However, density perturbations are generated only when $k_y \leq k_x$, as it was shown in the paper [3]. The following important result was also obtained: the linear generation of Spatial Fourier Harmonics (SFH) of acoustic waves by the related SFH of vortex modes takes place only when the vortex modes cross the K_x axis.

Consequently, the acoustic analogy linear source located in the quadrants *II* and *IV* (and having $k_x k_y < 0$) is the fault of acoustic analogy treatment. In our opinion, this is a very important result of the presented investigation.

Comparative analysis of linear and nonlinear aerodynamic sound generation by turbulent perturbations. The energy of the linearly generated acoustic waves is defined by the mean flow shear parameter and the potential vorticity of the turbulent perturbations and the spectrum, by the k_x spectrum of the potential vorticity at $k_y = 0$. The nonlinear source we define by the nonlinear part of the acoustic analogy source:

$$S^{(nl)} = \frac{\partial^2}{\partial x^2} (\rho u_x^2) + 2 \frac{\partial^2}{\partial x \partial y} (\rho u_x u_y) + \frac{\partial^2}{\partial y^2} (\rho u_y^2). \quad (5)$$

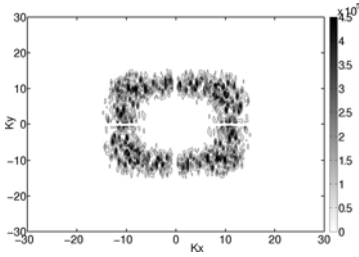


Fig. 3 Potential vorticity field at $t = 0$ in $K_x K_y$ plane.

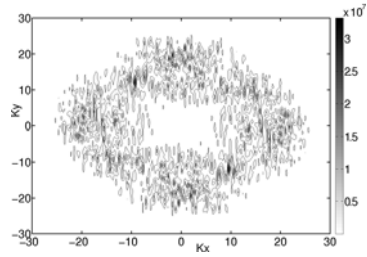


Fig. 4 Acoustic analogy nonlinear source $S^{(nl)}(k_x, k_y, 0)$ at $t = 0$.

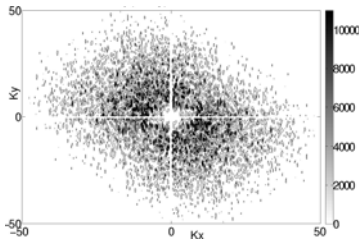


Fig. 5 Density field in $K_x K_y$ plane at $t = 0.1$.

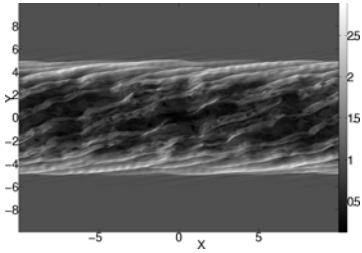


Fig. 6 Density field in physical plane at $t = 2$.

The spectrum of these sources at $t = 0$ are presented in Figs. 3 and 4. Fig. 3 shows that the potential vorticity of the perturbations along the K_x axis is located in a streamwise wavenumber range $[k_0 - \Delta k_0, k_0 + \Delta k_0]$. Consequently, the linear aerodynamic sound should be located in the same range of k_x (compare Figs. 2 and 3). At the same time Fig. 4 shows that $S^{(nl)}(k_x, k_y, 0)$ is located in a streamwise wavenumber range $[2k_0 - 2\Delta k_0, 2k_0 + 2\Delta k_0]$, i.e. its location along the K_x axis about twice farther than the potential vorticity (i.e. linear aerodynamic sound source) from the center of the plane.

The density field in the wavenumber plane for parameters $B = 0.5 \times 10^4$, $L_t = 3$, $k_0 = 10$, $c_s = 1$, $A = 4$ at $t = 0.1$ is presented in Fig. 5. The density field in the physical plane for the same parameters at $t = 2$ (in basic units $[m]$ and $[sec]$) is shown in Fig. 6. Fig. 5 shows that the density field of the perturbations along K_x axis is mainly located around k_0 with an extension to $2k_0$. The density field around k_0 relates to the linear mechanism of the wave generation. The density field close to $2k_0$ relates to the nonlinear mechanism. The figure shows that in the considered case the linear aerodynamic sound is stronger than the nonlinear one. According to Fig. 3 for the considered parameters, the mean flow vorticity is larger than the perturbation potential vorticity – the case when Rapid Distortion Theory (RDT) of turbulence is at work. So, the dominance of the linear aerodynamic sound occurs up to quite large amplitudes of the turbulent perturbations. According to our study the

linear aerodynamic sound dominates over nonlinear one at moderate and high shear rates: $R \equiv A/k_0 c_s \geq 0.3$.

References

1. Lighthill, M.J.: On sound generated aerodynamically I. General Theory. Proc. R. Soc. London, Ser. A 211, 564 (1952)
2. Lighthill, M.J.: On sound generated aerodynamically II. Turbulence as a source of sound. Proc. R. Soc. London, Ser. A 222, 1 (1954)
3. Chagelishvili, G., Tevzadze, A., Bodo, G., et al.: Linear mechanism of wave emergence from vortices in smooth shear flows. Phys. Rev. Lett. 79, 3178 (1997)
4. Mignone, A., Bodo, G., Massaglia, S., et al.: PLUTO: A Numerical Code for Computational Astrophysics. Astroph. JS 170, 228 (2007)

Exact Coherent State with Travelling Hairpin Vortex in Plane Couette Flow

K. Deguchi and M. Nagata

Abstract. A new type of travelling wave solution is obtained in plane Couette flow. The solution appears via a Hopf bifurcation from the so-called stationary hairpin vortex state found recently by [1] and [2]. The most striking feature of the solution is an anti-symmetric mean flow profile. The fluctuating flow patterns propagate in the streamwise direction with the phase velocity being zero at its onset and increasing gradually as the Reynolds number is increased.

1 Introduction

The transition to turbulence in canonical unidirectional shear flows, such as plane Couette flow (PCF) and pipe flow (PF), is still an unsolved problem in fluid mechanics, mainly due to the fact that PCF and PF are linearly stable against arbitrary three-dimensional perturbations at any finite Reynolds number, so that transitions from the basic laminar states must be abrupt. The absence of a linear instability mechanism has previously prevented the discovery of nonlinear solutions to these linearly stable canonical flows. However, following the first presentation of non-trivial equilibria in PCF by [3], and the first presentation of travelling waves by the same author [4], a large number of equilibria and travelling-waves have been computed for PCF. These are well documented in [1], [5] and [6], for example. Similarly, several nonlinear solutions have been obtained for PF, first by [7], and independently by [8], using the idea of a self-sustaining process of turbulence proposed by [9]. The onset of turbulence for these flows is believed to be related to the appearance of coherent states, caused by disturbances of finite amplitude which takes the flows out of the basin of attraction of the laminar state in the phase space.

K. Deguchi · M. Nagata

Department of Aeronautics and Astronautics,
Graduate School of Engineering, Kyoto University
Yoshida-Honmachi, Sakyo-ku, Kyoto 606-8501 Japan

e-mail: ken5-d@t06.mbox.media.kyoto-u.ac.jp,
m.nagata@aero.mbox.media.kyoto-u.ac.jp

Of our particular interest here are the equilibrium solutions in Couette flow found by [1] recently. According to [1], these solutions might be the same as the solutions, found a decade ago, by [5]. Furthermore, these solutions are believed to be identical to the so-called hairpin vortex solutions which have been obtained independently by [2]. In the interests of conciseness, following [2], we call these steady states HVS (hairpin vortex state), hereafter.

In the following, we first reproduce HVS in plane Couette flow and use this flow as a starting point in an investigation to continue this flow to sliding Couette flow [10]. As a byproduct of this investigation we obtain a new travelling wave solution.

2 Homotopy Approach in Sliding Couette Flow

Sliding Couette flow (SCF) denotes the an incompressible fluid flow between two infinitely long concentric cylinders caused by a mutual sliding motion of the cylinders in the axial direction. Let the cylinders with radii a and $b(> a)$ move in the opposite direction with the same speed, U . We take half the gap, $(b - a)/2$, as the length scale and half the mutual axial velocity difference, U , as the velocity scale, so that the Reynolds number R is defined by

$$R = \frac{(b - a)U}{2\nu}, \quad (1)$$

where ν is the kinematic viscosity. The basic flow of SCF is given as the exact solution of the Navier-Stokes equation by

$$U_{SCF} = R \frac{2 \ln(r(1 - \eta)/2) - \ln \eta}{\ln \eta}, \quad (2)$$

where r is the radial coordinate and $\eta = a/b$ is the radius ratio. We further introduce the additional coordinate transformation $z = r - \bar{r}$, where \bar{r} is the mean radius $\bar{r} = (1 + \eta)/(1 - \eta)$, in order to transform the region between the cylinders, $r \in [2\eta/(1 - \eta), 2/(1 - \eta)]$, to $z \in [-1, 1]$.

In the narrow limit of a gap between the cylinders ($\eta \rightarrow 1$), SCF becomes PCF. Using HVS as a seed, we investigate the behavior of the equilibria as η changes from 1 (PCF) to the wide gap case ($\eta < 1$). The basic flow of PCF is given by

$$U_{PCF} = -Rz. \quad (3)$$

Let α be the streamwise wavenumber of finite amplitude disturbances superimposed on the basic states for both SCF and PCF. The azimuthal wavenumber m in SCF for $\eta \approx 1$ is approximated by $m = \bar{r}\beta$, where β is the spanwise wavenumber in PCF.

The continuation of HVS in PCF to the wide gap case is shown in Fig. 1, where η is used as a homotopy parameter. The nonlinear measure in Fig. 1(a) is the momentum transport M on the outer cylinder at $z = 1$ (or $r = r_+ = 1 + \bar{r}$):

$$M = -\frac{r_+ U'|_{z=1}}{\bar{r}}. \quad (4)$$

Along the continuation path we fix $R = 200$, $\alpha = 0.75$ and $\beta = 1.37$. Note that m does not necessarily take an integer value for arbitrary $\eta < 1$. However, this does not cause any mathematical problems.

The two curves in Fig. 1(a) start from the upper and lower branch HVS solutions indicated by the closed circles. They experience turning points at $\eta \simeq 0.67$ and $\eta \simeq 0.21$ as η is decreased from 1. After going around the turning points both curves direct toward a larger η and terminate at the same point on $\eta = 1$ indicated by the open circle. As shown in Fig. 1(b), the phase velocity c in the axial direction departs from zero as soon as the solutions move away from HVS (the closed circle on $\eta = 1$) and takes non-zero values when the continuation paths return to the PCF limit (the two open circles on $\eta = 1$).

Next, we investigate how the solutions at the three points on $\eta = 1$ in Fig. 1 behave as R is changed. The three circles in Fig. 2(a) correspond to those in Fig. 1(a). We confirm that the upper and lower HVS branches form a saddle-node bifurcation point at $R = 137$ for $(\alpha, \beta) = (0.75, 1.37)$ as reported in [2]. We call the solutions on the upper and lower HVS branches \mathbf{u}^{EQ+} and \mathbf{u}^{EQ-} , respectively. We note that the wiggle on the upper HVS branch at $R \approx 275$ disappears when calculations are done for $(\alpha, \beta) = (1.0, 2.0)$ as in Fig. 2 of [2]. Fig. 2(a) shows that the branch, indicated by the dashed curve with the open circle, terminates on the upper HVS branch at $R = R_B = 143.1$. As shown in Fig. 2(b), along this new branch the phase velocity is $\pm c$ with $c > 0$ except at $R = R_B$. This implies that a new solution of a travelling wave type bifurcates from HVS and that its phase velocity is zero only at the bifurcation point. The bifurcation is a pitchfork type. The travelling wave solution branch in Fig. 2(a) is actually composed of two identical curves: \mathbf{u}^{TW+} travelling in one direction and \mathbf{u}^{TW-} travelling in the opposite direction. The double structure of

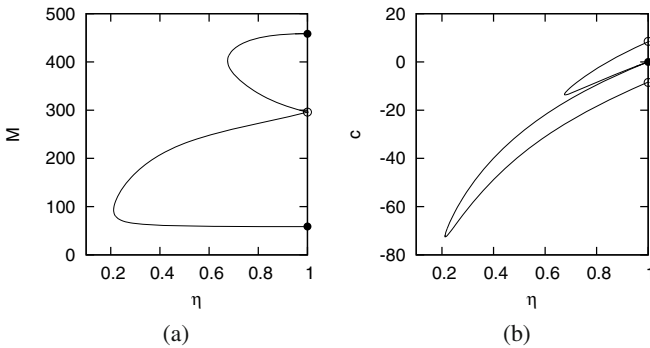


Fig. 1 The continuation of the solution under the radius ratio η for wavenumbers $(\alpha, \beta) = (0.75, 1.37)$ and $R = 200$. (a): the momentum transport M and (b): the phase velocity c . The two closed circles on $\eta = 1$ indicate the solutions on the upper and lower HVS branches. The open circle on $\eta = 1$ indicates the travelling hairpin vortex in PCF.

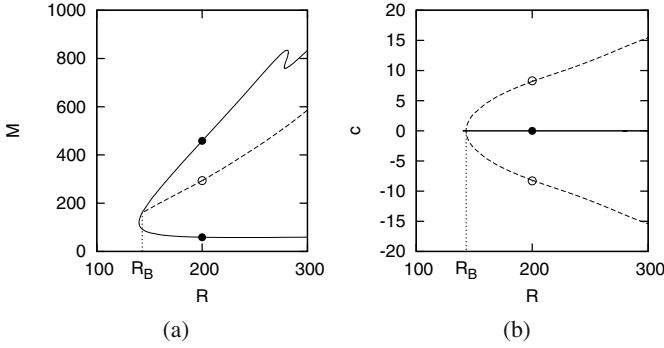


Fig. 2 The bifurcation of the travelling wave solution with $(\alpha, \beta) = (0.75, 1.37)$ in PCF. (a): the momentum transport M and (b): the phase velocity c . The solid and dashed curves indicate the solution branches of HVS and the travelling wave, respectively. The two closed circles and the open circle on $R = 200$ correspond to those in Fig. 1.

the travelling waves can be inferred from the fact that the point on $\eta = 1$ indicated by the open circle in Fig. 1 (a) is the end point of the two curves. We call these travelling wave solutions on the new branch \mathbf{u}^{TW+} and \mathbf{u}^{TW-} , corresponding to $+c$ and $-c$, respectively.

We analyze the flow structure of the new travelling wave solutions by comparing it with that of HVS. Let x and y denote the coordinates in the streamwise and spanwise directions, respectively, and define the following three symmetry operations:

$$\begin{aligned} S_1[u, v, w](x, y, z) &= [u, -v, w](x + \pi/\alpha, -y, z), \\ S_2[u, v, w](x, y, z) &= [-u, v, -w](-x + \pi/\alpha, y + \pi/\beta, -z), \\ S_3[u, v, w](x, y, z) &= [u, v, w](x + \pi/\alpha, y + \pi/\beta, z), \end{aligned}$$

where u , v and w are the velocity components in the x , y and z directions, respectively. Then, we can find that HVS satisfies $S_1\mathbf{u}^{EQ\pm} = \mathbf{u}^{EQ\pm}$, $S_2\mathbf{u}^{EQ\pm} = \mathbf{u}^{EQ\pm}$ and $S_3\mathbf{u}^{EQ\pm} = \mathbf{u}^{EQ\pm}$. On the other hand the travelling wave solution also satisfies $S_1\mathbf{u}^{TW\pm} = \mathbf{u}^{TW\pm}$ and $S_3\mathbf{u}^{TW\pm} = \mathbf{u}^{TW\pm}$, but the symmetry S_2 for the travelling wave solution is broken. The symmetry S_2 is, however, satisfied against the cross parity for the travelling wave solution, namely $S_2\mathbf{u}^{TW\pm} = \mathbf{u}^{TW\mp}$.

3 Flow Structure

Fig. 3 shows the mean flow \bar{u} for these solutions with $(\alpha, \beta) = (0.75, 1.37)$ at $R = 200$. It can be seen that the mean flows of HVS are anti-symmetric about the midplane $z = 0$ for both its upper and lower branch solutions, \mathbf{u}^{EQ+} and \mathbf{u}^{EQ-} , whereas those of the travelling wave solutions, \mathbf{u}^{TW+} and \mathbf{u}^{TW-} , are asymmetric. Isosurfaces of the streamwise velocity component u and the streamwise vorticity component ω_x for \mathbf{u}^{EQ+} , \mathbf{u}^{EQ-} and \mathbf{u}^{TW+} are plotted in Fig. 4. All of the

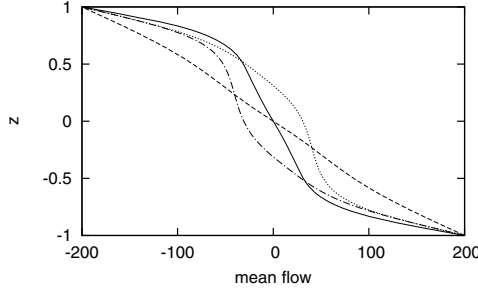


Fig. 3 The mean flow \bar{u} of HVS and the travelling wave solutions with wavenumbers $(\alpha, \beta) = (0.75, 1.37)$ at $R = 200$. The solid curve: the upper HVS branch solution \mathbf{u}^{EQ+} . The dashed curve: the lower HVS branch solution \mathbf{u}^{EQ-} . The dash-dotted curve: the travelling wave solution \mathbf{u}^{TW+} . The dotted curve: the travelling wave solution \mathbf{u}^{TW-} .

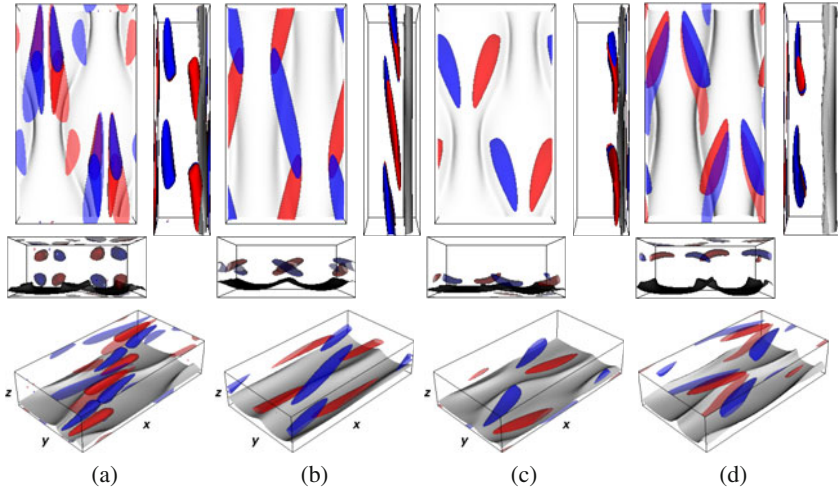


Fig. 4 Isosurfaces of the streamwise velocity component u (grey) and the streamwise vorticity component ω_x (red: positive and blue: negative) for wavenumbers $(\alpha, \beta) = (0.75, 1.37)$ at $R = 200$. (a): $u = 120$, $|\omega_x| = 300$ for \mathbf{u}^{EQ+} , (b): $u = 120$, $|\omega_x| = 100$ for \mathbf{u}^{EQ-} , (c): $u = 120$, $|\omega_x| = 250$ for \mathbf{u}^{TW+} and (d): $u = 120$, $|\omega_x| = 250$ for \mathbf{u}^{TW-} .

plots are presented for a domain comprising the full height of the channel and one period in both the streamwise and spanwise directions, $(x, y, z) \in [-\pi/\alpha, \pi/\alpha] \times [-\pi/\beta, \pi/\beta] \times [-1, 1]$. We can see in Fig. 4 that there exists a plane of mirror symmetry about $y = \pm\pi/(2\beta)$ for all these flows: $S_3(S_1[u, v, w](x, \pi/(2\beta) + d, z)) = S_3[u, -v, w](x + \pi/\alpha, -\pi/(2\beta) - d, z) = [u, -v, w](x + 2\pi/\alpha, \pi/(2\beta) - d, z) = [u, -v, w](x, \pi/(2\beta) - d, z)$ and $S_1(S_3[u, v, w](x, -\pi/(2\beta) + d, z)) = S_1[u, v, w](x + \pi/\alpha, \pi/(2\beta) + d, z) = [u, -v, w](x + 2\pi/\alpha, -\pi/(2\beta) - d, z) = [u, -v, w](x, -\pi/(2\beta) - d, z)$. High speed streaks corresponding to the ridges of the isosurface of

$u = 120$ are located near the boundary at $z = -1$ for \mathbf{u}^{EQ+} , \mathbf{u}^{EQ-} . Consistent with the symmetry S_2 , high speed streaks are also located near the boundary at $z = 1$, but these are not plotted for clarity. It can be seen that the streaks vary in a varicose way in the streamwise direction for \mathbf{u}^{EQ+} . In contrast, for \mathbf{u}^{EQ-} , the streaks comprise straight sections parallel to the streamwise direction separated by wide, flat varicose bulges. We can see strong streamwise vortices situated near the boundaries at $z = \pm 1$ for \mathbf{u}^{EQ+} , whereas they are located near the center $z = 0$ for \mathbf{u}^{EQ-} . For the \mathbf{u}^{TW+} flow, it can be seen that both high speed streaks and strong streamwise vortices are located in a neighborhood of the bottom boundary $z = -1$. Such high speed streaks and strong streamwise vortices are also found near the upper boundary $z = 1$ for \mathbf{u}^{TW-} , consistent with the symmetry S_2 , but are not presented in the figure.

4 Conclusion

Mirror symmetric travelling wave solutions in plane Couette flow are found. They bifurcate from the so-called (stationary) hairpin vortex state. The new travelling wave solutions are characterized by the asymmetric, rather than antisymmetric, mean flow profile. Furthermore, the quasi-streamwise vortices are located more close to the walls than in the hairpin vortex state.

References

1. Gibson, J.F., Halcrow, J., Cvitanović, P.: Equilibrium and travelling-wave solutions of plane Couette flow. *J. Fluid Mech.* 639, 243–266 (2009)
2. Itano, T., Generalis, S.C.: Hairpin Vortex Solution in Planar Couette Flow: A Tapestry of Knotted Vortices. *Phys. Rev. Lett.* 102, 114501–1–4 (2009)
3. Nagata, M.: Three-dimensional finite amplitude solutions in plane Couette flow: bifurcation from infinity. *J. Fluid Mech.* 217, 519–527 (1990)
4. Nagata, M.: Three-dimensional traveling-wave solutions in plane Couette flow. *Phys. Rev. E* 55, 2023–2025 (1997)
5. Schmiegel, A.: Transition to turbulence in linearly stable shear flows. Ph.D.thesis, Philipps-Universität Marburg, Marburg, Germany (1999)
6. Viswanath, D.: Recurrent motions within plane Couette turbulence. *J. Fluid Mech.* 580, 339–358 (2007)
7. Faisst, H., Eckhardt, B.: Traveling Waves in Pipe Flow. *Phys. Rev. Lett.* 91, 224502–1–4 (2003)
8. Wedin, H., Kerswell, R.R.: Exact coherent structures in pipe flow: travelling wave solutions. *J. Fluid Mech.* 508, 333–371 (2004)
9. Waleffe, F.: Three-dimensional Coherent States in Plane Shear Flows. *Phys. Rev. Lett.* 81, 4140–4143 (1998)
10. Deguchi, K., Nagata, M.: Bifurcations and instabilities in sliding Couette flow. *J. Fluid Mech* (2011) (in press)

Travelling Wave Solutions in Square Duct Flow

Shinya Okino, Masato Nagata, Håkan Wedin, and Alessandro Bottaro

Abstract. Three nonlinear travelling wave solutions for square duct flow are discovered. One of them, the asymmetric solution, which is predicted by the stability analysis, bifurcates from the mirror-symmetric solution found by Okino *et al.*, *J. Fluid Mech.* **657**, 413 (2010). The solution is characterized by asymmetric cross-sectional flow patterns with streamwise vortices attached to one of the side walls. The other two solutions, which have rotational symmetry by π and $\pi/2$, respectively, are found by a homotopy approach using artificially arranged body forces. Each of the new solutions shows striking similarity to that of pipe flow.

1 Introduction

Incompressible viscous flow through a straight duct with a square cross section driven by a constant pressure gradient is believed to be linearly stable as in the case of pipe flow. Therefore, there exists no solution which bifurcates from the laminar state and the transition to turbulence is abruptly caused by a finite amplitude disturbance. The turbulent state for these flows is considered to be represented by the trajectory in the phase space wandering around unstable nonlinear solutions, which are disconnected to the laminar state. Hence, identifying the nonlinear solutions is important to understand the turbulent dynamics and the laminar-turbulent transition. In pipe flow a number of nonlinear solutions have been computed (e.g. [2], [4], [5], [10]). In contrast, only three nonlinear solutions have been reported so far in square duct flow [3], [8], [11]. The nonlinear travelling waves in [8] and [11] are obtained

Shinya Okino · Masato Nagata

Department of Aeronautics and Astronautics, Graduate School of Engineering,
Kyoto University, Kyoto 606-8501, Japan

e-mail: okino@nowake.kuaero.kyoto-u.ac.jp

Håkan Wedin · Alessandro Bottaro

Dipartimento di Ingegneria, delle Costruzioni, dell'Ambiente e del Territorio,
University of Genova, Via Montallegro 1, 16145 Genoa, Italy

by an approach based on the self-sustaining process. In [3], a nonlinear analysis of internally heated square duct flow was performed by extending the linear stability analysis of [6], whereby the isothermal solution is obtained by the continuation approach in the parameter space.

2 Configuration

We take the Cartesian coordinates (x_*, y_*, z_*) with the origin at the centre of the duct, where the x_* -axis is directed along the duct and the y_* and z_* -axis are parallel to the sides of the square cross section. A constant pressure gradient is applied along the duct. The motion of the fluid in the duct is governed by the continuity equation, the Navier-Stokes equation and the no-slip boundary condition. The governing equations are nondimensionalized by the length scale b_* , the time scale b_*^2/ν_* and the velocity scale ν_*/b_* , where b_* is half the side of the duct and ν_* is the kinematic viscosity of the fluid. The flow is characterized by the Reynolds number, $Re = U_{c*}b_*/\nu_*$, where U_{c*} is the centreline velocity of the laminar flow. The centreline velocity has a proportionality with the pressure gradient. The subscript $*$ denotes dimensional variables. The periodicity $2\pi/\alpha$ in the x -direction with the wavenumber α is imposed. We assume a travelling wave as a nonlinear solution: the velocity $\mathbf{u} = (u, v, w)$ is represented by $\mathbf{u}(x - ct, y, z)$, where c is the phase velocity.

3 Asymmetric Solution

The travelling wave found in [3], which we refer to as ONWB hereafter, is invariant under the following transformations: the shift-and-reflection, $\mathbf{S}: (u, v, w)(\xi, y, z) \rightarrow (u, -v, w)(\xi + \pi/\alpha, -y, z)$, and the mirror-reflection, $\mathbf{Z}: (u, v, w)(\xi, y, z) \rightarrow (u, v, -w)(\xi, y, -z)$, where $\xi = x - ct$. Investigating the linear stability of ONWB, we have obtained a neutral point with respect to perturbations which break the \mathbf{Z} symmetry and retain the \mathbf{S} symmetry. Using the eigenfunction at the neutral points as an initial guess of the Newton-Raphson method, we obtain a solution, which bifurcates from ONWB with $\alpha = 1.14$. The skin friction for this solution is plotted against the bulk Reynolds number indicated by the dashed curve in Fig. 1. The bulk Reynolds number, $Re_b = U_{b*}b_*/\nu_*$ (U_{b*} is the mean axial velocity), is a measure of the nonlinearity. The skin friction λ is defined by $\lambda = 4\chi/Re_b^2$, where χ is the nondimensional pressure drop in the streamwise direction. The solid curve in Fig. 1 indicates ONWB with $\alpha = 1.14$. The asymmetric solution, which only retains the \mathbf{S} symmetry, bifurcates subcritically from the lower branch of ONWB at $Re_b = 468$, undergoes two turning points, and terminates on the upper branch of ONWB at $Re_b = 490$. The instantaneous disturbance of the asymmetric flow solution is shown in Fig. 2. The mirror-symmetry with respect to $z = 0$ of ONWB is broken and strong disturbances, which are composed of a pair of quasi-streamwise vortices and a low-speed streak, are observed near the side wall $z = +1$. The flow, which has the same structure near the opposite wall $z = -1$, is also a solution by the symmetry of the system.

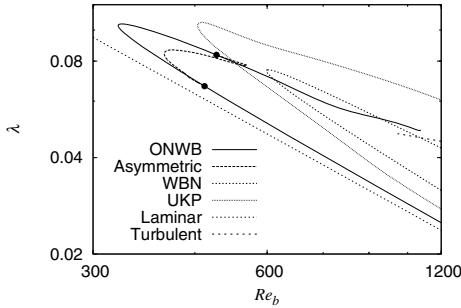


Fig. 1 The skin friction λ against the bulk Reynolds number Re_b . The solutions found by Wedin *et al.* [11] and Uhlmann *et al.* [8] are referred to as WBN and UKP, respectively. The bifurcation points of the asymmetric solution are indicated by closed circles.

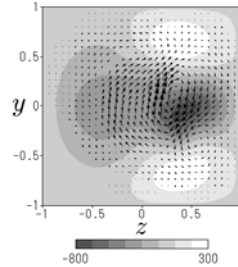


Fig. 2 The instantaneous disturbance velocity field of the asymmetric solution with $\alpha = 0.7$ at $Re = 3000$ ($Re_b = 1342$). The velocities on the cross-section and along the duct axis are indicated by arrows and grey scale, respectively.

4 Rotation-Symmetric Solutions

In order to obtain other nonlinear solutions, we follow a homotopy approach, which is developed by [9]. We introduce an artificial body force to the fluid, which can generate streamwise vortices. A linear critical point of the system, which is associated with the real eigenmode, is calculated and we find the solution, which bifurcates subcritically from the neutral point. We, then, reduce the strength of the forcing to zero to obtain a nonlinear solution to square duct flow. We apply the shift-and-reflect symmetry \mathbf{S} and the rotation symmetry, $\mathbf{R}: (u, v, w)(\xi, y, z) \rightarrow (u, -v, -w)(\xi, -y, -z)$, to the solutions. The instantaneous disturbances of two solutions obtained by this approach are plotted in Fig. 3. The solution shown in the left (right) frame has the rotational symmetry by π ($\pi/2$).

5 Concluding Remarks

In addition to the three new nonlinear travelling waves in a square duct described in this paper, all the travelling waves, which have been reported so far, are listed in Table I. Surprisingly, we have found that each of them has its counterpart in circular pipe flow (for example, compare Fig. 2 to the top-left frame of figure 1 in [4]). The similarity between square duct flow and pipe flow implies that these two pressure driven flows become turbulent through a common mechanism despite the difference between their cross-sectional geometries. The presence of the corners of a square does not seem to play a crucial roll in transition to turbulence.

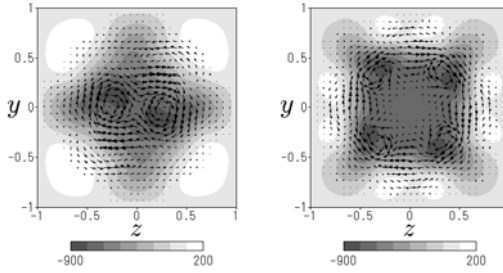


Fig. 3 Same as figure 3 for the rotationally symmetric solutions. (Left) π -rotation-symmetric solution at $Re = 2507$ with $\alpha = 1.10$. (Right) $\pi/2$ -rotation-symmetric solution at $Re = 3064$ with $\alpha = 3.20$.

Table 1 Travelling wave solutions in square duct flow

Solution	Symmetry	$\min Re_b(Re, \alpha)$	$\min Re(\alpha)$	pipe*
WBN [11]	Z, S	598 ($Re = 1968, \alpha = 0.85$)	1952 ($\alpha = 0.87$)	N1
UKP [8]	R, S	455 ($Re = 1579, \alpha = 0.90$)	1535 ($\alpha = 0.88$)	N2
ONWB [3]	Z, S	332 ($Re = 836, \alpha = 1.14$)	828 ($\alpha = 1.13$)	M1
Asymmetric	S	365 ($Re = 952, \alpha = 1.38$)	924 ($\alpha = 1.36$)	S1
π -rotation	R, S	498 ($Re = 1627, \alpha = 1.10$)	1607 ($\alpha = 1.08$)	S2
$\pi/2$ -rotation	R, S	1011 ($Re = 2726, \alpha = 3.20$)	2714 ($\alpha = 3.12$)	S4

* This column shows the counterpart in circular pipe flow. The nomenclature is based on [5].

References

- Biau, D., Bottaro, A.: *Phil. Trans. Roy. Soc. A* 367, 529 (2009)
- Faisst, H., Eckhardt, B.: *Phys. Rev. Lett.* 91, 224502 (2003)
- Okino, S., Nagata, M., Wedin, H., Bottaro, A.: *J. Fluid Mech.* 657, 413 (2009)
- Pringle, C.C.T., Kerswell, R.R.: *Phys. Rev. Lett.* 99, 074502 (2007)
- Pringle, C.C.T., Duguet, Y., Kerswell, R.R.: *Phil. Trans. Roy. Soc. A* 367, 457 (2009)
- Uhlmann, M., Nagata, M.: *J. Fluid Mech.* 551, 387 (2006)
- Uhlmann, M., Pinelli, A., Kawahara, G., Sekimoto, A.: *J. Fluid Mech.* 588, 153 (2007)
- Uhlmann, M., Kawahara, G., Pinelli, A.: *Phys. Fluids* 22, 084102 (2010)
- Waleffe, F.: *Phys. Rev. Lett.* 81, 4140 (1998)
- Wedin, H., Kerswell, R.R.: *J. Fluid Mech.* 508, 333 (2004)
- Wedin, H., Bottaro, A., Nagata, M.: *Phys. Rev. E* 79, 065305 (2009)

Main Instabilities of Coaxial Jets

A. Segalini and A. Talamelli

Abstract. An experimental analysis of the dominant instabilities in the initial merging region of two coaxial jets is presented. Different inner/outer jet velocity pairs (U_i, U_o) have been tested in order to investigate the effect of both velocity ratio $r_u = U_o/U_i$ and Reynolds number in the instability characteristics. Three main instabilities have emerged depending on the velocity ratio. For $r_u < 0.75$ the coaxial jets dynamic is driven by the inner shear layer. For $r_u > 1.6$ the outer shear layer dominates the near field vortex dynamics, while for velocity ratios nearly unitary the vortex shedding behind the separating wall imposes its own dynamics.

1 Introduction

Two coaxial jets which interact and mix belong to the class of flows which are of great interest from both the research and industrial point of view. Even though they have a simple geometry, the relevant flow field depends on many different parameters which, if they can be easily changed, make coaxial jets suitable for studies of different phenomena related to stability, mixing and turbulence.

The definition of the variables capable to effectively control the flow dynamics has high applicative potential because coaxial jets can be considered a prototype of many industrial burners. On the other hand, they are simple enough to be

A. Segalini

Dept. of Mechanical and Aerospace Engineering (DIEM), University of Bologna,
47100 Forlì, Italy

and

Linné FLOW Centre, KTH Mechanics, Royal Institute of Technology,
SE-100 44 Stockholm, Sweden

e-mail: antonio.segalini@unibo.it

A. Talamelli

Dept. of Mechanical and Aerospace Engineering (DIEM), University of Bologna,
47100 Forlì, Italy

e-mail: alessandro.talamelli@unibo.it

experimentally characterized in laboratory. However, due to the high number of parameters which in principle affect the flow evolution, a complete characterization of such flow is still missing and, therefore, motivates this research. Here an experimental analysis of the dominant instabilities in the near field of two coaxial jets has been performed in order to determine the leading processes which start the transition from the initial laminar state, where the two streams are segregated, to the final turbulent state.

Many experimentalists investigated the flow behavior for low velocity ratio $r_u \ll 1$ [1] and for high velocity ratio $r_u \gg 1$ [2, 3], where here the velocity ratio is defined as $r_u = U_o/U_i$, and U_i and U_o are the inner and outer jet velocity, respectively. While for low velocity ratios the inner and outer shear layers seem to have only a weak interaction, for high velocity ratios a clear coupling takes place. For this reason, several control strategies have been focused solely on the control of the outer layer for high r_u (see for instance [4]).

Buresti *et al.* [5] studied the flow field produced by a coaxial jet for nearly unitary velocity ratios. In particular, they found that a resonant phenomenon, producing a significant vortex shedding from the separating wall, was clearly observable in the near exit region. In the same paper, they proposed a scaling relationship between the frequency of the vortex shedding f , the separating wall thickness t and the average velocity U_m , obtaining $St_t = ft/U_m \approx 0.24$.

More recently Talamelli & Gavarini [6] performed an inviscid stability analysis of coaxial jets flow, showing that an absolute instability is present, inside a certain range of velocity ratios with a weak dependence on the side boundary layers thickness, which is the responsible for the formation of the shedding.

The aim of the present paper is to provide further evidence about this shedding phenomenon and its dependence on the operating parameters. This analysis is of course fundamental where a design of a new passive flow control strategy is required.

All the experiments have been carried out in the *Coaxial Air Tunnel* (CAT) facility in the laboratory of the *Second Faculty of Engineering* at the *University of Bologna* in Forlì by means of hot-wire anemometry and flow visualizations (see [7] for details of the experimental set-up as well as the measurement technique).

2 Results

Different inner/outer jet velocity pairs (U_i, U_o) have been tested in order to investigate the effect of both velocity ratio r_u and Reynolds number. For all the measurements an X-wire probe has been placed at $x/D_i = 0.5$ in the wake of the separation wall in order to describe the instabilities of the inner shear layer. More than 1700 combinations of inner/outer jet velocity have been tested and from each time-series, the power density spectra of the radial velocity has been calculated. The absolute maximum of each spectra has been associated to the dominant frequency related to the main instability present in the flow field.

Three instability characters have emerged depending on the velocity ratio as can be appreciated from figure 1, where isocontours of the dominant frequencies have been plotted together with the intensity of the rms of the radial velocity v scaled with the outer jet velocity. For $r_u < 0.75$, the coaxial jet dynamics is driven by the inner shear layer instability, in agreement with Ko & Kwan [1]. For $r_u > 1.6$, the outer shear layer dominates the near field vortex dynamics [2, 8] while, for r_u nearly unitary (namely $0.75 < r_u < 1.6$), the vortex shedding behind the separating wall imposes its own dynamic [5] and the radial velocity fluctuations have a local maximum.

Figure 2a shows the frequencies scaled with the average velocity and the wall thickness [5]. Although they are around the value 0.24, much scatter is present showing a Reynolds number as well as a velocity ratio effect. An improved scaling relationship for the Strouhal number St_x is therefore proposed in order to calculate the shedding frequency inside the intermediate velocity ratio region. This relationship takes into account Reynolds number effects by considering the δ_{99} thickness of the

Fig. 1 Variation of the preferred frequency with the inner/outer jet velocity. The two solid thick lines are composed by velocity pairs with $r_u = 0.75$ and $r_u = 1.6$. Filled contour is the scaled radial velocity standard deviation at the control point v'/U_0 .

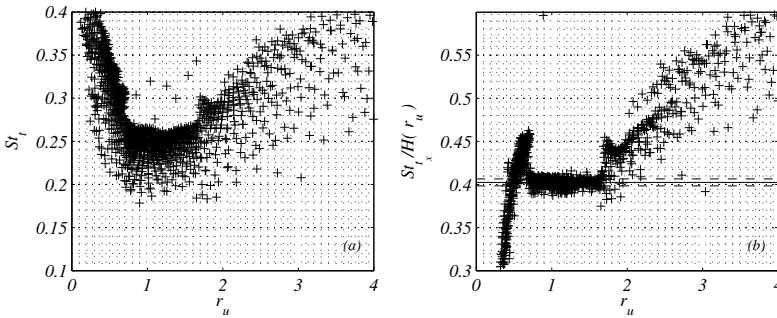
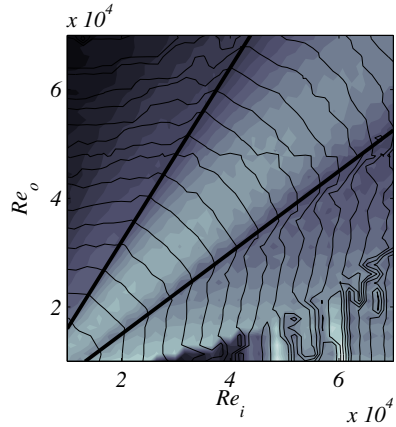


Fig. 2 Strouhal number scaling in the intermediate region. (a) Classical scaling $St_t = \frac{ft}{U_m} \approx 0.24$ (b) Proposed scaling $\frac{St_{tx}}{H(r_u)} = \frac{ft_x}{U_m H(r_u)} \approx 0.4$

side boundary layers, defining a new characteristic thickness $t_x = t + \delta_{1,99} + \delta_{2,99}$. Also velocity ratio effects have been empirically corrected with a simple quadratic function $H(r_u)$ [7] which leads to a constant Strouhal number value $St_{t_x}/H(r_u) \approx 0.4$ observable in the whole region where vortex shedding is present, as showed in figure 2b.

3 Conclusions

In the present paper an experimental analysis has been performed in order to study the intermediate velocity ratio region of coaxial jets and to provide further evidences to the theoretical results of Talamelli & Gavarini [6], who proposed that the wake behind the separation wall between the two streams of two coaxial jets creates the conditions for the onset of an absolute instability.

The characterization of this operating region is of utmost importance because the vortex shedding provides a continuous forcing mechanism which in principle may control the near flow field without introducing any external energy contribution like in conventional strategies which typically use active methods focused to control the outer shear layer dynamics [8].

Finally, these results may provide some improvements in the design of industrial apparatus, where coaxial jets are employed, simply by means of a proper choice of their exit geometry.

Acknowledgements. We wish to thank Prof. Guido Buresti for giving us the possibility to use the experimental set-up. Italian MIUR is acknowledged for the financial support. This work has been partly supported by STINT through a collaboration between KTH and University of Bologna.

References

1. Ko, N.W.M., Kwan, A.S.H.: The initial region of subsonic coaxial jets. *J. Fluid Mech.* 73, 305–332 (1976)
2. Dahm, W.J.A., Frieler, C.E., Tryggvason, G.: Vortex structure and dynamics in the near field of coaxial jet. *J. Fluid Mech.* 241, 371–402 (1992)
3. da Silva, C.B., Balarac, G., Métais, O.: Transition in high velocity ratio coaxial jets analysed from direct numerical simulations. *J. Turbulence* 4, 1–18 (2003)
4. Angele, K.P., Kurimoto, N., Suzuki, Y., Kasagi, N.: Evolution of the streamwise vortices in a coaxial jet controlled with micro flap-actuators. *J. Turbulence* 6, 1–19 (2006)
5. Buresti, G., Talamelli, A., Petagna, P.: Experimental characterization of the velocity field of a coaxial jet configuration. *Exp. Thermal Fluid Sci.* 9, 135–146 (1994)
6. Talamelli, A., Gavarini, I.: Linear instability characteristics of incompressible coaxial jets. *Flow Turbulence Combust.* 76, 221–240 (2006)
7. Segalini, A.: Experimental analysis of coaxial jets: instability, flow and mixing characterization. Ph.D. Thesis at the University of Bologna (2010)
8. Wicker, R.B., Eaton, J.K.: Near field of a coaxial jet with and without axial excitation. *AIAA J.* 32, 542–546 (1994)

Set-Up of Anisotropy in a Spanwise Rotating Channel

S. Tardu and J. Baerenzung

Abstract. Development of anisotropy in a spanwise rotating channel is analyzed in time and space through direct numerical simulations. The aim is to understand how the anisotropy sets-up both in time and space in a supercritical flow, the role of rotation being rather generic in this particular context. Several techniques to quantify anisotropy are used such as the trajectories in time and space of the Lumley invariants, the dissipation tensor invariants and local anisotropy characterization in the spectral domain. It is shown that large excursions within the Lumley triangle occur near the centerline, and the local perturbation hesitates for long time between a one component to a nearly isotropic state. The wall damps these excursions; the local turbulence structure changes only slightly near the wall and it remains basically axisymmetric.

1 Introduction

Investigating the response of forced wall turbulence is difficult because, it is generally hard to identify a turbulent structure, isolate it from its rush environment and track it in time and space. Furthermore, the interaction of the given structure with its incoherent surrounding renders the analysis delicate. The strategy to resolve this problem, at least partially, is to proceed by a by-pass like method, i.e. to inject an individual structure in a supercritical flow and determine its development in time and space, until it leads to a fully developed turbulence. That is the methodology adopted here with the main aim to study how a structure with given initial anisotropy characteristics respond to the structural changes and how the anisotropy develops in time and space. A supercritical spanwise rotating channel flow is chosen as the generic case for this purpose. Different methods to identify the anisotropy both in physical and spectral domains are subsequently used and analyzed.

S. Tardu · J. Baerenzung

Laboratoire des Écoulements Géophysiques et Industriels (LEGI), B.P. 53 X, 38041, Grenoble, Cedex, France

e-mail: sedat.tardu@hmg.inpg.fr

2 Base Flow Configuration and Results

A local perturbation in the form of a quasi-streamwise pair of vortices is followed in time and space, in a way quite similar to the investigations dealing with by-pass transition [2]. The perturbation takes rapidly the form of a local turbulent spot as it is seen in Fig.1 for Rossby and Reynolds numbers that are respectively $Ro = \frac{U_c}{2\Omega h}$, $Re = \frac{U_c h}{\nu}$ and (here Ω is the angular rotation velocity, U_c is the centerline velocity, h is the channel half width and ν is the viscosity). Hereafter, the flow quantities are scaled by h and U_c . Direct numerical simulations are used for this purpose. The computational domain extends to $16\pi h \times 2\pi h \times 8\pi h$ in the streamwise, wall normal and spanwise directions and the number of computational modes are respectively $256 \times 128 \times 256$. Stretched coordinates are used in the wall normal direction. The critical Reynolds number under these circumstances is $Re_c = 150$ according to [1] and the flow is supercritical here. The perturbation becomes a developed turbulent spot before it leaves the computational domain. For this reason, the rotation is rather generic in this investigation allowing the time tracking of the local spot from its early until its developed stages. A similar analysis in the canonical channel flow without rotation would require a much longer computational domain and/or a stronger initial perturbation. We could determine the frontiers of the developing perturbation simply by sweeping the instantaneous vorticity field through a threshold method, in the homogeneous y planes (x, y and z are respectively the longitudinal, wall normal and spanwise directions, with u, v and w being the corresponding fluctuating velocity components-in the indicial notations we use x_i and u_i where $i = 1, 2$ and 3 correspond in order to x, y and z , idem for the velocity field). The flow indeed becomes fully developed turbulent as early as at $t = 240$ as it is seen in Fig. 2 that shows the distribution of the longitudinal $u' = \sqrt{\overline{u'u}}$, wall normal $v' = \sqrt{\overline{v'v}}$ and spanwise $w' = \sqrt{\overline{w'w}}$ turbulent intensity scaled by the arithmetic mean of the pressure-suction sides wall shear stress. The classical reaction of the wall turbulence under spanwise rotation is observed in Fig. 2, with the wall activity increasing at the pressure side.

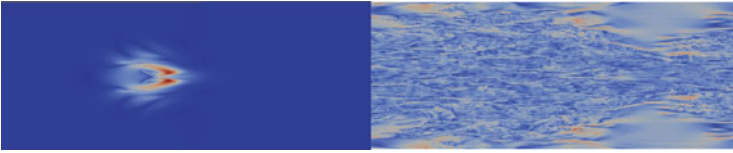
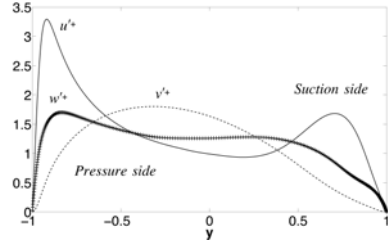


Fig. 1 Time-space evolution of the localized perturbation at $Ro = 6$ and $Re = 1500$ at $t = 20$ (left) and $t = 110$ (right) in terms of instantaneous turbulence kinetic energy contours.

Fig. 3 shows the time variations of the invariants II and III of the shear stress tensor at respectively the channel centerline $y = 0$ and $y = -0.95$ near the wall at (the lower wall is at $y = -1$). The shear stress tensor is defined as usual by

$$b_{ij} = \frac{\overline{u_i u_j}}{\overline{u_k u_k}} - \frac{1}{3} \delta_{ij} \quad (1)$$

Fig. 2 Turbulent intensity profiles at $t = 240$ in the fully developed turbulent spanwise rotating channel flow ($Ro = 6$ and $Re = 1500$).



where u_i is the fluctuating velocity component and δ_{ij} is the Kronecker symbol [4]. The trajectories in the Lumley chart have been followed in time in the homogeneous planes. It was noticed that near the centerline, the local perturbation hesitates for a while between a 2 component and a rod-like axisymmetric structural form along which it finally continues its journey before reaching an equilibrium state. The transformation from one component to a nearly isotropic state takes time in this region. This behavior is common in the part of the flow that would correspond to the external layer in a fully developed turbulent rotating channel flow. Large excursions within the Lumley triangle also occur in the intermediate zone $-0.8 \leq y \leq -0.5$ with turnovers upon 2 component to rod-like structures. Beginning from $y = -0.8$, i.e. in the inner layer in return, there is no such *hesitation*, and the excursions take place along 2 component to one component axisymmetric line. The time oscillations of the invariants seen in Fig. 3 and 4 are strongly non linear near the centerline, while there is a clear effect of damping near the wall. A closer look to the data revealed that the temporal response of the shear stress tensor invariants could be modeled as a Duffing non-linear oscillator with damping increasing towards the wall (not shown here). The response of the dissipation tensor invariants is qualitatively similar, yet there are quantitative differences in their temporal variations compared with the shear stress invariants.

The local isotropy of high and low frequency structures has been determined by computing the modulus of Fourier transforms of local shear stresses in the homogeneous planes and by determining the invariants of the related normalized tensor in a way much similar to [3]. In this short paper we cannot go into the detailed

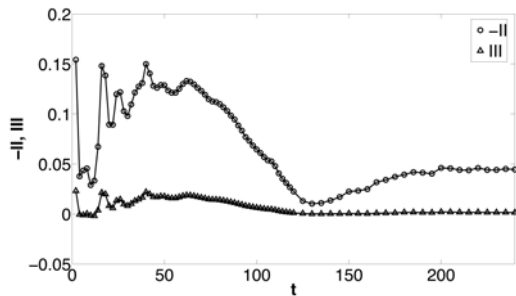
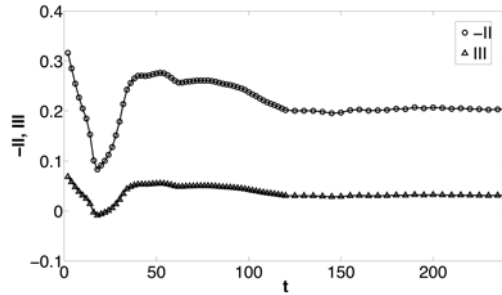


Fig. 3 Temporal evolution of the second and third invariants of shear stress tensor at the centerline

Fig. 4 Temporal evolution of the second and third invariants of shear stress tensor near the wall at $y = -0.95$



results that will subsequently be published elsewhere. Let us indicate here that the invariants deduced from this specific tensor revealed to be highly intermittent, and appeared clearly as granular. The small-scale singularities observed in the invariants diluted rapidly in space as the time was increased, but the high intermittency and the granular geometry persisted even at large development times.

3 Conclusions

The development of a local perturbation is analyzed in a subcritical spanwise rotating channel flow, with the aim to determine how the anisotropy involves in time and space. The time-space tracking of invariants of the shear stress and dissipation tensors shows that the local disturbance hardly reaches its isotropic state near the centreline. The time response of the shear stress invariants is strongly non linear in the outer layer. The trajectories of the invariants within the Lumley triangle follow basically the axisymmetric line near the wall whose strong damping effect results in rather smooth temporal variations. The observed behaviours can be modelled through a non-linear Duffing oscillator whose damping coefficient increases progressively from the centreline to the wall.

References

1. Alfredsson, P.H., Persson, H.: Instabilities in channel flow with system rotation. *J. Fluid Mech.* 202, 543–557 (1989)
2. Henningson, D.S., Lundbladh, A., Johansson, A.V.: A mechanism for bypass transition from localized disturbances in wall-bounded shear flows. *J. Fluid Mech.* 250, 169–207 (1993)
3. Liu, K., Pletcher, R.H.: Anisotropy of a turbulent boundary layer. *Journal of Turbulence* 9-18, 1–18 (2008)
4. Simonsen, A.J., Krogstad, P.A.: Turbulent stress invariant. Clarification of existing terminology. *Phys. Fluids* 17, 88–103 (2005)

Streamwise and Radial Decomposition of a Turbulent Axisymmetric Jet

Maja Wänström, William K. George, and K.E. Meyer

Abstract. Planar PIV was used to acquire 10,000 independent samples of the far field of a free, turbulent round air jet flow of exit Reynolds number 20,000. The objective was to test the two-point similarity theory of Ewing et al. [1]. After applying the similarity mapping, two-point velocity correlation analysis showed independence of streamwise origin, confirming the hypothesized streamwise homogeneity in two-point similarity coordinates. The velocity data was subsequently spatially decomposed by applying Fourier transformation in the 'homogenized' streamwise direction and POD to obtain orthogonal basis functions in the radial direction.

1 Introduction

Ewing et al. [1] applied two-point equilibrium similarity theory to the two-point Reynolds stress equations of the far, fully developed turbulent region of a free, axisymmetric jet and deduced that the turbulence statistics should be independent of streamwise origin when scaled by the local mean centerline velocity, $U_c(x)$ and evaluated on the similarity coordinates system $\xi = \ln[(x - x_o)/D]$, $\eta = r/\delta_{1/2}$. Here x_o , r and $\delta_{1/2}(x)$ denote the virtual origin, radial coordinate and half-width of the jet respectively. The goal of this work was to confirm the deduced streamwise 'homogeneity' in the infinite domain ξ . Homogeneous fields of infinite extent are optimally represented by Fourier transforms. In the finite radial extent of the jet, the flow is inhomogeneous and must be represented by a set of empirical orthogonal basis functions, obtained by for example POD.

M. Wänström

Swedish Energy Agency, 531 04 Eskilstuna Sweden

e-mail: maja.wanstrom@gmail.com

W.K. George

U. Lille Nord de France, EC Lille, LML, F-59650 Villeneuve d Ascq, France

K. E. Meyer

Dept. Mech. Engr., Technical University of Denmark, DK-2800 Lyngby, DK

2 Experiment and Results

The experimental setup consisted of a jet flow issuing from a $D = 1\text{ cm}$ diameter nozzle into a large enclosure. Two HiSense 4Mpxl cameras were used to estimate the in-plane velocity components in a composite field-of-view that covered $30D \leq x \leq 100D$ and $|\eta| = |r/\delta_{1/2}| \leq 2$. The large streamwise extent of the field was chosen to minimize finite window effects in the streamwise spatial spectral analysis. The number of independent samples acquired was 10 000. Wänström [2] contains all relevant details. Figures 1(a) and 1(b) show the growth of the jet half-width and the decay of the mean centerline velocity relative to their common virtual origin, indicating that the flow is behaving like a free, far jet. For all downstream positions, the mean velocity profiles, scaled by the local centerline velocity and half-width, exhibit a considerable degree of collapse as shown in Figures 1(c) and 1(d).

Fig. 2 shows the velocity correlation coefficient tensor resulting from the two-point similarity mapping of Ewing et. al [1]. For each element of the tensor, the correlation coefficients have been evaluated from several non-overlapping

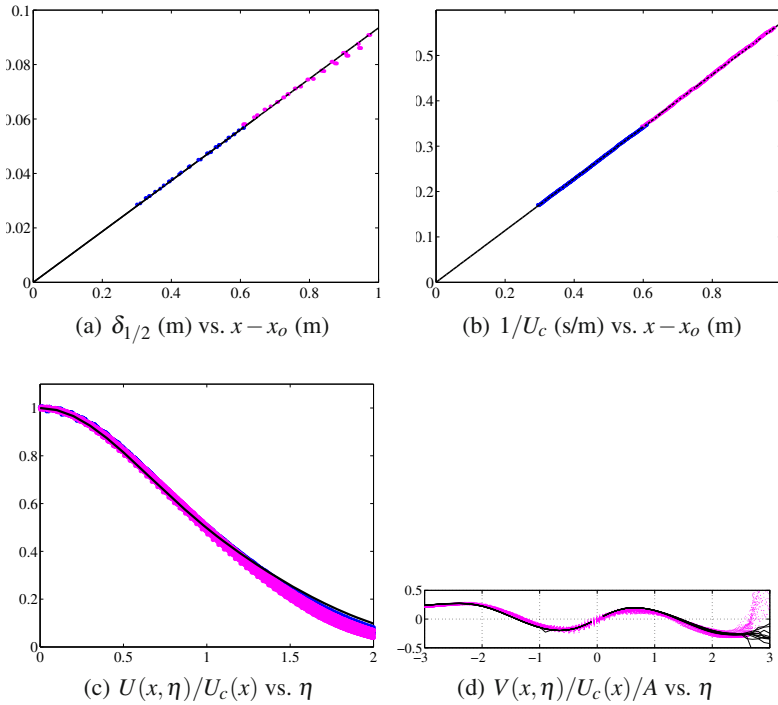


Fig. 1 Streamwise growth of the (a) local jet half-width, $\delta_{1/2}$ and (b) inverse of the mean centerline velocity, $1/U_c$. Mean velocity profiles in single-point similarity scaling; (c) streamwise component $U(x, \eta)/U_c(x)$ and (d) radial component $V(x, \eta)/U_c(x)/A$, where A is the growth rate of $\delta_{1/2}$.

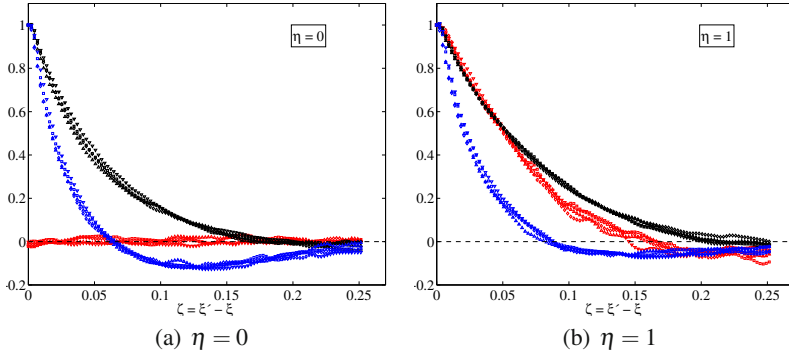


Fig. 2 Correlation coefficient tensor $C_{i,j}(\zeta, \eta, \eta')$ evaluated from several non-overlapping downstream positions for two radial locations. Black symbols correspond to $i = j = 1$, blue symbols $i = 2 = 2$ and red ones to $i = 1, j = 2$.

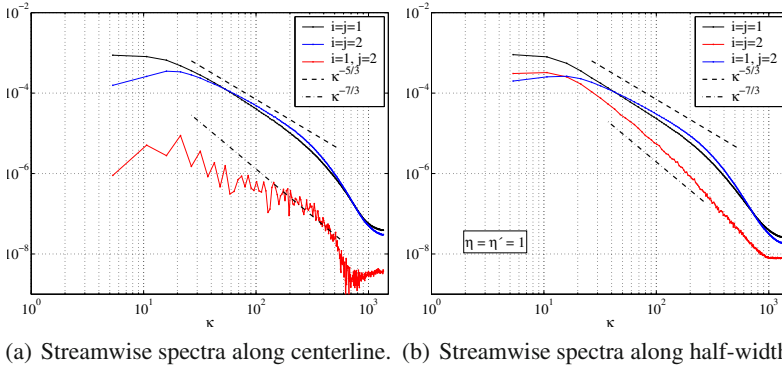


Fig. 3 One-dimensional spectral tensor $\Phi_{i,j}^1(\kappa)$ along the jet centerline. Black curves represent $i = j = 1$, blue $i = j = 2$ and red $i = 1, j = 2$. Dashed lines indicate slopes of $\kappa^{-5/3}$ and $\kappa^{-7/3}$.

downstream locations $\xi = \ln[(x - x_o)/D]$. The degree of collapse among the curves supports the theory that the two-point statistics depend only with the separation variable $\zeta = \xi' - \xi$, as hypothesized by Ewing et al. [1].

The mapped turbulence fields were decomposed by FFT in ξ . For each Fourier mode of wavenumber κ , a two-point cross-spectral tensor $\Phi_{i,j}(\kappa, \eta, \eta')$ was estimated. Sets of empirical radial basis functions were established by POD.

Fig. 3 shows true spatial cross-spectral estimates along the centerline and along the half-width $r = \delta_{1/2}$. The POD eigenvalue spectrum is shown in Fig. 4 for each POD-mode number and wavenumber. Fig. 5 shows the radial POD eigenvectors for POD mode numbers $1 \leq n \leq 12$ of the lowest non-zero wavenumber κ . The eigenvectors exhibit increasing frequency with increasing POD mode number.

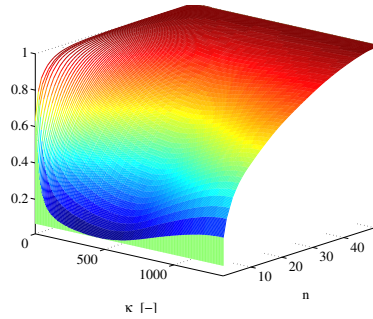


Fig. 4 Comparative distribution of the POD eigenvalue spectra represented by the partial sums of the POD eigenvalues normalized by the total spectral density available at each wavenumber κ .

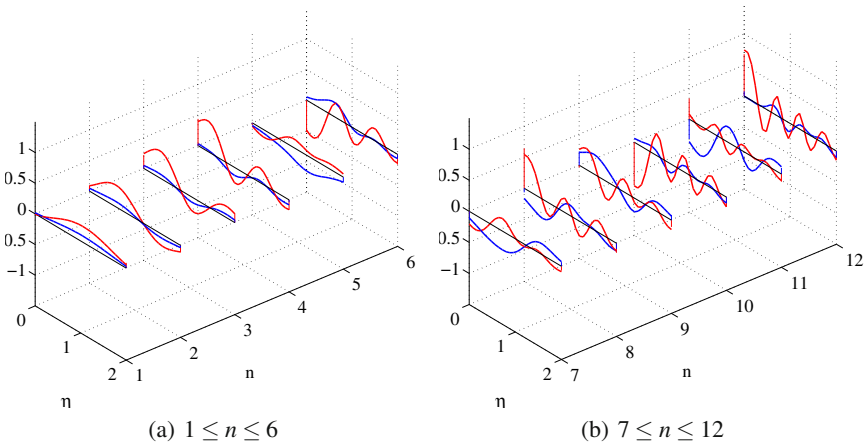


Fig. 5 Real parts of streamwise (red) and radial component (blue) of POD eigenvectors.

References

1. Ewing, D., Frohnappfel, B., George, W.K., Pedersen, J.M., Westerweel, J.: Two-point similarity in the round jet. *Journal of Fluid Mechanics* 557, 309–330 (2007)
2. Wänström, M.: Spatial Decompositions of a Fully Developed Turbulent Jet Sampled with Particle Image Velocimetry. Ph.D. diss., Chalmers U. of Tech., Gothenburg, Sweden (2009), <http://www.turbulence-online.com>

The Turbulent Flow in the Close-Up Region of Fractal Grids

Stefan Weitemeyer, Robert Stresing, Michael Hölling, and Joachim Peinke

Abstract. Turbulence generated by fractal square grids differs substantially from all other documented turbulent flows. Previous experiments indicated that the turbulence intensity reaches its maximum at a position proportional to the length and thickness of the largest bar in the grid [2]. The goal of this work was to investigate the evolution of the flow behind grids with different smallest scales. Hot wire measurements were conducted close to the grid in two different wind tunnels using three different fractal grids. It was found that the positions of the flatness peak and turbulence intensity peak change by altering the numbers of iterations and the blockage ratio respectively. Furthermore, it was shown that this result is invariant to the investigated different boundary conditions.

1 Introduction

The initial paper that dealt with turbulence generated by fractal grids was published as recently as 2007 [1]. The turbulent flow behind these grid is very different from all previously documented turbulent flows [1, 2, 3], it is even considered to define a new class of turbulence [4].

One of the characteristics of the highly turbulent and intermittent flow behind fractal grids is that both the turbulence intensity and flatness have their maximum well behind the grid. The exact positions of these maxima, however, depend on the choice of parameters for the grid design (e.g. length and thickness of bars) [1, 2]. In this work, results are presented from experiments that continue the work of [2] to find parameters that cause the position of the flatness peak and turbulence intensity peak to change. Subsequently, designing grids with selectable characteristics would be possible.

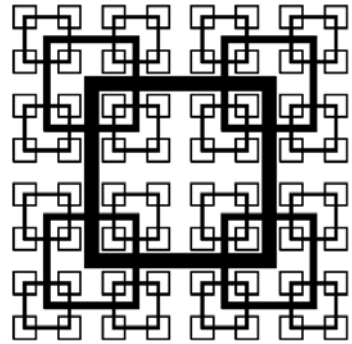
Stefan Weitemeyer · Robert Stresing · Michael Hölling · Joachim Peinke
ForWind - Institute of Physics, University of Oldenburg, D-26111 Oldenburg, Germany
e-mail: stefan.weitemeyer@uni-oldenburg.de

2 Fractal Grids and Experimental Setup

Experiments were conducted using three different space-filling fractal square grids. The basic layout of the N=4 grid and the design parameters are given in figure 1. The grids were water-jet cut from a 5 mm thick aluminum plate and have a size of about 25 x 25 cm².

Two ways were chosen to study the influence of the smallest scales in the grid. The first one was to alter the number of iterations by adding a fourth iteration to the N=3 grid, changing the thickness of the smallest bar from about 2 mm (N=3) to about 1 mm (N=4). The second way was to change the thickness of the bars in the N=3 grid, causing the blockage ratio σ to be different for the two grids. The thicknesses of the smallest bars are about 2 mm (N=3, $\sigma=20\%$) and about 2.5 mm (N=3, $\sigma=26\%$) respectively.

Fig. 1 Space-filling fractal square grid with N=4 iterations, $L_0 = 132\text{mm}$ and $t_0 = 8\text{mm}$, where L_i is the length and t_i is the thickness of the bars at iteration i ($i=0, \dots, N-1$). From iteration i to $i+1$, the length of the bars in all three grids changes by a factor of $R_L=0.5$ and the thickness changes by $R_t=0.49$. The blockage ratio σ for the N=4 grid is 26%.



The measurements were done in a closed-loop wind-tunnel which has a background turbulence intensity of less than 0.2%. A closed test section was put inside the normally open, 1.80 m long test section of the tunnel. Due to the experimental setup measurements were taken along the centerline up to a distance of about 1.20 m in steps of 5 cm. To investigate the effects of the missing walls, the closed test section was removed for a second experiment. By using string, the 25 x 25 cm² grids were centrally position in the 80 x 100 cm² outlet of the tunnel, resulting in a free flow around the grids.

The flow was studied by hot-wire anemometry using a Dantec 55P01 single wire. For each position four million data points were recorded with a sampling frequency of 60 kHz, corresponding to about 70 seconds of measurement.

3 Results

Hot-wire measurements were carried out with an incoming mean velocity of 5 m/s. The resulting data were analyzed using a statistical description approach. This work

focusses on the evolution of the turbulence intensity and the flatness behind the grids.

The development of the turbulence intensity in the closed wind tunnel behind all three grids is shown in figure 2 (left), with the turbulence intensity normalized to its respective peak value. It can be seen that the peak positions do not collapse. Changing the thickness of the bars and therefore altering the blockage ratio seems to have a smaller effect ($N=3$ grids with different σ), while reaching the same blockage ratio by adding another iteration significantly pushes the peak position further downstream. Hence, one can conclude that the position of the maximum turbulence intensity depends also on the thickness of the smallest bar in the grid.

Previous results suggested that the turbulence intensity peak position $x_{peak}^{(TI)}$ scales with the largest bar in the grid [2]

$$x_{peak}^{(TI)} \propto \frac{L_0^2}{t_0} =: x_* \quad . \quad (1)$$

Figure 2 (right) shows the turbulence intensity for our three grids over the normalized distance x/x_* . In addition, data from one of the grids used by [2] are plotted. Using the normalization by x_* (eq. 1) does not lead to the same peak position. Hence, the previous results by [2] have to be adjusted to take into account differences at the smallest scale of the grid. The current dataset is not sufficient, though, to give a reasonable adjustment.

Another important statistical parameter when looking at an intermittent flow is the flatness F as the fourth normalized central moment: $F = \frac{\langle u'^4 \rangle}{\sigma^4}$. Figure 3 (left) shows the flatness along the centerline for all three grids in the closed tunnel. The flow is strongly non-Gaussian ($F > 3$) for a large portion of the test section. A clear shift in the peak position is only observed for grids with different numbers of iterations. Comparing all the grids, one can conclude that the flatness value at the peak position depends on the thickness of the smallest bar in the grid.

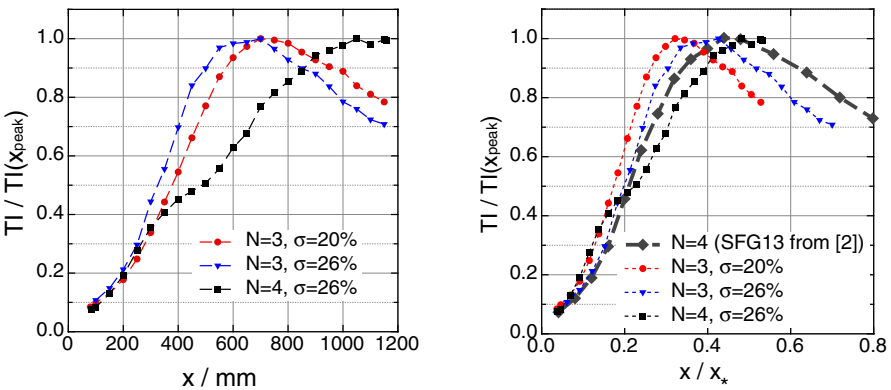


Fig. 2 Turbulence intensity evolution along centerline **Left:** for all three grids in closed tunnel, normalized to peak value **Right:** with distance normalized by x_*

To investigate the influence of the missing wall, the evolution of turbulence intensity $TI = \frac{\sigma_u}{\langle u \rangle}$ for the $N=3$, $\sigma=20\%$ grid is shown in figure 3 (right) both for the open and the closed tunnel. For both conditions, the turbulence intensity reaches its maximum value at almost the same distance from the grid (open 65 cm, closed 70 cm), whereupon the difference is within measurement tolerance. Similar results are achieved when looking at the $N=4$ grid or the skewness and flatness of the data. Thus, it was shown that the position of the maxima are independent of the two investigated boundary conditions.

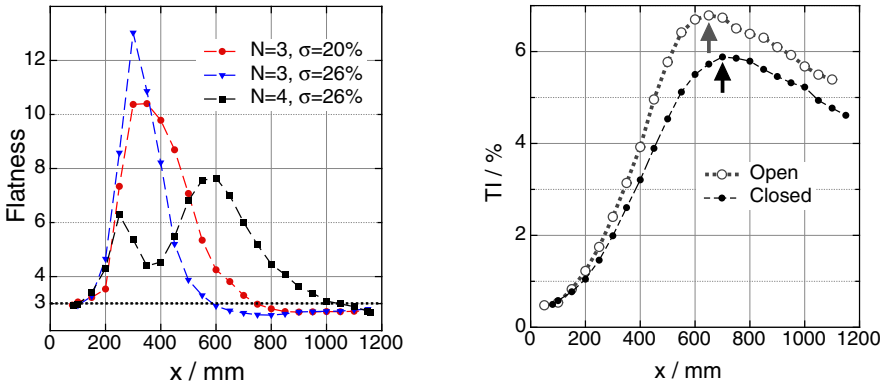


Fig. 3 Left: Flatness along centerline for all three grids in closed tunnel **Right:** Turbulence intensity along centerline for $N=3$ grid for open and closed tunnel

4 Conclusions

This work has shown that the evolution of the flow behind a fractal grid depends on the smallest scales in the grid as well. Further experiments with varying parameters are needed to investigate the influences of each parameter in more detail. Blocking parts of the grid might identify the crucial elements of the grid that cause the special characteristics of the flow.

References

1. Hurst, D., Vassilicos, J.C.: Scalings and decay of fractal-generated turbulence. *Phys. Fluids* 19, 035103 (2007)
2. Mazellier, N., Vassilicos, J.C.: Turbulence without Richardson-Kolmogorov cascade (2010), <http://arxiv.org/abs/0911.0841>
3. Seoud, R.E., Vassilicos, J.C.: Dissipation and decay of fractal-generated turbulence. *Phys. Fluids* 19, 105–108 (2007)
4. Stresing, R., Peinke, J., Seoud, R.E., Vassilicos, J.C.: Defining a new class of turbulent flows. *Phys. Rev. Lett.* 104, 194501 (2010)

Session 6

Atmospheric Boundary Layer

Statistical Characteristics of a 3×3 Neutrally Stratified Wind Turbine Array Boundary Layer

Raúl Bayoán Cal and Max Gibson

Abstract. The near- and far-wake characteristics of wind turbine arrays are studied using PIV data taken from wind tunnel experiments. Proper orthogonal decomposition (POD) is employed to gain information about the energetically coherent structures present in the flow. Specifically, the structures responsible for the entrainment of turbulent kinetic energy in the near- and far-wake are explored. Furthermore, the important POD modes are determined, not only in relation to remediation of the momentum deficit, but also in relation to the extraction and dissipation of kinetic energy by the turbine.

1 Introduction

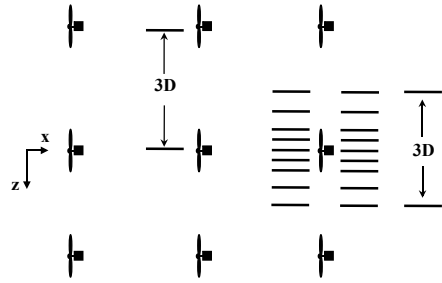
For wind energy to become a significant contributor to the global energy supply, more and larger wind turbine arrays must be brought to production. As wind farms grow in extent, they approach the so-called “fully developed wind-turbine array boundary layer”. In this regime the kinetic energy to be captured by the wind turbines must first be entrained from the flow above the wake. As recently shown using model wind tunnel experiments in Cal *et al.* (2010) and using Large Eddy Simulation as shown by Calaf *et al.* (2009), for very large wind turbine array boundary layers, the power extraction is dominated by vertical transport of kinetic energy rather than by horizontal differences between flux of kinetic energy in the mean flow.

2 Experiment

The experiment was conducted in the Corrsin Wind Tunnel at Johns Hopkins University, a return-type, two-story tunnel with two contractions. The test section is

Raúl Bayoán Cal · Max Gibson
Portland State University, Dept. of Mechanical and Materials Engineering,
Portland, OR, USA 97201
e-mail: cal@me.pdx.edu

Fig. 1 Top view schematic of the PIV plane density around the middle turbine of the last row



10 m long, 0.9 m high, and 1.2 m wide. Strakes and an active grid at the inlet are employed to generate a mean shear profile and significant free stream turbulence. Inside this test section, a platform was elevated 20.5 cm off the floor. A 3×3 array of lightly loaded model turbines of rotor diameter $D = 12$ cm and tower height $H = 12$ cm were placed 3 m from the front of the platform and immersed within turbulent boundary layers over a rough surface and an inflow velocity of 9.4 m/s. The turbulence intensity of the incoming flow was about 6% and the velocity gradient was The turbines were spaced $3D$ in the transverse direction and the spacing between rows was $7D$ in the streamwise direction. Further details about the turbines, their position, and the experimental setup is provided in Cal *et al.* (2010).

High spatial resolution velocity data were acquired using a TSI stereo-PIV system. A double pulsed, 120 mJ/pulse Nd:YAG laser is pulsed at a rate of 4 Hz, with a $100 \mu\text{s}$ gap between pulses. The thickness of the laser sheet is 1.2 mm. Two auto-correlation CCD cameras are used to capture the images. Eighteen interrogation areas of 16 cm^2 were placed around the middle turbine of the last row, as shown in figure 1. In the schematic, the downstream, wall-normal and span wise directions are represented by x , y and z variables, respectively. Nine planes in both the front and back of the model turbine were spaced 3 cm apart in the rotor area and 6 cm apart in the outer wake area, for a total of $3D$ spacing across all nine planes. In each interrogation plane, the PIV system was calibrated to ensure accuracy of at least 2% of the x and y velocity vectors. For the post-turbine planes, an optical sensor was used to phase lock the PIV image capture. Reflective tape mounted on the rear of the blades triggered the capture of 2000 images in 20° phase increments to ensure a phase independence in the post-plane measurements. Comparison of phase averaging showed no significant phase dependence in the data.

3 Analysis Method

Proper orthogonal decomposition, particularly snapshot POD is briefly described here as implemented by the authors. For a detailed exposition of the technique of classical POD, the reader is referred to Holmes, Lumley & Berkooz (1996) and Berkooz, Holmes & Lumley (1993), while Sirovich (1987) details the snapshot method.

The goal of POD is to seek a vector, ψ , that obtains a maximum normalized average squared correlation with the flow field. That is,

$$\psi : \max_{\psi \in L^2[0,1]} \frac{\langle |u, \psi|^2 \rangle}{\|\psi\|^2}, \quad (1)$$

This is an eigenvalue problem, with $\psi = \phi$ and ψ is contained in the set L . When determined from a covariance matrix, eigenvalues will give a quantification of the coherent turbulent kinetic energy contained in each eigenvector. Reordering the eigenvalues, and corresponding eigenvectors, such that $\lambda_{k+1} \leq \lambda_k$, allows a reduced order reconstruction of the flow.

POD is typically performed on zero mean velocity fields, though a POD of instantaneous velocity fields is possible; the first mode in this case will return the mean flow field. For a snapshot decomposition, the fluctuating velocity data are arranged in a matrix $V_{i,j}$, where each column of V represents a particular time measurement ("snapshot") of the flow field, and each row comprises the entire spatial domain.

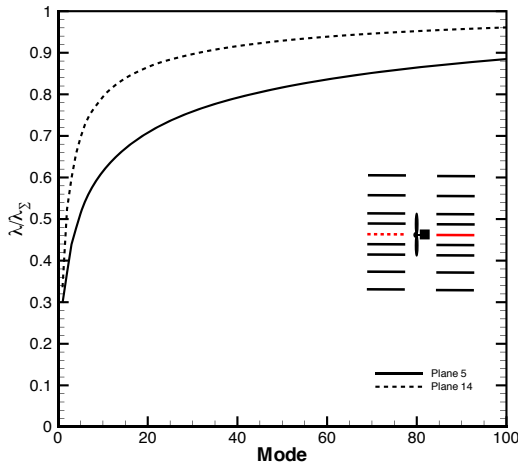
$$V_{i,j} = \{v_j\} \quad v = (v_{i,1}, v_{i,2}, \dots, v_{i,N})^T \quad (2)$$

$$j = 1 \dots M \quad i = 1 \dots N$$

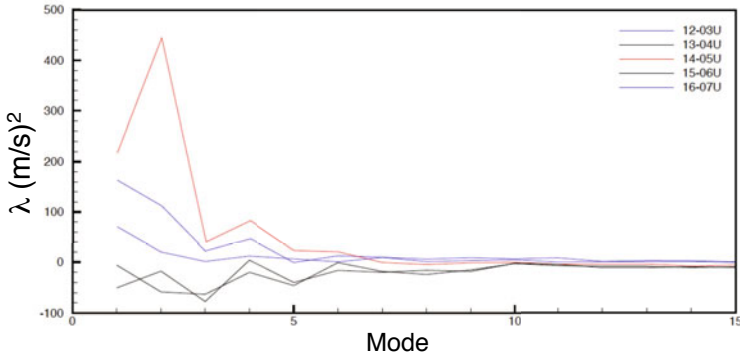
where M is the number of snapshots and N is the number of spatial locations. An important consideration for each j in $V_{i,j}$ is, as outlined by Sirovich (1987), the snapshots must be uncorrelated by choosing temporal spacing larger than the correlation time of the flow under consideration. v is the velocity snapshot containing all of the data points. In the present paper, every sample from the front planes were utilized in the decomposition (for a total of 2000 snapshots), while every seventh sample in the back planes was for the decomposition (for a total of 1715 snapshots). Averaging of the back plane subsample showed a difference of less than 0.1% from full sample average in the streamwise direction.

4 Results

Figure 2(a) shows the cumulative fractional energy content of each mode (up to 100) directly fore (plane 14) and aft (plane 5) of the rotor midplane ($z = 0$ m). The energy content of mode one is 34% and 30%, respectively. At 100 modes, plane 14 has accounted for 96% of its turbulent kinetic energy, while plane 5 has accounted for only 88%. While the convergence rate of the fore plane is slower than that found in other studies with a steadier inflow profile (eg. Saranyasontorn and Manuel [2006]), normalizing by the total number of modes shows this decomposition to be more efficient. Furthermore, the convergence rate of the aft plane, while lower than the inflow plane, is the same as that found in the Bernero and Fiedler (2000) application of POD to a jet in counterflow. An observed difference in slope of the two lines reveals plane 14 to have a higher energy accumulation rate in the lower modes, while plane 5 has a higher energy accumulation rate in the higher modes. The difference in energy recapture rate in this analysis indicates a reduction in the energetic



(a) Energy recapture rate for the front and back rotor midplane.



(b) The difference in energy across the turbine for all rotor planes. Only the streamwise direction is shown.

Fig. 2 Assessment of energy capture by the turbines in the different planes.

coherence of the flow, as energy is redistributed from the low-frequency, large-scale coherence found in the lower modes to the smaller-scale turbulent structures of the higher modes.

The low level of energetic coherence in most of the modes suggests a “difference” analysis to analyze the reduction in coherence as the flow passes through the turbine. Figure 2(b) reveals this difference, showing specifically the eigenvalue of the fore plane minus the eigenvalue of the corresponding aft plane for the first 15 modes. These have been denoted in the legend as the plane in front minus the plane in the back of the turbine. The center plane is denoted in red and the planes aligned with the tip of the rotor and in blue. Thus, for the center plane it is noted as 14-05 and subsequently for the other planes. Notice that the largest differences occur in the

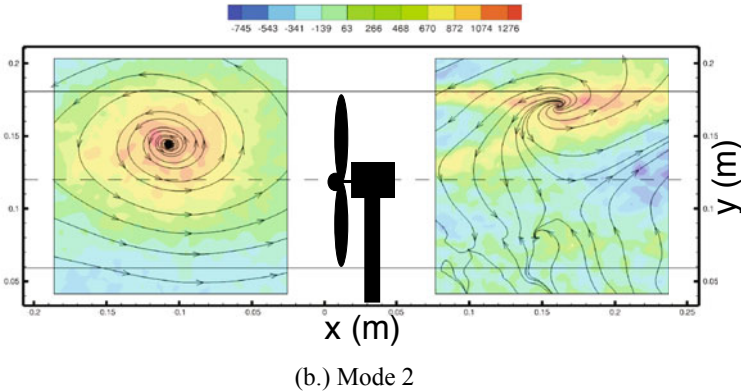
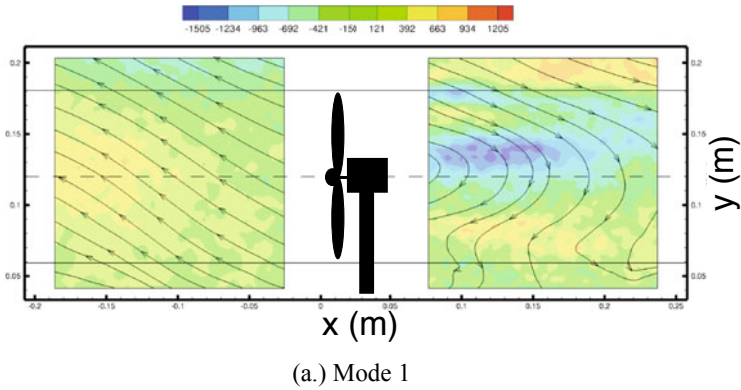


Fig. 3 Eigenflow streamlines and vorticity contours for modes 1 and 2. Units on contours intentionally removed, as values are relative only.

center plane (colored red) and the attention is brought to this particular curve. Most notable are the large spike in mode 2, a subsequent smaller spike in mode 4, and the negligible difference beyond mode 10. As such, only the first 10 out of 1715 modes needs to be considered.

In Figure 3, a time-independent reconstruction of the flow in modes 1 and 2 are provided. Streamlines are superimposed over vorticity contours to illustrate the coherent motions captured by each mode. In mode 1 and shown in figure 3(a), we can see a highly coherent, uniform ejection structure in front of the turbine, as well as uniform recirculation around the rotor and a reduced coherence at the bottom of the wake. Mode 2, where we saw the primary spike in figure 2(b), consists of a large vortex in front of the turbine and a vortex-stagnation pair behind the turbine at $x/D = 1.33$. This is shown in figure 3(b). Furthermore (not shown here), mode 3

shows a pair of counter-rotating vortices that appear to extend through the rotor, and mode 4, where we noted the secondary spike, also shows a critical point pair, with a vortex at the same location at the top of the wake at $x/D = 1.33$.

5 Conclusion

POD has been effectively applied on a wind turbine array boundary layer. Flow structures have been identified based on the energy difference which is being extracted out of the turbine. It is found that modes one and two contain signatures of coherent motion, while showing convergence in the application of POD. Representing the flow with the first seven modes is enough to account of the important motions in this flow. It is also shown that applied this low dimensional technique can prove useful when understanding the flows around the array of wind turbines by extracting energetic events and the large scale motions.

Acknowledgements. This work is in part funded by NSF (CBET-1034581 and CBET-0953053).

References

1. Calaf, M., Meneveau, C., Meyers, J.: Large Eddy simulations study of fully developed wind-turbine array boundary layers. *Phys. Fluids* 22(1) (2009)
2. Cal, R.B., Lebrón, J., Kang, H.-S., Castillo, L., Meneveau, C.: Experimental study of the horizontally averaged flow structure in a model wind-turbine array boundary layer. *J. Renewable and Sustainable Energy* 2, 013106 (2010)
3. Berkooz, G., Holmes, P., Lumley, J.L.: The proper orthogonal decomposition in the analysis of turbulent flows. *Annu. Rev. Fluid Mech.* 25, 539–575 (1993)
4. Holmes, P., Lumley, J.L., Berkooz, G.: *Turbulence, Coherent Structures, Dynamical Systems and Symmetry*. Cambridge University Press (1996)
5. Sirovich, L.: Turbulence and the dynamics of coherent structures. *Q. Appl. Math.* 45(3), 561–590 (1987)
6. Saranyasoontorn, K., Manuel, L.: Low-dimensional representations of inflow turbulence and wind turbine response using proper orthogonal decomposition. *J. Sol. Energy Eng.* 127(4), 553 (2005)
7. Bernero, S., Fiedler, H.E.: Application of particle image velocimetry and proper orthogonal decomposition to the study of a jet in a counterflow. *Exp. Fluids* 29(1), 274–281 (2000)

Enhancing the Simulation of Turbulent Kinetic Energy in the Marine Atmospheric Boundary Layer

Richard J. Foreman and Stefan Emeis

Abstract. Improvements in the calculation of turbulent kinetic energy (TKE) by the Mellor-Yamada-Janjic (MYJ) turbulence closure scheme in the Weather Research and Forecasting (WRF) model are presented with a focus on turbulence as measured by the offshore measurement platform in the North Sea, FINO1. Updates to the MYJ scheme to be presented here are however expected to be equally valid over land as well as the sea, since they are based on recent high Reynolds number boundary layer experiments in the laboratory. Improvements of 40% (RMS) in the calculation of TKE by the updated MYJ scheme for a high wind speed period at FINO1 during January 2005 are reported here.

1 Introduction

The development of offshore wind energy is ongoing and in the next few years is expected to meet a large fraction of the energy generated by renewable sources in a number of countries. With that there is a need to further understand the peculiarities of offshore turbulence for both the prediction of energy yields and the design of wind energy converters. Numerical weather prediction models can be used in part as a tool for the prediction of wind energy yields, as well as estimating the level of turbulence expected at a particular site. The following work briefly describes some attempts at improving boundary layer parameterisation schemes in weather forecasting models with a focus on the turbulence over the sea. A simple modification to the closure constants used in the Mellor-Yamada-Janjic (MYJ) scheme in WRF (The Weather Research and Forecasting model [8]), based on some relatively recent boundary layer measurements conducted in the laboratory, suggest an improvement in the calculation of turbulent kinetic energy (TKE). One immediate application of

R.J. Foreman · S. Emeis

Institute for Meteorology and Climate Research, Karlsruhe Institute of Technology,
Garmisch-Partenkirchen, Germany

e-mail: richard.foreman@kit.edu

this work is the enhanced ability to simulate offshore turbulence intensity, which is important for wind turbine blade fatigue assessments. The assessment of other potential benefits such as improved wind speed profiles will be the subject of further work.

2 Initial Model Results

An initial inspection of the performance of a numerical weather prediction model, WRF revealed that the MYJ turbulence closure of the planetary boundary layer equations [3] consistently underpredicted the TKE as measured by the FINO1 research platform in the North Sea [6]. For example, consider Fig. 1 which depicts the predicted 90 m wind speed (top) and TKE (bottom) as given by the WRF-MYJ model (red points) and compared with FINO1 measurements (solid black line) for the period January 1-10, 2005. Also shown are our updates (broken blue line) to be explained below. It can be seen that while the mean wind is predicted well enough, the turbulent kinetic energy is underpredicted and so led us to investigate reasons for this anomaly.

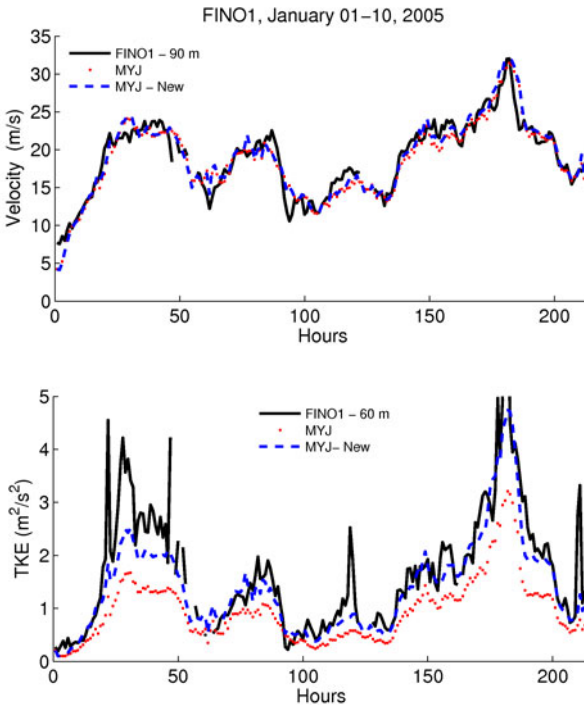


Fig. 1 January 01-10, 2005: Comparison of measured wind speeds (top, 90 m) and turbulent kinetic energy (bottom, 60 m) at FINO1 with the WRF-MYJ model.

3 MYJ Model Closure Constants

Within the current WRF model, the MYJ turbulence closure model assumes $q/u_* = 2.28$, giving $B_1 = 11.88$, where the closure constant, B_1 is related to the dissipation of turbulent kinetic energy by [4]

$$\varepsilon = \frac{q^3}{B_1 l}, \tag{1}$$

and B_1 is related to q/u_* once production is assumed to balance dissipation by

$$B_1 = \left(\frac{q}{u_*} \right)^3. \tag{2}$$

Here, l is the turbulent length scale and is specified algebraically throughout the boundary layer, reducing to κz (von Karman’s constant multiplied by the altitude) in the logarithmic layer (the MYJ model is essentially a one-equation model in WRF). While this may have been reasonable at the time (see the Table 1 in [4]), more recent results [7, 2] shown in Table 1 suggest that $q/u_* = 2.28$ should be quite a bit higher. Experimental methods, particularly the resolution near the wall where statistics are obtained [4], should have advanced since the publication of [4]. This is important since the precise prediction of q/u_* is critical due to the 3rd power dependency in eq. (2). The turbulent statistics measured in high Reynolds number boundary layers by [7] and [2] are in good agreement and we have selected $B_1 = 26.000$ which gives $\frac{q}{u_*} = 2.963$ and have used this as a starting point for updating MYJ model coefficients (see [4] for this procedure).

Table 1 Summary of turbulent statistics from recent high Reynolds number boundary layer experiments [7, 2] and statistics assumed in model constants by [4], the current version of MYJ in the WRF model [3] and that updated here.

Author	Re (x 10 ⁴)	$\frac{u'}{u_*}$	$\frac{v'}{u_*}$	$\frac{w'}{u_*}$	$\frac{q}{u_*}$	$B_1 = \left(\frac{q}{u_*}\right)^3$
[7]	2.25	2.30	1.55	1.05	2.97	26.2
[2]	2.06	2.31	1.52	1.06	2.96	25.9
<u>Mellor-Yamada Models:</u>						
[4]	-	1.90	1.20	1.20	2.55	16.6
Current WRF	-	1.70	1.07	1.07	2.28	11.9
Updated here	-	1.97	1.57	1.57	2.96	26.0

4 Summary of Updates and Results

Further steps to improving the MYJ scheme are the calibration of turbulent velocity components (u' , v' , w') and l for the purposes of achieving realistic dimensionless wind and temperature gradients as a function of atmospheric stability [1]. This is achieved by selecting particular turbulent velocity components u' , v' and w' (the

model assumes $v' = w'$) and a function for l based on [5]. In particular, l is made an explicit function of stability.

Already presented above in Fig. 1 is a comparison between model and field measurements at FINO1. The RMS difference between the measurements and model has been improved by approximately 40% (broken blue line) with the updated model constants. Tests of the updated model over land using the Hamburg weather mast also compare well with modelled TKE (not shown).

Acknowledgements. This work was done within the VERITAS project (work package 5 of OWEA) which is funded by the German Ministry of the Environment (BMU) via the PTJ (FKZ 0325060). The FINO1 and Hamburg data were kindly provided by DEWI (German wind energy institute) and Ingo Lange (Hamburg University), respectively. The WRF model is provided by UCAR/NCAR/MMM.

References

1. Businger, J.A., Wyngaard, J.C., Iyumi, Z., Bradley, E.F.: Flux-profile relationships in the atmospheric surface layer. *J. Atmos. Sci.* 28, 181–189 (1971)
2. Carlier, J., Stanislas, M.: Experimental study of eddy structures in a turbulent boundary layer using particle image velocimetry. *J. Fluid Mech.* 535, 143–188 (2005)
3. Janjic, Z.I.: Nonsingular implementation of the mellor-yamada level 2.5 scheme in the ncep meso model. Technical report, National Centers for Environmental Prediction, Office Note No. 437 (2001)
4. Mellor, G.L., Yamada, T.: Development of a turbulence closure model for geophysical fluid problems. *Rev. Geophys. Space Phys.* 20, 851–875 (1982)
5. Nakanishi, M.: Improvement of the mellor-yamada turbulence closure model based on large-eddy simulation data. *Boundary-Layer Meteorology* 99, 349–378 (2001)
6. Neumann, T., Nolopp, K.: Three years operation of far offshore measurements at fino1. *DEWI Magazine* 30, 42–46 (2007)
7. Österlund, J.M.: Experimental studies of zero pressure-gradient turbulent boundary layer flow. PhD thesis, Royal Institute of Technology, Department of Mechanics, Stockholm, Sweden (1999)
8. Skamarock, W.C., Klemp, J.B., Dudhia, J., Gill, D.O., Barker, D.M., Duda, M.G., Huang, X.Y., Wang, W., Powers, J.G.: A description of the advanced research wrf version 3. Technical report, National Center for Atmospheric Research (2008)

Numerical Modeling of a WECs Power Performance under the Influence of Atmospheric and Synthetic Wind Fields

Tanja Mücke, Matthias Wächter, Patick Milan, and Joachim Peinke

Abstract. Power curves for wind energy converters (WECs) provide an essential relation between wind speed and electrical power output. The current industry standard IEC 61400-12-1 defines a unified procedure for the derivation of power curves. Recently, a novel method has been proposed to obtain power curves for WECs from high frequency data of power output $P(t)$ and wind speed measurements $u(t)$, the dynamical or Langevin power curve $P_L(u)$. This approach models the short-time dynamics of the wind power conversion as a relaxation process, driven by the turbulent wind. In this contribution, we show the independence of the Langevin approach from the turbulence characteristics of the inflow.

1 Introduction

The IEC has defined a so-called power curve $P(u)$ that quantifies the relation between wind speed and electrical power output [3]. Power curves enable the monitoring of proper operation, or the estimation of the annual energy yield at a certain site, and establish an important characteristic of a wind energy converter (WEC). Recently, a novel method has been proposed to obtain power curves for WECs from high frequency data of power output $P(t)$ and wind speed measurements $u(t)$, the dynamical or Langevin power curve $P_L(u)$ [1]. Wächter et al. have already shown that the dynamical approach can be successfully applied to power curve measurements related to LIDAR wind measurements of the Leosphere WindCube [7]. Here, we present a further application to wind energy based on this dynamical approach. The Langevin power curve (LPC) can also be used to characterize the dynamics of a numerical turbine model. Therewith, we have the possibility to quantify and validate the LPC under well defined inflow and operating conditions. In the following,

Tanja Mücke · Matthias Wächter · Patick Milan · Joachim Peinke

ForWind - Institute of Physics, University of Oldenburg, D-26111 Oldenburg, Germany

e-mail: tanja.muecke@forwind.de,

matthias.waechter@uni-oldenburg.de,

patrick.milan@forwind.de, peinke@uni-oldenburg.de

we investigate the influence of measured atmospheric and synthetic IEC wind fields on the LPC. Both wind fields are specified in section 3.

2 Langevin Power Curve

The Langevin approach models the short-time dynamics of the wind power conversion as a relaxation process, driven by the turbulent wind. For the (clearly hypothetical) case of a steady inflow with a constant wind speed u , the electrical power output would be uniquely related to fixed values $P_L(u)$. Mathematically, these power values $P_L(u)$ are called stable fixed points of the power conversion process. The wind speed measurements are divided into bins u_i of 0.5 m/s width, as it is done in 3. Now we can derive for each wind speed bin u_i the drift function

$$D_i(P) = \lim_{\tau \rightarrow 0} \frac{1}{\tau} \langle \tilde{P}(t + \tau) - \tilde{P}(t) | u(t) \in u_i, \tilde{P}(t) = P \rangle, \quad (1)$$

where the conditions mean that only those power values $\tilde{P}(t)$ are considered for which $u(t)$ is within u_i and $\tilde{P}(t) = P$. The average $\langle \cdot \rangle$ is thus performed over t , but separately for each wind speed bin u_i and each power value P . If we consider the state of the system as defined by u and P , we could therefore speak of a *state-based* averaging in contrast to the temporal averaging in 3. $D_i(P)$ has the meaning of an average slope of the power signal $P(t)$, depending on the power value P . Because for constant u the power would also be constant, the average slope of the power signal in that case would vanish, and the drift function would thus be zero. The task is therefore to find the zeros of the drift function $D_i(P)$ for every wind speed bin u_i and every power value P . To be a stable fixed point, the slope of $D_i(P)$ at this $D_i(P) = 0$ should additionally be negative. The stable fixed points for the different wind speeds are then defining the LPC 11.

3 Numerical Modeling

During January 1984 and February 1987 wind field measurements were taken near the German coastline of the North Sea. Two metmasts were erected next to each other in flat terrain at the GROWIAN site in Kaiser-Wilhelm-Koog. The horizontal wind speeds were recorded simultaneously by 16 propeller anemometers placed at the two metmasts over a grid of 76×100 m. Starting at 50 m, we obtain information about the wind field in five different heights up to 150 m. Several data sets exist, which are highly time-resolved with a sampling frequency of 2.5 Hz 2. Altogether 334 datasets have been carefully selected for our investigation. One dataset lasts 10 minutes, and all of them have different mean wind speeds and wind profiles, respectively. The GROWIAN measurement campaign provides the spatio-temporal turbulent structure of the atmospheric wind field over the whole rotor area of a large wind turbine. With this information we can model a realistic turbulent inflow for computing the expected power output of a wind turbine. Additionally, we

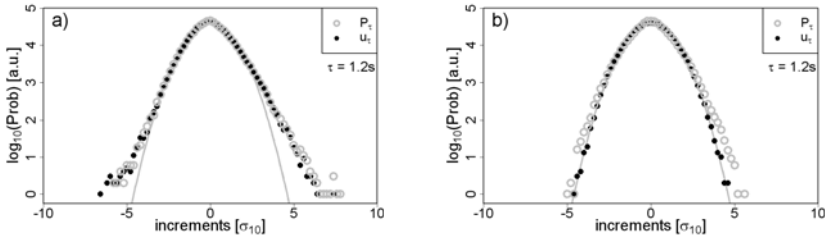


Fig. 1 Normalized probability density function (pdf) of velocity increments $u_\tau = u(t + \tau) - u(t)$ at hub height and electrical power increments $P_\tau = P(t + \tau) - P(t)$ for $\tau=1.2s$. Normalization factors are the standard deviations σ_{10} of the 10 min increments, respectively. The results are displayed for (a) measured GROWIAN wind fields and (b) synthetic IEC wind fields. The gray line depicts the Gaussian distribution with the same standard deviation ($\sigma=1$) as the normalized increment pdfs. The different statistics of the two wind fields and the corresponding power output is clearly seen in the heavy tailed (intermittent) distribution showed in (a). A higher probability of e.g. large velocity increments on small time scales means a higher probability of wind gusts although the pdfs have the same standard deviation.

investigate synthetic IEC wind fields with the same mean wind speed and turbulence intensity at hub height as the measured GROWIAN wind fields. The synthetic wind fields are generated with TurbSim [5] according to the IEC 61400-1, Ed 3 with the Kaimal turbulence model and a logarithmic wind profile which fits the mean profile of the GROWIAN data. Both investigated turbulence fields, intermittent measured GROWIAN and Gaussian synthetic Kaimal, are used as inflow for the numerical model to calculate the electrical power output of the virtual wind turbine. The simulations of the power output are performed with the aeroelastic code FAST designed by NREL and the WindPact 1.5 MW wind turbine [4]. This virtual wind turbine is pitch regulated and has a rotor with a diameter of 70 m at 100 m hub height. As expected from earlier results [6], the resulting power output reflects the intermittent or Gaussian behavior of the inflow (figure 1).

4 Results and Conclusions

From the results of the numerical turbine model we could successfully derive the power characteristics of the virtual WEC, following the IEC standard as well as the novel Langevin approach. Figure 2 shows the LPC for the computed power output together with the IEC and the theoretical power curve resulting from sheared steady inflow. For power curve calculation, the wind speed is taken from the grid point of the measured GROWIAN wind fields at hub height and reflects in this way a conventional one-point measurement according to the IEC standard [3]. The Langevin power curve $P_L(u)$ follows the expected theoretical power curve. The transition to rated power is clearly marked, unlike the IEC power curve. The LPC do not suffer the averaging limitations of the IEC power curve [1] and is unaffected by the two different turbulent inflow fields investigated. Although the intermittent non-Gaussian

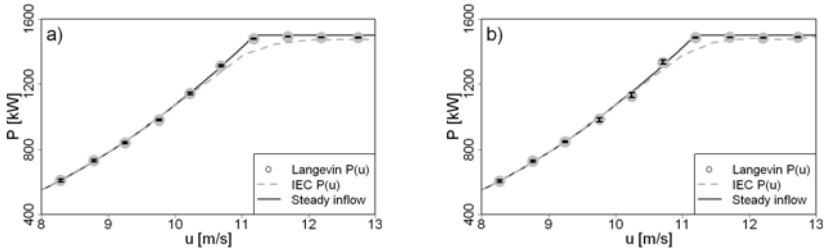


Fig. 2 LPC (dots with corresponding error bars) of the computed power output in comparison with the IEC power curve (dashed line) for (a) atmospheric inflow, (b) Kaimal inflow. The solid line depicts the ideal theoretical curve for a steady inflow with logarithmic wind profile.

structure of small scale wind turbulence plays an essential role for the working condition of a wind turbine and leads to mechanical loads as well as fluctuations of the power production with many short term extreme events [6], the Langevin approach could derive nearly the same fixed points. Thus, the LPC is independent from the turbulence characteristics of the inflow.

References

1. Gottschall, J., Peinke, J.: How to improve the estimation of power curves for wind turbines. *Environmental Research Letters* 3(1), 015005 (2008)
2. Günther, H., Hennemuth, B.: Erste Aufbereitung von flächenhaften Windmessdaten in Höhen bis 150m, Deutscher Wetter Dienst, BMBF-Projekt 0329372A (1988)
3. International Electrotechnical Commission, Wind turbines – Part 12 revision 1: Power performance measurements of electricity producing wind turbines, IEC 61400-12-1 (2005)
4. Jonkman, J.: NWTC Design Code FAST v6.01, National Renewable Energy Laboratory (2005)
5. Kelley, N., Jonkman, B.: NWTC Design Code TurbSim v1.40, National Renewable Energy Laboratory (2007)
6. Mücke, T., Kleinhans, D., Peinke, J.: Atmospheric turbulence and its influence on the alternating loads on wind turbines. *Wind Energy* 14, 301–316 (2010), doi:10.1002/we.422
7. Wächter, M., Rettenmeier, A., Kühn, M., Peinke, J.: Wind velocity measurements using a pulsed lidar system: first results. In: *IOP Conference Series: Earth and Environmental Science*, vol. 1, pp. 012066 (6pp) (2008)

ABL-Flow over Hills: A Review of Theory and Wind Tunnel Studies

Graciana Petersen, Bernd Leitl, and Michael Schatzmann

1 Introduction

Flow over complex terrain and hills is a concern in many research areas such as determination of air pollution zones, predictions of smoke movement from forest fires, wind energy assessment and siting of wind energy converting systems (WECS). It can be examined by means of field studies, theoretical analysis, wind tunnel simulation and numerical modelling. Concerning numerical modelling of flow over hills, a problem is scaling up the unresolved effects of flow interactions with the fine-scale topography and combining this in regional or global scale models, [2]. Linear models, such as WAsP, are not valid for steep terrain, due to the closure assumptions in separation areas. It is still a challenge for computer modellers to determine recirculation zones in high resolution models such as Reynolds Averaged Navier-Stokes (RANS) or large-eddy simulation (LES), [25].

In regard to field studies, a prominent example is the Askervein Hill in Scotland where an extensive field study has been made in 1982 and 1983, the interested reader is referred to [22] and [17]. The results, including a weak separation zone on the lee of the hill, have been used frequently as test case, for example RANS-simulation, [8], and LES-simulation, [13]. Further established field studies include Black Mountain (Canberra, Australia 1977, [4]), Kettles Hill (Alberta, Canada 1984, [19]), Nyland Hill (Somerset, United Kingdom 1984, [15]), and Bolund (Denmark, 2007 and 2008, [3]). Theory of atmospheric boundary layer (ABL) flow over hills is summarized in chapter 2. A discussion on recent wind tunnels studies is given in chapter 4.

Graciana Petersen · Bernd Leitl · Michael Schatzmann
Meteorological Institute, KlimaCampus, University of Hamburg, Germany
e-mail: graciana.petersen@zmaw.de, bernd.leitl@zmaw.de,
michael.schatzmann@zmaw.de

2 Theory on Flow over Hills

Examination of ABL flow over hills exists since the 1930s, on phenomenological investigation of lee waves.

Historical overview: In 1975, Jackson and Hunt develop an innovative theoretical ansatz for turbulent flow over a low hill in neutral stratification, [11]. They use a first order perturbation formula for perturbed vertical and horizontal velocity components in order to treat the two-dimensional equation of motion. But the theory is, strictly speaking, only valid for infinitely low hills. Since 1975, research in pure analytical theory has been overtaken by numerical modeling due to an increase in computational capacities. Reviews are given in [16], [12], [18] and [25].

Summary of theory: In brief, due to the Bernoulli effect wind speed up over hill crest occurs and can double the speed of upstream flow. Furthermore, in stable stratification lee wave phenomena can be observed, which are gravity waves depending on Froude number. This idea is linked to the dividing streamline concept for three-dimensional hills in stable stratification which determines the dividing height in which the upper part of the flow has enough kinetic energy to rise over hill top whereas the lower part flows around the hill, [20].

Maximum wind speed up in stable stratification is assumed to occur behind hill top, [4], [21], [20] and [18]. In neutral stratification, maximum wind speed up usually occurs at hill crest close to the ground. Although it is not clear at which height since divergent observations exist in field studies, wind tunnel simulation or numerical and theoretical models. Moreover, the maximum speed up height depends on hill shape, hill roughness length and inflow conditions.

In addition to lee waves and wind speed up, flow separation is an important point for ABL flow over hills. For two-dimensional hills, 0.31 can be assumed to be the critical slope for which flow separation occurs, and 0.63 in 3dimensional case [24]. For unstable stratification, no detailed examination for ABL flow over hills exists so far, but in field studies wind speed up is found to be lower than in the neutral case.

3 Wind Tunnel Simulation of ABL-Flow over Hills

Historical overview: In 1929, neutral flow over the Rock of Gibraltar was modelled by Field and Warden, a historical start for wind tunnel simulation of flow over hills. Important work has been done in the 1980s, [5], also in relation with the Askervein Hill Project [23], [22], [17]. Meroney's literature review, [16], is highly recommended to the reader.

Recent wind tunnel studies: Regarding wind tunnel simulations of the last 15 years, unfortunately, it has to be pointed out that experimental set ups often are not well documented, [9], [10], [1], [2], [7], [6], [14]. For example inflow conditions and measurement details are not documented completely, influence of the Reynolds number is not clear or experiments are not Reynolds independent. Interpretation of

wind tunnel experiments with regard to real terrain without discussion of the insufficient Reynolds number is not possible.

If real existing terrain is to be modeled questions that arise include how to choose the full-scale detail to ensure an expedient scaling rate in conjunction with matching flow characteristics of a given full-scale ABL flow. Altogether, the literature review shows shortcomings of recent wind tunnel simulations. In fact, no uniform practice in documentation and conduction of wind tunnel experiments on turbulent flow over hills exists so far.

4 Conclusion

Wind speed up of atmospheric boundary layer flow over hills and turbulence effects due to topography are very important for many research areas such as siting of wind energy converting systems. Theory can currently not explain turbulent flow over hills sufficiently. Therefore, advanced computer models are needed for wind predictions. To validate computer models properly or gain more structural insight of ABL flow in complex terrain, wind tunnel simulations must be conducted carefully. No uniform practice in documentation and methods for wind tunnel experiments concerning ABL flow over hills exists. Suggested considerations for uniformity include: Selection of model scaling, model material, surface roughness, discussion of Reynolds number influence and report of measurement repeatability and reproducibility. With a wind tunnel experiment on an idealized Bolund hill the authors plan to address these considerations.

References

1. Athanassiadou, M., Castro, I.P.: Neutral flow over a series of rough hills: A laboratory experiment. *Boundary Layer Meteorology* 101, 1–30 (2001)
2. Ayotte, K.W., Hughes, D.E.: Observations of boundary-layer wind-tunnel flow over isolated ridges of varying steepness and roughness. *Boundary-Layer Meteorology* 112, 525–556 (2004)
3. Bechmann, A., Johansen, J., Sorensen, N.N.: The bolund experiment -design of measurement campaign using cfd (2007)
4. Bradley, E.F.: An experimental study of the profiles of wind speed, shearing stress and turbulence at the crest of a large hill. *Quart. J. Roy. Meteorol. Soc.* 106, 101–124 (1980)
5. Britter, R.E., Hunt, J.C.R., Richards, K.J.: Air flow over a two-dimensional hill: studies of velocity speed-up, roughness effects and turbulence. *Quart. J. R. Met. Soc.* 107(451), 91–110 (1981)
6. Cao, S., Tamura, T.: Effects of roughness blocks on atmospheric boundary layer flow over a two-dimensional low hill with/without sudden roughness change. *Journal of Wind Engineering and Industrial Aerodynamics* 95, 679–695 (2007)
7. Cao, S., Tamura, T.: Experimental study on roughness effects on turbulent boundary layer flow over a two-dimensional steep hill. *Journal of Wind Engineering and Industrial Aerodynamics* 94, 119 (2006)

8. Castro, F.A., Palma, J.M.L.M., Silva Lopes, A.: Simulation of the askervein flow. part 1: Reynolds averaged navier–stokes equations. *Boundary Layer Meteorology* 107, 501–530 (2003)
9. Ferreira, A.D., Lopes, A.M.G., Viegas, D.X., Sousa, A.C.M.: Experimental and numerical simulation of flow around two-dimensional hills. *Journal of Wind Engineering and Industrial Aerodynamics* 54/55, 173–181 (1995)
10. Ishihara, T., Hibi, K., Oikawa, S.: A wind tunnel study of turbulent flow over a three-dimensional steep hill. *Journal of Wind Engineering and Industrial Aerodynamics* 83, 95–107 (1999)
11. Jackson, P.S., Hunt, J.C.R.: Turbulent wind flow over a low hill. *Quart. J. R. Met. Soc.* 101, 929–955 (1975)
12. Kevlahan, N.K.-R.: Rapid distortion of turbulent structures. *Applied Scientific Research* 51, 411–415 (1993)
13. Silva Lopes, A., Palma, J.M.L.K., Castro, F.A.: Simulation of the askervein flow. part 2: Large-eddy simulations. *Boundary Layer Meteorology* 125, 85–108 (2007)
14. Lubitz, W.D., White, B.R.: Wind-tunnel and field investigation of the effect of local wind direction on speed-up over hills. *Journal of Wind Engineering and Industrial Aerodynamics* 95, 639–661 (2007)
15. Mason, P.J.: Flow over the summit of an isolated hill. *Boundary Layer Meteorology* 37, 385–405 (1986)
16. Meroney, R.N.: Wind-tunnel modelling of hill and vegetation influence on wind power availability task1: Literature review. Technical report, Meteorological Services U.S. Windpower (1993)
17. Mickle, R.E., Cook, N.J., Hoff, A.M., Jensen, N.O., Salmon, J.R., Taylor, P.A., Tetzlaff, G., Teunissen, H.W.: The askervein hill project: Vertical profiles of wind and turbulence. *Boundary Layer Meteorology* 43, 143–169 (1988)
18. Miller, C.A., Davenport, A.G.: Guidelines for the calculation of wind speed-ups in complex terrain. *Journal of Wind Engineering and Industrial Aerodynamics* 74-76, 189–197 (1998)
19. Salmon, J.R., Teunissen, H.W., Mickle, R.E., Taylor, P.A.: The kettles hill project: Field observations, wind-tunnel simulations and numerical model predictions for flow over a low hill. *Boundary Layer Meteorology* 43, 309–343 (1988)
20. Snyder, Thompson, Eskridge, Lawson, Castro, Lee, Hunt, Ogawa: The structure of strongly stratified flow over hills: dividing-streamline concept. *J. Fluid. Mech.* 152, 249–288 (1985)
21. Snyder, W.H.: Guideline for fluid modeling of atmospheric diffusion. Technical report, United States Environmental Protection Agency (1981)
22. Taylor, P.A., Teunissen, H.W.: The askervein hill project: Overview and background data. *Boundary Layer Meteorology* 39, 15–39 (1987)
23. Teunissen, H.W., Shokr, M.E., Bowen, A.J., Wood, C.J., Green, D.W.R.: The askervein hill project: Wind-tunnel simulations at three length scales. *Boundary Layer Meteorology* 40, 1–29 (1987)
24. Wood, N.: The onset of separation in neutral, turbulent flow over hills. *Boundary Layer Meteorology* 76, 137–164 (1995)
25. Wood, N.: Wind flow over complex terrain: A historical overview and the prospect for large-eddy modelling. *Boundary Layer Meteorology* 96, 11–32 (2000)

Application of Meteorological Data in Computational Modelling of Wind over Real Terrain Topography

K. Wędołowski and K. Bajer

Abstract. Owners of wind farms are interested in both annual mean wind speed and in forecasting wind speed for a few days. Considerable research effort is focused on computational modelling for wind energy assessment [1]. Local winds are influenced by synoptic situation as well as by specific topography. Therefore one should couple a Numerical Weather Prediction (NWP) model with additional small scale model. Especially in a complex terrain dependence of the local flow on the wind direction cannot be neglected. In this study we analyse this phenomenon for a particular site in a moderately complex terrain.

1 Introduction

Short-term forecast of the energy production is an important issue in the wind power systems [4]. The mean wind speed and direction for the entire wind farm site can be obtained from a NWP model. However such models typically have horizontal resolution comparable with the size of the site. Therefore, such prediction does not take into account detailed topography and roughness of the site. These factors may cause strong dependence of the wind speed on the direction of the geostrophic wind. This fact motivates us to carry out an analysis of the wind speed distribution over a wind farm site using a CFD code. Sections 2 and 3 describe our models while some preliminary results are presented in section 4.

K. Wędołowski
Interdisciplinary Centre for Mathematical and Computational Modelling,
Warsaw University, Poland
e-mail: kjwed@icm.edu.pl

K. Bajer
Institute of Geophysics, Faculty of Physics, Warsaw University, Poland
e-mail: Konrad.Bajer@fuw.edu.pl

2 NWP Model

Prediction of wind conditions for a wind farm requires modeling of atmosphere over a larger area. It is done by a regional NWP model, which takes initial and boundary conditions from a global NWP model (e.g. GFS or NOGAPS). COAMPS (The Coupled Ocean/Atmosphere Mesoscale Prediction System) an operational NWP model is used in our experiments.

The model solves nonhydrostatic fully compressible equations of motion. It contains parametrization for subgrid mixing, cumulus, radiation and moist physics. COAMPS uses a level 2.5 scheme that solves both a prognostic equation for turbulent kinetic energy (TKE) and diagnostic equations for second-moment quantities such as primary fluxes of heat, moisture, and momentum [7].

COAMPS uses the terrain-following vertical coordinate. Horizontal grids can be nested in order to achieve desired resolution. Each child grid length has to be one-third of the parent grid length [3].

Output from the weather forecast is available on a grid which has 30 vertical levels and 4.3 kilometres horizontal resolution. This data might be used as an input for a CFD code (coupled through friction velocity).

3 CFD Model

In order to model the wind flow over topography the so-called simpleFoam solver implemented in the OpenFOAM@toolbox was used. It solves Reynolds averaged Navier-Stokes (RANS) equations for incompressible steady flow using the SIMPLE algorithm. For this moment only neutrally stratified atmosphere was considered but in the future buoyancy will be taken into account.

To close the set of equations a model of turbulence is required. OpenFOAM provides a few turbulence models. So far the standard $k - \epsilon$ model was used but we plan to analyse its influence on the obtained results and consider using other models.

To prepare an appropriate mesh for our case the snappyHexMesh utility was used. It generates the three-dimensional mesh from triangulated surface (STL) geometries by iteratively refining the mesh close to the surface. First of all a digital elevation model (DEM) of considered site was obtained [5]. The mesh and triangulated terrain are presented in figure 1.

4 Simulations and Results

The main goal of these preliminary simulations was to examine importance of the wind direction for moderately complex terrain. For the analysed site we generated the mesh (see figure 1), covering the site and some area beyond it (3km x 3km). In order to compare vertical profiles of velocity and turbulence characteristics for winds blowing from eight sectors of the wind rose we rotated the meshes so that the wind at the inlet is always perpendicular to the inlet side of the rectangle.

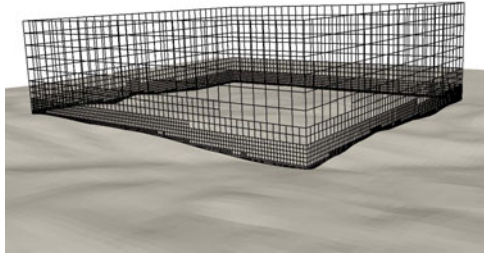


Fig. 1 The mesh used in our simulations situated on the digital model of the terrain.

We used boundary conditions proposed by Richards and Hoxey [6] which include at the inlet logarithmic profile of the velocity, uniform value of the turbulent kinetic energy and its dissipation rate decaying as an inverse of the height above the terrain. It required consistent gradients of these quantities at the top of the domain. Note that air is still allowed to enter or flow out from the domain through the top side.

Boundary conditions on the ground require wall functions. OpenFOAM has a built-in wall function for rough surfaces. Since it is a *ks*-type wall function, the problem with defining roughness length occurs. For more detailed discussion see [2]. For this reason we implemented a *z₀*-type wall function which simplify defining the roughness length. So far we have run simulations with uniform roughness. However, in the near future we plan to obtain roughness maps for the considered site.

In figure 2(a) one can see vertical profiles of the velocity magnitude for winds blowing from eight sectors of the wind rose. They differ significantly, especially near the ground. A horizontal line marks the characteristic height of a wind turbine

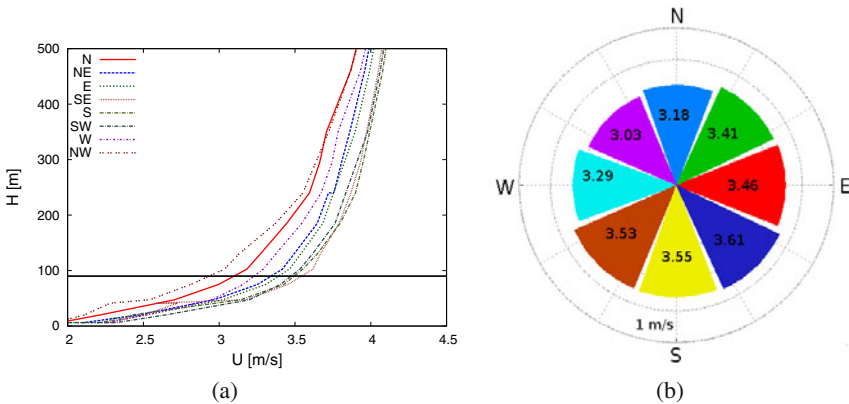


Fig. 2 Comparison of the velocity profiles (a) and the wind speed at 100m above the ground (b) in the centre of the domain for winds blowing from eight sectors of the wind rose. The differences are caused by the topographic features of the terrain which is hilly in the southern part of the domain.

(approximately 100 m). In figure 2(b) the comparison of the wind speed at this altitude is presented in the form of a wind rose graph. The maximal difference is about 0.6 m/s, which is almost 20% of the mean wind speed. Having in mind that the electric power available from the wind turbine is roughly proportional to U^3 , we can state that it is really important to analyse local winds in a complex terrain.

Of course, it is very difficult to impose appropriate boundary conditions (especially on the inflow) when wind is simulated in a complex terrain. One can obtain non-physical speed-ups. When the terrain is highly anisotropic not only the direction of the inflow, but also its vertical profile may need adjusting with varying geostrophic wind direction. This issue requires a separate study. Wind measurements available from the site appeared to have very low quality and unfortunately could not be used to verify our numerical results in detail. However, they do confirm significant dependence of the wind speed at the turbine level on the geostrophic wind direction derived from the nested mesoscale NWP model.

Acknowledgements. We thank prof. M. Grad and M. Polkowski for helpful information about the digital elevation model. This research was conducted as part of the PROZA project (Platform of Support for Operational Decisions Dependent on the State of the Atmosphere) in the Interdisciplinary Centre for Mathematical and Computational Modelling, University of Warsaw (ICM UW).

References

1. Ayotte, K.W.: Computational modelling for wind energy assessment. *Journal of Wind Engineering and Industrial Aerodynamics* 96, 1571–1590 (2008)
2. Blocken, B., Stathopoulos, T., Carmeliet, J.: CFD simulation of the atmospheric boundary layer: wall function problems. *Atmospheric Environment* 41, 238–252 (2007)
3. Chen, S., Hodur, R.: Overview. In: COAMPS Version 3 Model Description General Theory and Equations. Naval Research Laboratory (2003), http://www.nrlmry.navy.mil/coamps-web/base/docs/COAMPS_2003.pdf (cited September 14, 2010)
4. Lei, M., Shiyan, L., Chuanwen, J., Hongling, L., Yan, Z.: A review the forecasting of wind speed and generated power. *Renewable and Sustainable Energy Reviews* 13, 915–920 (2009)
5. Michalak, J.: DEM Data Obtained from the Shuttle Radar Topography Mission - SRTM-3. *Annals of Geomatics* 2, 34–44 (2004)
6. Richards, P.J., Hoxey, R.: Appropriate boundary conditions for computational wind engineering models using the $k\epsilon$ turbulence model. *J. Wind Eng. Ind. Aerodyn.* 46, 47, 145–153 (1993)
7. Thompson, W.: Surface and Planetary Boundary Layer Parameterization. In: COAMPS Version 3 Model Description General Theory and Equations. Naval Research Laboratory (2003), http://www.nrlmry.navy.mil/coamps-web/base/docs/COAMPS_2003.pdf (cited September 14, 2010)
8. Weller, H.G., Tabor, G., Jasak, H., Fureby, C.: A tensorial approach to computational continuum mechanics using object-oriented techniques. *Computers in Physics* 12, 620–631 (1998)

Session 7
Boundary Layer

A New Way to Determine the Wall Position and Friction Velocity in Wall-Bounded Turbulent Flows

P.H. Alfredsson and R. Örlü

1 Introduction

Studies of turbulent boundary layers are often focussed on the near wall region. In experiments an accurate determination of the wall (say within $10\ \mu\text{m}$) with respect to the measurement probe is not easily achieved through optical or mechanical measurements (see e.g. Ref. [1]). Also the friction velocity (u_τ) is hard to determine with high accuracy. One possibility is to utilize the linear velocity profile ($U^+ = y^+$) to determine one or both of the mentioned quantities, but is usually impeded by the fact that the hot-wire readings are affected by heat transfer to the wall. The motivation here is to utilize the cumulative distribution function (CDF) of the streamwise velocity in a way so that the influence of the heat transfer can be avoided and thereby obtain accurate estimates of both the wall position and friction velocity.

2 Velocity Fluctuations in the Near Wall Region

Hot-wire measurements of the probability density function (PDF) for the streamwise velocity component in a zero pressure-gradient (ZPG) turbulent boundary layer (TBL) are shown in figure 1. The low velocity contour lines in figure 1(b) demonstrate that the position where the lowest measured fluctuations are unaffected by heat conduction effects, are limited to y -values above 7-8 wall units. On the other hand the higher velocity levels seem to be unaffected much closer to the wall. Recently the so called diagnostic plot has been proposed [3] to determine where such effects affect the mean readings and it seems that measurements of both the mean and rms of the streamwise velocity below $y^+ = 3-4$ are significantly affected by heat conduction to the wall.

P.H. Alfredsson · R. Örlü

Linné FLOW Centre, KTH Mechanics, Royal Institute of Technology, S-100 44 Stockholm, Sweden

e-mail: hal@mech.kth.se, ramis@mech.kth.se

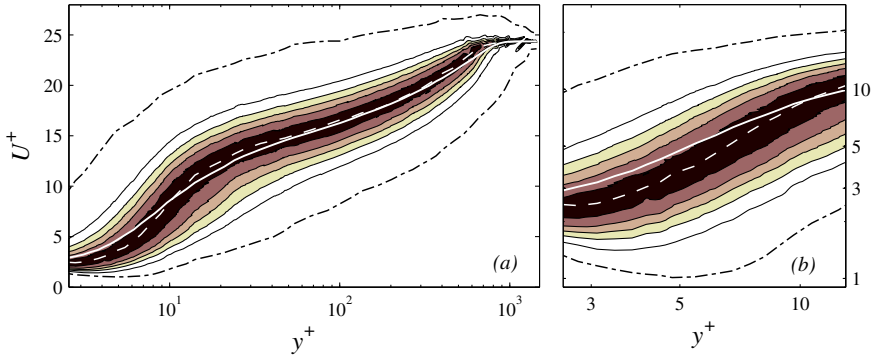


Fig. 1 Mean streamwise velocity as function of the wall normal position scaled in inner variables (white line), U^+ vs. y^+ , plotted above the PDF of the instantaneous streamwise velocity for $Re_\theta \approx 2500$, where Re_θ denotes the Reynolds number based on free stream velocity and momentum loss thickness. Filled contours indicate 10, 30, 50, 70, and 90 % of the local peak PDF value (marked as a dashed white line), whereas the dash-dotted lines include all sampled velocity signals, i.e. the extreme values of the PDF. Experimental data from Ref. [2].

Related to the probability density distribution (f) is the cumulative distribution function (F) through the following relation

$$F(u) = \int_{-\infty}^u f(s) ds, \text{ where } 0 \leq F(u) \leq 1 \text{ and } F(u) \rightarrow 1 \text{ as } u \rightarrow +\infty$$

By using DNS data from turbulent boundary layer simulations it can be shown that for $y^+ < 5$ the PDFs are very close to self-similar. The same is true for F which is plotted in figure 2(a) for several different y^+ . Here the horizontal axis is normalized with the distance from the wall which takes into account that the mean value increases almost linearly with y . An interesting aspect of F is that the low velocity end (up to $F \approx 0.5$) seems to be independent of y^+ up to about $y^+ = 7$.

3 Determination of the Wall Location and Friction Velocity from Near Wall Hot-Wire Measurements

For hot-wire measurements of F obtained for various positions in the wall region it is clear that the turbulent signal is mainly affected by heat transfer to the wall during periods of low streamwise velocity and not for periods of high velocity (see figure 2(b)). This makes it possible to use only the velocity data where F is unaffected by heat transfer, i.e. where the velocity corresponding to a given value of F varies linearly with the wall distance. This means that by plotting the u -value versus the y -position for a given F should result in a straight line that should go through the origin of the yu -plane. By doing so for a number of values of F a good estimate of the wall position is possible to obtain.

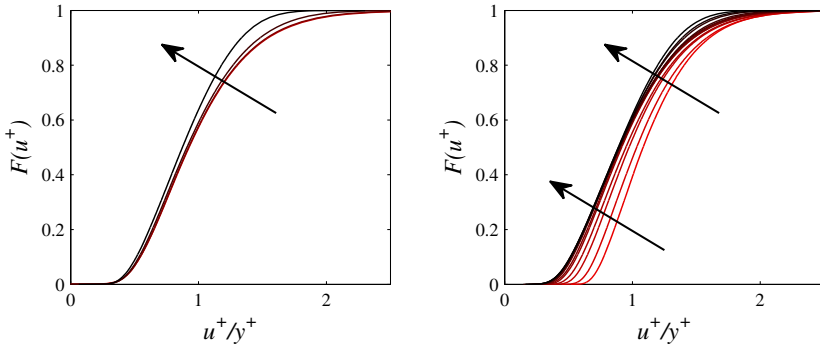


Fig. 2 The CDF for the streamwise velocity fluctuations near the wall *a)* obtained from DNS data from Ref. [4] at $y^+=1.7, 2.8, 5.0$ and 7.8 , and *b)* experimental data from Ref. [2] at $y^+=2.5, 2.8, 3.1, 3.4, 3.8, 4.1, 4.6, 4.8, 5.4, 6.1, 6.8, 7.5$. y^+ increases in the direction of the arrows.

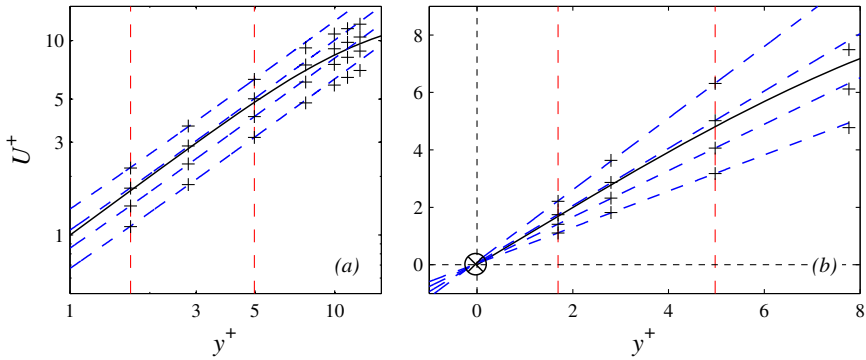


Fig. 3 Proof of concept for the employment of the self-similarity of the CDFs in the sublayer to extract the wall position by utilizing $F(u)=0.2, 0.4, 0.6$ and 0.8 . Linear fits through the closest three near-wall points (+) are indicated through dashed lines. Solid line indicates the mean streamwise velocity component and \otimes the extracted wall position. Vertical dashed lines indicate the region in which the linear fit was applied to the CDF contour levels. DNS data from Ref. [4].

Figure 3(a) depicts four CDF contours together with a linear fit through the three available near-wall points within $y^+ \leq 5$ for the DNS from Ref. [4]. True self-similarity would lead the contour lines to be parallel or intersect with each other at the wall in a log-log or linear-linear plot, respectively, which is what actually is observed in figure 3(a-b). In figure 4(a-b) the experimental data are plotted and it is clearly seen that by using only the linear portion of the CDF contours a good estimate of the wall position is obtained.

To obtain a value of the friction velocity is slightly more cumbersome. Here we use the information from the DNS that the lower part of the CDF ($F < 0.5$) is self

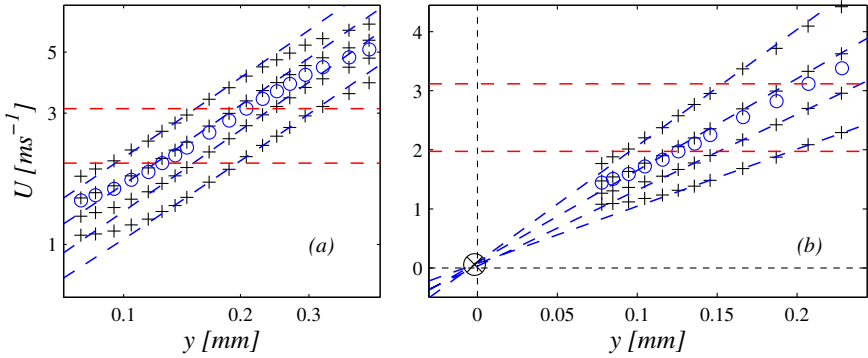


Fig. 4 Application of concept for the employment of the self-similarity of the CDFs in the sublayer to extract the wall position. Levels and symbols as in figure 3 and the circles indicate the mean streamwise velocity component from the experimental data. Region between the dashed horizontal lines indicates the part of the CDF contour levels data to which the linear fit was applied.

similar up to about $y^+ = 7$ (see figure 2(a)). An estimate of u_τ can now be obtained by iterating the value of u_τ until the experimental CDF overlaps with the CDF of the simulation for values of y^+ in the approximate range 4-7, where heat conduction does not affect the lower part of the experimental CDF. If this is done for some different y -values a good estimate of u_τ may be established.

4 Conclusion

In summary we have shown a method, that uses the CDF of the streamwise velocity, to obtain accurate estimates of both the wall position and the friction velocity even though the hot-wire measurements are affected by heat transfer to the wall. Whether it is possible to extend this method to flows with a pressure gradient is an open question and will be investigated in the future.

A more detailed and extended version of this manuscript has also been published very recently in Ref. [5].

Acknowledgements. This work has been partly supported by STINT through a collaboration between KTH and the University of Bologna. Dr. Philipp Schlatter is acknowledged for giving us access to his DNS data.

References

1. Örlü, R., Fransson, J.H.M., Alfredsson, P.H.: On near wall measurements of wall bounded flows – the necessity of an accurate determination of the wall position. Prog. Aero. Sci. 46, 353–387 (2010)

2. Örlü, R.: Experimental studies in jet flows and zero pressure-gradient turbulent boundary layers. PhD thesis, KTH Mechanics, Stockholm, Sweden (2009)
3. Alfredsson, P.H., Örlü: The diagnostic plot – a litmus test for wall bounded turbulence data. *Eur. J. Fluid Mech. B/Fluids* 29, 403–406 (2010)
4. Schlatter, P., Örlü, R.: Assessment of direct numerical simulation data of turbulent boundary layers. *J. Fluid Mech.* 659, 116–126 (2010)
5. Alfredsson, P.H., Örlü, R., Schlatter, P.: The viscous sublayer revisited—exploiting self-similarity to determine the wall position and friction velocity. *Exp. Fluids* 51, 271–280 (2011)

DNS of Turbulent Boundary Layers Subjected to Adverse Pressure Gradients

Guillermo Araya and Luciano Castillo

Abstract. Direct Numerical Simulations (DNS) of spatially-developing turbulent boundary layers with prescribed moderate and strong adverse pressure (APG) gradients are performed. A method for prescribing realistic turbulent velocity inflow boundary conditions is employed based on the on the dynamic multi-scale approach proposed by [1] [2]; and, it is an extension of the rescaling-recycling method by [6]. Comparison with data from more costly DNS ([7][5]) yields accurate results. In addition, the dynamic multi-scale approach does not require lengthy computational domains as in [7] and [5]. Furthermore, it is shown that in APG flows the presence of a second outer peak in $u'_{rms}{}^+$ is more pronounced than in ZPG flows. Additionally, the plateau between the inner and outer peaks suggests the presence of an overlap (i.e., meso-layer) in the mean velocity profile, as discussed in GC-97 [3]. Moreover, these outer peaks are also observed in the production of turbulence even at low Reynolds numbers. Finally, the mean velocity profiles in wall-units show that the wake region is magnified as the APG strengths increases. This suggests that the large scales in the outer flow dominate most of the boundary layer.

1 Numerical Results in APG Flows

For simulations of moderate and strong APG, the curvature at the upper surface of the computational box is prescribed in such a way to obtain a power-law variation of the freestream velocity, i.e. $U_\infty \sim (x - x_0)^m$ with $m = -0.17$ and -0.22 . Table 1 summarizes the different APG cases with the corresponding Re_θ , domain dimensions,

Guillermo Araya

Civil & Computational Engineering Centre, Swansea University, Swansea, UK

e-mail: araya@mailaps.org

Luciano Castillo

Dept. of Mechanical, Aeronautical and Nuclear Eng., Rensselaer Polytechnic Institute, Troy, USA

e-mail: castil2@rpi.edu

Table 1 Table showing proposed DNS cases and domain parameters for APG flows.

Parameter	APG	
	Moderate	Strong
Re_θ	438-633	1029-1512
L_x/δ_{inl}	15	12
L_y/δ_{inl}	3.8	3
L_z/δ_{inl}	1.6	3.2
$N_x N_y N_z$	$120 \times 65 \times 50$	$150 \times 90 \times 100$
Δx^+	20	21
$\Delta y_{min}^+/\Delta y_{max}^+$	0.2/6.8	0.2/17
Δz^+	5	8
Δt^+	0.59	0.22
$T_{sample} \frac{u_z^2}{v}$	1770	1540
δ_{inl}^+	161	271

number of mesh points, mesh resolutions, time step, the collected sample in viscous time scales and the prescribed inlet boundary layer thicknesses.

The turbulence intensities (u'_{rms} , v'_{rms} and w'_{rms}) and Reynolds shear stresses ($-\overline{u'v'^+}$) are depicted in Fig. 1(a), at $Re_\theta = 580$ and moderate APG. The pressure gradient effects are mostly manifested as outer peaks in the outer region around $y^+ \approx 100$. This phenomenon is more evident in the streamwise velocity fluctuations, u'_{rms} , of APG than those of ZPG flows ([4]). As the adverse pressure gradient becomes stronger, the outer peak in u'_{rms} at $y^+ \approx 200$ in Fig 1(b) is almost as high as the inner peak at $y^+ \approx 10$. Notice that maxima of the Reynolds shear

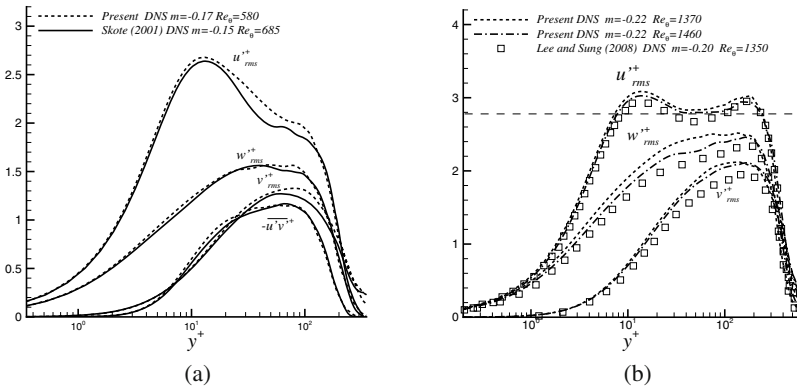


Fig. 1 Turbulence intensities and Reynolds shear stresses of moderate APG (a) and turbulence intensities of strong APG (b).

stresses ($-\overline{u'v'}^+$), shown in Figs. 1(a) and 2(a), move away from the wall as the adverse pressure gradient strength increases. It is also observed that the Reynolds shear stress profiles have slopes given by the pressure gradient as expected, which becomes very steep for the strong APG case. In addition, the agreement of present velocity fluctuations with simulations by [7] and [5] at similar Reynolds numbers (Re_θ) and APG strengths (m) is quite good. The observed agreement is particularly encouraging considering that the streamwise domain lengths of these prior studies by [7] and [5] were 4 and 14 times larger, respectively, than those of presently reported simulations using the dynamic multi-scale method. Furthermore, the effects of the APG strengths are also appreciated in the main term of the turbulence production (see fig. 2(b)) as peaks in the outer layer due to the influence of large scales in this zone. Note the excellent agreement of present turbulence production at moderate APG with the more costly DNS results from [7]. Figure 3 exhibits the mean velocities together with the streamwise turbulence intensities for both APG cases in wall units. One can observe the highly pronounced wake regions in U^+ as the APG strength increases. Notice that the regions between the inner and outer peaks of u'_{rms} are probably overlap regions mainly characterized by a meso-layer due to the low Re_θ and not an inertia sub-layer or the log-layer as stated in [4] for much higher Re_θ , where a plateau in the normal Reynolds stresses exists. This meso-layer is very important since a direct interaction between the small and large scales exists. According to fig. 1 in [4], these outer peaks are also observed in the energy spectra at length scales that usually are several times larger than the boundary layer thickness ($\approx 6\delta$). In ZPG flows the second peak in u'_{rms} occurs at much higher Re_θ than those in APG flows. For instance, in [4] the $Re_\theta \approx 21,000$ whereas in present simulations is in the order of 1,500.

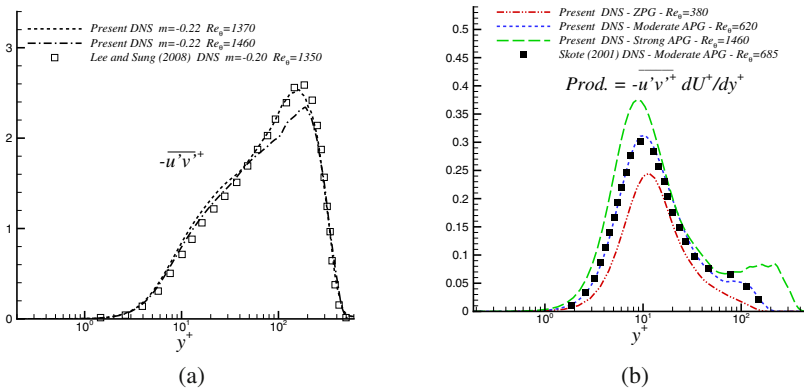


Fig. 2 Reynolds shear stresses of strong APG (a) and turbulence production in ZPG and APG flows (b).

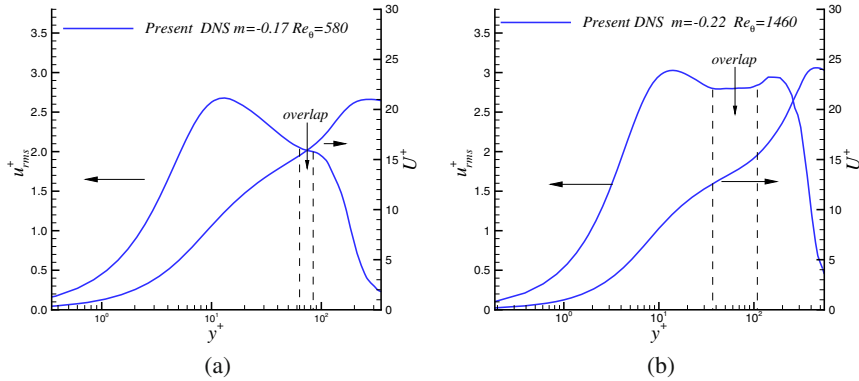


Fig. 3 Mean velocity and streamwise turbulence intensity profiles in wall units for moderate (a) and strong (b) APG.

2 Final Remarks

A generalized dynamic multi-scale method has been proposed and evaluated as turbulent inflow generator in spatially-developing boundary layers subjected to APG. The effects of adverse pressure gradients on turbulent boundary layers are mainly manifested in the outer region, as a second local peak; particularly, in profiles of u_{rms}^{+} even at low Reynolds numbers. This clearly provokes high levels of production in the outer region. Additionally, a plateau is observed between the inner and outer peaks of u_{rms}^{+} and it demonstrates the presence of an overlap (i.e., meso-layer) in the mean velocity profiles, as described in GC-97 [3] for low Reynolds numbers data.

References

1. Araya, G., Jansen, K., Castillo, L.: Inlet condition generation for spatially-developing turbulent boundary layers via multi-scale similarity. *Journal of Turbulence* 10(36), 1–33 (2009)
2. Araya, G., Castillo, L., Meneveau, C., Jansen, K.: A dynamic multi-scale approach for turbulent inflow boundary conditions in spatially-developing flows. *Journal of Fluid Mechanics* (2011), doi:10.1017/S0022112010005616
3. George, W.K., Castillo, L.: Zero-pressure-gradient turbulent boundary layer. *Appl. Mech. Rev.* 50, 689–729 (1997)
4. Hutchins, N., Marusic, I.: Large-scale influences in near-wall turbulence. *Philosophical Transactions of The Royal Society A* 365, 647–664 (2007)
5. Lee, J., Sung, H.: Effects of an adverse pressure gradient on a turbulent boundary layer. *Int. J. of Heat and Fluid Flow* 29(3), 568–578 (2008)
6. Lund, T.S., Wu, X., Squires, K.D.: Generation of turbulent inflow data for spatially-developing boundary layer simulations. *J. Comp. Phys.* 140, 233–258 (1998)
7. Skote, M., Studies of turbulent boundary layer flow through Direct Numerical Simulation. PhD thesis, Royal Institute of Technology, Stockholm, Sweden (2001)

Do Flexible Surface-Hairs Manipulate Near-Wall Turbulence?

Christoph Brücker

Abstract. Turbulent boundary layer flow over a flat plate with an artificial hairy coating is investigated. Flexible hairs of appropriate dimensions are chosen to achieve strong reconfiguration in streamwise direction with the mean flow such that their long cylindrical trailing bodies are placed in the buffer layer. Elasticity, anisotropic flow-opposing body forces and hydrodynamic interaction of the hairs in combination with the travelling wave-type nature of near-wall turbulence lead in sum to an energy transfer from small scale motion to a more coherent motion pattern near the wall with increased coherence in streamwise and spanwise direction. It is concluded from the experiments that appropriate geometrical arrangements of surface-hairs can be beneficial for reduction of turbulent skin friction.

1 Introduction

The near wall region has a crucial role in turbulent drag generation. Recently, Iwamoto et al. (2005) numerically simulated a fully developed turbulent channel flow under a constant flow rate with idealized damping of velocity fluctuations in the near-wall layer. As a result, they found that the largest contribution of drag reduction is achieved when the fluctuation at $z^+ \leq 10$ is damped. This theoretical analysis suggests that the basic mechanism of turbulent drag reduction involves the attenuation of turbulence in the near-wall layer. For technical applications the question arises what type of technical surface is useful to achieve a similar attenuation effect without any additives in the fluid? Surfaces with hairy coatings have proven to be useful for wake stabilization (Favier et al. 2009). However, the effect on turbulence modification is not yet known. As an experimental model, surfaces with a dense carpet of homogeneous flexible micro-hairs were designed to study the local fluid-structure interaction in the buffer layer.

Christoph Brücker
Institute of Mechanics and Fluid Dynamics
TU Freiberg, 09599 Freiberg, Germany
e-mail: bruecker@imfd.tu-freiberg.de

2 Experiments

Experiments were carried out in an oil flow-channel which has been already used for previous studies of 2D wall shear-stress dynamics with small sensory-hairs (Brücker 2008). Now, a dense field of considerably longer surface-hairs was applied with a specific geometrical arrangement - *regular streamwise rows with a spanwise spacing of the order of the characteristic streak width* - to simulate the situation of streamwise wires discussed by Bartenwerfer & Bechert (1991) for possible turbulent drag reduction. The dense carpet with 60×30 flexible slender micro-cylinders was mounted flush with the flat plate at a distance of $x = 1.8m$ downstream from the leading edge. The Reynolds-number built with the free stream velocity $U = 4.5m/s$ is $Re = 1.2 \times 10^6$ and the mean wall friction velocity at the measurement location is $u_\tau = 0.2m/s$ (working fluid: Odina oil at 30C working temperature, kinematic viscosity $\nu \approx 6.7 \times 10^{-6}m^2/s$, density $\rho \approx 840kg/m^3$). Geometry of the micro-hairs in viscous units is $D^+ = 2.5$, $L^+ = 30$, and the spacing within the carpet is $\Delta x^+ = 15$ in streamwise and $\Delta y^+ = 30$ in spanwise direction (viscous length-scale $l_v \approx 33\mu m$, hair diameter $D \approx 85\mu m$, hair length $L \approx 1000\mu m$). The slender hairs have a near uniform circular cross-section and are made of an elastomere (Poly-Dimethylsiloxane). The high viscosity of the working fluid ensures that the dynamic response is weakly overdamped (Q-factor of 0.62, see equations 13 in Brücker et al. 2007). A digital high-speed camera (Photron APX-RS, recording rate 3000 fps) equipped with a long-range microscope (M=1) was used to record the hair motion from top.

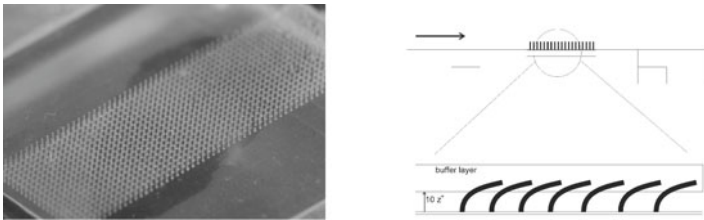


Fig. 1 Photograph of a typical rectangular carpet of flexible micro-hairs made from PDMS under dry conditions after manufacturing. A square-shaped section in form of a regular grid of 60×30 micro-hairs ($n_x \times n_y$) was placed flush on the flat plate wall

In general, the system of a wall-attached elastic cantilever beam in a viscous fluid represents a frequency transfer of a second-order system for small bending. A rough estimate of the minimum response time λ_S neglecting higher-order terms can be determined by a simplified lumped element model described in Brücker et al. (2007). The conditions in our experiments leads to a value of $\lambda_S \approx 1.6ms$. The ratio of hair response time to the smallest turbulent time scales can be understood as a Weissenberg number Wi , which is herein of the order of $Wi = 10$. It is important to note, that the combination of wall-attachment and repulsive forces exerted by the elastic bending means that hair motion in the streamwise x -direction is coupled

to the dynamics in the z - and y - direction. Hence, flow-induced fluctuations of the hairs in spanwise direction contribute to the temporal fluctuations measured in the streamwise x direction and vice versa.

3 Results

The measured hair dynamics is given by the evolution of the end to end vector \mathbf{Q} in between the base fixation of the micro-hair and the tip position in the extended situation. The results are plotted as pdf distribution in Fig. 2. The thick continuous line marks the limiting contour of micro-hair configuration.

The shift of the peak position in Fig. 2 to a lower streamwise value than the mean is analogue to the skewness of the pdf of streamwise wall shear-stress signals in turbulent near wall flow measured by Khoo et al. (2001). The time-history of the micro-hair motion is characterized by the frequent occurrence of large scale positively load peaks, which is the reason for this shift. These load peaks are coupled with "downwash" or sweep events forming high-speed streaks which are the most violent Reynolds shear stress producing events and are responsible for the increase of turbulent wall shear-stress. The arc segment shown as a dashed lines in Fig. 2 indicates the range of fluctuating hair motion and demonstrates a limit in the angle of the configuration vector relative to the streamwise direction x with a maximum value of $\pm 35^\circ$. This limit is smaller than the maximum values reported for the angle of the wall shear-stress vector of 40° recorded in a turbulent boundary layer of the same type (Brücker 2008). The mechanical constraints under strong bending of the hairs leads to restricted maximum spanwise response in comparison to the imposed fluid forces, thus contributing to the dampening of spanwise fluctuations.

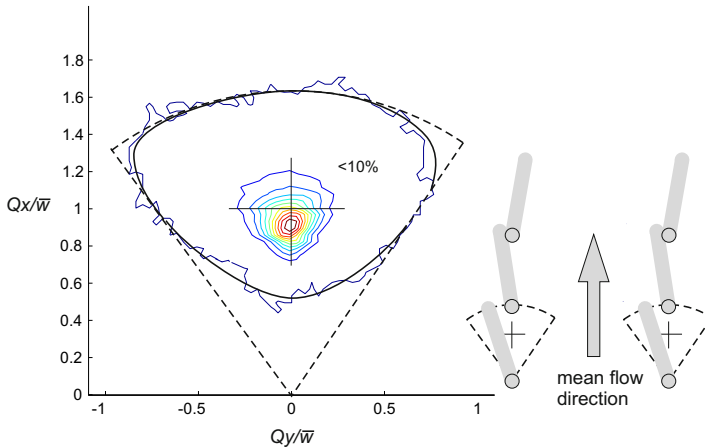


Fig. 2 Contours of 2D distribution of probability density of micro-hair configuration vector \mathbf{Q} in the x - y -plane in the turbulent boundary layer (mean streamwise bending $\bar{w} = 300\mu m$).

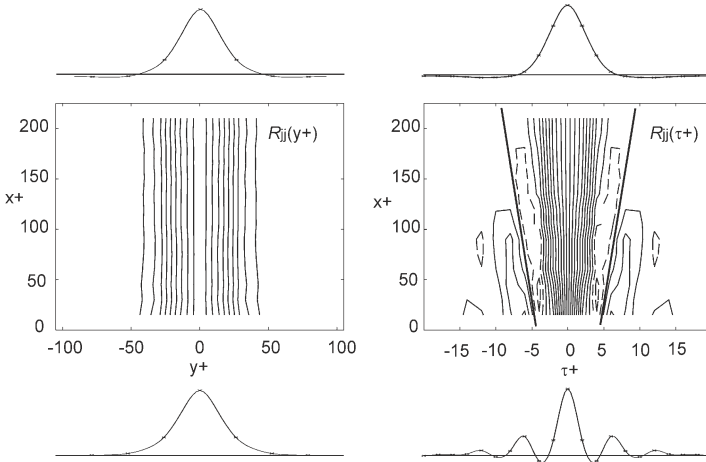


Fig. 3 Distribution of autocorrelation function $R_{jj}(y+, \tau+)$. Isolines are from 0.1 to 0.9 by 0.1 (solid lines) and from -0.1 to -0.9 by -0.1 (dashed lines). The thick line connects spatial locations of $R=0$; the profiles at bottom and top of the diagrams show the spanwise variation of the correlation at $x+=0$ and $x+=215$.

Fig. 3 shows the autocorrelation functions R_{jj} of spanwise component Q_y . All correlation data refer to a null separation in the streamwise direction. Spatial correlations in y -direction $R_{jj}(y+)$ are obtained for each spanwise row x_i of micro-hairs and are stored in a 2D data stack along the streamwise direction $x+$. The temporal correlations $R_{jj}(\tau+)$ for the spanwise component Q_y are processed in a similar way with one axis of the 2D data stack being the time-scale. The autocorrelation distribution function is then plotted as contour lines of the 2D field.

In the front part of the carpet the correlation profiles $R_{jj}(\tau+)$ reveal a periodicity indicating an spanwise oscillatory motion of the micro-hairs with a coherence value above 0.1 for a time interval of $30\tau+$. This is manifested in a wavy form of the autocorrelation profile. Sweep-type events convecting over the carpet are responsible for the excitation of oscillations in the front rows. Further downstream, the frequencies of the oscillatory motion decrease about a factor of 2-3. This transformation happens in a rather continuous form over the course along the carpet. Simultaneous to the decrease of frequencies one can observe an increase in spanwise coherence of the hair-motion along the carpet. The autocorrelation profile of $R_{jj}(y+)$ at the front row shows positive values above a coherence of 0.1 over a spanwise range of approximately $90y+$ ($\pm 45y+$). Over the course along the carpet, the autocorrelation values at the flanks become negative and the overall spanwise coherence increases with values close to -0.1 over a spanwise range of $150y+$ ($\pm 75y+$), see the profile on top of the diagram on the left side in Fig. 3. This is an indication of the statistical predominance of anti-symmetric motion patterns over sinusoidal meandering patterns. The varicose wave-type nature of the near-wall turbulent events have already been documented in previous measurements of wall shear-stress patterns (Brücker 2008).

As these wavy flow structures exit similar motion patterns of the surface-hairs as shown above it is of interest to understand the feedback of excited micro-hair motion back onto the flow. Therefore, a reference experiment was carried out with a similar hair carpet positioned in a flow box under controlled conditions of mechanically excited hair-tip motion, see Brücker (2010). Figure 4 illustrates the recorded streaming flow pattern generated by streamwise travelling varicose waves of hair-tip motion along the carpet.

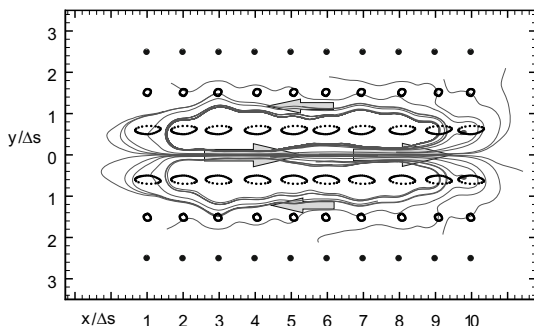


Fig. 4 Streaming motion induced in an array of micro-hairs by excitation of orbital tip-motion in form of varicose waves travelling in streamwise direction (from left to right).

The resulting streamlines show a pronounced concentration of forward streaming flow generated between the two adjacent hair rows centered to the axis of the travelling wave excitation. The forward flow is compensated by backward flow at the flanks of the hairs in the adjacent rows. The close spacing of the micro-hairs leads to a cooperative interaction in the way that the small-scale motions generated at each individual spanwise pair of hairs adds up to a more coherent motion pattern over all successive pairs during the course of the waves travelling downstream along the carpet. The fact that successive waves travel the same path in a short distance (compared to the succession of 3-4 varicose waves in one packet in near-wall turbulence) leads to homogenization and increase of streamwise coherence. The observed negative autocorrelation of Q_x in spanwise direction, see Fig. 3, is a consequence of the induced streaming pattern shown above.

4 Conclusion and Summary

Surface-hairs with an elastic flexibility introduce a mechanism of dynamical energy transfer with the near-wall flow. The specific geometric arrangement of the micro-hairs in parallel streamwise rows shows a specific receptivity of the hair motion to varicose-type wave-trains in the fluid, which are part of the near-wall turbulence auto-generation cycle. The induced wavy hair motion in the carpet generates a streaming flow pattern by hydrodynamic coupling. Thus the micro-hairs convert their elastic energy by cooperative action into larger coherence of the flow

in streamwise and spanwise direction. Though the hairs induce parasitic drag, the overall effect may lead to a measurable turbulent drag reduction. The contributing mechanisms are summarized as follows:

- each individual flexible hair in the viscous fluid acts as a second-order low-pass damping element. With the minimum response time λ_S , a Weissenberg-number can be defined as a characteristic parameter of the interaction which determines the influence of elastic bend-recoil onto the flow;
- hair reconfiguration in streamwise direction imposes anisotropic damping to flow fluctuations. The stronger the mean load the larger becomes the mechanical restriction of spanwise hair fluctuations. In addition, the cylindrical trailing end of the bent hairs impose a flow-opposing body force which is anisotropic in spanwise- and streamwise direction;
- fluid coupling in the dense hair-carpet increases spatial coherence and generates streaming. An appropriate geometric arrangement as described herein can stabilize the velocity streaks.
- because of the self-adaptive reconfiguration, the above described mechanisms remain effective for a larger range of Reynolds-numbers.

Acknowledgements. Part of the study was funded by the German Research Foundation DFG.

References

1. Bartenwerfer, M., Bechert, D.W.: Viscous flow on hairy surfaces. *Zeitschrift fuer Flugwissenschaften und Weltraumforschung* 15, 19–26 (1991)
2. Brücker, C., Bauer, D., Chaves, H.: Dynamic response of micro-pillar sensors measuring fluctuating wall-shear stress. *Exp. Fluids* 42(5), 737–749 (2007)
3. Brücker, C.: Signature of varicose wave packets in the viscous sublayer. *Phys. Fluids* 20, 061701 (2008), doi
4. Brücker, C.: Interaction of near wall turbulence with flexible micro-hairs. *J. Phys.: Condens. Matter* 22 (2010) (accepted July 2010, printed version to appear December 2010)
5. Favier, J., Dauptain, A., Basso, D., Bottaro, A.: Passive separation control using a self-adaptive hairy coating. *J. Fluid Mech.* 627, 451–483 (2009)
6. Iwamoto, K., Fukagata, K., Kasagi, N., Suzuki, Y.: Friction drag reduction achievable by near-wall turbulence manipulation at high Reynolds number. *Phys. Fluids* 17, 011702 (2005)

Analysis of Development of Vortical Structures in a Turbulent Boundary Layer under Adverse Pressure Gradient Based on VITA Method

Artur Drozd, Witold Elsner, and Stanislaw Drobniak

Abstract. The paper concerns experimental investigation of a turbulent boundary layer (TBL) developing on a flat plate under an adverse pressure gradient (APG) for a $Re_\theta \approx 3000$. In particular, the paper deals with the analysis of bursting phenomena in TBL with the use of VITA technique. For interpretation of structure behaviour the shape of conditionally averaged velocity traces recorded by X-wire probe were analysed. It was found that bursting process under the influence of APG is damped near the wall and this phenomenon is emphasized in the outer region of TBL.

1 Introduction

The near wall region is characterised by the presence of low-speed streaks and hairpin vortices assembled into large-scale coherent groups termed vortex packets. Those structures are qualitatively consistent with the horseshoe vortex model proposed by Theodorsen [4]. The oscillation and then the breakup of these structures, termed as bursting phenomena, cause high gradients of velocity in time and in space. One of the methods which allows for the detection and analysis of bursting process was proposed by Blackwelder & Kaplan [1] VITA (Variable Interval Time Average), which relies on rapid changes in the velocity time signal recorded with a hot-wire anemometry technique. To describe the relation of u - streamwise and v - normal velocity components in xy plane a quadrant analysis is commonly

Artur Drozd

Czestochowa Univ. of Technology, Armii Krajowej 21, Poland
e-mail: arturdr@imc.pcz.czest.pl

Witold Elsner

Czestochowa Univ. of Technology, Poland, Armii Krajowej 21
e-mail: welsner@imc.pcz.czest.pl

Stanislaw Drobniak

Czestochowa Univ. of Technology, Poland, Armii Krajowej 21
e-mail: drobniak@imc.pcz.czest.pl

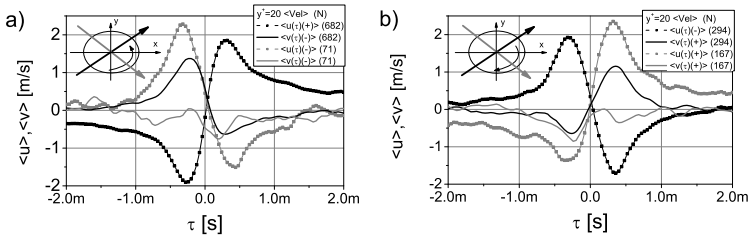


Fig. 1 Phase averaged velocities courses during detections with the vortex passage directions schemes: retrograde (a), prograde (b)

used. This analysis allows identifying the effect of ejection in $Q2$ and the effect of sweep in $Q4$ quadrants. Main VITA bursting events, which produce fluctuations in $Q2$ and $Q4$ quadrants, can be classified as so-called "retrograde" vortical structure of positive vorticity and "prograde" vortical structure of negative vorticity. Prograde vortical structures can be interpreted as hairpin head, and retrograde as a result of inclined shear layers between to consecutive hairpins. Two convection directions for both vortical structures also exist: ascending (moving away from the wall) and descending (moving towards the wall). In the current research the VITA technique was used and applied for the analysis of two velocity components recorded by an X-wire probe in a flow under the APG. Furthermore, the motion of vortices was deduced from phase averaged velocity distributions.

2 Experimental Methods

The experiment was performed in an open - circuit wind tunnel, where the TBL developed along a flat plate, which was 2807 mm long and 250 mm wide (the details of experimental rig and measuring procedures may be found in [3]). The upper wall was shaped according to the distribution of pressure gradient, and corresponded to the conditions encountered in stator passages of turbomachinery. The mean velocity at the inlet plane outside the boundary layer was 15m/s, while the turbulence intensity was equal $T_u \approx 0.4\%$. Two velocity components were measured in several cross-sections of APG region with an X-wire probe (Dantec Dynamics 55P52). For the purpose of the current investigation four cross-sections at $x_s = 487, 577, 667$ and $787mm$ of relative distances $Sg = 0.456, 0.541, 0.625, 0.728$ were chosen. The X-wire probe was combined with the DISA 55M hot-wire anemometer and connected to PC computer. The VITA detection scheme is based on analysis of the running variance $var(t, T)$ of detection parameter $a(t)$ given by equation:

$$var(t, T) = \frac{1}{T} \int_{t-T/2}^{t+T/2} a(t')^2 dt' + \frac{1}{T} \left[\int_{t-T/2}^{t+T/2} a(t') dt' \right]^2 \quad (1)$$

Parameters of the detection process were properly tuned in order to obtain the best possible efficiency of this procedure. To obtain better instantaneous time derivative of a signal streamwise u velocity component was selected as a basic detection

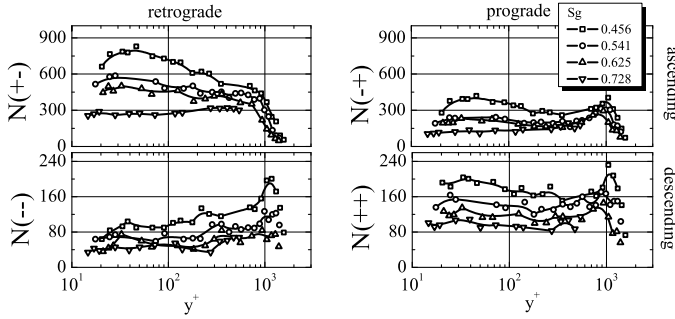


Fig. 2 Changes in number of events N in y^+ coordinate along the flow for four types of detections

parameter $a(t)$. Signs of derivatives du/dt and dv/dt were used to distinguish between four possible quadrants of bursting events discussed above. For the current research a threshold value $k(u_{rms})^2$ of detection function $D(t, T)$ was properly adjusted and a time averaging window T was related to the scale of main event. To distinguish between individual vortical structures the following values $\{-2, -1, 0, 1, 2\}$ were assigned to the detection function $D(t)$.

3 Results and Conclusions

The detailed analysis of flat plate TBL performed by Materny et al. [3] showed that the APG induced a rapid build-up of the boundary layer, which was accompanied by the decrease of wall shear stresses. It was demonstrated that the near wall region grew much more slowly than the outer part of the boundary layer, which in turn implied that most of the contribution to APG boundary layer growth originated from areas located far from the wall. This conclusion was supported by the analysis of u' and v' distributions, where the single maximum located in the immediate vicinity of the wall gradually decays, while the outer maximum becomes the more pronounced in the downstream area (see Fig. 3a). The attempt to further clarify the process is presented within the paper. To describe four possible VITA events the sample time traces of phase averaged velocities $\langle u \rangle$ and $\langle v \rangle$ for normalized coordinate $y^+ \approx 20$ for the first plane are presented at Fig. 1. Schemes present types of vortices passing through the sensor location and arrows show the passage directions of the vortices. Identified retrograde vortical structures are shown at Fig. 1a) and prograde at 1b). Distributions of the $\langle u \rangle$ and $\langle v \rangle$ are approximately 180° out of phase for ascending structures (black arrows and distribution lines) and in the phase for descending ones (grey arrows and distribution lines). The first important quantity describing the change of bursting frequency is presented at Fig. 2 as a number of four types of VITA events detected along the flow. Each of four distributions represents the particular measuring station. It is seen that for each type of VITA event the number of structures decreases along the flow, but the stronger

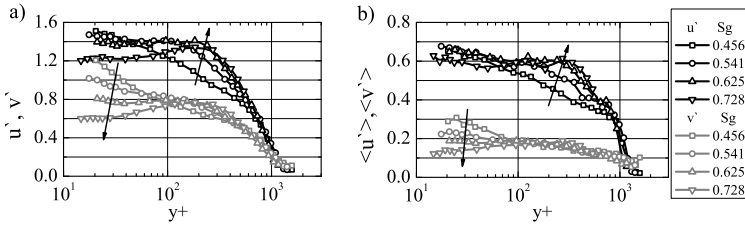


Fig. 3 u' , v' profiles a) and phase averaged $\langle u' \rangle$, $\langle v' \rangle$ profiles b) along the flow

decrease is observed for $N(+)$ retrograde ascending vortex in inner part of boundary layer $y^+ < 200$. The decrease in the number of vortices along the flow indicates that the bursting frequency is reduced under APG conditions, and to clarify the process the changes of mean value of fluctuation of detected events were calculated within the boundary layer. The mean value of fluctuations was obtained from a phase averaged velocity distribution during vortex passage. Fig. 3b presents conditionally averaged (VITA) velocity fluctuations as a function of y^+ coordinate for four consecutive cross-sections. One can observe a small drop of both values in the inner layer (below $y^+ \approx 80$) and an increase in the outer layer (above $y^+ \approx 80$) may be noticed along the flow. The behavior is similar to the change of u' , v' distributions shown in Fig. 3a.

Our analysis confirms that the turbulent kinetic energy production is closely related to the bursting events, but is modified by APG conditions. This modification explains change of velocity fluctuation profiles near the wall where these vortices dominate and confirms a less pronounced contribution of near-wall region to the downstream development of TBL. In parallel, the higher energy is produced by a bursting process in the outer region of TBL where the outer peak in intensity is observed.

Acknowledgements. The investigations was supported by the European Social Funding project no.: POKL. 04.01.01-00-059/08, (2009-2010) as well as Grant no.: N N501 098238 (2010-2011).

References

1. Blackwelder, R.F., Kaplan, R.E.: On the wall structure of the turbulent boundary layer. *JFM* 76, 89–112 (1976)
2. Krogstad, P.A., Skare, P.E.: Influence of a strong adverse pressure gradient on the turbulent structure in boundary layer. *Phys. Fluids* 7(8) (1995)
3. Materny, M., Drozd, A., Drobnik, S., Elsner, W.: Experimental Analysis of Turbulent Boundary Layer Under the Influence of APG. *Archives of Mechanics* 60, 1–18 (2008)
4. Theodorsen, T.: Mechanism of turbulence. In: Proc. 2nd Midwestern Conference on Fluid Mechanics, pp. 1–19. Ohio State University, Columbus (1952)

New Insights into Adverse Pressure Gradient Boundary Layers

W.K. George, M. Stanislas, and J.-P. Laval

Abstract. We hypothesize that far enough downstream the *mean* velocity profile in any non-separating adverse pressure gradient turbulent boundary layer will become inflectional. While this evolution is underway a universal scaling for the outer flow is impossible. Once the profile is fully-developed, however, there is significant support for the Castillo/George [2, 4] theory.

Introduction

The theory proposed by Castillo and George [2, 4] (hereafter referred to collectively as GC) for adverse pressure gradient boundary layers was quite successful in accounting for the flow development in a number of relatively high Reynolds number experiments as cited in their paper. It has also been confirmed by the more recent data of Skåre and Krogstad [7] and Elsberry et al. [3] (see their appendix). In particular CG argued that the outer flow could be scaled with the free stream velocity, U_e (or mathematical equivalent U_∞) and the boundary layer thickness, δ_{99} . The turbulence normal stresses scaled with U_e^2 , but the Reynolds shear stresses scaled as $U_e^2 d\delta/dx$. Also, and quite surprisingly (even to them) they deduced that $\Lambda = [\delta_{99}/(d\delta_{99}/dx)][1/(\rho U_e^2)]dP_e/dx = -[\delta_{99}/(d\delta_{99}/dx)][1/U_e]dU_e/dx = \text{constant}$, where the constant depended on the initial conditions. They also showed that Λ can be most easily determined graphically as the negative of slope of a straight line fit to $\log U_e$ versus $\log \delta_{99}$ (since $\delta \propto U_e^{-1/\Lambda}$). Unlike previous theories which assume various power laws for U_e in x , the CG theory applies

W.K. George · M. Stanislas

Univ Lille Nord de France, ECLille, LML, F-59650 Villeneuve d'Ascq, France

e-mail: georgewilliamk@gmail.com, michel.stanislas@ec-lille.fr

J.-P. Laval

Univ Lille Nord de France, CNRS, UMR 8107, F-59650 Villeneuve d'Ascq, France

e-mail: jean-philippe.laval@univ-lille1.fr

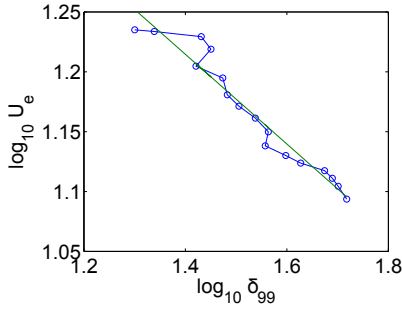


Fig. 1 Castillo/George diagram of $\log U_e$ versus $\log \delta_{99}$ using data of Skåre and Krogstad [7]. $\Lambda = 0.227 \pm 1.2\%$.

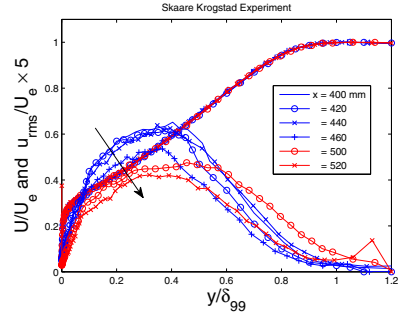


Fig. 2 Mean and RMS (multiplied by 5) streamwise velocity normalized by U_e versus y/δ_{99} . Data of Skåre and Krogstad [7].

to any imposed free stream velocity (or pressure gradient) variation as long as the flow remains attached.

Fig. 1 shows the CG diagram for the data of Skåre and Krogstad [7]; clearly the data fall on a straight line from which Λ can be determined to be $0.227 \pm 1.2\%$. Fig. 2 shows plots of the mean and RMS streamwise velocity in CG variables for all reported downstream positions (from 4m to 5.2m). The collapse of the mean velocity profile is quite spectacular, but the RMS streamwise fluctuating velocity is still evolving. Here and elsewhere the arrow indicates increasing downstream distance. The Elsberry et al. [3] data go farther downstream so this evolution is completed for all the turbulence moments. It is also important to note that the *mean* velocity profile in both experiments is an inflectional profile with the location of the inflection point at $y/\delta_{99} \approx 0.5$. This seems to have been noticed only by Elsberry et al. [3].

1 Developing APG Boundary Layers

By contrast with the experiments cited above, the CG theory has been less successful, however, in accounting for other recent experiments and DNS, a number of which were considered in a recent paper by Shah et al. [6]. They documented adverse pressure gradient flows (APG's), with and without wall curvature, in which the turbulence intensity peak moved quite sharply away from the wall with increasing distance downstream from the point at which the APG was imposed. To quote them: “*Different experimental and numerical data-sets have been analyzed for the flow in a turbulent boundary layer with different adverse pressure gradients. The development of a turbulence peak is evidenced, which is present both with and without wall curvature. This peak is quite different from the one found in ZPG turbulent layers: it is wider, stronger and moving away from the wall. This means that this peak should have a different physical origin from the standard near wall peak.*” They

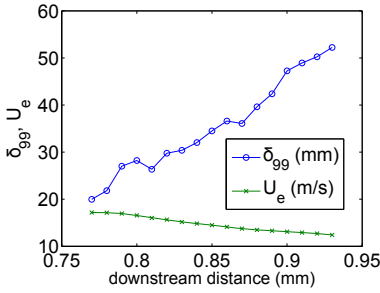


Fig. 3 δ_{99} and U_e vs. downstream distance, data of Materny et al. [5].

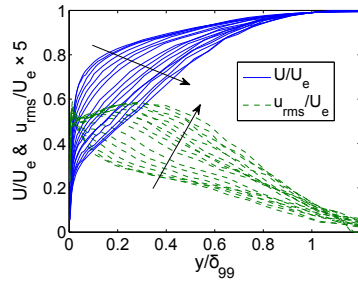


Fig. 4 Mean and RMS streamwise velocity normalized by U_e vs. y/δ_{99} , [5].

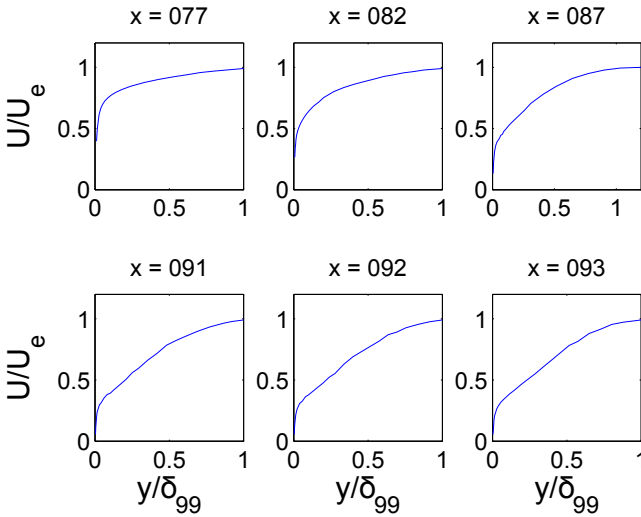


Fig. 5 Plots of U/U_e vs. y/δ_{99} showing downstream evolution, Materny et al. [5].

further suggested that this peak was triggered by the adverse pressure gradient and had its origin in an instability hidden in the turbulent boundary layer, developing soon after the change of sign of the pressure gradient. They then offered that this may explain the difficulties encountered up to now in finding a universal scaling for turbulent boundary layers.

Typical of these experiments is the non-separating APG boundary layer of Materny et al. [5] for which Re_θ varies from 1767 to 5705 and the shape factor from 1.27 to 1.86. Fig. [3] shows how the boundary layer thickness and outer flow velocity change with downstream distance. Fig. [4] shows the downstream evolution of the streamwise mean velocity and turbulence intensity,

both normalized in CG variables. The labeled positions are mm from the leading edge, and the adverse pressure gradient begins at the first position shown ($077\ mm$). The mean velocity profiles clearly change shape continuously and cannot be made to collapse. Fig. 5 shows how the mean velocity profiles flatten downstream towards inflectional profiles like those seen in the Skåre/Krogstad and Elsberry et al. experiments cited above. The inflection point locations correspond closely to the developing outer peak in the streamwise turbulence intensity. The Aubertine-Eaton [1] experiment shows approximately the same behavior.

Summary and Conclusions

Thus there is clear evidence for the development of an inflectional mean velocity profile downstream of the imposition of an adverse pressure gradient; and it is quite independent from whether the flow ultimately separates or not. Its location is not far from the observed peak in the streamwise turbulence intensity in the main part of the boundary layer. The distance over which this evolution occurs depends on the upstream boundary layer and the manner in which the APG is imposed. While this evolution is underway a universal scaling for the outer flow is impossible. Once the profile is fully-developed, however, there is significant support for the claims of the CG theory.

References

1. Aubertine, C., Eaton, J.K.: *J. Fluid Mech.* 532, 345–364 (2005)
2. Castillo, L., George, W.K.: *AIAA J.* 39, 1–41 (2001)
3. Elsberry, K., Loeffler, J., Zhou, M.D., Wynanski, I.: *J. Fluid Mech.* 423, 227–261 (2000)
4. George, W., Castillo, L.: In: So., R.M.C., Speziale, C.G., Launder, B.E. (eds.) *Near Wall Turbulent Flows*, pp. 901–910. Elsevier (1993)
5. Materny, M., Drozd, A., Drobniak, S., Elsner, W.: *Archv. Mech.* 60, 449–466 (2008)
6. Shah, S.-I., Laval, J.-P., Stanislas, M.: In: Stanislas, M., Jimenez, J., Marusic, I. (eds.) *Progress in Wall Turbulence: Understanding and Modelling*, pp. 257–265. Springer (2010)
7. Skåre, P.E., Krogstad, P.-A.: *J. Fluid Mech.* 272, 319–348 (1994)

Flat Plate Boundary Layer By-Pass Transition by Joint Action of Surface Roughness and External Turbulence

O. Hladík, P. Jonáš, O. Mazur, and V. Uruba

Abstract. Flat plate boundary layer by-pass transition by joint action of surface roughness and external turbulence is investigated. The transition process is promoted by both free-stream turbulence and surface roughness. Two independent methods for transition region identification are suggested giving the similar results in various situations. The method of determination of the instantaneous values of wall friction on smooth and rough surface is suggested. The distribution of intermittency factor is evaluated from records of the instantaneous values of wall friction. Estimations of onset and the end of the transitional region from intermittency factor are compared with those from distribution of skin friction coefficient.

1 Introduction

The investigated boundary layer was developed over a smooth and rough surface flat plate ($0.9m$ wide and $2.75m$ long) placed inside a closed circuit wind tunnel ($0.5 \times 0.9m^2$). The rough surface consisted of $60 - grit$ sandpaper, typical height of the roughness elements was $0.435mm$.

Mean flow velocity outside the boundary layer was $5.2m/s$ ($\pm 3\%$) in average. Free stream turbulence was controlled by means of square mesh plane grid. The turbulence intensity was 0.3% without the turbulence generator and 3% with it. The dissipation length parameter was $Le = 33.5mm$ in the later case in the leading edge plane $x = 0$. For more details see Ref. [3].

2 Measurement and Evaluation Methods

Evaluation of the mean velocity profiles was based on pressure measurements with combined flattened Pitot tube and round nosed static pressure probe. The probes

O. Hladík · P. Jonáš · O. Mazur · V. Uruba

Institute of Thermomechanics ASCR, v.v.i., Dolejskova 5, 180 00 Praha 8, Czech Rep.

e-mail: hladik@it.cas.cz

were moving together in the streamwise direction x and in the direction of the normal to the surface. Details on the measurement and evaluation techniques are given in [5].

The evaluated distributions of the time average skin friction coefficient C_f follow the Blasius solution for laminar flow structure and the Ludwig and Tillmann formulae for turbulent boundary layer. Therefore it can be used for estimation of the onset and the end of the transitional region.

The measurement of instantaneous wall friction with hot wires (HWs) was done. To ensure constant distance of the probe from the wall a device with 3 wheels has been developed. It was connected to the traversing system and it was dragged in the streamwise direction along the surface. It was carrying the probe with two heated parallel wires (DANTEC t.55P71) oriented parallel to the surface. The wall proximity corrections were applied on the HW readings, as the probe is moving in a close proximity along the surface. The classical Willis correction was applied.

In principle, direct calculation of the skin friction τ_w and shift of the zero level y_0 could be possible:

$$\tau_w = \mu(T)(\partial U/\partial y)_w = \mu(T)(U_2 - U_1)/\Delta y, \quad y_0 = \Delta y U_1/(U_2 - U_1) - y_1. \quad (1)$$

In reality, an additional calibration of skin friction is necessary as the wall correction is not exactly known and the shift y_0 was changed with moving the probe streamwise, in x direction. Therefore the distributions of the time averaged skin friction coefficient C_f evaluated from pressure measurements were applied during an indirect local calibration assuming

$$\overline{\tau_w} = 0.5 \cdot \rho_e \cdot U_e^2 \cdot C_f = K_i \cdot \overline{U}_i; \quad i = 1, 2. \quad (2)$$

Next, the coefficients K_i are valid at the same boundary conditions as for the pressure measurement. Evaluation of the instantaneous values of wall friction τ_w' is obvious.

This intermittent signal was analyzed to evaluate the intermittency factor γ . In literature a lot of methods of intermittent signal analysis could be found. A review of classical methods is given in [1], more recent methods are shown in [6].

In our case the TERA (Turbulent Energy Recognition Algorithm) method was chosen. The method consists of several consecutive steps. The first obtained records of the instantaneous values of wall friction τ_w' are filtered using the Butterworth filter with low pass frequency 1kHz to eliminate noise from the signal. At the second step the detector function $D(t)$ is derived as to emphasize the differences of the signal time behaviour during turbulent and non-turbulent periods. Here the detector function has been computed by the formula:

$$D(t) = |u(\partial^2 u/\partial t^2)|, \quad (3)$$

where u is fluctuation of the stream wise velocity component. Then the detector function is smoothed to eliminate the scales much smaller than those we are going to recognize, thus the criterion function $K(t)$ is created (details are presented in [2]).

The next step is evaluation of the indicator function $I(t)$ that can be used to distinguish between the non-turbulent and turbulent portions of signal. It is defined as follows:

$$K(t) \leq C \Rightarrow I(t) = 0 \quad \text{and} \quad K(t) > C \Rightarrow I(t) = 1, \quad (4)$$

where C is dimensionless threshold constant for the given criterion function. The indicator function $I(t)$ is equal to 0 in the non-turbulent signal portions of the signal and it is equal to 1 in the turbulent portion. Having determined the indicator function $I(t)$ the intermittency factor γ can be calculated in usual way. The long time average of the indicator function with the physical meaning of probability that the turbulent flow occur within the given flow field point.

For analysis 750 thousand samples were acquired with frequency $25kHz$ for each x position.

3 Results

The streamwise distributions of the transitional intermittency factor as well as the distributions of skin friction coefficient are shown in Figs. 1 and 2. First, the separate influence of surface roughness and free-stream turbulence was examined. In Fig. 1 the turbulence generator was used on smooth surface (left) and natural free-stream turbulence on rough plate (right). Then, Fig. 2 shows joint action of free-stream turbulence and rough surface. The onset of transition process is characterized by departure of skin friction curve from Blasius solution and in the end approaches the Ludwig and Tillmann curve. In terms of intermittency curve, onset of transition corresponds to minimum of its value (ideally 0) and the end of transition region is indicated by $\gamma \approx 1$. Increasing value of the intermittency coefficient upstream the transition onset could be explained by disturbances penetrated from outside the boundary layer.

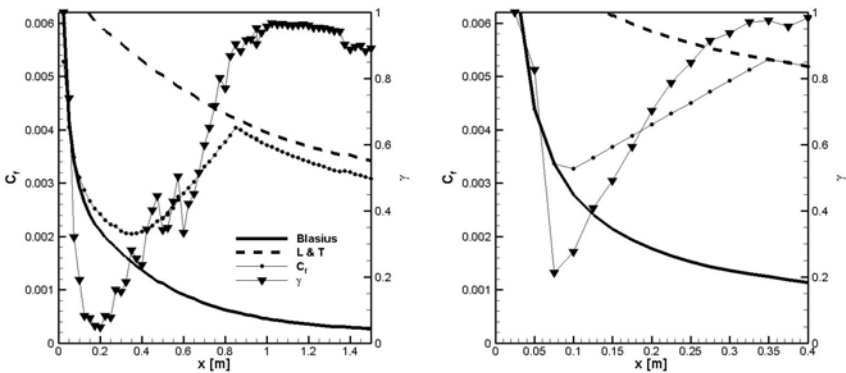
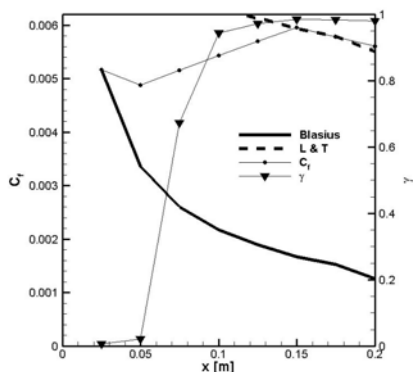


Fig. 1 Distributions of skin friction and intermittency coefficients on flat plate affected by increased free-stream turbulence (left) and surface roughness (right)

Fig. 2 Distributions of skin friction and intermittency coefficients on rough flat plate affected by increased free-stream turbulence



Conclusions

Position and length of transition region is strongly affected by surface roughness and free-stream turbulence, joint action increases the effect. Two methods of transitional region determination for various cases are shown.

Acknowledgements. This work was supported by the Grant Agency of the Academy of Sciences of the Czech Republic IAA200760614 and by the Grant Agency of the Czech Republic projects No. 101/08/1112.

References

1. Hedley, T.B., Keffer, J.F.: Turbulent/non-turbulent decision in an intermittent flow. *J. Fluid Mech.* 64, pt. 4, 625–644 (1974)
2. Hladík, O., Uruba, V.: Analysis of intermittent signal. *Mechanical Engineering J.*, 69–70 (June 2009) ISSN 1335-2938
3. Jonáš, P., Mazur, O., Uruba, V.: On the receptivity of the by-pass transition to the length scale of the outer stream turbulence. *Eur. J. Mech. B Fluids* 19, 707–722 (2000)
4. Jonáš, P., Mazur, O., Uruba, V.: Some properties of boundary layer under the joint effect of external flow turbulence and surface roughness. In: Schlatter, P., Henningson, D.S. (eds.) *Seventh IUTAM Symposium on Laminar-Turbulent Transition*. IUTAM, vol. 18, pp. 505–508. Springer, Heidelberg (2009)
5. Jonáš, P., Mazur, O., Uruba, V.: Comparison between the wall roughness effect and the free stream turbulence impact and their joint action on boundary layer development. *ER-COFTAC Bulletin* 80, 82–86, EPFL Lausanne (2009)
6. Uruba, V., Jonáš, P., Mazur, O.: The Methods of Intermittency Analysis. In: *Proceedings of Engineering Mechanics 1998*, Svratka, May 11-14, vol. 4, pp. 781–786 (1998)

Low Speed Streaks Instability of Turbulent Boundary Layer Flows with Adverse Pressure Gradient

J.-P. Laval, M. Marquillie, and U. Ehrenstein

Abstract. A Direct Numerical Simulation of turbulent flow subjected to an adverse pressure gradient (APG) was performed. As already noticed by many authors in such configurations, a second outer peak of turbulent kinetic energy is observed in the region of APG. In the present configuration, this peak is due to the production of intense vortices which are shown to be related to the instability of low speed streaks.

The turbulent boundary layer flow subjected to an adverse pressure gradient (APG) induced by curvature is of crucial importance for many applications including aerodynamics of airfoils, ground vehicles or turbine blades. Significant progress is needed in understanding the near wall turbulence in order to improve the theoretical and numerical models. The available numerical models usually fail to predict flows at the onset of separation as they are based on scalings which are no more valid with pressure gradient. In flows with adverse pressure gradients, a strong secondary peak of turbulent kinetic energy has been observed in many configurations and is not yet fully explained [7]. Therefore, a careful analysis of turbulent structure generation is an opportunity to make progress in designing accurate statistical models for turbulence. Using the numerical solution procedure documented in [4] a database of channel flow with curved wall has been generated at Reynolds number $Re_\tau \approx 600$. The flow slightly separates at the lower curved wall and is at the onset of separation at the upper wall. Therefore, two different configurations of pressure gradient as well as the effect of wall curvature can be investigated and compared.

J.-P. Laval · M. Marquillie

Univ Lille Nord de France, CNRS, UMR 8107, F-59650 Villeneuve d Ascq, France

e-mail: jean-philippe.laval@univ-lille1.fr,

matthieu.marquillie@univ-lille1.fr

U. Ehrenstein

Aix Marseille Univ, IRPHE UMR 6594, CNRS, F-13384 Marseille 13, France

e-mail: ehrenstein@irphe.univ-mrs.fr

As reported for the same simulation at lower Reynolds number [4], the statistics of the turbulent kinetic energy production exhibit a strong peak at the beginning of the adverse pressure gradient region. This corresponds to the generation of vortices much stronger than typical vortices in the buffer and log region of a boundary layer without pressure gradient. The observed production of intense vortices in the APG regions is likely to be associated with some instability mechanism of coherent flow structures, such as streamwise velocity streaks which are known to be key features of wall turbulence [1].

The presence of elongated streaks gives rise to inflectional velocity profiles in the surrounding flow, exciting secondary instabilities which evolve into streamwise vortices, leading to a self-sustained process in shear flows (cf. [8]). Streak instabilities have been studied in zero-pressure gradient shear flows, such as channel flows, confirming that the instability is of inflectional type and that the instability induces spanwise oscillations of the streak ([2], [6]). Anti-symmetric perturbations are likely to be selected for inflectional streak base flow profiles in the spanwise direction, whereas wall-normal inflection points rather trigger varicose (symmetric) instability modes. In the present configuration, streaks are affected by the pressure gradient and the different models of low speed streaks extracted from experiments in zero pressure gradient boundary layers are irrelevant. In the present study, low speed streaks structures were not modeled but have been directly extracted from our database using methods known as *skeletonization* in image processing [5]. The algorithm is described in [3] and includes successive steps of thresholding and filtering which were tuned to the detection of low speed streaks. An example of instantaneous streak-skeletons near the lower curved wall is shown in Fig. 1. Individual streaks in the wall normal plane (y, z) averaged in time and superimposed on the mean streamwise velocity have been used as basic states for a linear stability analysis (see Fig. 2).

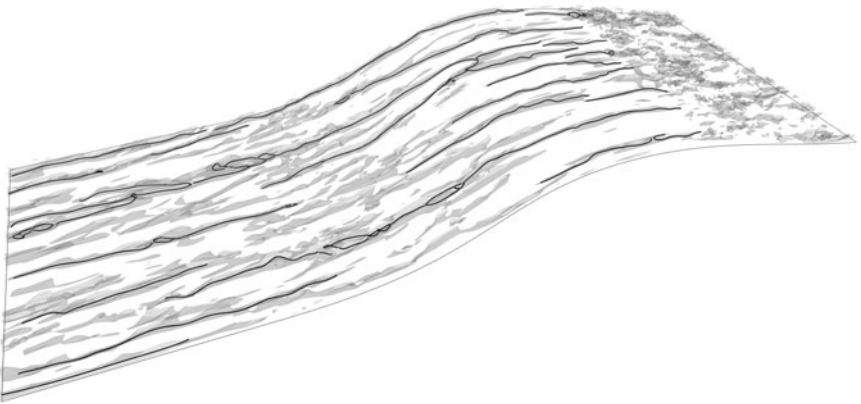


Fig. 1 Results of the 3D detection of low speed streaks at the curved wall of the channel (the skeletons are indicated in black) which are destroyed by the adverse pressure gradient downstream the summit of the bump.

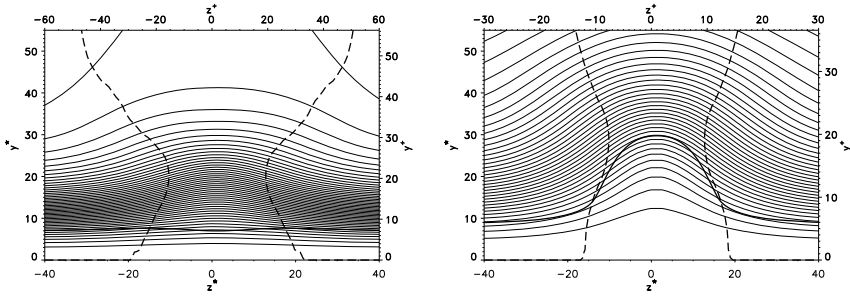


Fig. 2 Contour plot of lower streak base flow (left) upper streak base flow (right) at the location of instability. The continuous lines and the dash lines indicate the position of normal and spanwise inflexion points respectively and the Y-axis are given in local wall unit (+) and reference wall unit (*) based on the friction velocity at the summit of the lower bump.

Two-dimensional modes $\hat{\mathbf{u}}(y, z)e^{i\alpha x}$ have been computed at positions along the lower curved wall as well as the upper wall. The instability onset is shown to coincide with the strong peak of turbulent kinetic energy observed in the direct numerical simulation. The shape and the size of the (varicose) instability modes (see Fig. 3) is governed by the streak structure, while the instability is mainly associated with the inflectional mean velocity profile in the wall-normal direction. An example of typical coherent vortices observed in the direct numerical simulation, with the associated streak skeleton, is shown in Fig. 3. In contrast to the lower wall with a stronger APG, at the upper wall the mean velocity profiles are stable and the streak structure itself plays the dominant role in the instability mechanism. This is shown in Fig. 4 where intense vortices are seen to emerge from the streak skeletons.

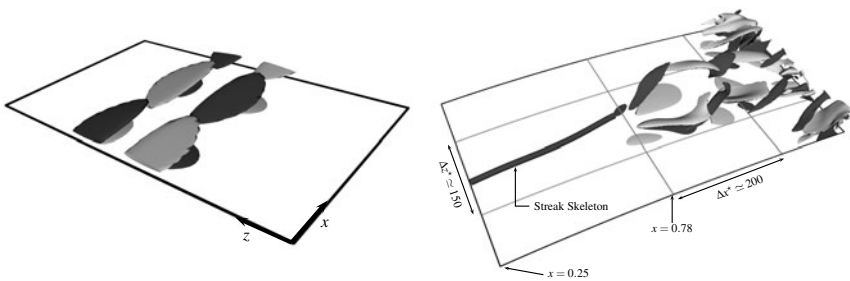


Fig. 3 Left: Visualization of the most unstable mode (varicose) from the stability analysis of streamwise velocity conditionally averaged by streaks. The size of the vortical structures are comparable to the size of the coherent structures observed in the DNS. Right: Positive (dark grey) and negative (light grey) streamwise vorticity of coherent structures from DNS at the origin of the peak production of turbulent kinetic energy. The end of the low speed streak skeleton aligned with a vorticity structure is visualized by a back tube.

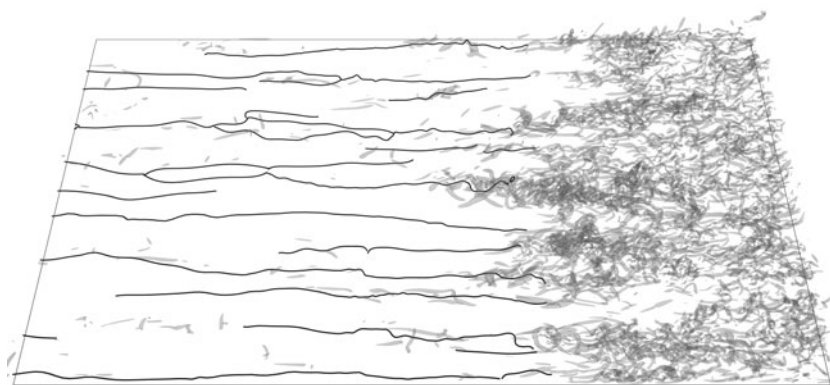


Fig. 4 Iso value of the Q-criterion (light grey) and skeleton of the low speed streaks (black tubes) at the upper wall in the region of instability.

One may conjecture, whether the reported results are generic for adverse-pressure wall turbulence and can explain the strong peak of turbulent kinetic energy which is a general feature in the presence of APG. Streak breakdown will certainly to be interpreted in the light of turbulence modeling of APG flow. Indeed, the mean turbulent velocity gradients are at the heart of RANS-modeling, which is unlikely to be reliable in the presence of turbulence production peaks as a result of a streak instability mechanism.

References

1. Asai, M., Manigawa, M., Nishioka, M.: The instability and breakdown of near wall low-speed streaks. *J. Fluid Mech.* 455, 289–314 (2002)
2. Elofsson, P.A., Kawakami, M., Alfredsson, P.H.: Experiments on the stability of stream-wise streaks in plane poiseuille flow. *Phys. Fluids* 11, 915–930 (1999)
3. Marquillie, M., Ehrenstein, U., Laval, J.-P.: Instability of streaks in wall turbulence with adverse pressure gradient. *J. Fluid Mech.* 681, 205–240 (2011)
4. Marquillie, M., Laval, J.-P., Dolganov, R.: Direct numerical simulation of separated channel flows with a smooth profile. *J. Turbulence* 9(1), 1–23 (2008)
5. Palágyi, K., Kuba, A.: A parallel 3D 12-subiteration thinning algorithm. *Graphical Models and Image Processing* 61, 199–221 (1999)
6. Reddy, S.C., Schmid, P.J., Baggett, J.S., Henningson, D.S.: On the stability of stream-wise streaks and transition thresholds in plane channel flow. *J. Fluid Mech.* 455, 269–303 (1998)
7. Shah, S.I., Stanislas, M., Laval, J.-P.: A Specific Behavior of Adverse Pressure Gradient Near Wall Flows. In: Stanislas, M., Jimenez, J., Marusic, I. (eds.) *Progress in wall turbulence: understanding and modelling*, April 21–23, 2010. ERCOFTAC, pp. 203–209. Springer, Heidelberg (2010)
8. Waleffe, F.: On a self-sustaining process in shear flows. *Phys. Fluids* 9, 883–900 (1997)

Turbulent Boundary-Layer Flow: Comparing Experiments with DNS

R. Örlü and P. Schlatter

1 Background

Since the first direct numerical simulation (DNS) of turbulent channel flows became available more than two decades ago a large number of DNS have been performed for various flow cases, and steadily increased the Reynolds number (Re) extent, finally reaching those ranges put forward by well-resolved experiments. Hence, it was not surprising that a detailed comparison between DNS and experiments in turbulent channel flow [1] showed good agreement for the first and second order moment as well as spectral distributions of the streamwise velocity component.

DNS of spatially developing flows, such as the zero pressure-gradient (ZPG) turbulent boundary layer (TBL), on the other hand, have only recently become feasible reaching up to Re comparable to those of DNS from high Re channel flows. Furthermore, a recent assessment of published DNS data [2] has revealed that there exists considerable scatter even in basic integral quantities, *e.g.* up to 5 and 20 % in the shape factor H_{12} or skin friction coefficient c_f , as well as first and second order statistics not only within the wake region, but throughout the entire boundary layer far into the buffer region. Despite these differences good agreement between a recent DNS and experiment with similar boundary conditions at $Re_\theta \approx 2500$ has been reported in Ref. [3] for the shape factor and skin friction as well as the first two moments of the streamwise velocity component.

The present contribution aims at deepening the work in Ref. [3] and utilises very recent DNS (up to $Re_\theta = 4300$, obtained using $8 \cdot 10^9$ grid points) [2] and experimental [4] data from a ZPG TBL flow. In addition to detailed comparison of integral quantities, higher order moments, also probability density and spectral distributions are analysed. Despite the challenges of such a flow for both DNS (long boxes due to streamwise development, intermittency in the outer region, dependence on inflow

R. Örlü · P. Schlatter

Linné FLOW Centre, KTH Mechanics, Royal Institute of Technology, SE-100 44 Stockholm, Sweden

e-mail: ramis@mech.kth.se, pschlatt@mech.kth.se

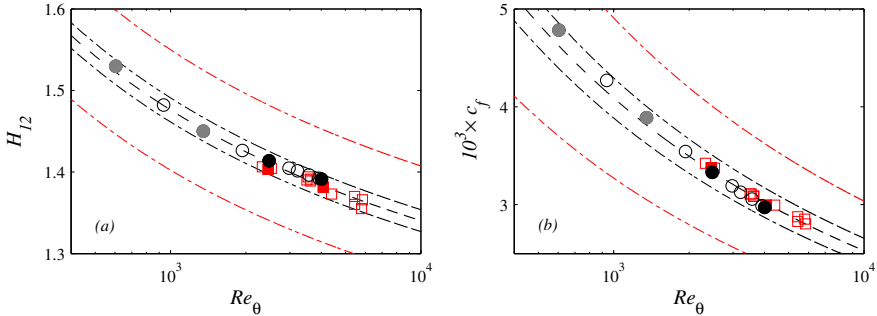


Fig. 1 (a) Shape factor, H_{12} , versus Re_θ . Dashed line represents integration of composite profile [5] and the black and red dash-dotted lines indicate a 1 and 5 % tolerance. (b) Skin friction coefficient, c_f , versus Re_θ . Dashed line represents the correlations by [5] and black and red dash-dotted lines indicate a 5 and 20 % tolerance. While all experimental [4] and DNS [2] data are indicated through \square and \circ , respectively, filled symbols at $Re_\theta \approx 2500$ and 4000 indicate data points listed in Table 1 and are compared in detail in Figs. 2 and 3

conditions/turbulence tripping, *etc.*) and experiments (spatial and temporal resolution, direct skin friction measurements, upstream effects, *etc.*) excellent agreement could be found between both numerical and physical (hot-wire) experiment throughout the entire boundary layer. Minor differences in the buffer region, on the other hand, can directly be related to and explained by insufficient spatial resolution of the hot-wire.

2 Employed Experimental and Numerical Data

The employed DNS and experimental data from a turbulent ZPG TBL flow covers a range of $Re_\theta = 500\text{--}4300$ and $2400\text{--}6000$, respectively, thus featuring an overlapping region in which detailed comparisons can be performed. Consequently, Fig. 1 depicts the shape factor, H_{12} , and skin friction coefficient, c_f , versus Re_θ of the employed data together with a recent correlation [5] for “well-behaved”, *i.e.* “canonical” flows, that agrees well with both data sets. Also indicated are aforementioned tolerances of 5 and 20 % in the shape factor and skin friction, which have been observed in the recent compilation of available DNS of ZPG TBL flows [2].

Note that the experimental c_f values are directly measured by means of oil-film interferometry and hence provide an independent measure of the canonical state of the ZPG TBL flow. A detailed comparison will here be presented for two cases at $Re_\theta \approx 2500$ and 4000 , indicated through filled symbols in Fig. 1 and listed in Table 1, where the experimental and numerical parameters are given and re-evaluated as described in Ref. [2]. The spanwise resolution in the experimental data, due to the length of the hot-wire (indicated through L^+), is less than in the DNS data.

3 Results and Discussion

Based on the good agreement between both data sets in the characteristic integral quantities, depicted in Fig. 1 and recalling that the shape factor is a sensitive indicator of the quality of the boundary layer [5], it can be anticipated that the mean streamwise velocity profiles at a certain Re should agree well between DNS and experiment. This is indeed the case throughout the boundary layer, as shown in Fig. 2(a). While this agreement can also be observed for the turbulence intensity profile, Fig. 2(b), differences become apparent in the insert, in which the near-wall peak region is enlarged. The observed differences can, however, completely be explained by insufficient spatial resolution of the hot-wire probe [6]. This is demonstrated by the dashed lines, which indicate the DNS data evaluated on a larger grid to match the experimental resolution L^+ , *i.e.* $\Delta z^+ \approx L^+$.

A similarly good agreement is obtained for the skewness and flatness factors (not shown here), a result which could be anticipated by the probability density function (pdf) map depicted in Fig. 3(a). Note, that the deviation of the experimental data in the vicinity of the viscous sublayer is an effect of additional heat losses of the hot-wire to the wall and becomes apparent only for low velocity fluctuations. A global view of the energy distribution throughout the boundary layer is presented in the spectral map depicted in Fig. 3(b), that highlights and supplements the already established overall good agreement between the experiments and the DNS.

In summary, the presented comparisons clearly show that the two data sets, obtained both experimentally and numerically, closely match. This result is even more important in the light of the difficulty to obtain “canonical” flow conditions, both in DNS and the wind tunnel; effects such as boundary treatment, pressure gradient, turbulence tripping as well as inflow/upstream effects need to be considered [5, 7]. Therefore, we believe that due to the given cross-validation the data sets, at least for the present Re_θ -range, provide important reference data for future studies.

Table 1 Details of the employed hot-wire [4] and DNS [2] data. Re based on free stream velocity, U_∞ , and momentum-loss thickness, θ , as well as friction velocity, u_τ , and boundary layer thickness, δ_{99} , are denoted by Re_θ and Re_τ , respectively. The grid spacing (in physical space) of the DNS in streamwise, wall-normal and spanwise direction, Δx^+ , Δy^+ , Δz^+ , as well as the hot-wire length, L^+ , are given in wall units, as is the sample interval Δt^+ . The time histories range for about 16 000 viscous time units. Note that for case 4000 only the time-averaged quantities are available, hence $T_B:5$ is compared to case 3900 for pdfs and spectra, and 4000 for time-averaged quantities.

Case	Re_θ	Re_τ	U_∞ [ms ⁻¹]	u_τ [ms ⁻¹]	δ_{99} [mm]	θ [mm]	H_{12}	$c_f \times 10^3$	L^+	Δt^+
$T_B:2$	2 450	830	12.1	0.50	25.6	3.1	1.41	3.38	15	0.27
$T_B:5$	4 030	1 280	20.1	0.78	25.1	3.1	1.38	2.99	24	0.66
			Δx^+	Δy_{min}^+	Δy_{max}^+	Δz^+				
2500	2 470	820	8.9	0.034	11.26	3.8	1.41	3.33		0.30
3900	3 920	1 220	8.5	0.033	10.7	3.6	1.39	2.99		0.27
4000	4 010	1 250	8.5	0.032	10.6	3.6	1.39	2.97		0.27

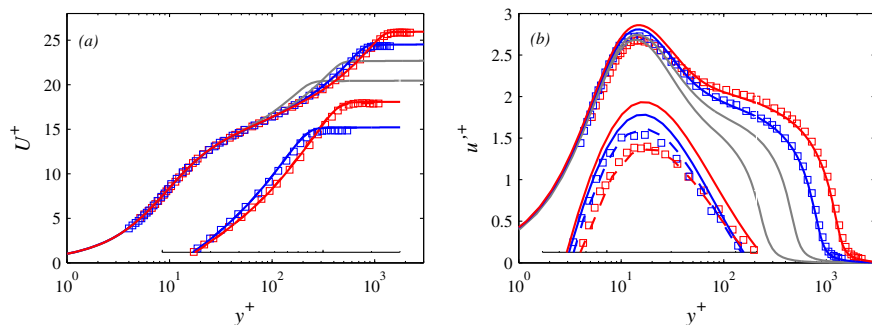


Fig. 2 (a) Inner-scaled mean streamwise velocity profile. (b) Inner-scaled turbulence intensity profile. Insert enlarges the near-wall peak region, in which profiles from spanwise averaged DNS data with equivalent experimental L^+ values are given (---) as well. Numerical (—) and experimental data (\square) shown are those with filled symbols in Fig. 1

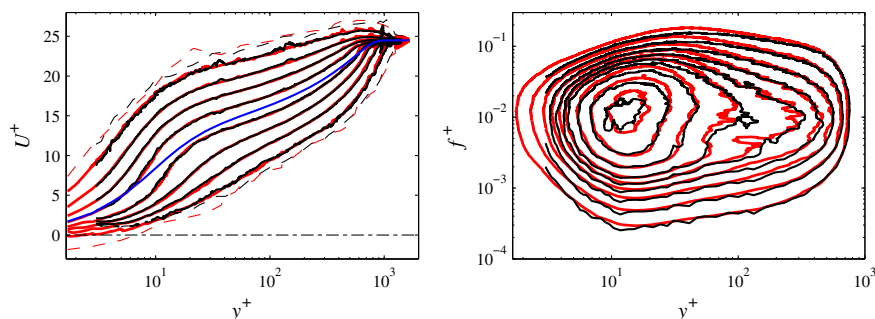


Fig. 3 Experimental (—) and numerical (---) data at $Re_\theta \approx 2500$. (a) Contour map of the inner-scaled pdf with contour levels (solid lines) at 0.001 (outermost), 0.05, 0.35, and 0.85 (innermost) of the pdf maximum. Mean velocity profile from the DNS (—) and pdf extrema (---) are given as well. (b) Spectral map representing the inner-scaled pre-multiplied spectra with contours at 0.175 (outermost), 0.3, 0.45, 0.6, 0.75, 0.9, 1.2, 1.6, and 2 (innermost).

Acknowledgements. This work has been partly supported by STINT through a collaboration between *KTH* and the *University of Bologna*. Computer time was provided by SNIC via a grant from the Knut and Wallenberg Foundation (KAW).

References

1. Monty, J.P., Chong, M.S.: *J. Fluid Mech.* 633, 461–474 (2009)
2. Schlatter, P., Örlü, R.: *J. Fluid Mech.* 659, 116–126 (2010)
3. Schlatter, P., Örlü, R., Li, Q., Brethouwer, G., Fransson, J.H.M., Johansson, A.V., Alfredsson, P.H., Henningson, D.S.: *Phys. Fluids* 21, 051702 (2009)
4. Örlü, R.: Ph. D. thesis, Royal Institute of Technology, Stockholm, Sweden (2009)
5. Chauhan, K.A., Monkewitz, P.A., Nagib, H.M.: *Fluid Dyn. Res.* 41, 021404 (2009)
6. Örlü, R., Alfredsson, P.H.: *Exp. Fluids* 49, 101–110 (2010)
7. Castillo, L., Johansson, T.G.: *J. Turbulence* 3, 1–19 (2002)

Identifying an Artificial Turbulent Spot in the Boundary Layer

B. Rehill, E.J. Walsh, L. Brandt, P. Schlatter, and T.A. Zaki

Abstract. An artificial turbulent spot in a boundary layer with zero freestream turbulence and zero pressure gradient is studied through direct numerical simulation. The spot, generated by a vortex pair disturbance, is identified from the surrounding non-turbulent fluid using six different methods of identification. These techniques involved setting thresholds for: instantaneous wall normal velocity, spanwise velocity, turbulent dissipation, λ_2 -criterion, Q-criterion and the Finite Time Lyapunov Exponent. A sensitivity analysis was performed based on the sensitivity of the maximum spot dimensions to the change in threshold level from its original value. The maximum height, width, length and volume of the spot was recorded for changes in threshold level. Based on this analysis the Q-criterion was found to be the most suitable for identifying a turbulent spot in a flow with zero freestream turbulence.

1 Introduction

A transitional boundary layer comprises of juxtaposed zones of turbulent and non-turbulent flow. Localised patches of turbulence, termed turbulent spots, appear irregularly in time and space with significantly different flow properties than the surrounding non-turbulent fluid [1]. Statistics and other quantities from this flow may give insight into how turbulence develops and sustains itself. To obtain these statistics, the turbulent spot must be treated independently from the surrounding

Brendan Rehill · E.J. Walsh
Univeristy of Limerick, Ireland
e-mail: brendan.rehill@ul.ie

Luca Brandt · Phillip Schlatter
KTH, Stockholm, Sweden
e-mail: luca@mech.kth.se

Tamer A. Zaki
Imperial College London, UK
e-mail: t.zaki@imperial.ac.uk

non-turbulent flow, known as conditional sampling. Many techniques have been used to conditionally sample the flow including derivatives of the instantaneous streamwise velocity fluctuations, u' , or instantaneous turbulent shear stress, $-u'v'$ [9]. A key question is how robust are these methods. The current work focuses on establishing a robust method of identifying these turbulent spots. Direct numerical simulations of a single turbulent spot in a flat plate boundary layer with zero freestream turbulence and zero pressure gradient were performed. The spot was initiated at $x/\delta_0^* = 60$ using a vortex pair disturbance, where δ_0^* is the displacement thickness at the beginning of the computational domain. Similiar vortex pair disturbances have previously been used to trigger turbulent spots [6, 7, 8]. The spot is considered artificial as it was initiated by the vortex pair disturbance.

2 Identification Techniques

The methods of identification employed in the current study are setting threshold levels for (i) instantaneous wall normal velocity, v , (ii) instantaneous spanwise velocity, w , (iii) instantaneous turbulent dissipation, (iv) λ_2 -criterion, (v) Q-criterion and (vi) the Finite Time Lyapunov Exponent. Techniques (i) - (v) are derived from the instantaneous velocity field and its gradient. The Q-criterion locates regions where rotation dominates strain [4]. The λ_2 -criterion identifies vortex cores as pressure minima in a 2-D plane perpendicular to the vortex core [5]. The Finite Time Lyapunov Exponent (FTLE) is a lagrangian technique that measures the rate of separation of neighbouring particle trajectories [2, 3]. Threshold levels for techniques (i)-(iii) needed to vary in the wall normal direction and were based on the spanwise- and streamwise-averaged values of the quantity in question. An advantage of the other techniques is that one threshold could be set for the entire domain. These thresholds however were based on visual analysis of the spot data.

3 Results

The identification techniques were applied to a single turbulent spot with zero freestream turbulence and zero pressure gradient baseflow. Visualisations of the spot shape at a wall parallel plane, $y/\delta_0^* = 4$, are shown in Fig. 1 with the spot edge denoted by the solid black line. Significant differences can be seen in the spot shape depending on identification technique used. It appears that dissipation is concentrated to the rear and centre of the spot leaving this as the most compact representation of the spot shape. The FTLE method shows the spot extending much further in the streamwise direction.

3.1 Sensitivity Analysis

The sensitivity of the overall spot dimensions to the change in threshold level was examined to determine the robustness of each technique. The maximum width,

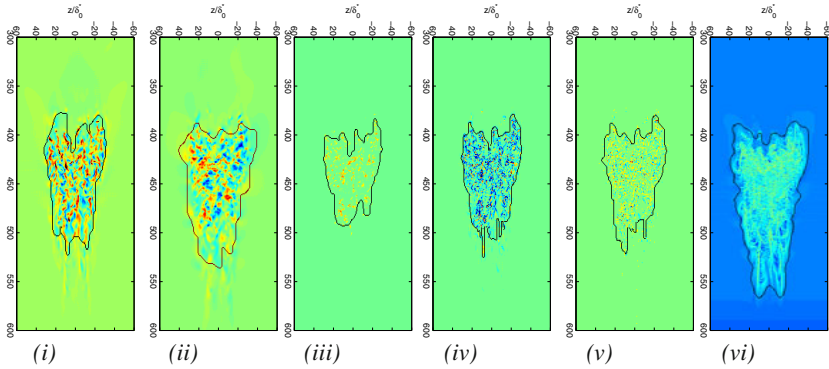


Fig. 1 Visualisation of wall parallel plane at $y/\delta_0^*=4$ showing edge of the turbulent spot denoted by the black line for various identification methods. (i) instantaneous wall normal velocity, v' , (ii) instantaneous spanwise velocity, w' , (iii) instantaneous turbulent dissipation, (iv) λ_2 -criterion, (v) Q-criterion and (vi) the Finite Time Lyapunov Exponent. Flow direction is from top to bottom.

length, height and volume of the spot were recorded to determine which was least sensitive to changes in threshold. Shown in Fig. 2 is the change in maximum volume for a $\pm 20\%$ range of threshold value. The Q-criterion shows the least variation in spot volume with changing threshold, while the FTLE method shows a significant change in spot volume for the same percentage change in threshold value.

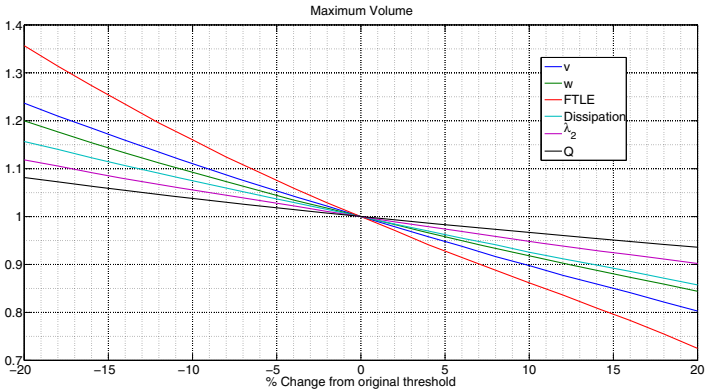


Fig. 2 Variation in maximum volume of the spot for a range of $\pm 20\%$ change from original threshold. Results are normalised with respect to the maximum volume value at the original threshold level.

4 Conclusions

Six techniques have been used to identify a single turbulent spot in an otherwise non-turbulent boundary layer. These techniques involved setting thresholds for: instantaneous wall normal velocity, spanwise velocity, turbulent dissipation, λ_2 -criterion, Q-criterion and the Finite Time Lyapunov Exponent. The Q-criterion performed best based on the sensitivity of the spot dimensions to changes in threshold level. The techniques will now be applied to identify an artificial turbulent spot in the presence of organised streaks, an artificial spot with freestream turbulence and then to natural spots with high levels of freestream turbulence.

Acknowledgements. This work has been supported by the Irish Research Council for Science Engineering and Technology Embark Initiative.

References

1. Emmons, H.W.: The laminar-turbulent transition in a boundary layer. *J. Aero. Sci.* 18, 490–498 (1951)
2. Green, M.A., Rowley, C.W., Haller, G.: Detection of Lagrangian coherent structures in 3D turbulence. *J. Fluid Mech.* 572, 111–120 (2007)
3. Haller, G.: Lagrangian coherent structures from approximate velocity data. *Phys. Fluids* 14(6), 1851–1861 (2002)
4. Hunt, J.C.R., Wray, A.A., Moin, P.: Eddies, stream, and convergence zones in turbulent flows. Center for Turbulence Research Rep. CTR-S88 (1988)
5. Jeong, J., Hussein, F.: On the identification of a vortex. *J. Fluid Mech.* 285, 69–94 (1995)
6. Jocksch, A., Kleiser, L.: Growth of turbulent spots in high-speed boundary layers on a flat plate. *Int. J. Heat Fluid Flow* 29(6), 1542–1557 (2008)
7. Levin, O., Henningson, D.S.: Turbulent spots in the asymptotic suction boundary layer. *J. Fluid Mech.* 584, 397–413 (2007)
8. Lundbladh, A., Johansson, A.V.: Direct simulation of turbulent spots in plane Couette flow. *J. Fluid Mech.* 29, 499–516 (1991)
9. Volino, R.J., Schultz, M.P., Pratt, C.M.: Conditional sampling in a transitional boundary layer under high free-stream turbulence conditions. *J. Fluids Eng.* 125, 405–416 (2003)

Session 8

Wind Energy

Comparison between Wind Tunnel and Field Experiments on Wind Turbine Wake Meandering

S. Aubrun, T.F. Tchouaké, G. España, G. Larsen, J. Mann, and F. Bingöl

1 Introduction

In order to determine the physics driving the wind turbine wake meandering process [4], a previous study has been performed in an atmospheric boundary layer wind tunnel focusing on the unsteady behaviour of a modelled wind turbine wake (i.e. physical modelling based on the actuator disc concept). It was proven that the presence of turbulent scales larger than the wind turbine diameter could be responsible for a random flapping of the whole wake (i.e. wake meandering) [2]. This is indeed the case in full-scale environments, since the large turbulent scales of the atmospheric boundary layer typically are several hundred meters, whereas the diameter of a modern wind turbine rotor is around one hundred meters. PIV measurements of the scaled wind turbine wakes have been performed, and a specific image processing technique enabled to determine the instantaneous deviations of the wake position from its time-average location, as well as the width of the instantaneous wake. The image processing technique originally applied was based on determination of the wake deficit borders through a velocity threshold applied on the instantaneous velocity fields. This first step has already given valuable results [2], but the high turbulence level contained in the flow leads to very noisy velocity fields, making determination of the instantaneous wake deficit border both difficult and uncertain, and thus in turn leading to a lot of rejections. In consequence, an alternative approach, inspired from our Risø-DTU partners, is currently tested [3, 5]. It is based on the determination of a Gaussian profile which optimally fits the instantaneous velocity wake deficit downstream of the modelled wind turbine. The detection of wake borders is then subsequently based on the fitted profile. The new

S. Aubrun · T.F. Tchouaké · G. España
Institut PRISME, University of Orléans, Orléans, France
e-mail: sandrine.aubrun@univ-orleans.fr

G. Larsen · J. Mann · F. Bingöl
Risø-DTU National Laboratory for Sustainable Energy, Roskilde, Denmark, UK
e-mail: gula@risoe.dtu.dk

approach is expected to improve the significance of the obtained statistical information on the unsteady wake properties. The same processing method is applied on full-scale field measurements performed by Risø-DTU using a LIDAR system fixed on the hub of a 20m diameter Tellus turbine [1]. Special care will be given to select field data referring to neutral or quasi-neutral atmospheric stability conditions and with freestream turbulence intensities comparable to those in the wind tunnel experiments. Wind tunnel and field results are then compared.

2 Experimental Set-Up and Signal Processing

In this study, the return test section (5m high, 5m wide and 20m long) of the PRISME Institute wind tunnel "Lucien Malavard" is used to reproduce the properties of two different neutral atmospheric boundary layers at a geometric scale of 1 : 400. Many previous studies enable the choice of the proper parameters to model a moderately rough ABL (roughness length $z_0 = 1\text{cm}$, power law coefficient $\alpha = 0.14$) [6]. At $z = 40\text{m}$ and 140m (in full scale), the upstream turbulence intensity is $I_{u_0} = 18\%$ and 12.5% , respectively. Turbulence length scales are 300m and 450m , respectively. The wind turbine rotor is modelled in wind tunnel with the help of a porous disc made of metallic mesh (solidity 45%) with a diameter of $d = 10\text{cm}$ (40m in full scale) fixed on a tower with a diameter of $0.05d$. The velocity deficit generated by the porous disc is representative of an axial induction factor $a = 0.19$, corresponding to a thrust coefficient $C_T = 0.62$. 2D-2C PIV (TSI) measurements are performed in an horizontal plane downstream of the disc, giving access to 500 snapshots of the horizontal instantaneous velocity field up to a downstream distance $X/d = 6$. For the purpose of comparison with field data explained below, only the horizontal instantaneous velocity profiles at $X/d = 3$ are extracted from the PIV data. Two configurations are tested: the case *WT1* where the centre of the disc (relative to hub height) is located at $z = 40\text{m}$ in full scale, and the case *WT2* where it is located at $z = 140\text{m}$ (See [2] for more details). The latter is not really a realistic configuration but it was chosen in order to locate the disc in a lower turbulent approach flow in order to be in flow conditions closer to field configurations.

Field measurements are performed at the Risø-DTU site in Roskilde, Denmark. The test site is a relatively flat and homogeneous terrain and the dominant wind direction is approximately 290° . The experimental set-up consists of a continuous wave LIDAR system (QinetiQ ZephIR prototype) mounted on the rear of a Tellus wind turbine along with a meteorological mast. The test turbine is a stall-regulated, three-bladed, Tellus 95 kW. The hub height is $H_{hub} = 29.3\text{m}$, and rotor diameter is $d = 19\text{m}$. The line scan mode is adopted: the LIDAR focuses at a single distance ($3d$) and pans between $\pm 30^\circ$ generating an arc scan behind the wind turbine. Each line scan takes 1.6s , which means that the wind speed is measured nearly 200 times on different positions along the arc. Each time series is 10min long, giving 375 snapshots. Two times series of 10min each are selected, because the operating point of the wind turbine and the upstream velocity conditions are similar to the wind tunnel cases. The case *FIELD1* was collected on November the 15th, 2005 from

Fig. 1 A gaussian-type law is applied to each instantaneous velocity deficit profiles

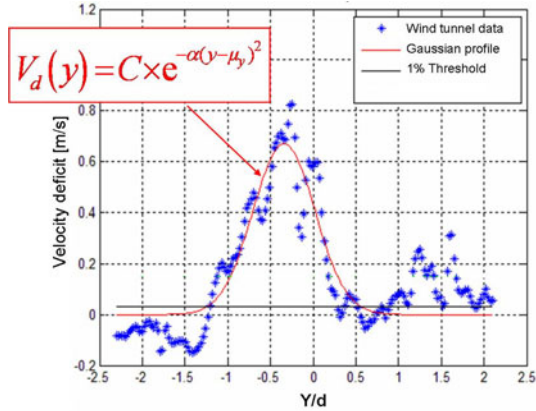


Table 1 Comparison between field and wind tunnel data on the statistics on instantaneous wake center locations and wake widths at hub height at a downstream distance of $X/d = 3$

Case	Hub height	Turb. int. [%]	Turb. length scales [m]	Mean wake centre location [d]	Stand. dev. of wake centre locations [d]	Mean wake centre wake width [d]	Mean of instant. wake widths [d]	Stand. dev. of instant. wake widths [d]
WT2	1	18	300	0.05	0.3	2.3	1.7	0.8
FIELD2	1.54	16.7	286	-0.12	0.17	1.1	0.7	0.4
WT1	3.5	12.5	450	0.07	0.26	2.3	1.8	0.6
FIELD1	1.54	12.9	159	-0.18	0.11	1.1	1.0	0.4

6:20 to 6:30pm. The thrust coefficient was $C_T = 0.62$ and the upstream turbulence intensity was 12.9%. The case *FIELD2* was collected the same day from 4:50 to 5:00pm. The thrust coefficient was $C_T = 0.62$ and the upstream turbulence intensity was 16.7%. See [11] for more details. The horizontal instantaneous velocity profiles are processed in order to determine the instantaneous velocity deficits representative of the wind turbine wake. A Gaussian-type law is fitted to each profile (Figure 1) : $V_d(y) = C \times e^{-\alpha(y-\mu_y)^2}$, where μ_y identifies the centre of the instantaneous velocity deficit. A threshold of 99% of the reference velocity is chosen to determine the borders of the wake (i.e. 1% of velocity deficit). Applying this processing procedure to each wind tunnel and field snapshots enables to compare statistics on the instantaneous wake centre locations and wake widths (Table 1).

3 Discussion and Conclusion

Cases *WT2* and *FIELD2* present similar ambient flow conditions regarding the turbulence intensity and turbulence length scales. However statistics on instantaneous wake center locations and wake widths show discrepancies. First, the mean of wake centre locations should be for both cases close to zero. The field data present a modest asymmetry, which could be explained by a small alignment error of the

LIDAR. The average of the instantaneous wake widths in the field case is surprisingly small (close to $1d$) since one expects an expansion of the wake due to the momentum conservation close to the rotor, amplified further downstream by the turbulence diffusion. One possible explanation is that the LIDAR scan line is not focused at the altitude where the wake is widest. From detailed CFD simulations (LES combined with actuator line modeling of the turbine), it has been identified a tendency of upwards moving deficits for ambient flows with shear as caused by the induced vorticity field. These possible misalignment problems could be solved by processing data from 2D-scanning techniques (see [5]). Regarding the standard deviation of the instantaneous wake centre locations and wake widths, it is seen that the wind tunnel data show systematically more variability than the corresponding field ones, although the turbulence intensity and the turbulence length scales are approximately similar. If the scatter is larger in wind tunnel, it means that the content of turbulent eddies responsible of the meandering (i.e. size at least of the same order as the wake width) is more pronounced in the wind tunnel. A single characteristic scale as the turbulence length scale is therefore not enough to compare the turbulence content of the upstream flows, and a deeper look on the turbulence spectra seems to be necessary to explain these discrepancies. Cases *WT1* and *FIELD1* present also similar ambient flow conditions, except for the turbulence length scales which are quite different (twice larger in wind tunnel than in field). Though, the differences between field and wind tunnel data are of the same order of magnitude than for the previous case. One could expect that the discrepancy in turbulence length scale would amplify the gap even more. It leads again to the conclusion that the turbulence spectra must be carefully compared to ensure that field and wind tunnel data are obtained under similar flow conditions.

References

1. Bingöl, F., Mann, J., Larsen, G.C.: Light detection and ranging measurements of wake dynamics Part I: One-dimensional Scanning. *Wind Energy* 13, 51–61 (2010)
2. España, G., Aubrun, S., Loyer, S., Devinant, P.: Spatial study of the wake meandering using modelled wind turbines in a wind tunnel. *Wind Energy* (2011), doi:10.1002/we.515
3. Hansen, K.S., Larsen, G.C., Enevoldsen, K., Mann, J.: LiDAR measurements of full scale wind turbine wake characteristics. In: Proceedings for Euromech Colloquium 508 on Wind Turbine Wakes, Madrid, Spain, October 20-22 (2009)
4. Larsen, G.C., Madsen, H.A., Thomsen, K., Larsen, T.J.: Wake meandering: a pragmatic approach. *Wind Energy* 11, 377–395 (2008)
5. Trujillo, J.J., Bingöl, F., Larsen, G.C., Mann, J.: Light detection and ranging measurements on wake dynamics; Part II: Two-dimensional Scanning. *Wind Energy* 14, 61–75 (2010)
6. VDI-guideline 3793/12. Physical modelling of flow and dispersion processes in the atmospheric boundary layer, application of wind tunnels. Beuth Verlag, Berlin (2000)

Is the Actuator Disc Concept Sufficient to Model the Far-Wake of a Wind Turbine?

S. Aubrun, G. España, S. Loyer, P. Hayden, and P. Hancock

1 Introduction

In order to study the wind turbine wake and its eventual interactions with neighbouring wind turbines, several numerical and physical modelling approaches are used. Some model the wind turbine with the simplest model, that is the actuator disc concept, adding a drag source (i.e. pressure loss) within the surface swept by the blades (numerical [2], physical [1]). Some use the Blade Element Momentum Theory, which takes into account the blade rotation effect on the wake and the aerodynamic features of the blades [3]. Some use Large Eddy Simulation to compute the unsteady flow around the entire rotor [5]. In a wind resource assessment context, the latter one is not practical enough to be used since the computation times are extremely long. The second one has more acceptable computation time but the first one is still the most attractive to model the far wake, according to its simplicity of implementation and short computation time. On the other hand, the issue is that it is difficult to assess the errors induced by the absence of blades and associated rotation momentum on the wake development. Furthermore, the level of turbulence intensity encountered in the atmospheric incoming flow plays a role on this issue : First, the higher the turbulence intensity is, the faster the spectral signature of the blades disappears in the wake and the faster the azimuthal velocity induced by the rotational momentum is overwhelmed in ambient velocity fluctuations. These observations need to be quantified. In this context, the present study compares the wake properties of a model of a three-blade rotating wind turbine [4] and of a porous disc made of metallic mesh, generating the same velocity deficit as the wind turbine. Both models are tested in an atmospheric boundary layer wind tunnel.

S. Aubrun · G. España · S. Loyer
Institut PRISME, University of Orléans, Orléans, France
e-mail: sandrine.aubrun@univ-orleans.fr

P. Hayden · P. Hancock
Environmental Flow Research Centre (EnFlo), University of Surrey, Surrey, UK
e-mail: P.Hancock@surrey.ac.uk

The mean flow and the spectral content are studied in order to determine whether the additional rotation momentum and the blade signature in flow are still visible at the beginning of the far wake, expected at $x \simeq 3D$).

2 Experimental Set-Up and Results

In this study, the return test section (5m high, 5m wide and 20m long) of the PRISME laboratory wind tunnel is used to reproduce the properties of an neutral ABL at a geometric scale of 1 : 300. Many previous studies enable the choice of the proper parameters to model a moderately rough ABL (Roughness length $z_0 = 1\text{cm}$ in full scale, power law coefficient $\alpha = 0.14$). At $z = 300\text{mm}$ (hub height), the upstream mean velocity is $U_0 = 2.5\text{m/s}$ and the turbulence intensity is $Iu_0 = 13\%$ (ratio between the standard deviation of streamwise velocity and its time average). The 3-blade rotating wind turbine (Fig. 1) has a diameter $D = 416\text{mm}$, its rotation is controlled and its tip-speed-ratio is fixed to $TSR = 5.8$. According to the upstream velocity, it ensures a thrust coefficient of $C_T = 0.50$ (C_T had been experimentally assessed using the global momentum theory,). A porous disc made of metallic mesh (Fig. 2) is designed in order to reproduce the same velocity deficit at $x = 0.5D$ downstream of the disc as downstream of the 3-blade rotating wind turbine. The porous disc has the same diameter as the wind turbine, the mesh has a solidity of 45% and a circle of different solidity (35%) of $0.1D$ of diameter is fixed at the center of the main disc. The choice of solidities was driven by a previous parametrical study [1]. The disc is fixed on a mast to be located at the same height as the wind turbine rotor.

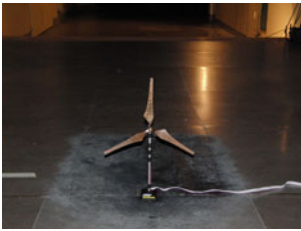


Fig. 1 Three-blade rotating wind turbine (EnFlo)

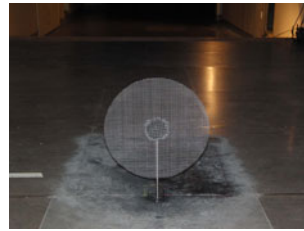


Fig. 2 Porous disc generating similar velocity deficit as the rotating wind turbine (PRISME)

The 3D flow properties are measured from $x = 0.5D$ to $3D$ downstream of the wind turbine with a triple-sensor gold-plated wire probe (Dantec 55P91). A single wire probe (Dantec 55P11) is used to measure the flow properties downstream of the porous disc. Hot wires are controlled with a Dantec Streamline CTA system.

Mean and RMS velocities are compared, as well as power spectral densities (PSD). Figures 3 and 4 show the streamwise mean velocity and turbulence intensity profiles versus the horizontal direction y/D , respectively, at $x/D = 0.5$ and 3 downstream of the porous disc and of the wind turbine. As seen on Fig. 3, the porous

disc has been correctly designed since one reaches the similarity of both wakes at $x/D = 0.5$. On the other hand, the wake development is free and it is visible that the wakes stay similar up to $x/D = 3$. Regarding the turbulence intensity profiles, it is clear that they show some differences at $x/D = 0.5$ due to discrepancies in turbulence production. In the wake of the porous disc, the turbulence production is confined to the borders of the wake, in the annular shear layer due to the existence of a velocity deficit. The mesh itself does not generate significant added turbulence. A production of turbulence is also visible in the central part of the wake, due to the velocity recovery. In the wake of the wind turbine, these latter sources are visible but the turbulence production due to the blades is also noticeable in the middle part of the wake. On the other hand, these discrepancies in turbulence intensity distribution between both wakes disappear at $x/D = 3$ due to the turbulence diffusion. In order to check whether the rotational momentum induced by the rotation of the wind turbine is still visible in the far-wake of a wind turbine, Fig. 5 and 6 present the horizontal profile of the mean transversal velocity and the vertical profile of the mean transversal velocity, respectively, downstream of the wind turbine. they show that the velocity signature of the rotation of the global wake is visible in the near-wake of the wind turbine but becomes insignificant at $x/D = 3$ at hub height. On the other hand, the velocity signature remains visible above the hub height on the vertical profile of transverse velocity. One explanation is that the ambient turbulence intensity is lower at higher altitude and that the turbulence diffusion, responsible of the turbulence mixing, is locally smaller, hiding less the rotational momentum. One other remaining question is related to the persistence of the tip-vortex signature in the wake of a wind turbine. The velocity PSD downstream of the wind turbine has been determined across the wake. At $X/D = 0.5$, two frequency peaks are noticeable, at $f_0 = 11Hz$, the rotation frequency of the wind turbine, and at $3 \times f_0$, signature of the transit of each blades. On the other hand, no signature of the tip vortex remains visible at $X/D = 3$, wherever the transverse positions.

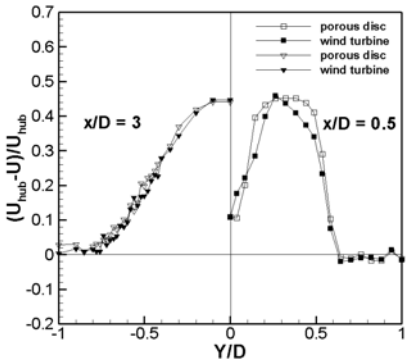


Fig. 3 Mean streamwise velocity downstream of the porous disc and the wind turbine

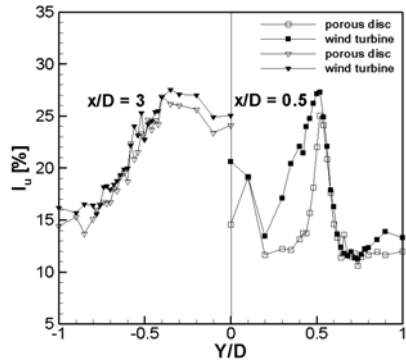


Fig. 4 Streamwise turbulence intensity downstream of the porous disc and the wind turbine

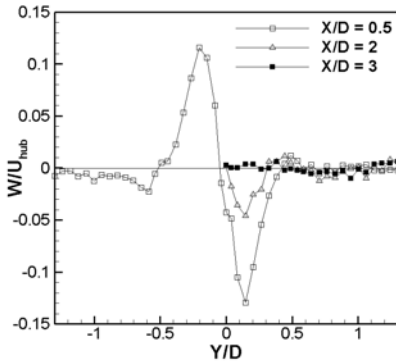


Fig. 5 Horizontal profile of the mean vertical velocity downstream of the wind turbine

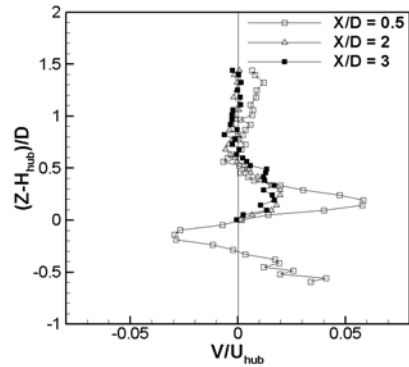


Fig. 6 Vertical profile of the mean transverse velocity downstream of the wind turbine

To conclude, the properties of the wake behind a three-blade rotating wind turbine and behind a porous disc generating a similar velocity deficit were compared through wind tunnel experiments. The goal was to determine whether a simple model as a porous disc (based on the actuator disc concept) to reproduce the wind turbine far wake is satisfactory. Results have shown that the mean velocity deficit and the streamwise turbulence intensity at the beginning of the far-wake ($X/D > 3$) are similar downstream of a wind turbine and of a porous disc. The rotational momentum generated by the rotor, as well as the tip vortex signature, were not detectable at the latter distance as far as the ambient turbulence intensity is high enough to contribute to accelerate the turbulent diffusion process.

References

1. Aubrun, S., Devinant, P., España, G.: Physical modelling of the far wake from wind turbines. Application to wind turbine interactions. In: Proceedings of the European Wind Energy Conference, Milan, Italy (2007)
2. Jimenez, A., Crespo, A., Migoya, E., Garcia, J.: Advances of large-eddy simulation of a wind turbine wake. The Science of Making Torque from Wind (2007), doi:10.1088/1742-6596/75/1/012041
3. El Kasmi, A., Masson, C.: An extended $k - \varepsilon$ model for turbulent flow through horizontal axis wind turbines. Journal of Wind Engineering and Industrial Aerodynamics 96, 103–122 (2008)
4. Pascheke, F., Hancock, P.E.: Influence of ABL characteristics on wind turbine wakes: surface roughness and stratification. In: Proceedings of the International Workshop Physmod 2009, Brussels, Belgium, vol. 2, pp. J.2.1–J.2.8 (2009)
5. Troldborg, N., Sorensen, J.N., Mikkelsen, R.: Numerical simulations of wake characteristics of a wind turbine in uniform inflow. Wind Energy (2009), doi:10.1002/we.345

Turbulent Wind Turbine Wakes in a Wind Farm

Arno J. Brand and Jan Willem Wagenaar

Abstract. A model of flow in a cluster of wind turbines has been developed. The model predicts average and standard deviation of wind speed in a wind farm as function of ambient wind speed, wind direction and turbulence intensity. In this paper the sub-models for velocity deficit and added turbulence of a single wind turbine are presented. In addition predictions of wind speed average and standard deviation for a row of wind turbines are compared to measurements.

1 Introduction

In this paper we present two sub-models of a model of flow in a cluster of wind turbines. The motivation for developing such a flow model is that in the future large-scale wind farms have to meet control objectives when operating as power plant, which is to be achieved by distributed wind farm control. To this end flow models are needed which model the control object wind farm, are valid over averaging periods of several minutes, and are part of the control algorithm.

The flow model presented in this paper is based on a combination of momentum theory and empirical knowledge. It is valid over averaging periods of several minutes, and predicts average and standard deviation of wind speed at turbine positions in a wind farm as function of ambient wind speed, wind direction and turbulence intensity.

2 Flow Model of Velocity Deficit and Added Turbulence

A wind turbine reduces wind speed and increases turbulence intensity. According to Milborrow [7] and Elliot [5], who are among the pioneers in wind turbine cluster

Arno J. Brand · Jan Willem Wagenaar
ECN Wind Energy, 1755 LE Petten, Netherlands
e-mail: brand@ecn.nl, j.wagenaar@ecn.nl

research, the wake of a wind turbine consists of a velocity wake and a turbulence wake. Velocity wake is the region where wind speed is lower than the upstream value, whereas turbulence wake is the region where turbulence intensity is higher than the upstream value. Wind speed deficit as well as added turbulence decay with streamwise and spanwise distance from a wind turbine.

The role of the wind farm flow model presented in this paper is to provide information to a wind farm controller on basis of measurement/model based predictions of wind speed. For this reason sub-models have been selected on basis of their ability to predict wind speed at turbine positions in a computationally fast and cheap way while using a minimum of information. To this end two assumptions have been made: wind turbine wake flow is governed by momentum theory [2, 3, 4 section 2.4, 6], and in a period of several minutes wind speed is Normal distributed.

Velocity deficit

On basis of experimental evidence [e.g. 1, 5, 7] we model average velocity μ at position (r, x) in the wake of a single turbine as follows (fig. 1, left):

$$\mu(r, x) = \mu_0 - \Delta\mu(r, x). \quad (1)$$

Here r is spanwise distance and x is streamwise distance from the wind turbine, and μ_0 is upstream velocity and $\Delta\mu$ is velocity deficit. Velocity deficit is given by:

$$\frac{\Delta\mu(r, x)}{\Delta\mu_{ini}} = \left(\frac{x}{2D}\right)^n \exp\left\{-\alpha_1 \frac{r^2}{\beta^2(x)}\right\} \quad (2)$$

where

$$\Delta\mu_{ini} = 2a\mu_0, n = -1.04 \pm 0.07, \alpha_1 = 0.693; \frac{2\beta(x)}{D} = \gamma\left(\frac{x}{D}\right)^\delta$$

with $\gamma = 0.3$ and $\delta = 0.63$.

The initial value of velocity deficit $\Delta\mu_{ini}$ is reached at a distance of two rotor diameters behind the wind turbine. According to momentum theory in the absence of turbulence initial velocity deficit has the value $2a\mu_0$ where a is axial induction factor.

Added turbulence

On basis of the assumption that velocity is a stochastic process and experimental evidence [5] we model turbulence in terms of velocity standard deviation σ (fig. 1, right). At position (r, x) in the wake of a single turbine velocity variance is sum of upstream velocity variance σ_0^2 and velocity variance σ_{add}^2 added by the wind turbine:

$$\sigma^2(r, x) = \sigma_0^2 + \sigma_{add}^2(r, x). \quad (3)$$

Added variance σ_{add}^2 is sum of two components, each originating from production of turbulence at the edge of the rotor disc:

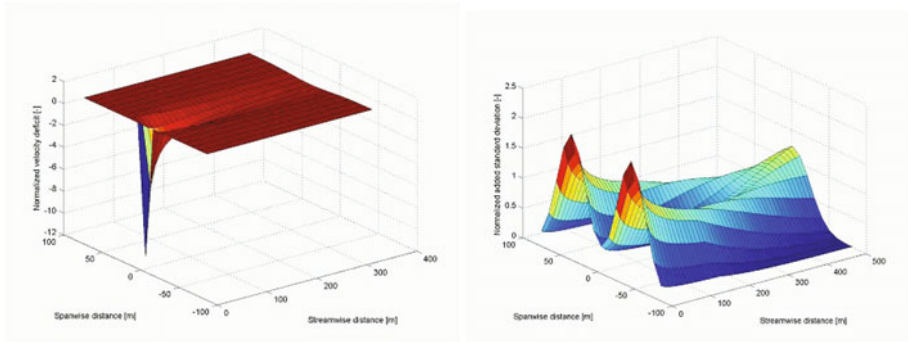


Fig. 1 Illustration of decay of velocity deficit (left) and added turbulence (right) as a function of streamwise and spanwise distance from a wind turbine

$$\sigma_{add}^2(r, x) = \sigma_{add,1}^2(r, x) + \sigma_{add,2}^2(r, x) \tag{4}$$

with $\sigma_{add,i} = f_i(r, x)\sigma_{add,x}(x), i = 1 \text{ or } 2$

where $f_1(r, x)$ and $f_2(r, x)$ take care of decay of turbulence in spanwise direction r and $\sigma_{add,x}(x)$ takes care of decay in streamwise direction x . We model $\sigma_{add,x}$ with a power function:

$$\sigma_{add,x}^2(x) = \sigma_{add,ini}^2 \left(\frac{x}{2D} \right)^m \tag{5}$$

where $\frac{\sigma_{add,ini}^2}{\mu_0^2} = c_{GCLA}$ with $c_{GCL} = 0.106$, and $m = -0.96$.

Here $\sigma_{add,ini}$ is initial added turbulence, which originates from thrust on the rotor as derived from the GCL model [4 section 2.4.1].

We model $f_1(r, x)$ and $f_2(r, x)$ with an exponential function:

$$f_1(r, x) = \frac{1}{2} \exp \left\{ -\alpha_2 \left(\frac{r - R_1(x)}{R} \right)^2 \right\}, f_2(r, x) = \frac{1}{2} \exp \left\{ -\alpha_2 \left(\frac{r + R_1(x)}{R} \right)^2 \right\};$$

where the $R_1(x)$ function causes the two peaks originating from the rotor disc edge to merge at a downstream position of eight rotor diameters:

$$\frac{R_1(x)}{R} = 1 \text{ if } 0 \leq \frac{x}{D} < 2, \frac{R_1(x)}{R} = \frac{1}{6} \left[8 - \frac{x}{D} \right] \text{ if } 2 \leq \frac{x}{D} \leq 8 \text{ or } \frac{R_1(x)}{R} = 0 \text{ if } \frac{x}{D} > 8.$$

Parameter α_2 sets spanwise size of the region with added turbulence; added turbulence at one edge of the disc due to the other edge is minimal if $\alpha_2 \approx 1.15$.

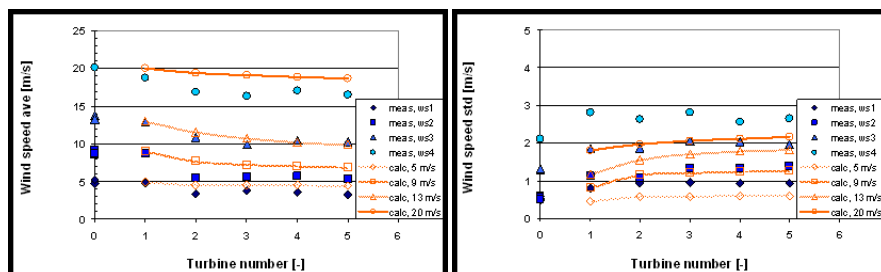


Fig. 2 Average wind speed (left) and wind speed standard deviation (right) in a row of five wind turbines. Wind is parallel to the row, from T1 to T5. Filled symbols are measured data and open symbols are model predictions; connecting lines are visual aids which do not reflect data

3 Measurements

Model predictions have been compared to measurements in the ECN Wind turbine Test site Wieringermeer EWTW. This test site consists of five 2.5 MW wind turbines separated over a distance of 3.8 rotor diameter of 80 m. Predicted and measured 10-minute wind speed averages and standard deviations are shown in figure 2. Main differences between predicted and measured values originate from un-modeled spatial variations in wind speed, un-modeled effect of turbine nacelle on wind speed, un-modeled effect of upstream turbulence on decay of added turbulence, and too gradually modeled decay of wind speed deficit and added turbulence.

Acknowledgements. This work was performed in the framework of the EU project FP7-ICT STREP 22548 / Aeolus "Distributed control of large-scale offshore wind farms".

References

1. Barthelmie, R., et al.: Efficient Development of Offshore Windfarms (ENDOW), Ris-R-1407(EN) (2003)
2. Barthelmie, R., et al.: Modelling the impact of wakes on power output at Nysted and Horns Rev. In: European Wind Energy Conference 2009, Marseille, France (2009)
3. Cleve, J.: Wake flow model for large wind farms. Euromech Colloquium 508 "Wind Turbine Wakes", Madrid, Spain (2009)
4. Dekker, J.W.M., Pierik, J.T.G. (eds.): European Wind Turbine Standards II, ECN-C-99-073 (1999)
5. Elliott, D.L.: Status of wake and array loss research. In: Windpower 1991, Palm Springs, California (1991)
6. Manwell, J.F., McGowan, J.G., Rogers, A.L.: Wind energy explained. John Wiley and Sons (2002)
7. Milborrow, D.J.: The performance of arrays of wind turbines. J. Ind. Aerod. 5, 403–430 (1980)

Characterization and Stochastic Modeling of Wind Speed Sequences

Calif and Emilion

Abstract. Wind energy production is very sensitive to turbulent wind, in particular when wind power variations range from few seconds to 1 hour, are considered. Indeed rapid changes in the local meteorological condition as observed in tropical climate can provoke large variations of wind speed. Consequently the electric grid security can be jeopardized due to these fluctuations. This is particularly the case of island networks as in the Guadeloupean archipelago (French West Indies) where the installed 20 MW wind power already represents 11% of the electrical consumption. From 1 million wind sequences of duration 10 minutes, sampled at 1 Hz during the trade season, we proceed toward two objectives: i) the characterization of the wind speed sequences, ii) the dynamical simulation of the wind sequences using Langevin equation.

1 Data Representation

The wind speed data were collected with a cup anemometer with a sample rate 1s. For this work, the wind speed data were segmented in time sequences of 10 minutes each. For each of these sequences (labeled n) we compute, over a $t = 10$ min period, the value of the mean wind speed $\langle U_n \rangle$ and the corresponding wind speed fluctuations u'_n now defined as:

$$u'_n(t) = u_n(t) - \langle U_n \rangle \quad (1)$$

Each sequence of 10 minutes measurements is summarized by the histograms of these measurements distribution and no parametric hypothesis is assumed on this

Calif

EA 4098 LARGE, University of Antilles Guyane, BP 592 UFR SEN Pointe-a-Pitre, France
e-mail: rudy.calif@univ-ag.fr

Emilion

MAPMO, UMR CNRS 6628 University of Orleans, BP 6759, Orleans, France
e-mail: richard.emilion@univ-orleans.fr

distribution. The 1 million histograms are then classified by fitting a finite mixture of Dirichlet distributions, each component of this mixture providing a class of we were looking for. This also yields the probability of a given sequence to belong a class. We consider a sample $(h_1, \dots, h_i, \dots, h_n)$ of $n = 1,000,118$ wind speed fluctuations histograms range into $l = 11$ intervals of equal length. Each histogram h_i has therefore l bins, say $h_i = (h_{i,1}, \dots, h_{i,l})$, such that and $h_{i,j} \geq 0$ and $\sum_{j=1}^l h_{i,j} = 1$. In the sequel it will be important to consider that conditionally to the observed data, $h_i = (h_{i,1}, \dots, h_{i,l})$, is a probability vector on the finite set $V = 1, \dots, l$. Wind speed histograms built on $l = 11$ compromise between accurate estimation of the distribution and the obtaining of nonempty bins.

2 Statistical Setting

2.1 Random Distribution

A random distribution (RD) is a measurable map from a probability space (Ω, F, P) to the space $P(V)$ of all probability measures defined on a fixed measurable set V . If $X : \Omega \rightarrow P(V)$ is a RD, its distribution is then a probability measure on $P(V)$. If $V = 1, \dots, l$ is the above finite set the note that $P(V) = \{x = (x_1, \dots, x_l) : x_i \geq 0, \sigma x_i = 1\}$. A well-known example of RD is the following one.

2.2 Dirichlet Distribution, Dirichlet Density and Mixture of Dirichlet Distributions

Consider l independent random variables Z_1, \dots, Z_l following a gamma distribution $\gamma(\alpha_1, 1), \dots, \gamma(\alpha_l, 1)^2$ respectively, where $\gamma(a, b)(x) = \frac{1}{\Gamma(a)} b^a e^{-bx} x^{a-1} I_{0,+\infty}(x) dx$. If we normalize each random variable Z_l by the sum $Z = Z_1 + \dots + Z_l$ then the distribution of the random vector $X = (\frac{Z_1}{Z}, \dots, \frac{Z_l}{Z})$ is called the Dirichlet distribution $D(\alpha_1, \dots, \alpha_l)$. Observe that since and $\frac{Z_j}{Z} \geq 0$ and $\sum_{j=1}^l \frac{Z_j}{Z} = 1$, X is a random distribution on $P(V)$, $V = 1, \dots, l$. Hence the Dirichlet distribution is a first natural example of distribution of a random distribution, that is a probability measure on $P(V)$, $V = 1, \dots, l$. It can be shown that the dimensional random $(\frac{Z_1}{Z}, \dots, \frac{Z_{l-1}}{Z})$ vector has the following density with respect to the Lesbegue measure on the set: $T_l = \{x = (x_1, \dots, x_{l-1})$ such that $x_j \geq 0$ and $\sum_{j=1}^{l-1} x_j \leq 1\}$ the so-called Dirichlet density:

$$F(x_1, x_2, \dots, x_{l-1} / \alpha_1, \alpha_2, \dots, \alpha_l) = \frac{\Gamma(\alpha_1 + \dots + \alpha_l)}{\Gamma(\alpha_1) \dots \Gamma(\alpha_l)} (\alpha_1) \prod_{l=1}^{L-1} x_l^{\alpha_l - 1} (1 - \sum_{l=1}^{L-1} x_l)^{\alpha_l - 1} \tag{2}$$

for $(x_1, \dots, x_{l-1}) \in T_l$.

Let $X : \Omega \rightarrow P(V)$ be a RD, with, $V = 1, \dots, l$ and $P_V = \{x = (x_1, \dots, x_n)$ such that $x_j \geq 0$ and $\sum_{j=1}^{l-1} \leq 1\}$. The distribution of P_X of X is a finite mixture of

Dirichlet distributions if it is a convex combination of K standard Dirichlet distributions $D(\alpha_1^k, \dots, \alpha_l^k)$:

$$P_X = \sum_{k=1}^K p_k (\alpha_1^k, \dots, \alpha_l^k) \text{ with } p_k > 0 \text{ and } \sum_{k=1}^K p_k = 1$$

The mixture problem consists of estimating the parameters p_k and $(\alpha_1^k, \dots, \alpha_l^k)_{1 \leq k \leq K}$. To achieve this aim, we use an iterative algorithm where the inputs are the n histograms vectors $h_i = (h_{i,1}, \dots, h_{i,l})$, $i = 1, \dots, n$ K denoting the number of classes. Note that method has been applied for internet traffic flow classification [7] and daily solar radiation classification [6]. To estimate the parameters of the mixture as well as the parameters of each Dirichlet distribution, we use the SAEM algorithm [3, 5].

The results of the method show the existence of 3 classes of wind speed distribution: i) A first class (90% of wind speed sequences) in which PDFs are symmetrical mono-modal pdf. correspond to wind regime with a weak turbulent agitation around 5. Recall that the turbulent intensity is defined by: $I_n = \frac{\sigma_n}{\langle U_n \rangle}$, σ_n and $\langle U_n \rangle$ are respectively the standard deviation and the mean value for each wind sequence u_n ii) A second class (9% of wind speed sequences) in which PDFs are dissymmetrical mono-modal modeled by a Gram-Charlier function. In a point of view meteorological, these times series have wind gusts, in other words, a large fluctuation rises during very short times (less than a minute) [8]. These wind speed sequences have a medium level of turbulent intensity around 10% . iii) A third class (1% of wind speed sequences) in which PDFs are bimodal. These ramp events, with a high level of turbulent intensity around 20%, are drastically for wind energy production.

3 Stochastic Modeling of Wind Speed Sequences

For modeling the wind speed sequences, we use the langevin equation considering the Gram-Charlier probability density function of turbulent velocity, trough which Gaussian (class I) and non gaussian (class II) turbulence conditions can be considered [2]:

$$dr = \frac{d\sigma}{eT_L} dt + \sigma \sqrt{\frac{2}{T_L}} dW_t \tag{3}$$

where $r = \frac{u}{\sigma}$, u is the wind speed fluctuation, dW_t denotes a Wiener process that is normally distributed (average 0 and variance dt) random increment, σ the standard deviation, T_L the integral time, d and e expressions written as:

$$d = -\frac{s}{2} - r\left(\frac{5k}{8} + 1\right) + sr^2 + \frac{5k}{12}r^3 - \frac{s}{6}r^4 - \frac{k}{24}r^5 \tag{4}$$

$$e = 1 + \frac{k}{8} - \frac{s}{2}r + \frac{k}{4}r^2 + \frac{s}{6}r^3 + \frac{k}{24}r^4 \tag{5}$$

Although the simulated signals are different of the experimental signals, theirs statistical (PDF) and dynamical (integral time scale) properties are similar. (see figure 1)

For the wind speed sequences belonging to class 3, with a bimodal shape for PDF, we use the following stochastic differential equation, as follows [11]:

$$du(t) = -\frac{\partial V(u(t))}{\partial u} dt + \sigma(u(t)) dw_t \quad (6)$$

The deterministic term on the right-hand side, $-\frac{\partial V(u(t))}{\partial u}$, is the drift function, while $\sigma(u(t))$ is the diffusion function and $w(t)$ is a Wiener process. $V(u(t))$ is a potential function. This preliminary work set some basis for further investigation to estimate the potential function.

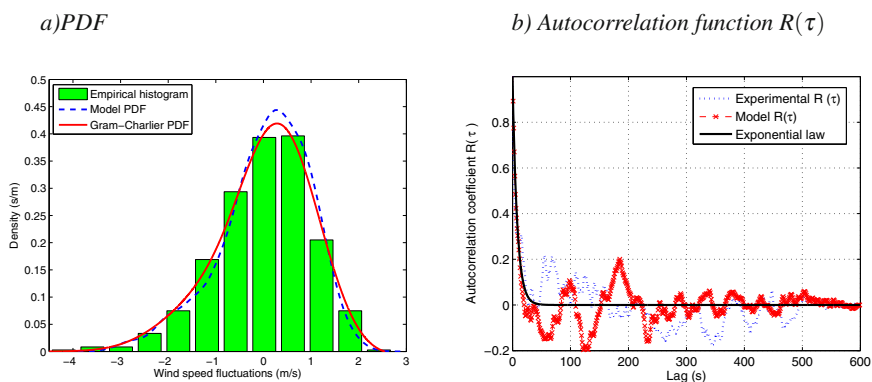


Fig. 1 For the class II: a) A distribution of an experimental wind speed fluctuations sequence compared to that of the simulated signal and superimposed to Gram-Charlier function. b) Autocorrelation function of experimental and generated wind speed fluctuations sequence.

References

1. Brillinger, H.K., Preisler, A.A., Kie, J.G.: The use of potential functions animal movement. *Data Analysis from Statistical Foundations* 45, 369–386 (2001)
2. Carvalho, G., Nichimura, E.R., de Vilhena, M.T.M.B., Moreira, D.M., Degrazia, G.A.: An iterative langevin solution for contaminant dispersion using the gram-charlier pdf. *Environ. Modell. Softw.* 20, 285–289 (2005)
3. Celeux, G., Diebolt, J.: S.A.E.M. Algorithm. *Stochastics. Stochastics Rep.* 41, 119–134 (1992)
4. Dempster, A., Laird, N., Rubin, D.: Maximum likelihood from incomplete data via the EM algorithm. *J. Roy. Stat. Soc. B* 39, 1–38 (1977)
5. Emilion, R.: Classification and mixture process. *CRAS I* 355, 189–193 (2002)
6. Soubdhan, T., Emilion, R., Calif, R.: Classification of daily solar radiations distributions using a mixture of Dirichlet distributions. *Sol. Energy* 83, 1056–1063 (2009)
7. Soule, A., Salamatian, K., Taft, N., Emilion, R.: Flow Classification Using Histograms or How To Go on Safari on the Internet. *Sigmatrics* 83, 49–60 (2004)
8. Böttcher, F., Barth, S., Peinke, J.: Small and large scale fluctuations in atmospheric wind speeds. *Stoch. Environ. Res. Ris. Asses.* 21, 299–308 (2007)

Wind Turbines in ABL-Flow: A Review on Wind Tunnel Studies

F. Cuzzola, B. Leitl, and M. Schatzmann

Abstract. Over the last fifteen years a substantial increase in the use of wind energy can be monitored. Presently, several wind farms are planned or under construction in which many wind turbines are arranged as grids. A successful design of a wind farm relies on a number of issues such as: the prediction of wind resource, the rotor-blade design and the optimal siting of the wind turbines. The energy extracted from the flow field by a wind farm depends on the performances of a single wind turbine and the effects of its wake on the wind turbines downstream. The extracted power performances are improving by the enhancement of the near wake research, while far wake research focuses more on the mutual influence among wind turbines and the role played by the terrain the wind farm is located on. Far wake research is important because downstream wind turbines experience a loss of power output as well as an increase of load. At the Meteorological Institute of Hamburg, within the FP7 project WAUDIT, the aim is to deliver quality assurance of wind assessment models. In order to work with reliable data, at the present time we are focusing on the physical modelling of a wind turbine. This paper will review some of the most important previous works analysing the design procedures applied.

1 Introduction

Wind energy research through wind tunnel testing of model wind turbine started in the late seventies in Europe. The modeling of these wind turbines is done with the objective of either achieving geometrical similarity or trying to achieve dynamic similarity within certain ranges. In the next sections we will review some of the previous work and classify them with respect to the concept used in the scaling procedure.

F. Cuzzola · B. Leitl · M. Schatzmann

Meteorological Institute, University of Hamburg, Germany

e-mail: francesco.cuzzola@zmaw.de, bernd.leitl@zmaw.de,
schatzmann@zmaw.de

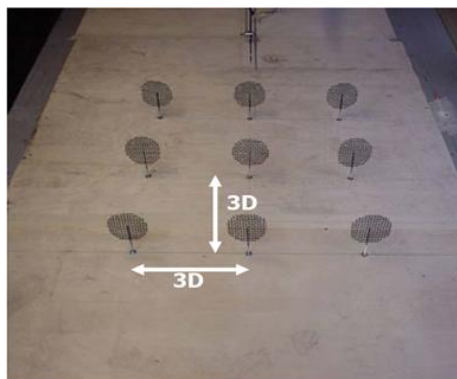


Fig. 1 Simulated wind farm through ADC, from [3]

2 Actuator Disc Concept Models

Actuator Disc Concept (ADC) approach was used first at the Energy research Centre of the Netherlands (ECN) by Vermeulen and Builtjes [7]. Atmospheric boundary layer was simulated and the authors claim that after several diameters not only the velocity structure of the wake was correctly simulated by the so-called "Tea Strainer". Also the turbulence structure compared fairly well with that of a rotor model.

S. Aubrun at the University of Orleans has been using this approach since 2005 [2, 3]. The author uses porous discs of 100mm, 200mm and 300mm in diameter made from metallic mesh. The experiments are carried out at the Malavard wind tunnel in Orleans with presence of simulated atmospheric boundary layer at 1 : 400 scale. The author, using different meshes and different sizes, is able to reproduce the desired velocity deficit and turbulence intensity in terms of mean values. The great advantage of this approach lies in the reliability of the mesh models and in the direct easiness of constructing them. Furthermore many numerical models are based on ADC and this means that comparisons can be made. The drawback of this approach is that one needs to know the desired wake characteristic of the wind turbine which is not properly known before it has been built. In addition, effects of rotation on the wake flow can not be investigated.

3 Rotor Models

Many researchers tried to investigate the behaviour of wind turbines reproducing them at small scales in wind tunnels. The Aeronautical Research Institute of Sweden is one of the most active institutions in this field starting the research work already in 1979 [1]. More recently a model wind turbine was used to investigate the phenomenon of meandering [5]. Different rotors were used but, due to the small size of the wind tunnel, the diameter of each model was 180mm only. The small



Fig. 2 Rotor models wind farm, from [4]

size of the blade chord led to small Reynolds numbers, and thus less performing aerodynamics. The resulting C_p is then much lower than the one of a commercial wind turbine.

Another important work came in 1988 from Colorado State University [6] suggesting that since wake characteristics are strongly dependent upon the thrust perceived by the rotor disc a wind turbine model has to be designed in order to produce an equivalent magnitude thrust coefficient. The authors clearly point out from dimensional analysis that the main parameters ruling wake behaviour are tip speed ratio, Reynolds number, thrust coefficient and power coefficient.

In 2003 at ECN Corten et al. [4] designed model wind turbines of 25cm diameter. These were tested at the Netherlands Organization for Applied Scientific Research (TNO) boundary layer wind tunnel, assembled as a wind farm. The low Reynolds number issue was faced by enlarging the chord of the blade. In this way it was possible to keep Reynolds number above the Re_{crit} of the airfoil used (NACA 0009) and thus achieving Reynolds number independency. They report that the simulated wake resembled the full scale behaviour in good approximation and claim that results in terms of performances are comparable with full scale wind turbine characteristics.

Following his design procedure it seems that the increase of drag due to the larger chord was neglected and, since at low speed viscous drag can be comparable to form drag, this might be reflected in lower performances and slightly different behaviour. Also the fact that there is a pressure gradient in the direction of the flow in the wind tunnel might have an effect on the behaviour of the wind turbine wake.

4 Outline of WP6

Judging from the mentioned references it is clear that to deliver high quality data from wind tunnel experiments it is necessary to reduce the degrees of freedom in the modelling strategy and geometrical uncertainties in the model itself. The objective of this research is to investigate the behaviour of the wake flow behind a wind

turbine and, before designing an experiment in ABL-flow, it was decided to describe the changes in the flow that might occur when all the dimensionless parameters vary. A 3-bladed rotor model tested in a wind tunnel allows to control wind speed, rotational speed and aerodynamic characteristics of the blades. For these reasons, at a sufficiently large scale, a rotor model might be the best option to reproduce physical behaviour. We believe also that the mutual influence between the turbulence of the incoming flow field with the turbulence produced by the wind turbine has a strong effect on wake behaviour and this must be taken into account when designing the experiment and the rotor model. Among the manufacturers Blade Element Momentum theory still is the most used tool to design the blades, for this reason we are confident that, using BEM, we should be able to design and build a rotor that can represent characteristics of a full scale wind turbine.

Once preliminary tests of the model are carried out, we will set up a test with presence of a simulated atmospheric boundary layer. Complementary work in Hamburg will be done on flow around hills and wind farms.

References

1. Alfredsson, P.H., Dahlbeg, J.: A preliminary wind tunnel study of windmill wake dispersion in various flow conditions. FFA TN AU-1499, Part 7, Stockholm (September 1979)
2. Aubrun, S.: Modelling wind turbine wakes with porosity concept. In: Peinke, J., Schumann, P., Barth, S. (eds.) Proceedings of the Euromech colloquium 464b. Wind Energy, pp. 265–270 (2005)
3. Aubrun, S., Devinant, P., Espana, G.: Physical modelling of the far wake from wind turbines. Application to wind turbine interactions. In: Proceedings of EWEC 2007, Milan, Italy (2007)
4. Corten, G.P., Schaak, P., Hegberg, T.: Turbine interactions in large offshore wind farms - wind tunnel measurements, ECN report ECN-C-04-048 (2004)
5. Medici, D., Alfredsson, P.H.: Measurements on a wind turbine wake: 3D effects and bluff body vortex shedding. Wind Energy 9, 219–236 (2006)
6. Neff, D.E., Meroney, R.N., McCarthy, E., Davis, E.: Upstream and lateral wake effects on wind turbine performances. Journal of Wind Engineering and Industrial Aerodynamics 36, 1405–1414 (1990)
7. Vermeulen, P.E.J., Builtjes, P.J.H.: Turbulence Measurements in Simulated Wind-Turbine Clusters. TNO report nr. 82-03003 (1982)

Intermittent Fingerprints in Wind-Turbine Interactions

Emil Hedevang, Klaus Biß, Jochen Cleve, and Martin Greiner

Abstract. We show that the turbulent wind observed at an offshore wind farm is non-Gaussian through analysis of velocity increments, extended self-similarity and intermittency in the energy flux. We then modify Gaussian turbulence using multifractal fields and reproduce most of the observed non-Gaussianity. By using cubed velocities as a simplistic wind-turbine interaction model, we demonstrate how the turbulence intensity, integral length, and the intermittency seen in non-Gaussian turbulence make fingerprints on the turbine power. These fingerprints are to some extent verified by comparing measured power with simulated power using a wind-turbine interaction simulator.

1 The Measured Wind and Its Deviations from Gaussianity

We have used wind data measured using a cup-anemometer at a meteorology mast at an offshore wind farm. In total 436 stationary (determined by looking at plots of each time series) ten minute time series with mean wind speed $U \approx 8$ m/s have been selected. The turbulence intensities $I = \sigma/U$ are 6% on average (ranging from 2% to 11%). The Fourier energy spectrum is as expected, following the Kolmogorov 5/3-law in the inertial range. The sampling frequency of the data is 1.25 Hz. In this

Emil Hedevang
University of Aarhus and Siemens Wind Power
e-mail: emilhedevang@gmail.com

Klaus Biß
Justus Liebig Universität
e-mail: klaus.biss@gmx.de

Jochen Cleve
Siemens Wind Power
e-mail: jochen.cleve@siemens.com

Martin Greiner
University of Aarhus
e-mail: greiner@imf.au.dk

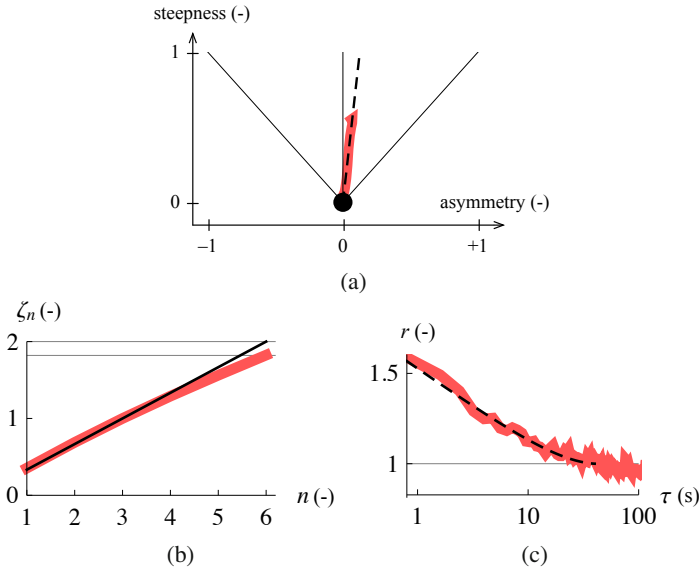


Fig. 1 (a) The NIG triangle for the measured velocity increments. The black dot represents the Gaussian distribution (with zero asymmetry and steepness) and the red curve represents the observed asymmetry and steepness of the velocity increments for different values of Δt ranging from $\Delta t = 0.8$ s to 204.8 s. As Δt increases we move from high to low steepness. (b) Extended self-similarity with exponent ζ_n plotted as a function of the order n . (c) Two point correlation of the surrogate energy flux plotted as a function of the delay τ .

section the time series are all linearly transformed to have turbulence intensity 6%, whereas in section 2 only the time series with turbulence intensity near 11% are used since the fingerprints of turbulence in the wind turbine power is most pronounced at high turbulence intensities.

The deviations from Gaussianity appear already in the distributions of the velocity increments $\Delta v(t) = v(t + \Delta t) - v(t)$. The distributions have tails heavier than Gaussian tails and the Normal Inverse Gaussian (NIG) distributions fit very well. See [1] for an introduction to the NIG distributions, their asymmetry and steepness, as well as the NIG triangle used in figure 1(a). Figure 1(a) shows the *asymmetry* and *steepness* (which are related to the third and fourth cumulants) of the velocity increments for values of Δt between 0.8 s and 204.8 s. As Δt increases, the steepness and asymmetry decrease towards zero, the Gaussian case. Similar shape is seen for other turbulence data sets. We see both clear positive asymmetry and steepness for the velocity increments which implies non-Gaussianity.

In the extended self-similarity (ESS, see [4]) we also see deviations from Gaussianity. In figure 1(b) the black line represents the Kolmogorov 1941 hypothesis which a Gaussian turbulence process must follow, and the red curve represents the measured wind. The deviation at order six is $\mu = 2 - 1.82 = 0.18$, also known as the *intermittency exponent* μ . Gaussian turbulence cannot exhibit any positive

intermittency exponent. (The statistics of the increments in figure 1(a) and (b) are calculated from the increments of all the time series pooled together).

Finally we see again deviations from Gaussianity in the surrogate energy flux here defined as $\pi(t) = |v(t + \Delta t) - v(t)|^3$ where $\Delta t = 0.8$ s. We consider the two-point correlator of the surrogate energy flux: $r(\tau) = E[\pi(t + \tau)\pi(t)]/E[\pi(t)]^2$. In [5] an analytical expression was derived for the above two-point correlator under the assumption of multifractal cascades: $r(\tau) = a(U\tau/L_{\text{casc}})^{-\mu} + (1 - a)(U\tau/L_{\text{casc}})$. Here μ is the intermittency exponent, $a \in [0, 1]$ determines the relative weight of the two terms, and L_{casc} is the cascade length which should be in the same order of magnitude as the integral length. Figure 1(c) shows the two-point correlator of the measured energy flux as well as the above analytical expression with $\mu = 0.15$, $a = 0.88$, and $L_{\text{casc}} = 320$ m. (For each time series the correlator is calculated, and then the average of all the correlators is plotted).

2 Multifractal Modification of Gaussian Turbulence and the Fingerprints in Turbine Power

The idea of multifractal modification is to take a Gaussian stochastic process v_{Gaussian} with the right spectrum and modify the velocity increments $\Delta v_{\text{Gaussian}}$ using a multifractal field m to add intermittency to the energy cascade: $\Delta v_{\text{modified}}(t) = m(t)^{1/3}\Delta v_{\text{Gaussian}}(t) - \partial_v\psi(v)$. Since we are working at a scale far away from the dissipation scale we use energy fluxes instead of energy dissipations, hence the exponent $1/3$ instead of $1/2$. The second term is using a potential ψ to restore stationarity which the modification otherwise breaks. We have used a quadratic potential, $\psi(v) = \frac{1}{2}a(v - U)^2$ where U denotes the mean wind speed.

By this procedure we can restore much of the steepness seen in figure 1(a), though not the asymmetry, most of the intermittency exponent seen in figure 1(b), as well as reproduce the behaviour of the two-point correlator of the surrogate energy flux seen in figure 1(c). Another, somewhat related, and promising approach to turbulence modelling using *ambit processes* is able to reproduce the asymmetry as well as many other observables of real turbulence. See [2, 3] for more information.

To get a feeling of what to expect from the wind-turbine interaction we consider first the *pseudo power* $P_{\text{ps}}(t) = v(t)^3$ which represents a kind of instantaneous interaction model and is the simplest possible model to consider. As input to our multifractal modification we use Gaussian turbulence from TurbSim [6]. We thereafter compare measured power with simulated power from FAST [7].

The two-point correlators of the power and of the squared increments of the power are interesting, the latter in particular since the heavier-than-Gaussian tails of the velocity increments imply that real turbulence brings more and larger surprises than Gaussian turbulence. In terms of power this should show in the power increments $\Delta P(t) = P(t + \Delta t) - P(t)$. For the pseudo power, an application of the famous inertial range property of the second order structure function will show that $\text{tpc}(P_{\text{ps}})(\tau) \approx 1 + 9(\sigma/U)^2(1 - (U\tau/L)^{2/3})$ and that

$$\text{tpc}(\Delta P_{\text{ps}}^2)(\tau) \approx [1 + 16(\sigma/U)^2(1 - (U\tau/L)^{2/3})] \cdot \text{tpc}(\Delta v^2)(\tau) \quad (1)$$

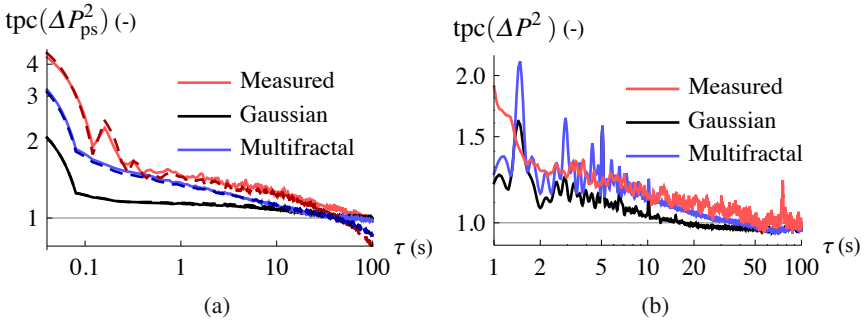


Fig. 2 Two-point correlations of squared increments of pseudo power and power, $\Delta t = 0.12$ s. (a) Pseudo power calculated from wind speeds. The dashed lines show the analytical expression from eq. (11) with $L = 320$ m and $\sigma/U = 10\%$ for the synthetic wind fields and 13% for the measured wind. (b) Power as measured at the turbine (red) or simulated using FAST (black and blue).

where $\text{tpc}(X)(\tau) = E[X(t + \tau)X(t)]/E[X(t)]^2$. Thus we may recover the turbulence intensity σ/U and the integral length L , and the intermittency seen in the velocity should carry through to the power increments. For brevity we shall here only look at the two-point correlator of the squared increments of power. Figure 2(a) shows $\text{tpc}(\Delta P_{ps}^2)$ calculated from data as well as from (11). It is clear how the multifractal modification is able to capture the intermittent structure seen as scaling in the two-point correlator which the Gaussian turbulence is otherwise not able to do. In figure 2(b) we move from pseudo power to real power (measured or simulated using FAST). Again we see that the simulated power using the multifractal modification agree better with the measured data than when using pure Gaussian turbulence.

References

1. Barndorff-Nielsen, O.E., Blæsild, P., Schmiegel, J.: A parsimonious and universal description of turbulent velocity increments. *Eur. Phys. J. B* 41, 345–363 (2004)
2. Barndorff-Nielsen, O.E., Schmiegel, J.: Lévy-based Tempo-Spatial Modelling; with Applications to Turbulence. *Uspekhi Mat. Nauk* 159, 65–91 (2003)
3. Barndorff-Nielsen, O.E., Schmiegel, J.: Ambit Processes; with Applications to Turbulence and Cancer Growth. In: Benth, F.E., Nunno, G.D., Linstrøm, T., Øksendal, B., Zhang, T. (eds.) *Stochastic Analysis and Applications: The Abel Symposium 2005*, vol. 2, pp. 93–124. Springer, Heidelberg (2007)
4. Benzi, R., Ciliberto, S., Tripicciono, R., Baudet, C., Massaioli, F., Succi, S.: Extended self-similarity in turbulent flows. *Phys. Rev. E* 48, 29–32 (1993)
5. Cleve, J., Dziekan, T., Schmiegel, J., Barndorff-Nielsen, O.E., Pearson, B.P., Sreenivasan, K.R., Greiner, M.: Finite-size scaling of two-point statistics and the turbulent energy cascade generators. *Phys. Rev. E* 71, 026309 (2005)
6. NWTCT Design Codes (TurbSim by Neil Kelley, Bonnie Jonkman), <http://wind.nrel.gov/designcodes/preprocessors/turbsim/>
7. NWTCT Design Codes (FAST by Jason Jonkman, Ph.D.), <http://wind.nrel.gov/designcodes/simulators/fast/>

The Relevance of Turbulence for Wind Energy Related Research

M. Hölling, A. Morales, J. Schneemann, T. Mücke, M. Wächter, and J. Peinke

Abstract. Wind turbines are operating in the turbulent atmospheric boundary layer where they are exposed to wind speed changes in time and space on different scales [3]. This paper deals with a statistical description of the turbulent wind field on the one hand and with the interaction of turbulent wind fields with rotor blade elements with respect to dynamical changes of the lift coefficient c_l on the other hand. In the first part we present a method to estimate the statistics of wind speed fluctuations $u' = u - \langle u \rangle$ and more importantly of extreme events on different time scales based on 10-minute averaged values for the measured turbulence intensity of wind fields. In the second part we present measurement data that illustrates the effects of atmospheric like turbulence on a FX 79-W-151A airfoil under static angles of attacks.

1 Estimation of Velocity Fluctuations

A standard description of atmospheric wind fields for, e.g. site assessment, is based on mean wind velocity and standard deviation averaged over 10 minutes. Due to this compression the description has no more information about the original distribution $p(u')$ of the fluctuations $u' = u - \langle u \rangle$ within the measured wind velocity even though, like in the case of cup anemometers, the data was measured at a temporal resolution of 1Hz. The fact that wind energy converter (WEC) have reaction times much shorter than 10 minutes, makes the knowledge of faster fluctuations indispensable to improve the understanding of WEC behavior.

Methodology. By looking at the distribution of the fluctuations $p(u')$ of non-averaged measurements it shows an intermittent behavior indicated by the strong deviation from a Gaussian distribution, see figure 1(a). Such intermittent distributions

Michael Hölling

ForWind - Center for Wind Energy Research, Institute of Physics, University of Oldenburg, Oldenburg, Germany

e-mail: michael.hoelling@uni-oldenburg.de

are also known for increment statistics ($u_\tau = u(t + \tau) - u(t)$) for stationary laboratory turbulence, for which Castaing et al. derived a formula to describe them [1]. In this description the intermittent shape is obtained by superimposing Gaussian distributions weighted with the distribution of the respective standard deviation. This approach has been adapted to describe the intermittent distribution of wind field fluctuations $p(u')$ based on the standard deviation $\sigma_{u'_T}$ of the standard 10-minute averaged wind speed measurements [2]. The modified formula for the distribution of u' is then given by

$$p(u') = \frac{1}{2\pi\alpha} \int_0^\infty \underbrace{\exp\left[-\frac{u'^2}{2\sigma_{u'_T}^2}\right]}_{\text{Gaussian for individual } T} \underbrace{\exp\left[-\frac{\left(\ln\left(\sigma_{u'_T}/\sigma_0\right)\right)^2}{2\alpha^2}\right]}_{\text{log-normal weighting}} \frac{d\sigma_{u'_T}}{\sigma_{u'_T}^2}, \quad (1)$$

where $\sigma_{u'_T}$ denotes the standard deviation of single 10-minute window, σ_0 the most probable standard deviation in the log-normal weighting and α the standard deviation of the log-normal distribution. The verification of this approach is illustrated in figure 1 based on 1 Hz measurement data, where **b)** shows the Gaussian shape for the distribution of the fluctuations for 10-minute windows $p(u'_T)$ and **c)** the log-normal distribution of the standard deviation of the 10-minute windows $p(\sigma_{u'_T})$. These properties of atmospheric wind field data allow for reconstructing the intermittent distribution of the fluctuations u' by superimposing Gaussian distributions weighted with the distribution of their standard deviations $\sigma_{u'_T}$ based on measured 10-minute averaged wind speed data as shown in figure 1a). With this model high-frequency properties of the wind speed fluctuations u' can be recovered from 10-minute averaged quantities. Especially for extreme values the statistics are significantly improved compared to a Gaussian assumption.

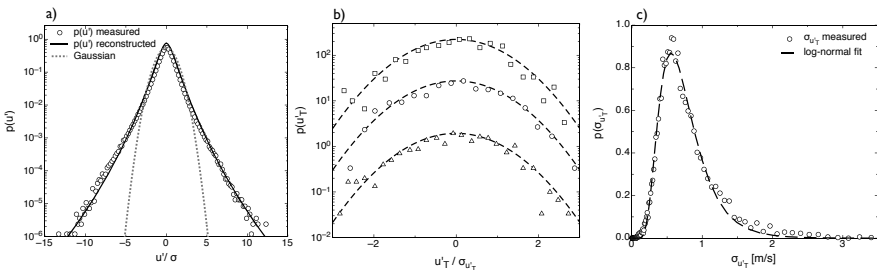


Fig. 1 a) Comparison of distribution of fluctuations $p(u')$ of measured wind data (circles), Gaussian distribution (dotted line) and reconstructed statistic (solid line). **b)** Distribution of velocity fluctuations $p(u'_T)$ of arbitrary 10-minute windows with Gaussian fit. **c)** Distribution of standard deviation of 10-minute windows $p(\sigma_{u'_T})$ with a log-normal fit.

2 Impact of Turbulence on Profiles

Turbulent wind fields with different turbulent intensities Ti exhibit constant changes not only in the wind velocity but also in the wind direction [4]. These changes, on the other hand, result locally in rapid changes in the angle of attack, AoA , at the rotor blades of wind energy converter. These varying angles of attack at the rotor profile in turbulent wind fields influence the lift coefficient and can also lead to effects like e.g. dynamic stall. To investigate not only the effect of different turbulence intensities but also the effect of the distribution of the wind speed fluctuations, lift force measurements at a FX 79-W-151A airfoil have been performed in the wind tunnel at the University of Oldenburg (for details see [5]). Two types of passive grids have been used for the generation of the turbulent inflow condition, a standard square grid with a mesh size of 10cm and a fractal grid with $N = 5$ iterations. The turbulence intensities were $Ti = 4.6\%$ for the fractal grid and $Ti = 6.7\%$ for the square grid experiment, respectively. The profile quarter point has been positioned 1.1m behind the grids. Figure 2 right side, shows the distribution of the measured fluctuations $p(u')$ of the wind velocity at the position of the profile for the fractal grid (open circles) and the square grid (triangles). It is clearly visible that $p(u')$ for the fractal grid shows intermittent properties, whereas $p(u')$ for the square grid is close to the Gaussian distribution (dashed line).

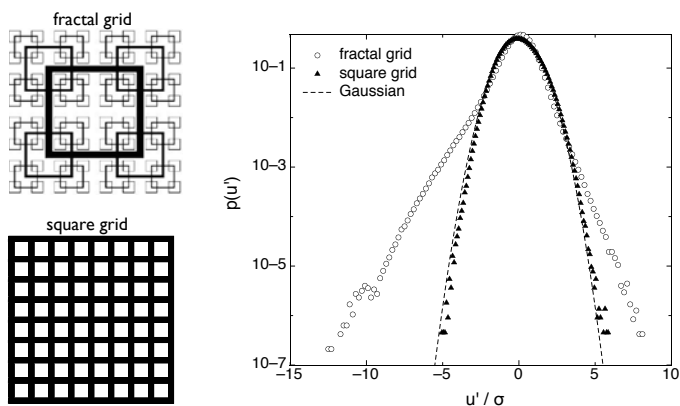


Fig. 2 Left: Sketch of a fractal grid and a square grid. Right: Distribution of measured velocity fluctuations $p(u')$ behind the fractal grid (open circles) and the square grid (triangles) at the position of the profile normalized to their standard deviation. The dashed line represents a Gaussian distribution.

Figure 3 shows the measured lift coefficients with their respective standard deviation for the square grid experiment (left) and for the fractal grid experiment (right). In both graphs the dashed line represents the lift coefficient for laminar inflow condition. The results show that for both turbulent inflow condition the maximum lift coefficient is shifted to a higher AoA and is slightly bigger compared to laminar inflow also known from dynamic stall measurements. Additionally, even though the

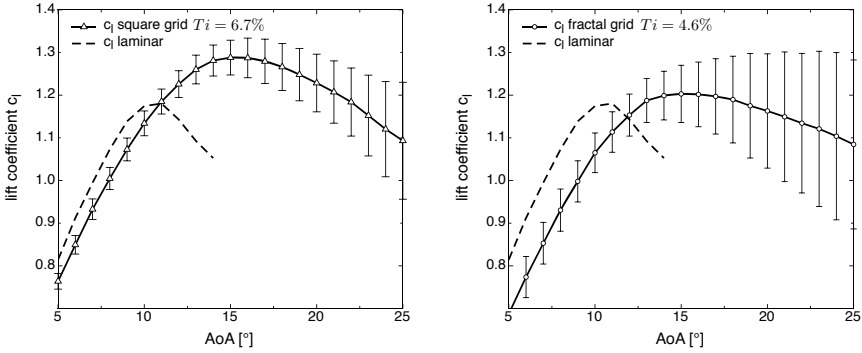


Fig. 3 Left: Measured mean lift coefficient c_l with standard deviation over angle of attack AoA for turbulent inflow generated by a square grid. The dashed line represents the c_l measurements for laminar inflow. **Right:** Measured mean lift coefficient c_l with standard deviation over angle of attack AoA for turbulent inflow generated by a fractal grid. The dashed line represents the c_l measurements for laminar inflow.

turbulence intensity for the fractal grid turbulence is smaller than the turbulence intensity for the square grid turbulence, the standard deviation of the lift coefficient is bigger for the fractal grid experiment.

3 Conclusions

The presented method in section 1 allows for the reconstruction of the distribution of the fluctuations $p(u')$ within a turbulent wind field based on 10-minute averaged measurement data. The experimental results in section 2 underline the necessity of that knowledge to better understand the dynamics of the aerodynamic forces at the rotor blades and therefore help to better estimate acting loads on wind energy converter [6].

References

1. Castaing, B., Gagne, Y., Hopfinger, E.J.: Velocity Probability Density Function of High Reynolds Number Turbulence. *Physica D* 46, 177–200 (1990)
2. Morales, A., Wächter, M., Peinke, J.: Advanced characterization of wind turbulence by higher order statistics. In: *Proceedings of EWEC* (2010)
3. Böttcher, F., Renner, C., Waldl, H.-P., Peinke, J.: On statistics of wind gusts. *Boundary-Layer Meteorology* 108, 163 (2003)
4. Stoevesandt, B., Peinke, J.: Changes in angle of attack on blades in the turbulent wind field. In: *Proceedings of EWEC* (2009)
5. Schneemann, J., Knebel, P., Milan, P., Peinke, J.: Lift measurements in unsteady flow conditions. In: *Proceedings of EWEC* (2010)
6. Mücke, T., Kleinhans, D., Peinke, J.: Influence of small scale wind velocity fluctuations on the aerodynamic alternating loads. In: *Proceedings of EWEC* (2008)

The Influence of Turbulence and Vertical Wind Profile in Wind Turbine Power Curve

A. Honrubia, A. Viguera-Rodríguez, and E. Gómez-Lázaro

Abstract. To identify the influence of turbulence and vertical wind profile in wind turbine performance, wind speed measurements at different heights have been performed. Measurements have been developed using a cup anemometer and a LIDAR equipment, specifically a pulsed wave one. The wind profile has been recorded to study the effect of the atmospheric conditions over the energy generated by a wind turbine located close to the LIDAR system. The changes in the power production of the wind turbine are relevant.

1 Introduction

It is known that both anemometers and wind turbines respond to turbulence in very specific ways. Hence, measurements of the power curve will naturally be affected by turbulence, [1], which is related to the topography where the wind turbine is located and, on the other hand, turbulence intensity as well as wind shear, are linked by the atmospheric stratification. In stable conditions, a low turbulence intensity and a high wind shear are found, whereas in unstable atmospheric conditions, the turbulence intensity is high and the wind speed hardly varies with height, [2-6].

In wind energy, turbulence is evaluated by the turbulence intensity, calculated by dividing the standard deviation of 10 minute wind speed series by its mean wind speed, according to eq. [1]:

$$I_v = \frac{\sigma_v}{\bar{V}_{mean}} \quad (1)$$

A. Honrubia · E. Gómez-Lázaro
Renewable Energy Research Institute, University of Castilla-La Mancha, Albacete, Spain
e-mail: andres.honrubia@uclm.es

A. Viguera-Rodríguez
Albacete Science & Technology Park, Albacete, Spain
e-mail: antonio.viguera@pcyta.com

The aim of the present paper is to study the changes in turbulence intensity at different heights above the ground and the impact of such variations over the production of a wind turbine. To measure the changes in wind speed, a LIDAR equipment has been used covering a period of three months, from June to August 2009, instead of installing several common wind speed meters because a high correlation degree between these devices is proven, [7]. The test was performed in a wind farm located in the south of Spain where a complex terrain is found, [8]. Close to the LIDAR was installed a meteorological mast equipped with a cup anemometer. Both were located at a distance less than 4 rotor diameters from the wind turbine used hereinafter.

2 Power Curve Performance

Firstly, to illustrate the importance of the wind profiles as a whole on the power production, figure 1 in the upper part shows a wind shear measurement during the 5th of June 2009. Whereas, the turbulence intensities are shown at the bottom.

It can clearly be seen in figure 1 that in the daytime, when the temperature near the ground is greater than at upper heights due to solar irradiation, the difference between the wind speed is small. Though, during nighttime, the opposite happens, which is called *Thermal Stratification*, [9].

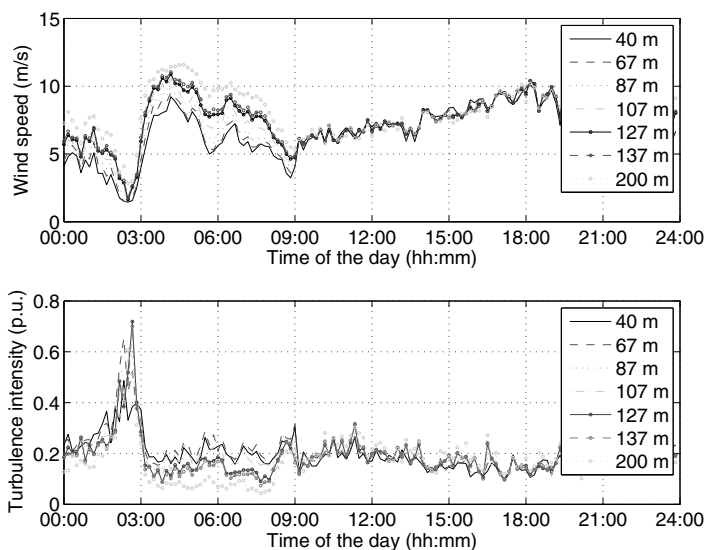


Fig. 1 Wind profile and turbulence intensity during the 5th of June 2009.

An analysis over the power generated by a wind turbine according to the wind profile and turbulent intensity is developed. In the current Standard for power curve characterization, IEC 61400-12-1, is outlined a method called “bin method”. In the

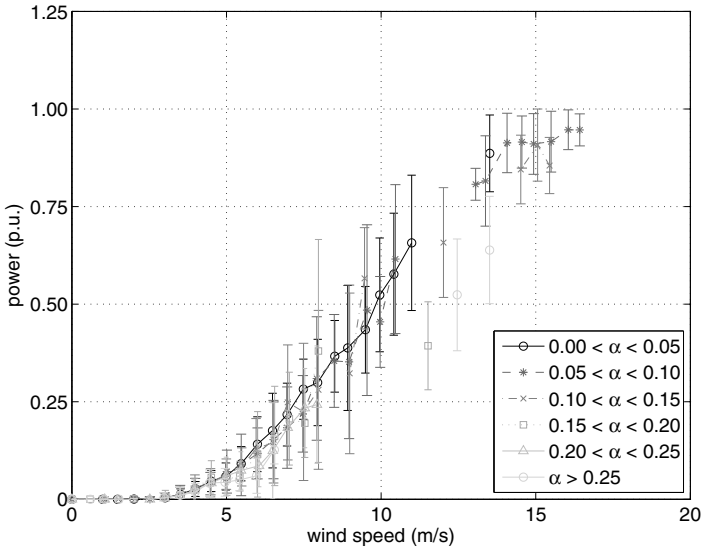


Fig. 2 Power curve related to different shear exponents, α .

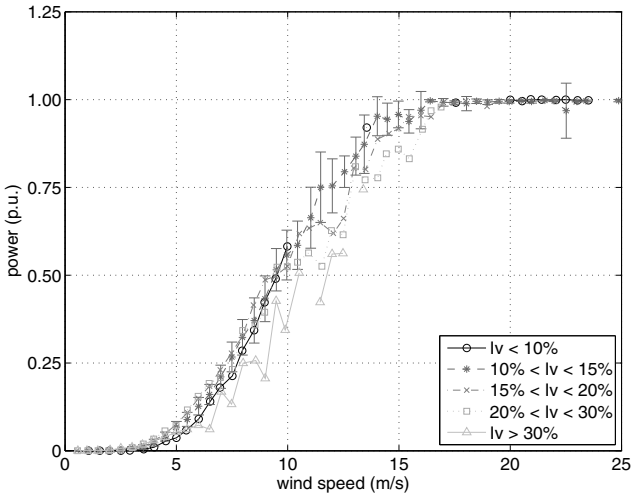


Fig. 3 Power curve according to several turbulent intensities.

present work the minimum number of points for each bin is 5. Besides, the error bars show the standard deviation of the power fluctuations in each bin.

In figure 2 is shown the power produced according to Hellman's exponent or shear exponent, α , obtained from the wind speed recorded by the LIDAR equipment at 40 m and 64 m above the ground using two months data. The figure shows that the

higher the shear exponent—equal to say “high wind shear” or “noflat wind profile”—the higher uncertainty in the power produced.

According to four months measurement period performed by cup anemometer, figure 3 shows the changes in the power output of the wind turbine when different turbulent intensities appeared. It can be noticed that for low wind speeds the higher turbulence intensity the higher production. Whereas, at medium-high wind speed, the turbulence influence is the opposite. However, due to the low amount of data measured, this trend needs further attention.

3 Conclusions

Based on an average of 3 months measurement period, results show an anomalous behavior of the power curve related to both turbulence intensity and wind shear. However, further investigation with larger measurement periods is needed to prove it.

Acknowledgement. The financial support provided by “Junta de Comunidades de Castilla-La Mancha” —PII1109-0273-2610— and “Ministerio de Ciencia y Innovación” —ENE2009-13106— is gratefully acknowledged.

References

1. Gottschall, J., Peinke, J.: How to improve the estimation of power curves for wind turbines. *Environmental Research Letters* 3(1), 015005 (7pp) (2008)
2. Honrubia, A., Viguera, A., Gómez, E., Rodríguez, D.: The influence of wind shear in wind turbine power estimation. In: *European Wind Energy Conference* (2010)
3. Wagner, R., Antoniou, I., Pedersen, S.M., Courtney, M.S., Jorgensen, H.E.: The influence of the wind speed profile on wind turbine performance measurements. *Wind Energy* 12, 348–362 (2009)
4. Antoniou, I., Pedersen, S.M.: Influence of turbulence, wind shear and low-level jets on the power curve and the aep of a wind turbine. In: *European Wind Energy Conference* (2009)
5. Langreder, W., Kaiser, K., Hohlen, H., Hojstrup, J.: Turbulence correction for power curves. In: *European Wind Energy Conference* (2004)
6. Bleiber, K., Kramkowski, T., Cosack, N., Braun, K.: The influence of meteorological parameters on the operational behavior of multi-megawatt wec. In: *German Wind Energy Conference* (2006)
7. Honrubia, A., Viguera, A., Gomez, E., Mejías, M., Lainez, I.: Comparative analysis between lidar technologies and common wind speed meters. In: *World Wind Energy Conference* (2010)
8. Honrubia, A., Viguera-Rodríguez, A., Gómez-Lázaro, E.: Vertical wind profile measurement using a pulsed lidar system. In: *International Symposium for the Advancement of Boundary Layer Remote Sensing* (2010)
9. Lange, M., Focken, U.: *Physical Approach to Short-Term Wind Power Prediction*. Springer (2005)

DNS of Actuator Disk Arrays in Ekman Boundary Layers: Preliminary Results

R. Johnstone, P.R. Spalart, and G.N. Coleman

1 Introduction

The power output of large wind farms is limited by the downward flux of kinetic energy through the atmospheric boundary layer, as ultimately all available power at turbine altitude is exhausted. This becomes relevant when the power extracted per unit area is sufficiently large, and the atmospheric boundary layer is significantly affected by the wind farm. Such coupling is therefore relevant to the design of farms, in terms of the spacing between turbines (typically roughly 5 diameters) and their resistance level (as compared with the Betz setting).

The work most relevant to this study is the LES of Calaf et al [1], which consisted of a series of cases with varying disk spacing, surface roughness, and thrust coefficients. However, Coriolis forces were not considered, and the boundary layer depth was fixed.

The overall strategy used here has the advantage of involving an Ekman layer, which is a much more realistic model of the atmospheric boundary layer than the one used by Calaf et al. The level of shear stress above the turbines is allowed to adjust to their presence, as are the boundary-layer thickness and the energy flux.

Here we present initial results of a study of large wind farms immersed in a turbulent neutral Ekman layer, which is simulated by DNS instead of LES, albeit at low Reynolds number. Note that the viscosity affects the mean velocity somewhat as surface roughness does, where the logarithmic law holds; this may be written, for smooth and rough walls respectively:

R. Johnstone
University of Southampton, Southampton, UK
e-mail: r.johnstone@soton.ac.uk

P.R. Spalart
Boeing Commercial Airplanes, Seattle, Washington, USA

G.N. Coleman
University of Southampton, Southampton, UK

$$u = \frac{u_*}{\kappa} \ln \left(E + \frac{zu_*}{\nu} \right) \quad (1)$$

$$u = \frac{u_*}{\kappa} \ln \left(\frac{z}{z_0} \right), \quad (2)$$

where z is the vertical coordinate, u the horizontal velocity, u_* the friction velocity, κ the Karman constant and z_0 the roughness length. The viscous emulation of roughness is not exact, but the roughness size over land and water is not known precisely to begin with. At or above the disk level, neither law of the wall holds, and the analogy fails. There, however, the local turbulence Reynolds number is much higher (the energy spectra show up to 4 decades of falloff).

The turbines are modelled as a periodic array of simple actuator disks. This ignores individual tip vortices, but retains the wake instabilities due to the momentum deficit, and the interaction with the surrounding turbulence. Both control the evolution of the wake before it strikes downwind turbines.

2 Numerical Method

The method used is that of Spalart, Moser and Rogers [2], [3]. Fourier transforms and periodic boundary conditions are employed in the horizontal directions, Jacobi transforms and an exponential mapping in the vertical.

The pressure difference Δp across the actuator disks is applied using a body force F . To avoid Gibbs phenomena, smoothing is used, so that the body force is a Gaussian curve on the disk axis, and an error function in the radial direction near the disk edge.

$$F = -\Delta p \frac{1}{\sqrt{\pi}\sigma_x} \exp \left(- \left[\frac{\Delta x}{\sigma_x} \right]^2 \right) \frac{1}{2} \left[1 - \operatorname{erf} \left(\frac{r^2 - R^2}{2R\sigma_r} \right) \right]. \quad (3)$$

Here Δx is the distance to the disk surface in the axial direction, and r the radial distance to the centreline. The radius of the disk is R , while σ_x and σ_r are smoothing parameters.

We follow Calaf et al [1] in relating the pressure difference Δp to the instantaneous mean velocity through the disk, U_D , as follows:

$$\Delta p = \frac{1}{2} C'_T \rho U_D^2, \quad (4)$$

where C'_T is a modified thrust coefficient. Here the orientation of the disk is also permitted to vary in time. The disk axis and F are made parallel to U_D . This mimics the yaw control of real horizontal-axis wind turbines; an additional advantage is that the direction of the (time-averaged) mean flow does not have to be known in advance.

3 Simulation Parameters

We consider a neutrally stratified, incompressible flow, in a rotating frame of reference characterised by a Coriolis parameter f . The latitude is 45 degrees. We define a Reynolds number $Re = G\delta_L/\nu$, where G is the geostrophic wind speed far above the surface, δ_L is the laminar Ekman layer depth given by $\delta_L = \sqrt{2\nu/f}$, and ν the kinematic viscosity. The results discussed below are at $Re = 1000$, and $\delta_L f/G$ is then 0.002.

The configuration of the disks is shown in figure 1 using isosurfaces of the body force F . The footprint of the ambient turbulence is plausible. We consider, for this initial study, a disk spacing of 5 diameters D and a disk centreline height of $7D/8$. Shown is a quarter of the largest domain, which is of size $L_x f/G = 0.094$; for a turbulent Ekman layer with no turbines, $fL_x/u_* \approx 1.8$ (sufficient to permit the two point correlation R_{ii} to drop below 0.1 [3]). The near-wall grid resolution in wall units is $\delta x^+ \approx 5$, $\delta y^+ = 2.5$ with 10 points below $z^+ = 4$; $\sigma_x = D/10$ and $\sigma_r = D/16$.

4 Results and Discussion

Simulations were first performed using a high thrust coefficient $C'_T = 60$ (approximating a disk of only slight porosity) on three domain sizes (containing 4, 16, and 64 turbines respectively); although the upper boundary layer was not quite independent of domain size, it is for the mean flow in the vicinity of the disks, at or above the intermediate domain size. Results for $C'_T = 2$, corresponding to the Betz setting and therefore much more realistic, were obtained on the intermediate grid and are shown in figures 2, 3 and 4, along with results at $C'_T = 60$ and $C'_T = 0$ (a turbulent Ekman layer with no turbines at the same Reynolds number).

A very strong effect is observed for the geostrophic velocity component in figure 3. The turbines are sparse enough for the results with nearly-solid disks to be

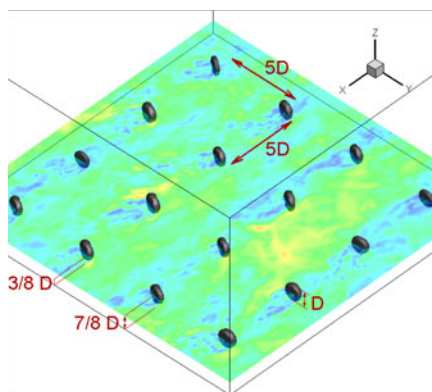


Fig. 1 Isosurfaces of body force F and contours of velocity magnitude. $C'_T = 60$.

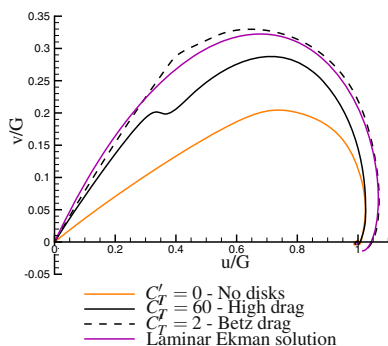


Fig. 2 Mean velocity hodograph.

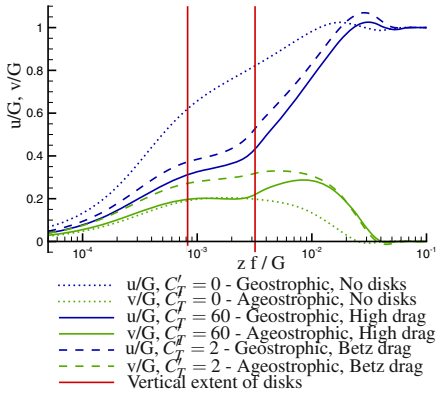


Fig. 3 Geostrophic (u/G) and ageostrophic (v/G) velocity profiles.

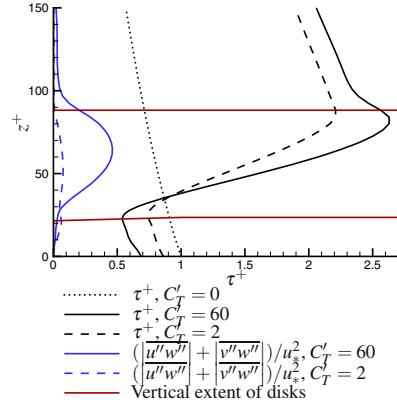


Fig. 4 Total and dispersive stresses. Nondimensionalisation is by the same u_* throughout, namely that of the $C_T' = 0$ case.

fairly close to those with realistic flow-through. The boundary layer thickness, defined as the lowest height at which the velocity becomes parallel to the geostrophic flow, increases when disks are present, by 35% for $C_T' = 2$ and nearly 50% for $C_T' = 60$. The entire atmospheric boundary layer is deeply modified, in a three-dimensional manner as confirmed by the hodographs. Therefore, expecting the Betz power output based on the wind velocity outside the farm would not make sense.

Figure 4 shows the total and dispersive shear stresses for $C_T' = 0, 2,$ and 60 . The shear stress above the disks is roughly tripled by the effect of the turbine farm.

The Reynolds number is believed to be high enough for the flow to be fully turbulent, and to approximate a rough-wall boundary layer at higher Reynolds number. The effect of increased Reynolds number on the turbulent Ekman layer is to reduce both the magnitude of the (nondimensional) wall shear stress, and its angle relative to the geostrophic flow ([3]). This would be expected both with disks present and absent. The drag of disks, however, is not very strongly affected by Reynolds number, and so it is expected that their strong influence on the flow will remain.

Acknowledgements. We acknowledge the support of the EPSRC under grant EP/G069581/1, and use of the facilities of HECToR, the UK’s national high performance computing service.

References

1. Calaf, M., Meneveau, C., Meyers, J.: Large eddy simulation study of fully developed wind-turbine array boundary layers. *Phys. Fluids* 22, 015110 (2010)
2. Spalart, P.R., Moser, R.D., Rogers, M.M.: Spectral methods for the Navier-Stokes equations with one infinite and two periodic directions. *J. Comp. Phys.* 96, 297–324 (1991)
3. Coleman, G.N.: Similarity statistics from a direct numerical simulation of the neutrally stratified planetary boundary layer. *J. Atmos. Sci.* 56, 891–900 (1999)

An Attempt to Characterize the Structure of Wake Turbulence Using a Combined Experimental and Numerical Approach

Gunner C. Larsen, K.S. Hansen, Niels Troldborg, Jakob Mann, Karen Enevoldsen, and Ferhat Bingöl

Abstract. This paper describes a combined numerical and experimental effort to characterize the structure of wake turbulence. The numerical approach is based on detailed LES. The experimental approach is based on an innovative analysis applied on full-scale wake recordings obtained using a newly developed 2D lidar technology. Consistency between the numerical and experimental approaches in terms of wake turbulence characteristics is observed. Compared to conventional atmospheric boundary layer (ABL) turbulence, the wake turbulence is inhomogeneous with reduced length scales, increased intensity, and increased coherence decay.

1 Introduction

The downstream advection of a wake from an upstream emitting turbine describes a stochastic pattern known as wake meandering [3]. It appears as an intermittent phenomenon, where winds at downwind positions may be undisturbed for part of the time, but interrupted by episodes of intense inhomogeneous turbulence and reduced mean velocity as the meandering wake hits the observation point. In order to facilitate correct predictions of power production and loading of wind turbines exposed to wake affected flow fields, two paths have been pursued to understand and characterize this complex flow field - one based on comprehensive CFD studies [4, 5] and the other based on detailed full-scale experimental studies using a newly developed 2D lidar technology [1, 2]. Whereas the investigation presented in [1] describes the large scale behavior of wake flow fields, the focus in [2] and the present paper is on

Gunner C. Larsen · Niels Troldborg · Jakob Mann · Karen Enevoldsen · Ferhat Bingöl
Risø DTU - National Laboratory for Sustainable Energy, P.O. Box 49,
4000 Roskilde, Denmark
e-mail: gula@risoe.dtu.dk

K.S. Hansen
Department of Mechanical Engineering, Building 403, DTU, 2800 Lyngby, Denmark
e-mail: ksh@dtu.nl

the characterization of the small scale wake turbulence as described in the meandering frame of reference. In particular, the focus of this paper is on inter-comparison of wake characteristics resulting from the numerical and the full-scale experimental approaches, respectively, and to simplify matters the investigation was restricted to single wake scenarios only (i.e. the flow field behind a single turbine).

2 Numerical Approach

The numerical approach is based on actuator line (ACL) large eddy simulations (LES) using turbulent and sheared inflow conditions – and resolved at downstream distances where the wake self-generated turbulence is fully developed. The ACL model combines a three-dimensional Navier-Stokes solver with a technique in which body forces, determined from the local angle of attack and a look-up table of airfoil data, are distributed along lines representing the blades of the wind turbine using a suitable smearing function. The main advantage of representing the blades by airfoil data is that much fewer grid points are required to resolve the influence of the blades compared to what would be needed for simulating the actual geometry of the blades. On the other hand, a drawback of the method is its reliance on tabulated airfoil characteristics as well as the models connected to these data, which are required for modeling phenomena such as dynamic stall, transition and three-dimensional effects. The ABL is modeled using a technique, where body forces applied to the entire computational domain are used to prescribe a given steady wind shear profile, while free-stream turbulence is modeled by superimposing synthetic turbulent velocity fluctuations to the mean flow in a cross-section upstream of the rotor. Thus, an underlying assumption for the model is consequently that the mean shear profile and the atmospheric turbulence can be modeled separately. For details such as resolution and sub-grid-scale model see [5]. Specific inflow conditions have been modeled corresponding to the specific experimental run defined below.

3 Experimental Approach

The experimental approach involves two full-scale campaigns [1, 2] with the common goal of resolving the instantaneous wake flow field with large temporal and spatial resolution in planes perpendicular to the undisturbed mean wind direction using an innovative technique based on CW lidar technology. Two analysis approaches have been attempted – one resolving wind speed variance information directly as based on the laser response characteristics, and the other in addition resolving the structure of the turbulence in terms of auto- and cross spectral properties, however, on the cost of a more elaborate analysis methodology, see [2]. An important result of the direct analysis is that the wake self-generated turbulence seems to be move with the meandering of the wake deficit as expected, which motivate the detailed analysis to be performed in the meandering frame of reference. For the detailed approach, we discretize the rotor longitudinal turbulence field by associating lidar cross sectional recordings within non-overlapping grid cells of $5 \times 10 \text{ m}^2$ (vertical times lateral

direction), belonging to a particular sweep of the laser beam, to the centre's of these cells. This is convenient because the spatial points, in which the lidar recordings are performed, change with the lidar sweep. Thereby a representation of time series referring to specific points in space is achieved. The approximate character of this approach, resulting from the spatial abstraction where the location of a physical observation is "moved" to the respective grid centre, is partly justified by the fact that the lidar measurements basically does not represent point measurements, but rather volume averaged quantities. The conducted investigation is based on one 10-minute recording period associated with a 200m downstream focus distance. This recording period is characterized by an ambient hub height mean wind speed of 9.1m/s, and an ambient turbulence intensity 6.9%.

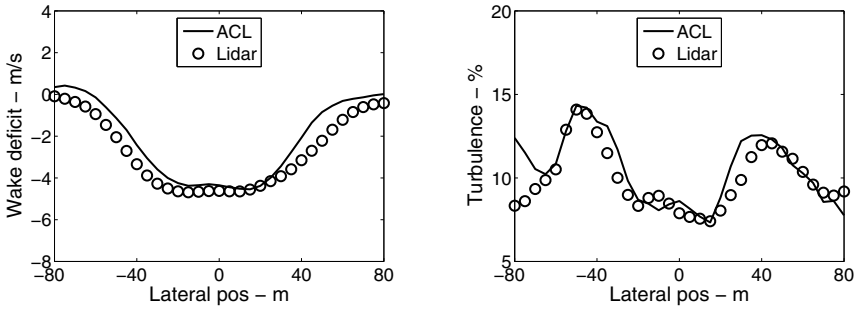


Fig. 1 Comparison of measured (lidar) and computed (ACL) stream wise velocity deficit (left) and turbulence intensity (right) at hub height.

4 Results, Discussion and Conclusion

In order to mimic the experimental results as closely, the computed data were analyzed using the same method as applied to the experimental data. I.e. the temporal variation of the wake center position and the associated wake flow characteristics in the meandering frame of reference were thus obtained in an identical way. Figure 1 shows the horizontal wake deficit and turbulence intensity profiles at hub height obtained from experiment and numerical simulation, respectively. The mean wake deficit is included because of its close relationship with the wake self generated turbulence. Figure 2 shows examples of corresponding auto-spectra resulting from the experimental- and the numerical analysis, respectively. The wake turbulence, as seen from Figure 1 displays inhomogeneous characteristics, and a close agreement between the experimental and numerical approach is seen. The auto-spectra, corresponding to the central part of the wake regime, shown in Figure 2 also show good agreement between the numerical- and experimental results, although the spectral decay beyond approximately 3×10^{-1} Hz is somewhat stronger for the computed results. This observation is even more pronounced for other spatial positions closer to the edge of the wake. For both approaches, the integral length scale of the wake turbulence seems to be of the order of a rotor radius and thus considerable less than

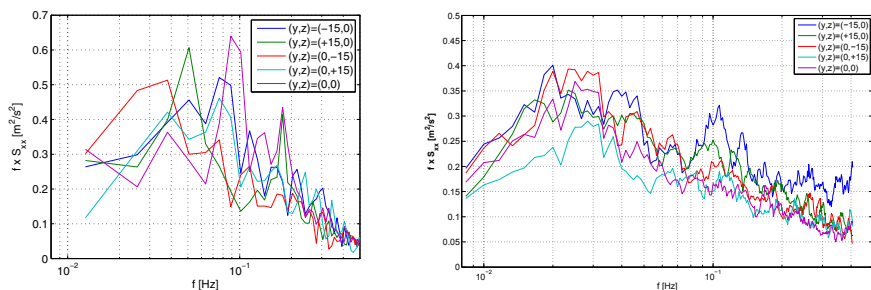


Fig. 2 Computed (left) and measured (right) spectra in the meandering frame of reference.

the length scale of conventional ABL turbulence. It should be mentioned that the present results seem to depend somewhat on the lidar scan patterns. This should be investigated more thoroughly. Tentatively, the coherence decay of the wake turbulence is stronger than for conventional ABL turbulence.

References

1. Bingöl, F., Mann, J., Larsen, G.C.: Lidar measurements of wake dynamics part I: One dimensional scanning. *Wind Energy* 13(1), 51–61 (2010)
2. Larsen, G.C., Hansen, K.S., Mann, J., Bingöl, F., Enevoldsen, K.: Full scale measurements of wind turbine wake turbulence. In: *The Science of making Torque from Wind*, Heraklion, Crete, Greece (June 2010)
3. Larsen, G.C., Madsen, H.A., Thomsen, K., Larsen, T.J.: Wake meandering: A pragmatic approach. *Wind Energy* 11(4), 377–395 (2008)
4. Larsen, G.C., Madsen Aagaard, H., Larsen, T.J., Troldborg, N.: Wake modeling and simulation. Technical report, Forskningscenter Risø, Roskilde (2008)
5. Troldborg, N., Sørensen, J.N., Mikkelsen, R.: Numerical simulations of wake characteristics of a wind turbine in uniform inflow. *Wind Energy* 13(1), 86–99 (2010)

Lidar Turbulence Measurements for Wind Energy

Jakob Mann, Ameya Sathe, Julia Gottschall, and Mike Courtney

Abstract. Modeling of the systematic errors in the second-order moments of wind speeds measured by continuous-wave (ZephIR) and pulsed (WindCube) lidars is presented. These lidars use the velocity azimuth display technique to measure the velocity vector. The model is developed for the line-of-sight averaging and the full extent of conical scanning. The predictions are compared with the measurements from the ZephIR, WindCube and sonic anemometers at a flat terrain test site, under different atmospheric stability conditions. It is observed that the systematic errors are up to 90% for the vertical velocity variance, whereas they are up to 70% for the horizontal velocity variances. The systematic errors also vary with atmospheric stability, being lowest for the very unstable conditions. It is concluded that with the current measurement configuration, these lidars cannot be used to measure turbulence precisely.

1 Introduction

Atmospheric turbulence is one of the main inputs in assessing loads on the wind turbines. Thus, accurate estimation of wind speed and turbulence at several heights is crucial for the successful development of a wind farm. In wind energy the current standard is the use of meteorological masts equipped with cup/sonic anemometers. However, tall meteorological masts are very expensive, and offshore, the costs increase significantly. The advent of remote sensing devices like lidars gives a further boost to the development of wind energy. In recent years with the introductions of the ZephIR and WindCube there has been a surge in the verification campaigns of

Jakob Mann · Julia Gottschall · Mike Courtney
Wind Energy Division, RisØ DTU, 4000 Roskilde, Denmark
e-mail: jmsg@risoe.dtu.dk

Ameya Sathe
L & R, Section Wind Energy, TU Delft, 2629 HS Delft, The Netherlands
e-mail: A.R.Sathe@tudelft.nl

comparing the lidar mean wind speed with that of a cup anemometer for wind energy applications [1, 2, 3, 4]. [3] discuss the advantages and disadvantages of CW and pulsed lidars. In order to use a lidar as a standard measuring instrument in the future, a fair degree of confidence is also required in the turbulence measurements.

Although lidars have been introduced in wind energy recently, for meteorology they have been investigated previously to measure turbulence using different scanning techniques. A comprehensive review is given in [5] that covers different remote sensing techniques for turbulence measurements including lidars. A review of the use of lidars for wind energy applications is also presented in [6]. Recently, studies have been carried out to model the spatial averaging effects [7] and compare the 3D turbulence measurements using three staring lidars [8]. [9] estimated the momentum fluxes using lidars and modelled the unfiltered turbulence from the CW lidar, where the model compares reasonably well with the measurements. In the present work, line-of-sight averaging and the full extent of conical scanning is considered.

A theoretical model is developed to estimate the systematic errors in the second-order moments of wind speeds measured by lidars. The systematic errors are the errors that arise due to the averaging effect in the line-of-sight and the quite large circle in which lidars measure wind speed. Two types of lidars are considered, the ZephIR developed by QinetiQ (Natural Power) as a continuous wave (CW) lidar and the WindCube developed by Leosphere as a pulsed lidar. The verification is carried out by comparing the variances measured by the ZephIR and WindCube with that of the sonic anemometers placed at different heights on a meteorological mast. The sonic anemometer has an averaging volume of $\approx (0.1\text{m})^3$ so in a wind energy context, where turbulence is measured at considerable heights over the surface, it can be considered a point measurement. The diameter of the measuring volume of the lidar is of the order of 100 m, so, clearly, it measures differently, and that difference can be termed ‘‘lidar error’’. Further details are given in [10].

2 Theory

The model in this study is developed for the velocity azimuth display (VAD) technique of lidar scanning.

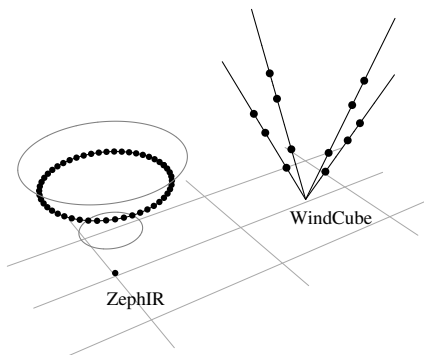
Fig. 1 shows the lidar emitting the laser beam in different ways for the two lidar systems treated here. The line-of-sight velocity (also called radial velocity v_r) is given as the dot product of the unit directional vector and the velocity field at the point of focus for a CW lidar, and the center of the range gate for the pulsed lidar,

$$v_r(\theta) = \mathbf{n}(\theta) \cdot \mathbf{v}(d_f \mathbf{n}(\theta)), \quad (1)$$

where θ is the azimuth angle, d_f is the focus distance for the CW lidar, and the distance to the center of the range gate for the pulsed lidar at which the wind speeds are measured, $\mathbf{v} = (u, v, w)$ is the instantaneous velocity field evaluated at the focus point $d_f \mathbf{n}(\theta)$, and $\mathbf{n}(\theta)$ is the unit directional vector given as,

$$\mathbf{n}(\theta) = (\cos \theta \sin \phi, \sin \theta \sin \phi, \cos \phi). \quad (2)$$

Fig. 1 Schematic of the velocity azimuth display scanning of the two lidar systems. The ZephIR scans at many points on the azimuth circle, with a typical scan consisting of measurements of v_r at 50 points on the azimuth circle.



In reality it is impossible to obtain the backscattered radiation precisely from only the focus point, and there is always backscattered radiation of different intensities from different regions in space along the line-of-sight. Hence, it is necessary to assign appropriate weights to the backscattered intensity such that the weight corresponding to the focus point is the highest. Mathematically, the weighted average radial velocity can be written as,

$$\tilde{v}_r(\theta) = \int_{-\infty}^{\infty} \varphi(s) \mathbf{n}(\theta) \cdot \mathbf{v}(s\mathbf{n}(\theta) + d_f \mathbf{n}(\theta)) ds, \tag{3}$$

where $\varphi(s)$ is any weighting function, integrating to one, and s is the distance along the beam from the focus. For simplicity we assume that $s = 0$ corresponds to the focus distance.

The following are the main assumptions of our model:

1. The terrain is homogeneous
2. The flow field is frozen during the scan
3. Eq. (3) with an appropriately chosen $\varphi(s)$ models the averaging well
4. The spatial structure of the turbulent flow is described well by the spectral tensor model of [11]

2.1 Systematic Turbulence Errors for the ZephIR Lidar

If we assume the coordinate system such that u is aligned to the mean wind direction, v is perpendicular to the mean wind direction, w is the vertical component, and the mean wind comes from the North then $\tilde{v}_r(\theta)$ can be expressed as,

$$\tilde{v}_r(\theta) = A + B \cos \theta + C \sin \theta, \tag{4}$$

where the coefficients $A = w_{qq} \cos \phi$, $B = u_{qq} \sin \phi$ and $C = v_{qq} \sin \phi$ and the sign ambiguity in $\tilde{v}_r(\theta)$ is neglected (see [9]). We use the subscript qq to denote the velocity components measured by ZephIR, since they are not the true velocity components u , v and w . The assumption that the mean wind comes from the North is

only made for simplicity. For a lidar measuring at many points on the azimuth circle the choice of the mean wind direction does not matter since averaging over the entire circle is carried out. The values of the coefficients A , B and C are found using least squares method by fitting Eq. (4) to the measured values of $\tilde{v}_r(\theta)$ at all the scanned azimuth angles. The coefficients can be written as the first few terms in the Fourier expansion of the function $\tilde{v}_r(\theta)$,

$$A = \frac{1}{2\pi} \int_0^{2\pi} \tilde{v}_r(\theta) d\theta, \tag{5}$$

$$B = \frac{1}{\pi} \int_0^{2\pi} \tilde{v}_r(\theta) \cos \theta d\theta, \tag{6}$$

$$C = \frac{1}{\pi} \int_0^{2\pi} \tilde{v}_r(\theta) \sin \theta d\theta. \tag{7}$$

We proceed by deriving expressions for the w_{qq} variance. The expressions for the (co-) variances of the remaining components of wind velocity can be derived in a similar manner.

The variance of A is written as $\sigma_A^2 = \langle A'^2 \rangle$, where $\langle \rangle$ denotes ensemble averaging of a variable. From the above definition of A we can write,

$$\sigma_A^2 = \langle w_{qq}'^2 \rangle \cos^2 \phi. \tag{8}$$

Using Eq. (5) we can also write,

$$\sigma_A^2 = \left\langle \left(\frac{1}{2\pi} \int_0^{2\pi} \tilde{v}_r'(\theta) d\theta \right)^2 \right\rangle. \tag{9}$$

Lengthy manipulations allow us to express σ_A^2 in terms of the three-dimensional spectral velocity tensor $\Phi_{ij}(\mathbf{k})$, which is the Fourier transform of the covariance tensor. First the squared integral in Eq. (9) is converted to a double integral, whereafter the ensemble average is moved inside the double integral. The product of velocities thus averaged can be written in terms of the covariance tensor, which then can be substituted by the three-dimensional Fourier transform of the spectral tensor. Now σ_A^2 is given in terms of the spectral tensor, and the expression can be considerably simplified, see (10). Let $\alpha_i(\mathbf{k}) = \left(\int_{-\infty}^{\infty} \varphi(s) \left[\frac{1}{2\pi} \int_0^{2\pi} n_i(\theta) e^{i(s+d_f)\mathbf{k}\cdot\mathbf{n}(\theta)} d\theta \right] ds \right)$. Eq. (9) can then be written as (using Eq. 8),

$$\langle w_{qq}'^2 \rangle \cos^2 \phi = \int \Phi_{ij}(\mathbf{k}) \alpha_i(\mathbf{k}) \alpha_j^*(\mathbf{k}) d\mathbf{k}, \tag{10}$$

where $*$ denotes complex conjugation. Thus the integral reduces to evaluating $\alpha_i(\mathbf{k})$ since the analytical expressions for $\Phi_{ij}(\mathbf{k})$ are given in (11). Eq. (10) can then be estimated numerically. For a CW lidar, $\varphi(s)$ is well approximated by a Lorentzian function (12),

$$\varphi(s) = \frac{1}{\pi} \frac{l}{l^2 + s^2}, \tag{11}$$

where l is the Rayleigh length ($= \lambda_b d_f^2 / \pi r_b^2$, where $\lambda_b = 1.55 \mu\text{m}$ is the wavelength of the emitted radiation, and $r_b = 19.5 \text{ mm}$ is the beam radius). The resulting $\langle w_{qq}^2 \rangle$ can now be evaluated and a similar approach is taken for deriving u_{qq} and v_{qq} variances, and for the variances measured by the WindCube. An additional complication for the ZephIR is that the beam rotates three times calling for an extra averaging in time, which is included in the theoretical prediction in figure 2b and 2a, see [10] for details. We present the systematic errors as the ratio of the lidar second-order moments and the true second-order moment.

3 Comparison of Models with the Measurements

Meteorological measurements are taken at 10, 20, 40, 60, 80 and 100 m at Risø DTU's test center at Høvsøre in Denmark. We use the high frequency (20 Hz) and 10-min mean sonic anemometer measurements at 40–100 m between December 2008 and November 2009. Sonic anemometers are placed at several heights on the North booms of the meteorological mast and the lidars are placed within a few tens of meters of the mast.

In order to avoid the influence of the wakes from the wind turbines and the met-mast on lidar measurements, and inhomogeneities due to the sudden change of roughness (sea-land transition), only the eastern sector (50° – 150°) is analyzed. Only observations of wind speeds greater than 4 m/s are used.

The estimation of Φ_{ij} using the model from [11] requires three input parameters, $\alpha \varepsilon^{2/3}$, which is a product of the spectral Kolmogorov constant α [13] and the rate of viscous dissipation of specific turbulent kinetic energy $\varepsilon^{2/3}$, a length scale L and an anisotropy parameter Γ . We use these input parameters obtained by fitting the sonic anemometer measurements under different atmospheric stability conditions, at several heights on the meteorological mast in the eastern sector [14].

Fig. 2 shows the comparison of the modelled systematic errors (section 2) with the measurements for u , v and w variances. The measurements are represented an error bar with the median, first and third quartiles as center point and end points, respectively. We infer the following:

- The systematic error varies considerably under different atmospheric stability conditions – The variation is up to 50% for u and v variances, and up to 20% for w variance. There is also a large variation in the length scales of different velocity components resulting in varying attenuation of the variances.
- For the ZephIR the systematic errors increase with height under all atmospheric stability conditions – This is due to a quadratic increase in the probe length with height [11]. The diameter of the scanning circle also increases with height. This results in a greater attenuation of the second-order moments with increasing height.
- For the WindCube the systematic errors decrease with height for the u and v variances under all atmospheric stability conditions, probably because the probe length is constant with height, and hence, at lower heights there is a combined averaging effect due to the probe length and the diameter of the scanning circle. Considering that at lower heights the length scales are smaller than at higher

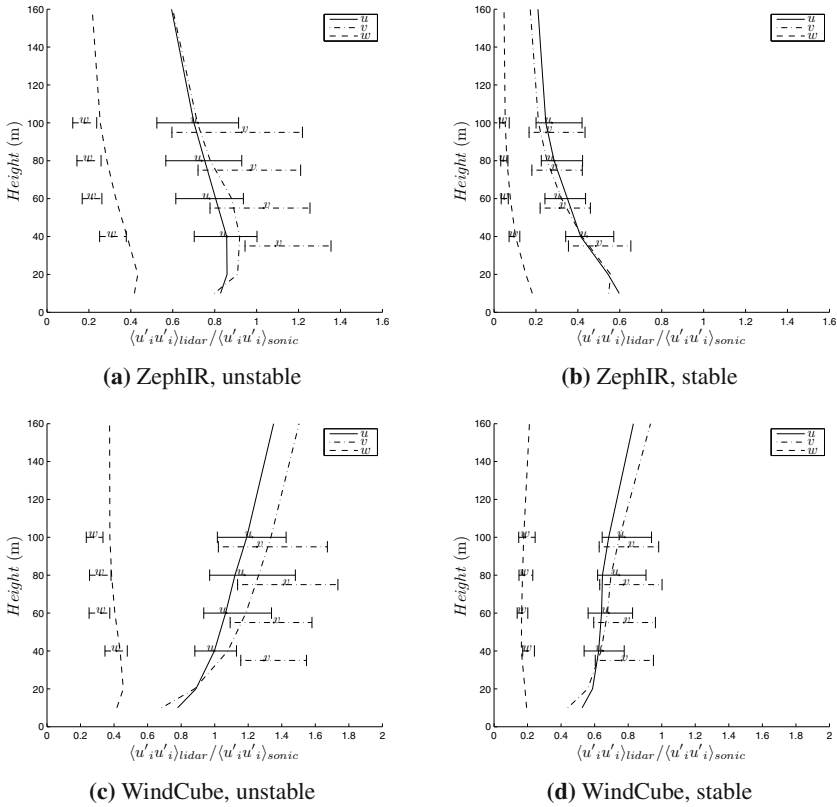


Fig. 2 Systematic errors under different atmospheric stability conditions. The markers indicate measurements, with the marker for v displaced 5 m downwards for clarity. The curves are the theoretical plots with the low-pass filter for the ZephIR. For the WindCube the theoretical error depends weakly on wind direction, so it is plotted as an average over all directions.

heights, it is likely that the variances are attenuated greater at lower heights than at higher heights.

- The systematic errors in w variance is much larger (approximately 3-5 times) than that of the u and v variances – This is due to the very small length scales of the w component as compared to those for u and v , resulting in the attenuation of the w variance of up to 90%. The u and v variances are attenuated up to 70%.
- The trend of the systematic errors predicted by both models is in agreement with the observations at all heights.

4 Conclusion

The main goal of this paper is to understand the systematic errors in the second-order moments of CW and pulsed lidars. In particular, we model the systematic errors for

the ZephIR and WindCube, which are used as CW and pulsed lidars respectively. In general, the model predicts the systematic errors quite well although there are many uncertainties associated with the assumptions made in the model.

As of now, with the current measurement configuration, the systematic errors of the second-order moments are quite large and depend strongly on stability, and hence, it is clear that the ZephIR and WindCube cannot be used to measure turbulence precisely.

We are currently looking into alternative ways of analyzing the lidar data and different beam configurations that would render turbulence measurements more feasible. One idea is to use two different half opening angles as in [15], who show that all terms in the Reynolds stress tensor can be obtained by using the single beam statistics, without resorting beam covariances, which is done in this paper. That would require serious hardware changes to the instruments treated here. Another idea is to supplement the analysis with information on the width of the Doppler spectra, as done for the momentum flux in [9], in order to neutralize the effect of along beam averaging.

References

1. Smith, D.A., Harris, M., Coffey, A.S., Mikkelsen, T., Jørgensen, H.E., Mann, J., Danielian, R.: Wind lidar evaluation at the Danish wind test site in Høvsøre. *Wind Energy* 9, 87–93 (2006)
2. Kindler, D., Oldroyd, A., Macaskill, A., Finch, D.: An eight month test campaign of the QinetiQ ZephIR system: Preliminary results. *Meteorologische Zeitschrift* 16(5), 479–489 (2007)
3. Courtney, M., Wagner, R., Lindelow, P.: Testing and comparison of lidars for profile and turbulence measurements in wind energy. In: 14th International Symposium for the Advancement of Boundary Layer Remote Sensing (2008)
4. Peña, A., Hasager, C.B., Gryning, S.-E., Courtney, M., Antoniou, I., Mikkelsen, T.: Offshore wind profiling using light detection and ranging measurements. *Wind Energy* 12(2), 105–124 (2009)
5. Engelbart, D.A.M., Kallistratova, M., Kouznetsov, R.: Determination of the turbulent fluxes of heat and momentum in the ABL by ground-based remote-sensing techniques (a review). *Meteorologische Zeitschrift* 16(4), 325–335 (2007)
6. Emeis, S., Harris, M., Banta, R.M.: Boundary-layer anemometry by optical remote sensing for wind energy applications. *Meteorologische Zeitschrift* 16(4), 337–347 (2007)
7. Sjöholm, M., Mikkelsen, T., Mann, J., Enevoldsen, K., Courtney, M.: Spatial averaging-effects on turbulence measured by a continuous-wave coherent lidar. *Meteorologische Zeitschrift* 18(3) (Sp. Iss. SI), 281–287 (2009)
8. Mann, J., Cariou, J., Courtney, M., Parmentier, R., Mikkelsen, T., Wagner, R., Lindelow, P., Sjöholm, M., Enevoldsen, K.: Comparison of 3D turbulence measurements using three staring wind lidars and a sonic anemometer. *Meteorologische Zeitschrift* 18(2) (Sp. Iss. SI), 135–140 (2009)
9. Mann, J., Peña, A., Bingöl, F., Wagner, R., Courtney, M.S.: Lidar scanning of momentum flux in and above the surface layer. *Journal of Atmospheric and Oceanic Technology* 27(6), 792–806 (2010), doi:10.1175/2010JTECHA1389.1

10. Sathe, A.R., Mann, J., Gottschall, J., Courtney, M.: Estimation of the systematic errors in lidar turbulence measurements. To be published in JTECH (2011)
11. Mann, J.: The spatial structure of neutral atmospheric surface-layer turbulence. *Journal of Fluid Mechanics* 273, 141–168 (1994)
12. Sonnenschein, C.M., Horrigan, F.A.: Signal-to-noise relationships for coaxial systems that heterodyne backscatter from atmosphere. *Applied Optics* 10(7), 1600 (1971)
13. Monin, A.S., Yaglom, A.M.: *Statistical Fluid Mechanics*, vol. 2. MIT Press (1975)
14. Peña, A., Gryning, S.-E., Mann, J.: On the length scale of the wind profile. *Quarterly Journal of the Royal Meteorological Society* (2010) (accepted)
15. Eberhard, W.L., Cupp, R.E., Healy, K.R.: Doppler lidar measurements of profiles of turbulence and momentum flux. *Journal of Atmospheric and Oceanic Technology* 6, 809–819 (1989)

Statistical Characteristics of Gusty Wind Conditionally Sampled with an Array of Ultrasonic Anemometers

K. Taniwaki, K. Sassa, T. Hayashi, Y. Hono, and K. Adachi

Abstract. The present field experiment aims to clarify statistical characteristics of gusty winds having dimensions relatively smaller than their parent convective systems. Three wind velocity components were measured by using 12 ultrasonic anemometers aligned along the Dai-ni Mogami river bridge in Shonai plain, Japan. The gust events were conditionally sampled referring to steep triangle wave. The extracted events were more than 9000 and concentrated in winter season. We separated incidence per day to over 10 events per day and under 10 per day. Scale of gust events for over 10 per day was larger than the case of under 10 per day.

1 Introduction

Gusty winds such as downburst, i.e. strong downdraft from cumulonimbus [1], or gust front [5] or tornado caused local damage within width of several ten meters or several hundred meters area [2]. Gusty winds were investigated by many researchers [3, 4]. They indicated that the scale of gusty winds was from tens meters to hundreds meters. But the characteristics of gusty winds are still not well understood. The aim of this paper is to clarify the characteristics of gusty winds, e.g., temporal and spatial scales of it, as the first step for researching microscale structure of it.

2 Observations

We used the 12 ultrasonic anemometers arranged within 1.2km from south to north at Dai-ni Mogami River Bridge in Shonai Plane facing the Japan Sea as shown in Fig. 1. The terrain around the observation point is almost flat. The ultrasonic anemometers measured three velocity components at an interval of 4 Hz. The

Koji Sassa
Kochi University, Akebonocho, Kochi, Japan
e-mail: sassa@kochi-u.ac.jp

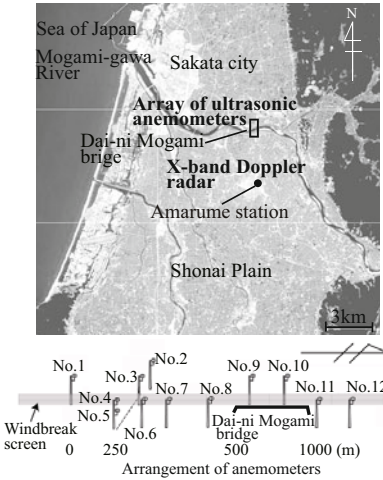


Fig. 1 Location of ultrasonic anemometers

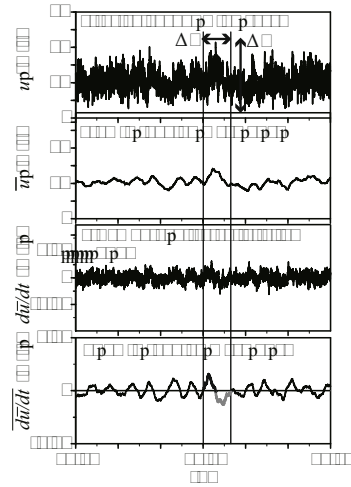
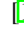


Fig. 2 Conditional sampling of gust event

location of the anemometer, No. 3, was set to the reference point for later analysis. We simultaneously observed convective systems with a Doppler radar located at about 4 km south from the array of the anemometers. Observation period is from March 2006 to March 2009. We conditionally sampled a gusty event through extracting a triangle wave pattern  in which the instantaneous peak exceeded 20 m/sec. from 2 minute running averaged wind velocity. Then evaluated some characteristics of the gust events; its duration, ΔT , the peak velocity, V_{max} , the maximum velocity difference, ΔV . We also examined the horizontal distributions of the gust events.

3 Results and Discussion

More than 9000 events were obtained during the observational period. The most of gusty events occurred in winter as shown in Fig. 3a. The main wind direction was northwest in winter on the other hand the opposite direction was appeared in summer (Fig. 3b). The former case shows the gust events with winter monsoon surge and the later shows "Kiyokawa-dashi" that is local easterly wind in Shonai plain. Figs. 3c,d show the frequency distributions of ΔV and ΔT . Mean values of ΔV and ΔT were 17.4 m/s and 5 min, respectively. The value of ΔT is almost the same with that of downburst. The gust events were observed less than 10 times per day in most of days when gust events were detected as shown in Fig. 4a. Such events may correspond to the passage of convective systems. However, total number of the events in days when the events were detected more than 10 per day was larger than that in the other days. This fact shows that winter monsoon surge causes frequent gusty events near surface. Fig. 5 shows instantaneous space correlation of gusty wind though the data

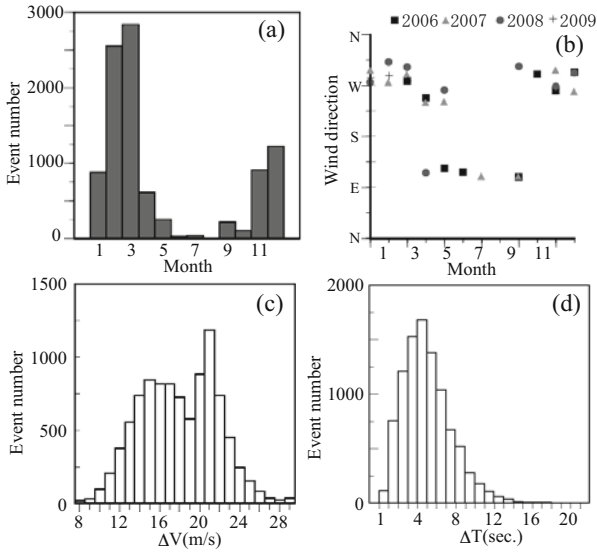


Fig. 3 Statistics of gust events, (a) monthly frequency of gust events, (b)seasonal variation of mean wind direction, (c) frequency of velocity difference, (d) frequency of the duration of gust events

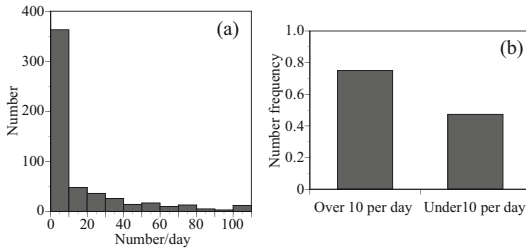


Fig. 4 (a) Frequency of gust events per day, (b) Frequency of gust events when they occur more than 10 per day and the other

were averaged for 10 sec. The velocity gradient near the anemometer No.3 in the case of over 10 per day was steeper than that in another case, but large velocity was found to maintain more than 500 m from No.3 in the case of over 10 per day. This fact shows that the special scale of gusty event in the case of over 10 per day is smaller than that in another case but mean wind velocity is high in wide area in this case. Fig.6 also illustrates such facts. The large wind speed spread in wide region in the case of over 10 per day whereas the high speed region is less than 400 m in width in another case. The latter case shows a typical pattern of gust yielded from a convective cell having several km in horizontal scale [5].

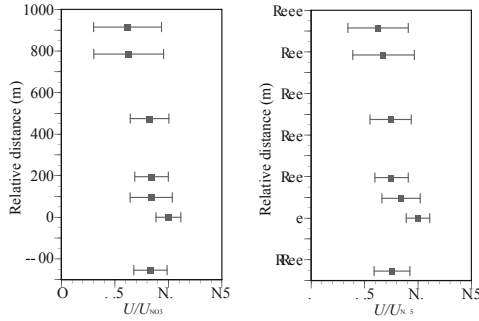


Fig. 5 Time-space distribution of wind speeds normalized by maximum speed of the anemometer No. 3, (a) Over 10 events per day, (b) Under 10 events per day

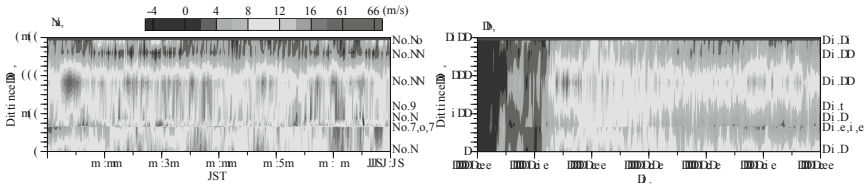


Fig. 6 Instantaneous distributions of wind speeds, (a) Over 10 events per day, (b) Under 10 events per day

4 Conclusion

We detected a large number of the gust events. The occurrence of the gust events showed seasonal variation. The dimensions of the gust events were slightly smaller than those of downbursts [1] and gust fronts [5]. The gust events accompanied by winter monsoon surge have more smaller scale and are buried in mean high speed wind of the surge.

References

1. Hjelmfelt, M.R.: Structure and life cycle of microburst outflows observed in Colorado. *J. Appl. Meteorol.* 27, 900–927 (1988)
2. Fujita, T.T.: Tornadoes and downbursts in the context of generalized 2 planetary scales. *J. Atmos. Sci.* 45, 3846–3879 (1981)
3. Shiotani, M., Iwatani, Y., Kuroda, K.: Horizontal space correlations of velocity fluctuations during strong winds. *J. Meteorol. Soc. Japan* 54, 59–67 (1976)
4. Hayashi, T.: The horizontal distribution of space correlation coefficients of wind fluctuations in the atmospheric surface layer. *Boundary-Layer Meteorol.* 55, 125–140 (1991)
5. Wakimoto, R.M.: The life cycle of thunderstorm gust fronts as viewed with Doppler radar and Rawinsonde data. *Mon. Wea. Rev.* 110, 1060–1082 (1982)

Free-Stream Turbulence Effects on the Flow around an S809 Wind Turbine Airfoil

Sheilla Torres-Nieves, Víctor Maldonado, José Lebrón, Hyung-Suk Kang, Charles Meneveau, and Luciano Castillo

Abstract. Two-dimensional Particle Image Velocimetry (2-D PIV) measurements were performed to study the effect of free-stream turbulence on the flow around a smooth and rough surface airfoil, specifically under stall conditions. A 0.25-m chord model with an S809 profile, common for horizontal-axis wind turbine applications, was tested at a wind tunnel speed of 10 m/s, resulting in Reynolds numbers based on the chord of $Re_c \approx 182,000$ and turbulence intensity levels of up to 6.14%. Results indicate that when the flow is fully attached, turbulence significantly decreases aerodynamic efficiency (from $L/D \approx 4.894$ to $L/D \approx 0.908$). On the contrary, when the flow is mostly stalled, the effect is reversed and aerodynamic performance is slightly improved (from $L/D \approx 1.696$ to $L/D \approx 1.787$). Analysis of the mean flow over the suction surface shows that, contrary to what is expected, free-stream turbulence is actually advancing separation, particularly when the turbulent scales in the free-stream are of the same order as the chord. This is a result of the complex dynamics between the boundary layer scales and the free-stream turbulence length scales when relatively high levels of active-grid generated turbulence are present.

1 Introduction

Many investigations have studied the aerodynamics of a wind turbine airfoil subject to high levels of free-stream turbulence (FST) [2, 5]. Aerodynamic studies have

Sheilla Torres-Nieves · Víctor Maldonado · José Lebrón
Rensselaer Polytechnic Institute, Troy, NY, US
e-mail: torres@rpi.edu

Hyung-Suk Kang
United States Naval Academy, Annapolis, MD, US
e-mail: hs kang@usna.edu

Charles Meneveau
Johns Hopkins University, Baltimore, MD, US
e-mail: meneveau@jhu.edu

Luciano Castillo
Texas Tech University, Lubbock, TX, US
e-mail: luciano.castillo@ttu.edu

shown that the addition of passive-grid generated free-stream turbulence to the flow over wind turbine blades delays flow separation [1]. The study and understanding of these complex conditions, such as active-grid generated turbulence, is crucial for the improvement of the design and performance of wind turbines.

Wind turbines are known to operate under the highly turbulent conditions present in the atmospheric boundary layer and subject to the wakes from upwind wind turbines. Although these conditions are known to affect the performance and lifespan of these massive structures, the mechanisms by which FST adversely impacts wind turbines are not known in enough detail to address these issues. The lack of velocity-field detailed data under complex conditions motivates the present study, particularly for wind energy applications. Therefore, the aim of this study is to analyze the influence of high levels of FST on the flow around a smooth and rough surface airfoil at various angles of attack. Specifically, this investigation examines how wind turbine airfoils are affected by highly turbulent flow under stall conditions.

2 Experimental Setup

Two-dimensional Particle Image Velocimetry (2-D PIV) experiments were performed over a smooth and rough surface around an airfoil with an S809 profile, common for horizontal-axis wind turbine applications [2], with and without additional levels of FST. A 0.25-m chord (c) model was tested in the Corrsin Wind Tunnel Facility at The Johns Hopkins University. The airfoil section has a maximum chord thickness of 21%. For all the cases, the mean velocity of the wind tunnel remained constant at 10 m/s, resulting in Reynolds numbers based on the chord of $Re_c \approx 182,000$ and turbulence intensity levels of 6.14%. For the smooth cases, a cylindrical trip-wire with a diameter of 1.6 mm was placed at a location 4 mm from the leading edge of the airfoil, to accelerate the transition to turbulent regime. For the rough surface cases, the airfoil was covered with a 24-grit Aluminum Oxide abrasive sheet; the roughness topography and other details of the rough surface used are described in a recent study by Brzek *et al.* [3].

The free-stream turbulence was generated by means of an active grid [4] located 5.5 m upstream of the airfoil. Further details of the active-grid generated turbulence were reported by Brzek *et al.* [3]. Two angles of attack, α , were examined (i.e., $\alpha = 0^\circ$ and 16°) to analyze the flow before and after separation.

Measurements were gathered using 2-D PIV for cases with and without FST over the smooth and rough surfaces airfoils. The resulting PIV interrogation area has dimensions of approximately 16 cm \times 16 cm, yielding a resolution of 3.09 mm. For both angles of attack, PIV measurements captured the airfoil from $0.5c$ until about 60 mm past the trailing edge. Moreover, to capture the separation point, an additional PIV plane was captured for the cases at $\alpha = 16^\circ$ to include a section upstream of the leading edge until $0.6c$. For each case, 3000 samples were taken at a rate of 7.25 Hz. Moreover, pressure measurements were acquired using 36 static pressure taps located along the upper and lower curves of the airfoil.

3 Aerodynamic Characteristics

Pressure coefficient distributions were approximated analytically through regression analysis and integrated to obtain the 2-D lift coefficient for these cases. Figures 1 and 2 show the upper (suction) surface and lower (pressure) surface chord-wise pressure coefficient distributions (i.e., $C_{p,U}$ and $C_{p,L}$), obtained for the smooth surface cases for $\alpha = 0^\circ$ and 16° , respectively. The static pressure distributions around the blade are used as an indication of lift generation. At $\alpha = 0^\circ$, the airfoil generates a slight amount of positive lift. With the addition of FST (fig. 1 (right)) the pressure differential between the suction and pressure surfaces is smaller and, hence, the lift coefficient is closer to zero. For $\alpha = 16^\circ$ (fig. 2), the blade is expected to generate more lift. At this angle, the addition of FST increases the suction peak at the leading edge of the blade. Moreover, analysis of the lift (L) and drag (D) coefficients indicate that at $\alpha = 0^\circ$, representative of fully attached flow, turbulence significantly decreases aerodynamic efficiency (lift to drag ratio, L/D, decreases from 4.894 to 0.908). On the contrary, when the flow is mostly stalled (i.e., $\alpha = 16^\circ$), the effect is reversed and aerodynamic performance is slightly improved, from L/D \approx 1.696 to 1.787. The error in the calculation of L/D is less than 2.4%.

Fig. 1 Pressure distributions for $\alpha = 0^\circ$ without (left) ($C_L \approx 0.074$) and with (right) ($C_L \approx 0.022$) FST

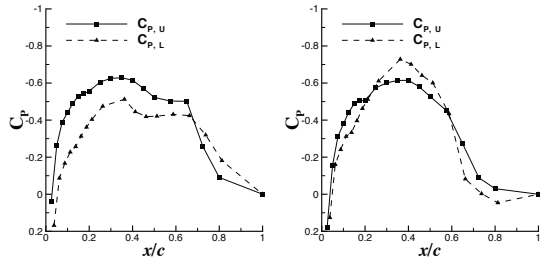
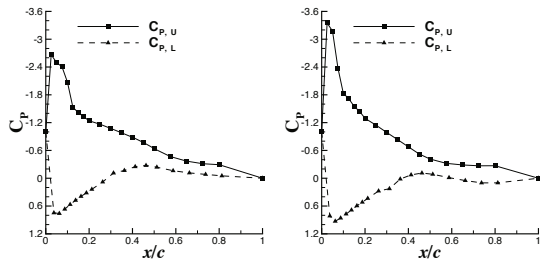


Fig. 2 Pressure distributions for $\alpha = 16^\circ$ without (left) ($C_L \approx 0.740$) and with (right) ($C_L \approx 0.832$) FST



4 Mean Velocity Profiles

The mean flow over the suction surface is analyzed to investigate the effects of a highly turbulent free-stream on the flow field over a smooth and rough surface wind

turbine blade. Figure 3 represents the streamwise mean velocity flow fields over the suction surface of the rear portion of the smooth surface blade, from $x/c = 0.48$ to $x/c = 1$ at $\alpha = 16^\circ$. It is seen that the addition of FST (fig. 3 (right)), is enhancing separation; note the increased recirculation region at the trailing edge of the airfoil when FST is present. Figure 4 shows the mean flow for the rough surface blade, without (fig. 4 (left)) and with FST (fig. 4 (right)). Notice that, for the case with FST, the point of separation is advanced and, thus, occurs further upstream than the separation point for the case without additional turbulence. The addition of FST is, then, resulting in the advancement of separation (i.e., promotes separation to occur at a location further upstream) and creates a larger and more intense area of reverse flow than when compared to the smooth case.

Hence, from these results it can be concluded that, for the present investigation, free-stream turbulence is actually advancing separation. Moreover, it is shown that separation is further advanced when the flow develops over a rough surface. These phenomena may be due to the lack of receptivity between the boundary layer

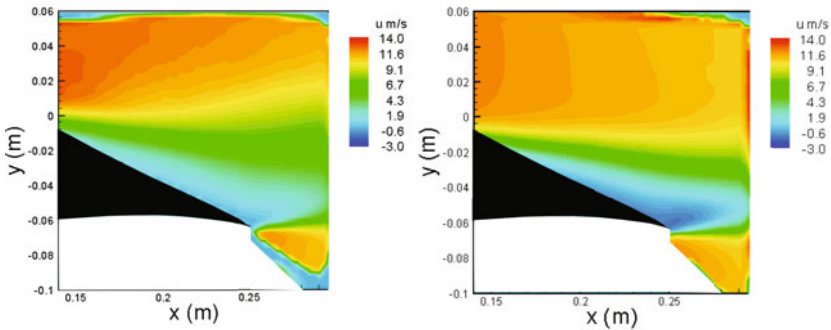


Fig. 3 Smooth surface streamwise mean velocity fields at $\alpha = 16^\circ$ without (left) and with (right) FST

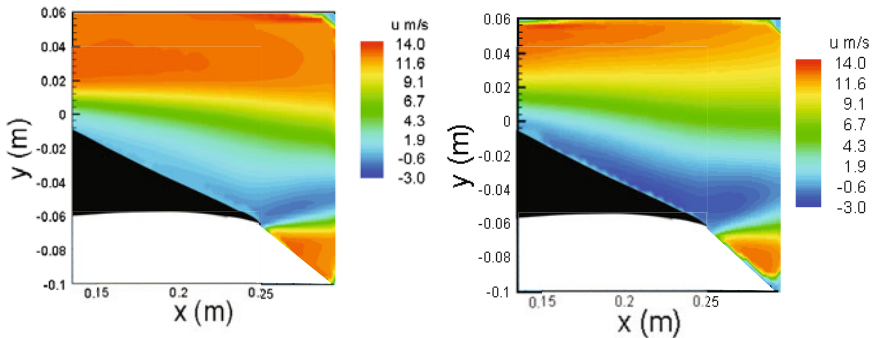


Fig. 4 Rough surface streamwise mean velocity fields at $\alpha = 16^\circ$ without (left) and with (right) FST

length scales and the length scales that characterize the highly turbulent free-stream. Of great interest is the fact that FST produces integral length scales of the order of the chord length, which dominates most of the flow dynamics in the outer flow.

Acknowledgements. Thanks to the Office of Naval Research, National Science Foundation (AGEP Program, Graduate Research Fellowship to S.T.N., and grants CBET-0553314, CBET-0730922, CBET-1033942, and HRD-0202171) and the Ford Foundation Predoctoral Diversity Fellowship to S.T.N.

References

1. Amandolese, X., Szechenyi, E.: Experimental study on the effect of turbulence on a section model blade oscillating in stall. *Wind Energy* 7, 267–282 (2004)
2. Bertagnolio, F., Sorensen, N.N., Rasmussen, F.: New insight into the flow around a wind turbine airfoil section. *J. Sol. Energ.-T ASME* 127, 214–222 (2005)
3. Brzek, B., Torres-Nieves, S., Lebrón, J., Cal, R.B., Meneveau, C., Castillo, L.: Effects of free-stream turbulence on rough surface turbulent boundary layers. *J. Fluid Mech.* 635, 207–243 (2009)
4. Kang, H.S., Chester, S., Meneveau, C.: Decaying turbulence in an active-grid-generated flow and comparisons with large-eddy simulation. *J. Fluid Mech.* 480, 129–160 (2003)
5. Steelant, J., Dick, E.: Modeling of Laminar-Turbulent Transition for High Freestream Turbulence. *J. Fluid Eng.-T ASME* 123, 22–30 (2001)

Session 9
Convection

3-d Measurements of the Velocity in the Boundary Layer of Turbulent Convection

L. Li and R. du Puits

Abstract. In our contribution we present local velocity measurements inside the boundary layers in turbulent Rayleigh-Bénard convection. The experiments were conducted at a Rayleigh number $Ra = 2.88 \times 10^{10}$ a Prandtl number $Pr = 0.7$ and an aspect ratio $\Gamma = 1$. The goal of this work was to create a set of reference data to compare it with recently performed numerical simulations at the same parameter range. Our measurements have shown that the profile of the mean horizontal velocity differs from the prediction of a laminar isothermal boundary layer and that thermal plumes create a significant wall-normal component of the velocity.

1 Introduction

One of the best known experiments to study the basics of thermal convection is the Rayleigh-Bénard (RB) experiment—a buoyancy driven fluid flow heated from below and cooled from above. The temperature difference produces a coherent flow structure, circling with a steady mean along the cooling plate and returning along the heating plate. In the middle of the circulation, is the bulk region, which is not affected by the boundary layers any more. One of the crucial questions of this type of flows is the heat transport throughout the fluid that is mainly determined by two very thin boundary layers close to the wall. Unfortunately our knowledge about these layers is still poor and highly resolved data of velocity or temperature is rare. First velocity measurements were undertaken by Deardorff and Willis [1] and Fitzjarrald [2] using a hotwire anemometer but those measurements were limited to small Ra numbers $Ra < 10^7$. Subsequent measurements were frequently carried out in water ($Pr \approx 5, \dots, 7$) or compressed gases where the boundary layers are very small and the spatial resolution is poor (see e.g. [3, 4]). Recent measurements by du Puits et al. in

L. Li · R. du Puits

Institute of Thermodynamics and Fluid Mechanics,

Ilmenau University of Technology, P.O.Box 100565, 98684, Ilmenau, Germany

e-mail: l.li@tu-ilmenau.de, ronald.dupuits@tu-ilmenau.de

a large-scale RB experiment with air ($Pr = 0.7$) were restricted to the velocity components parallel to the horizontal walls [5]. However, in order to fully understand the wall-normal momentum transport and the heat flux, this component is strongly required. The aim of this paper is to provide 3-component high resolution velocity data and to enhance the understanding of the boundary layers.

2 Experimental Setup

The experiment was conducted in a plastic cylinder of 2.5 m diameter and 2.5 m height, which was placed in the RB system, “Barrel of Ilmenau” - a cylindrical container with a heating plate at the bottom and a cooling plate at the top, which is sketched in Fig. 1.

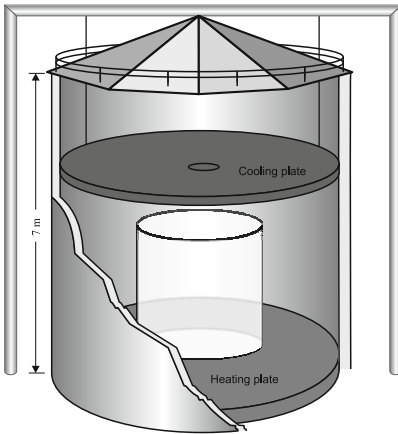


Fig. 1 Sketch of the “Barrel of Ilmenau”. The lower plate is heated. The upper (cooling) plate can be moved up and down, thus varying the aspect ratio.

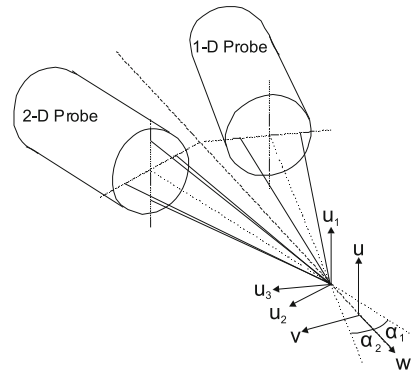


Fig. 2 Configuration of a 3-D LDA system. The measured velocity u_1 , u_2 and u_3 and the desired Cartesian velocities (u, v, w) .

The present work is to measure all three components of the velocity near the cooling plate through the central window embedded in it, at $Ra = 2.88 \times 10^{10}$ and aspect ratio $\Gamma = 1$ using a three-dimensional (3d) Laser Doppler Anemometry (LDA). It was measured by combining a 2d probe and a 1d probe (see Fig. 2). The probes were mounted on a high precision traverse system, which could be moved in vertical z -direction in steps of $\Delta z = 0.01$ mm. Cold-atomized droplets of Di-Ethyl-Hexyl-Sebacat (DEHS) with a size of about $10 \mu\text{m}$ were used as tracer particles. Time series of the horizontal velocity components and the wall-normal component were captured at 46 different z positions starting at $z = 180$ mm and up to the surface of the cooling plate. We took the time series of 3600 s for each position. The sampling

rate of the measurement was 100 Hz on average. Before we analyzed the data the measured non-cartesian velocity components u_1, u_2 and u_3 were transformed into cartesian coordinates, the horizontal velocity components u, v and the wall-normal component w .

3 Results and Discussion

We start our discussion by presenting the profiles of the mean horizontal velocity and the mean wall-normal velocity. Because of the oscillation of the mean flow, we calculate the magnitude $U = \sqrt{u^2 + v^2}$ as the mean horizontal velocity. We did the latest measurement at an aspect ratio of $\Gamma = 1$, at $Ra = 2.88 \times 10^{10}$. In this configuration the convective flow develops a stable single roll in RB cells of a cylindrical geometry. We first compare our mean horizontal velocity profile with Blasius' prediction of a laminar isothermal shear layer (see Fig. 3). For the inner region of the boundary layer, $z < 4\text{mm}$, the profile almost coincide with the Blasius solution. Following the shape of the profiles toward larger distances, the profiles noticeably deviate from the prediction of the laminar shear layer. In progress to our previous work we have added the profile of the wall-normal velocity component to the diagram and one sees that this component velocity tends to zero, which means there is no mean flow from the wall-normal component (There are some errors of the first three points, affected by the laser probes positioning). This flow is induced by thermal plumes dissolving from the boundary layer and traveling into the well-mixed bulk region. It is seen from the inset figure that the wall-normal velocity fluctuation is large compared with the mean wall-normal velocity. The existence of a significant wall-normal flow enhances the heat transport compared with the pure convective case of a laminar boundary layer and explains previously measured

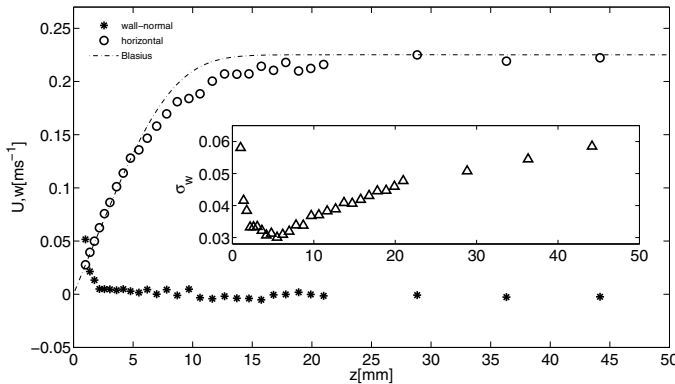


Fig. 3 Profiles of the mean horizontal velocity (circles) compared with the Blasius solution (dot dash line) and mean wall-normal velocity (stars) at constant aspect ratio $\Gamma = 1$, $Ra = 2.88 \times 10^{10}$. z is the extrapolated position. The inset is the standard deviation of wall-normal component velocity.

temperature profiles. In these profiles the boundary layer fraction in which the wall-normal temperature gradient remains constant is limited of the very inner region of the viscous sublayer [6].

4 Conclusions

We presented, highly resolved 3d velocity measurements inside the boundary layer of turbulent RB convection. at $Ra = 2.88 \times 10^{10}$ and $\Gamma = 1$. In the inner region of the boundary layer the profile of the mean horizontal velocity matches the Blasius prediction of a laminar isothermal shear layer. The outer region of the boundary layer is affected by thermal plumes generating a significant wall-normal flow fluctuation, which enhances the heat transport throughout the boundary layer compared with the laminar shear layer.

Acknowledgements. We wish to acknowledge the Deutsche Forschungsgemeinschaft (Grants No. Pui 436/1-1), the Thueringer Ministerium fuer Bildung, Wissenschaft und Kultur as well as the China Scholarship Council (Grants No. 2009608062) for the financial support of the work reported here.

References

1. Deardorff, J.W., Willis, G.E.: Investigation of turbulent thermal convection between horizontal plates. *J. Fluid Mech.* 28, 675 (1967)
2. Fitzjarrald, D.E.: An experimental study of turbulent convection in air. *J. Fluid Mech.* 73, 693 (1976)
3. Belmonte, A., Tilgner, A., Libchaber, A.: Temperature and velocity boundary layers in turbulent convection. *Phys. Rev.* 50, 269 (1994)
4. Sun, C., Cheung, Y.-H., Xia, K.-Q.: Experimental studies of the viscous boundary layer properties in turbulent Rayleigh-Bénard convection. *J. Fluid Mech.* 605, 79 (2008)
5. du Puits, R., Resagk, C., Thess, A.: Structure of viscous boundary layers in turbulent Rayleigh-Bénard convection. *Phys. Rev.* 80, 036318 (2009)
6. du Puits, R., Resagk, C., Thess, A.: Thickness of the diffusive sublayer in turbulent convection. *Phys. Rev. E* 81, 016307 (2010)

Experimental Study of the Near Wall Region of a Natural Convection Driven Flow Next to a Vertical Cylinder

Abolfazl Shiri and William K. George

Abstract. Temperature and velocity fields are measured in the boundary layer flow of air along a heated vertical cylinder using cold-wire thermometry, thermocouples and two-component laser Doppler anemometry. Detailed measurements are taken at three different heights, corresponding to Rayleigh numbers, ranging from $Ra = g\beta\Delta TL^4/\alpha\nu \approx 1.0 \times 10^{10}$ to $Ra \approx 1.7 \times 10^{11}$. The highest of these showed clearly evidence of confinement by the containment cylinder. This paper focuses on measurements of the mean and turbulence quantities in the near wall region where the varying thermal properties also affect the flow due to the strong temperature gradient there. A new set of boundary layer equations are established to represent the variable properties of the flow in this region. This experimental investigation also reveals that the strong temperature gradients adversely affect both the steady and unsteady temperature results because of the conduction to the supports of the temperature probes.

1 Near-Wall Equations of Momentum and Energy

The early attempts to study the natural convection were mainly focused on developing a better understanding of the heat transfer process next to flat surfaces. The measurement techniques (primarily hot-wire anemometry and thermocouples) in these experiments (e.g. [1]) were quite controversial, especially their use in the near-wall region of the boundary layer (c.f. [5], [2]). Also there were questions about the two-dimensionality of these flows. The goal of the present study was to study the axisymmetric boundary layer as an alternative to the two-dimensional vertical flat plate flow, hopefully thereby avoiding side-wall disturbances. This study is focused

Abolfazl Shiri

Dept. of Shipping & Marine Technology, Chalmers Univ. of Tech., Gothenburg, Sweden
e-mail: abolfazl@chalmers.se

William K. George

Departments of Aeronautics and Mechanical Engineering, Imperial College London, UK

on measuring and understanding the instantaneous temperature and velocity fields in a turbulent axisymmetric boundary layer next to a heated vertical cylinder. Laser Doppler anemometry and one-micron cold-wire thermometry were used for better accuracy and resolution.

The Reynolds-averaged momentum and energy equations for a steady flow in cylindrical coordinates can be derived by applying the Boussinesq approximation and the thin shear layer assumptions. The complete set of equations are presented in Shiri (2010) [4]. Using a scaling analysis of the governing equations, the momentum and buoyancy integral equations reduce to:

$$\frac{d}{dx} \int_R^\infty \left[U^2 + \overline{u^2} - \frac{1}{2} (\overline{v^2} + \overline{w^2}) \right] r dr = -R \frac{\tau_w}{\rho_\infty} + \int_R^\infty g \beta_\infty [T - T_\infty] r dr \quad (1)$$

$$\frac{d}{dx} \int_R^\infty (U[T - T_\infty] + \overline{ut}) r dr = R \frac{q_w}{\rho_\infty C_{p_\infty}} - \frac{dT_\infty}{dx} \int_R^\infty U r dr \quad (2)$$

where R is the radius of the cylindrical surface, x, r are the streamwise and radial coordinates, U, V are the mean streamwise and radial velocities, u, v, w are the fluctuating velocities, T and T_∞ are the mean absolute and ambient temperatures, t is the fluctuating temperature, τ_w and q_w are the wall shear stress and wall heat flux, β_∞ , ρ_∞ and C_{p_∞} are respectively the thermal expansion coefficient, density and specific heat at constant pressure at great distance from the cylinder. The choice of ρ_∞ and C_{p_∞} (instead of the near wall values) is because the major contribution to both integrals is in outer (or main) region of the boundary layer where the temperature is much closer to the outer limit than to the wall value. Equation (1) shows the balance among the vertical momentum integral, the momentum added into the turbulent velocity field by the buoyancy and that taken out by the effect of the wall shear stress. The relation between the heat transferred through the wall and the vertical thermal energy integral is shown in the equation (2) which includes the effect of the ambient stratification. These can be used in the experiment for independent checks on the wall shear stress and heat flux. For this purpose, several radial measurements in close vicinity of each other are necessary to provide the stream-wise derivatives in the left-hand-side of these equations. Application of these integral equations to the present data shows clearly that the highest position is not consistent with the assumed boundary conditions, implying the adverse influence of the return flow.

The strong temperature gradient in the near wall region of the flow (13,000 degK/m) considerably complicated the measurements, This necessitated a careful review of the differential momentum and energy equations very close to the wall in order to evaluate the accuracy of the shear stress and heat flux estimated from the measurements of the mean velocity and temperature profiles. These equation, and their integrals, were different than for the usual planar flows because of the radial geometry. This changed the nature of the near wall solutions to be logarithmic in r , only the leading term in a Taylor expansion of which is linear. Also the variation of thermal properties in the near wall region had to be included in the analysis because of the strong temperature gradient very near the wall. By assuming the air

to be an Enskog-Chapman fluid, the near wall mean temperature and mean velocity gradients (including variable viscosity) can be derived as:

$$T^{3/2} = T_w^{3/2} + \frac{3}{2} R T_w^{1/2} \left. \frac{\partial T}{\partial r} \right|_w \ln\left(\frac{r}{R}\right) \tag{3}$$

$$\frac{\partial U}{\partial r} = \left(\frac{R}{r}\right) \left. \frac{\partial U}{\partial r} \right|_w \left\{ 1 - \frac{g [\rho_w - \rho_\infty]}{2 \mu_w} \left[R \left. \frac{\partial U}{\partial r} \right|_w \right]^{-1} (r^2 - R^2) \right\} \left\{ 1 - \frac{(r-R)}{2 T_w} \left. \frac{\partial T}{\partial r} \right|_w \right\} \tag{4}$$

where the index w represents the properties of the flow evaluated at the wall temperature. Similar expressions can be derived for the radial turbulent heat flux, $\overline{v'}$ and the Reynolds shear stress, $\overline{u'v'}$, to evaluate the near wall data (see [4]).



Fig. 1 Picture of 6 m high natural convection rig: outside (right), inside (left) showing heated cylinder.

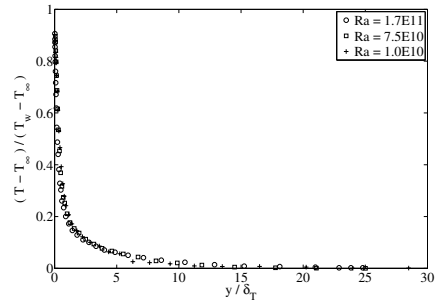


Fig. 2 Normalized mean temperature profiles from 1.5m, 3m and 4m.

2 Experimental Set-Up and Results

The experimental facility was the modification of the rig used by Persson and Karlsson [3]. The heated cylinder of radius $R = 0.075\text{ m}$ shown in Fig. 1 was placed inside a 1.5 m cylindrical tunnel of 4.5 m height through which air entered and exited entirely driven by natural convection. The velocity and temperature were measured simultaneously at three heights (1.5 m, 3 m, 4 m) along the developing boundary layer which corresponded to Rayleigh numbers of $Ra = g\beta T_w x^3 / \alpha \nu \approx 1.7 \times 10^{11}$, 7.5×10^{10} and 1.0×10^{10} , where x is the distance from the leading edge, T_w is the wall temperature, and ν and α are respectively the kinematic viscosity and thermal diffusivity. The normalized mean temperature profile is shown in Fig. 2. As noted above, stratification and return flow in the facility significantly affected the flow development, at the highest position. Thus the flow can not legitimately be considered to be a natural convection boundary layer next to a vertical cylinder, but

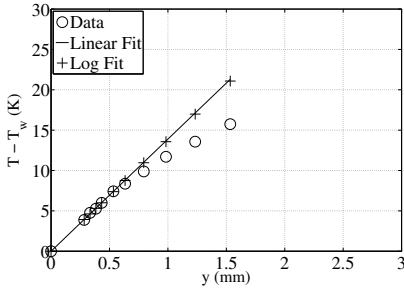


Fig. 3 Fits to mean temperature near wall, $Ra \approx 1.7 \times 10^{11}$.

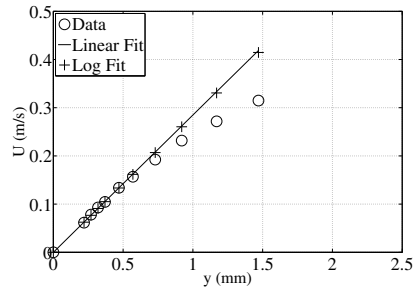


Fig. 4 Fits to mean velocity near wall, $Ra \approx 1.7 \times 10^{11}$.

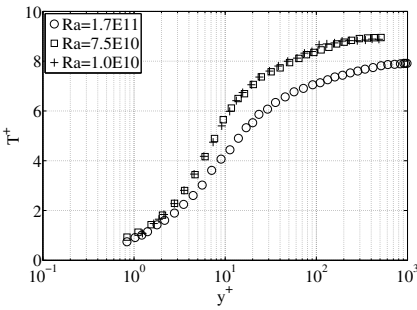


Fig. 5 Mean temperature profile in inner (wall) variables.

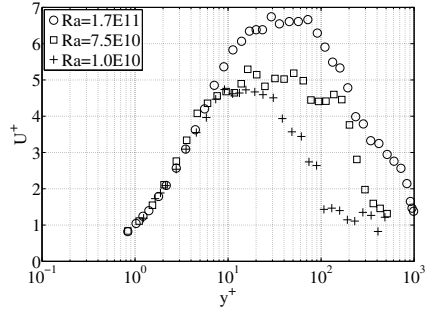


Fig. 6 Mean velocity profiles in inner (wall) variables.

rather is a developing one between concentric cylinders. Even so the near wall measurements are still of considerable interest. In practice the differences between the log and linear expansions near the wall were slight as shown in Figures 3 and 4 for $Ra = 1.7 \times 10^{11}$, although it did make a difference in the estimation of the wall shear stress and wall heat flux, as did the variable thermal properties.

Figures 5 and 6 show the profiles of mean temperature difference, $T_w - T$, and mean velocity, U , at all three heights and normalized in inner variables, $(r - R)u_* / \nu$, where u_* is the friction velocity. The collapse gives considerable confidence in both the near wall measurements and the determination of wall shear stress and wall heat flux. Similar plots for the turbulence moments are also presented in the [4]. It was possible to correct the mean thermocouple measurements for the effects of conduction along the leads arising from the strong gradients. It was not possible, however, to correct for similar effects on the fluctuating temperature measurements using 1 micron wires, the primary effect of which was to significantly reduce the frequency response (even by an order of magnitude). This problem was noted only by computing the horizontal turbulent heat flux from the energy balance and noting that it was an order of magnitude greater than the corresponding direct measurements.

References

1. Cheesewright, R.: Turbulent natural convection from a vertical plane surface. Transactions of the ASME. Series C, Journal of Heat Transfer 90(1), 1–8 (1968)
2. Cheesewright, R., Ierokipitis, E.: Velocity measurements in a turbulent natural convection boundary layer, Munich, Germany, pp. 305–309 (1982)
3. Persson, N.J., Karlsson, R.I.: Turbulent natural convection around a heated vertical slender cylinder. In: 8th Int. Symp. on Applications of Laser Techniques to Fluid Mechanics, Lisbon (1996)
4. Shiri, A.: Turbulence measurements in a natural convection boundary layer and a swirling jet. Ph.D. thesis, Chalmers Univ. of Tech. (2010), <http://www.turbulence-online.com/Publications/Theses/Theses/Shiri.pdf>
5. Tsuji, T., Nagano, Y.: Turbulence measurements in a natural convection boundary layer along a vertical flat plate. International Journal of Heat and Mass Transfer 31(10), 2101–2111 (1988)

Direct Numerical Simulations of Indoor Ventilation

Olga Shishkina and Claus Wagner

Abstract. DNS of turbulent mixed convection in a complicated 3D-domain are performed with a fast fourth order finite-volume method using a separation of variables method together with the capacitance matrix technique. The method generally allows to use hexahedral computational meshes, which are non-equidistant in all directions and non-regular in any two directions. We investigate instantaneous and statistical characteristics of turbulent mixed convection in parallelepiped convection cells with heated parallelepiped obstacles inside for Rayleigh number $Ra = 3 \times 10^8$, Prandtl number $Pr = 0.714$ and Reynolds number based on the velocity of the inlet flow $Re = 2.37 \times 10^4$ in comparison with results of purely forced convection for the same Reynolds number.

1 Introduction

Investigating turbulent mixed convection around heated obstacles has physical as well as engineering objectives. Such flows can be found for example in buildings, cars or aircrafts, where the temperature is important to provide comfortable and healthy conditions (for a review we refer to [5]).

Mixed convection in air on large scales has been investigated so far mainly in theoretical and experimental studies using geometries, which are much simpler than those relevant for realistic indoor ventilation problems. For example, in [3] parallelepiped rooms heated from below by uniform heat sources, without any obstacles inside, were considered. Numerical investigations have been conducted so far either for laminar cases [2] or by means of underresolved DNS, LES [4], or RANS [1]. Results of the latter often reveal large deviations in flow predictions depending on the turbulence models used.

Olga Shishkina · Claus Wagner
DLR - Institute for Aerodynamics and Flow Technology,
Bunsenstrasse 10, 37073 Göttingen, Germany
e-mail: Olga.Shishkina@dlr.de, Claus.Wagner@dlr.de

The objective of the present study is to investigate in detail instantaneous and statistical characteristics of turbulent mixed convection around heated obstacles in a generic room by means of well-resolved DNS. Further, the obtained results are compared to those of purely forced convection, in order to analyse the influence of buoyancy on the flow.

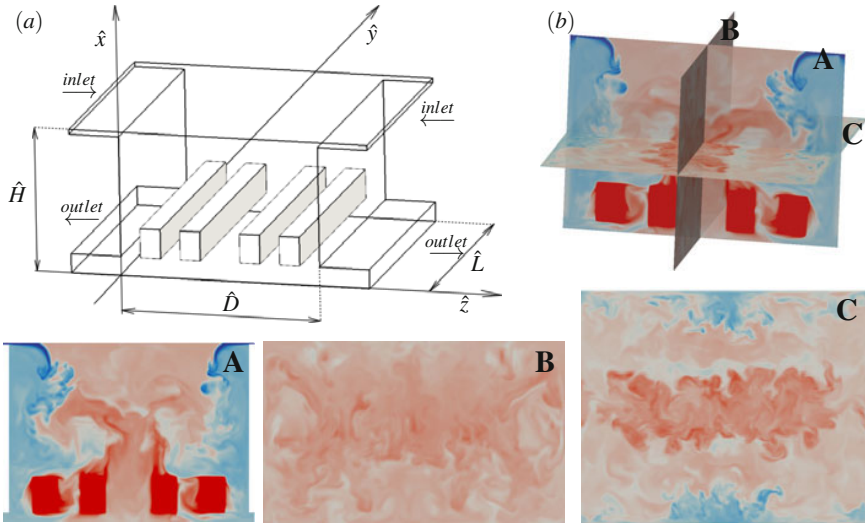


Fig. 1 (a) Sketch of the domain: the obstacles are heated and the inflows are cooled; (b) Snapshots of the temperature, as obtained in the DNS for $Ra = 3 \times 10^8$, $Re = 2.37 \times 10^4$. The scale ranges from blue (low values) to red (high values).

2 Computational Domain, Governing Equations and Numerical Method

We consider a parallelepiped computational domain with four outer parallelepiped ducts for the inlet and outlet flows and four parallelepiped heated obstacles inside the domain, as shown in Fig. 1(a). The length, height and width (without ducts) of the domain are $\hat{L} = 5\text{m}$, $\hat{H} = 3\text{m}$ and $\hat{D} = 4\text{m}$, respectively. Through two thin ducts with a width of $\hat{H}/150 = 2\text{cm}$, which are located close to the top, cold air enters the domain. Two outlet ducts with a width of $\hat{H}/20 = 15\text{cm}$ are located close to the bottom. The obstacles which are elevated at the distance $\hat{H}/20 = 15\text{cm}$ from the bottom are orientated in a parallel manner. The length, height and width of the obstacles are $\hat{L} = 5\text{m}$, $\hat{H}/5 = 60\text{cm}$ and $\hat{D}/10 = 40\text{cm}$, respectively. The distance between the central obstacles is $\hat{D}/5 = 80\text{cm}$ and the other distances between the obstacles or between the walls and the nearest obstacle equal $\hat{D}/10 = 40\text{cm}$.

Mixed convection is determined both by the buoyancy force like in natural convection and by inertia forces like in forced convection, while neither of these forces dominates. This type of convection is characterized by the Grashof number

$\mathcal{G}r = \alpha g \hat{H}^3 \Delta \hat{T} / \nu^2$ and the Reynolds number $\mathcal{R}e = \hat{H} \hat{u}_{inlet} / \nu$, where $\mathcal{G}r$ is of the same order as $\mathcal{R}e^2$ and α denotes the thermal expansion coefficient, ν the kinematic viscosity, g the gravitational acceleration, $\Delta \hat{T}$ the difference of the temperatures at the heated obstacles and the cold inlet flows, \hat{H} the height of the container and \hat{u}_{inlet} the velocity of the inlet flow.

The system of the governing equations for the velocity $\hat{\mathbf{u}}$, temperature \hat{T} , and pressure \hat{p} in the framework of the Boussinesq approximation reads:

$$\begin{aligned} \hat{\mathbf{u}}_t + \hat{\mathbf{u}} \cdot \nabla \hat{\mathbf{u}} + \rho^{-1} \nabla \hat{p} &= \nu \Delta \hat{\mathbf{u}} + \alpha g (\hat{T} - \hat{T}_0) \hat{\mathbf{e}}_x, \\ \hat{T}_t + \hat{\mathbf{u}} \cdot \nabla \hat{T} &= \kappa \Delta \hat{T}, \quad \nabla \cdot \hat{\mathbf{u}} = 0, \end{aligned}$$

where $\hat{\mathbf{u}}_t$ and \hat{T}_t denote the time derivatives of the velocity and temperature fields, respectively, ρ is the density, κ the thermal diffusivity and $\hat{T}_0 = 0.5(\hat{T}_H + \hat{T}_C)$. Here \hat{T}_H is the temperature of the heating obstacles, \hat{T}_C the temperature of the cool inlet flows and $\hat{\mathbf{e}}_x$ the unit vertical vector.

While the temperatures of the cold inlet flows and heated obstacles are set to \hat{T}_C and \hat{T}_H , respectively, at the outlets and outer rigid walls adiabatic boundary conditions $\partial \hat{T} / \partial \mathbf{n} = 0$, where \mathbf{n} is the normal vector, are prescribed. The velocities at the outer boundaries of the inlet ducts are fixed; one of the horizontal components of the velocity is set to \hat{u}_{inlet} , while the others are equal to zero. At the outer boundaries of the outlet ducts $\partial \hat{\mathbf{u}} / \partial \mathbf{n} = 0$. At all solid walls $\hat{\mathbf{u}} = 0$ according to the impermeability and no-slip conditions.

To simulate turbulent mixed convection, we use a finite-volume method, similar to that used in [11] and in our DNS of natural convection [8, 9, 10]. A major change was realized in the Poisson solver by using the capacitance matrix technique together with the separation of variables method described in details in [6]. The resulting computational code allows to conduct DNS of turbulent natural, forced or mixed convection in enclosures using computational meshes, which are non-equidistant in all three directions and irregular in any two directions. In order to resolve all scales of the turbulent flows in the bulk as well as in the boundary layers, one should use a fine enough computational mesh, according to [7]. To conduct our DNS of mixed and forced convection for $\mathcal{P}r = 0.714$ and $\mathcal{R}a = 3 \times 10^8$ we used a computational mesh, which is non-equidistant in all three directions and consists of 320 nodes in vertical direction and 384×600 nodes in two horizontal directions.

3 Results

By means of DNS we generated instantaneous and statistical characteristics of turbulent forced and mixed convection in the above described domain (Fig. 1a). The working fluid is air with $\mathcal{P}r = 0.714$, $\mathcal{R}a = 3 \times 10^8$ and $\mathcal{R}e = 2.37 \times 10^4$. In Fig. 1(b) distributions of the instantaneous temperature computed in this DNS are presented. They illustrate complicated turbulent flow structures which are typical for indoor ventilation problems.

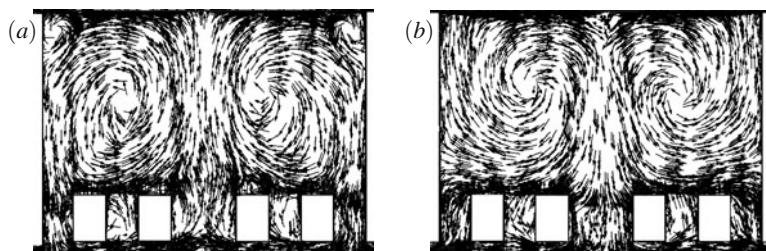


Fig. 2 Directions of the time-averaged fluid flows inside the domain in the cases of mixed convection with $Gr = 4.22 \times 10^8$ (a) and forced convection with $Gr = 0$ (b), both for the same $Re = 2.37 \times 10^4$ and $Pr = 0.714$.

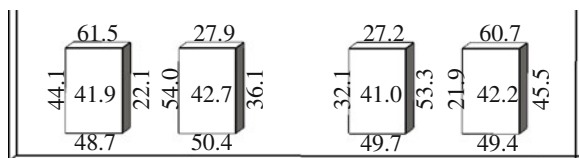


Fig. 3 Time- and surface-averaged heat fluxes at different boundaries of the heated obstacles for $Pr = 0.714$, $Gr = 4.22 \times 10^8$ and $Re = 2.37 \times 10^4$. The heat fluxes averaged over the whole obstacles surfaces are given at the centres of the obstacles.

The results of our DNS reveal that in the cases of forced and mixed convection different large-scale circulations develop inside the domain, although the same geometry and the same Re are considered (see Fig. 2). In particular, for $Re = 2.37 \times 10^4$ a downward flow is obtained in the case of forced convection, while mixed convection leads to an upward flow in the central part of the domain. Distributions of the mean heat fluxes at the surfaces of the obstacles are shown to be very irregular and they strongly depend on the positions of the surfaces (vertical or horizontal) as well as on their locations inside the domain, see Fig. 3.

The authors are grateful to A.Thess and J.Schumacher for useful discussions and to the DFG (project WA/1510) and LRZ for the support.

References

1. Costa, J.J., Oliveira, L.A., Blay, D.: *Int. J. Heat & Mass Transfer* 42, 4391–4409 (1999)
2. Ehrhard, P.: *J. Fluid Mech.* 439, 165–198 (2001)
3. Fitzgerald, S.D., Wood, A.W.: *J. Fluid Mech.* 591, 21–42 (2007)
4. Kenjeres, S., Gunarjo, S.B., Hanjalic, K.: *Int. J. Heat Fluid Flow* 26, 569–586 (2005)
5. Linden, P.F.: *Annu. Rev. Fluid Mech.* 31, 201–238 (1999)
6. Shishkina, O., Shishkin, A., Wagner, C.: *J. Comput. & Appl. Maths* 226, 336–344 (2009)
7. Shishkina, O., Stevens, R.J.A.M., Grossmann, S., Lohse, D.: *New J. Phys.* 12, 075022 (2010)
8. Shishkina, O., Thess, A.: *J. Fluid Mech.* 633, 449–460 (2009)
9. Shishkina, O., Wagner, C.: *J. Fluid Mech.* 599, 383–404 (2008)
10. Shishkina, O., Wagner, C.: *Phys. Fluids* 19, 085107 (2007)
11. Shishkina, O., Wagner, C.: *C. R. Mecanique* 333, 17–28 (2005)

Application of 3D Particle Tracking Velocimetry in Convection

A. Wegfrass, E. Lobutova, and C. Resagk

Abstract. Convection in large enclosures like theater halls, office rooms, and passenger compartments can be driven by the momentum flow of the inlet systems or buoyancy forces caused by internal heat sources. In many practical applications the overall flow field is clearly dominated by thermal convection and it is difficult to locate inlet devices by examining the large-scale flow structures. The characterization of these large-scale flow structures in ventilated rooms remains largely unresolved in experimental fluid mechanics.

In the present work large-scale circulation of air flow in a room has been investigated with three-dimensional particle tracking velocimetry (3D PTV). This technique has been refined for the large scales, enabling us to determine flow patterns, trajectories, and velocity vectors within the large Rayleigh–Bénard (RB) experiment “Barrel of Ilmenau”. The 3D PTV system consists of four cameras, two flash lamps, and an image recording and data processing system. Helium-filled latex balloons were used as tracer particles. First applications of the developed 3D PTV system showed different characteristic flow patterns of large-scale circulation outside the boundary layers.

1 Introduction

There are many well-known flow measurement techniques such as hot-wire anemometry (HWA), laser Doppler anemometry (LDA), particle image velocimetry (PIV), and particle tracking velocimetry (PTV). HWA and LDA, e.g. [1], provide high spatial and temporal resolution for up to three velocity components, but these measurement techniques are limited to point measurements. Moreover, these techniques are unable to capture the instantaneous flow pattern, also known as coherent

A. Wegfrass · E. Lobutova · C. Resagk

Ilmenau University of Technology, P.O.Box 100565, 98684, Ilmenau, Germany

e-mail: andre.wegfrass@stud.tu-ilmenau.de

{elka.lobutova,christian.resagk}@tu-ilmenau.de

flow structures. PIV (e.g. [2]) is useful to determine the flow field simultaneously at many points in the observation volume, but this measurement technique is applied to a two-dimensional analysis due to the lightsheet illumination.

However, there is still no universal three-dimensional method available to investigate the large-scale circulation, Lagrangian trajectories, and their statistics especially for room air flows. Although PTV is one of the oldest flow measurement techniques, e.g. [3], there is currently no 3D PTV technique application suited for the determination of velocity fields and particle trajectories in very large measurement volumes.

2 Experiment

The experiments are performed in a large Rayleigh–Bénard experimental facility called “Barrel of Ilmenau” (BOI). It consists of a cylindrical container with a diameter $D = 7.1\text{ m}$ and a height H , which can be varied between 0.05 m and 6.30 m . For our measurements we have chosen a constant height $H = 3.58\text{ m}$, corresponding to an aspect ratio $\Gamma = D/H = 2$. The working fluid is air. The temperature of the heating plate can be adjusted between $20\text{ }^\circ\text{C}$ and $80\text{ }^\circ\text{C}$, whereas the temperature of the cooling plate is kept at $20\text{ }^\circ\text{C}$. A detailed description of the BOI facility is given by du Puits et al. [4]. For the measurements described in this paper we setup a temperature difference $\Delta T = 40\text{ }^\circ\text{C}$ and a Rayleigh number $Ra = 1.3 \times 10^{11}$. The inner wall of the BOI is coated with low-reflecting black paint in order to increase the contrast between background and particles. The camera system consists of four CANON EOS 20D SLR cameras. Each one is equipped with wide-angle lenses CANON EFS 10–22mm f/3.5–4.5 USM. This arrangement covers up to 85% of the volume of the convection cell. As well as the camera system, the illumination units are mounted on the wall inside of the cell and the rest of the supporting equipment is placed above the cooling plate. As tracer particles we use up to ten helium-filled latex balloons, which can be added to the flow domain manually. The balloons are filled at the bulk temperature of the BOI until they show neither buoyancy nor gravity force action. By adding small weights we can ensure that the balloons move only a few centimeters per minute in calm air.

PTV systems are developed for different applications in which the size of the observation volume, the flow media, and the velocity range vary substantially. Nevertheless, all the systems are based on the same methodology. More detailed descriptions on the fundamentals of 3D PTV in small volumes are given by Maas et al. [5]. The measurement of flow fields in very large volumes requires the special modification of hardware components and an adjusted configuration.

3 Results

We perform 3D PTV measurements in the BOI at aspect ratio $\Gamma = 2$ using helium-filled latex balloons as tracer particles. The temperature difference between

cooling and heating plate was $\Delta T = 40^\circ\text{C}$, which corresponds to Rayleigh number $Ra = 1.3 \times 10^{11}$. The latex balloons are used to observe the large-scale circulations by recording long-term trajectories in the bulk region outside the boundary layers of the heating and cooling plate. The four cameras on the side wall of BOI capture up to 85% of the whole observation volume. A selection of representative snapshots of balloon trajectories in the BOI are shown in Fig. 1. Here we can see the expected different modes of large-scale flow patterns and their spatial and temporal properties. Fig. 1(a) depicts a projection of an LSR mode in the cross section (y - z plane) of the BOI. The movement of three balloons was followed for 60 time steps, which corresponds to 60 s time duration. The measured velocity varies between 0.06 and 0.6 ms^{-1} . The total time for one cycle of this mode ranges between 40 and 60 s and corresponds to the eddy turn-over time estimated from earlier ACF of temperature and velocity time series [6]. In contrast to the stable behavior of the LSR mode at aspect ratio $\Gamma = 1$ known from earlier boundary layer measurements, the LSR mode at aspect ratio $\Gamma = 2$ does not have a regular elliptical trajectory, does not fill out

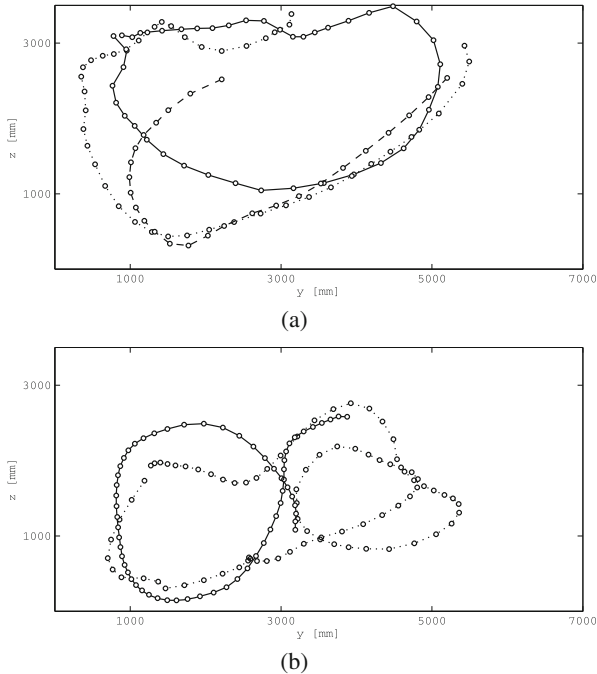


Fig. 1 (a) 2D plot of reconstructed long-term 3D trajectories representing large single roll (LSR) in the whole cross section of the convective cell. (b) 2D plot of reconstructed long-term 3D trajectory representing the transition between large single roll (LSR) and small single roll (SSR) in the whole cross section of the convective cell (dotted) and a small single roll in the half cross section of the cell (solid line). Both results have been measured at an aspect ratio of $\Gamma = 2$ and a Rayleigh number of $Ra = 1.3 \times 10^{11}$. Each point corresponds to one time step of 1 s.

the whole cross section, and tends particularly to pass into another large-scale flow pattern mode. We can clearly see the transition from LSR to SSR mode along one trajectory in Fig. 1(b), which confirms the unstable character of the bulk flow.

4 Conclusion

We report about the development and application of a 3D PTV technique which is especially suitable for investigating large-scale flow patterns in very large observation volumes. It is based on a four-camera image recording system, a full-volume illumination with two flash lamps, and latex balloons as tracer particles. The first application of the developed 3D PTV system in the large-scale convection cell BOI confirms the existence of different flow pattern modes in the bulk region and its strong unstable behavior. Furthermore, the results show that the chosen latex balloons are well suited for the application and can be used for the detection of large flow pattern modes. The recording and analysis of long-term Lagrangian trajectories offer turbulent velocity fluctuations in the large-scale circulation flow.

References

1. Tropea, C., Yarin, A., Foss, J.: Handbook of experimental fluid mechanics. Springer, Heidelberg (2007)
2. Raffel, M., Willert, C., Werely, S., Kompenhans, J.: Particle Image Velocimetry: a practical guide. Springer, Heidelberg (2007)
3. Gaydon, M., Raffel, M., Willert, C., Rosengarten, M., Kompenhans, J.: Hybrid stereoscopic particle image velocimetry. *Exp. Fluid* 23, 331–334 (1997)
4. du Puits, R., Resagk, C., Tilgner, A., Busse, F.H., Thess, A.: Structure of thermal boundary layers in turbulent Rayleigh-Bénard convection. *J. Fluid Mech.* 572, 231–254 (2007)
5. Maas, H.-G., Gruen, A., Papantoniou, D.: Particle tracking velocimetry in threedimensional flows. Part I. *Exp. Fluid* 15, 133–146 (1993)
6. du Puits, R., Resagk, C., Thess, A.: Breakdown of wind in turbulent thermal convection. *Phys. Rev. E* 75, 16302 (2007)

Author Index

- Adachi, K. 271
Alfredsson, P.H. 181
Araya, Guillermo 187
Aubard, Guillaume 81
Aubrun, S. 223, 227
- Baerenzung, J. 143
Bajer, K. 175
Battista, F. 63
Berera, A. 31
Bingöl, Ferhat 223, 259
Biß, Klaus 243
Bodo, G. 123
Bos, Wouter J.T. 25
Bosco, A. 111
Bottaro, Alessandro 135
Boyce, R. 111
Brand, Arno J. 231
Brandt, L. 217
Brethouwer, Geert 75
Brown, L. 111
Brücker, Christoph 191
- Cal, Raúl Bayoán 157
Calif 235
Casciola, Carlo Massimo 3, 63, 71
Castillo, Luciano 187, 275
Chagelishvili, G. 123
Chernyshov, A.A. 115
Cheviakov, A.F. 7
Cimarelli, A. 3
Cleve, Jochen 243
Coleman, G.N. 255
- Courtney, Mike 263
Cuzzola, F. 239
- Davidson, Lars 91
De Angelis, E. 3
Deguchi, K. 129
Drobnik, Stanislaw 197
Drozd, Artur 197
du Puits, R. 283
- Edis, Firat O. 91
Ehrenstein, U. 209
Elsner, Witold 197
Emeis, Stefan 163
Emilion 235
Enevoldsen, Karen 259
España, G. 223, 227
- Foreman, Richard J. 163
Friedrich, Rudolf 57, 67
- Gampert, Markus 35
George, William K. 147, 201, 287
Gibson, Max 157
Glahn, Manfred Schultz-von 119
Gloerfelt, Xavier 81
Gómez-Lázaro, E. 251
Gottschall, Julia 263
Greiner, Martin 243
Gualtieri, Paolo 71
Gülker, Gerd 97, 119
- Hancock, P. 227
Hansen, K.S. 259
Haut, Christopher 119

- Hayashi, T. 271
 Hayden, P. 227
 Hedevang, Emil 243
 Heißelmann, Hendrik 101
 Hindriksen, Christoph 97
 Hladík, O. 205
 Hölling, Michael 101, 151, 247
 Homeyer, Tim 97, 119
 Hono, Y. 271
 Honrubia, A. 251

 Johansson, Arne V. 75
 Johnstone, R. 255
 Jonáš, P. 205

 Kamps, Oliver 67
 Kang, Hyung-Suk 275
 Karelsky, K.V. 115
 Kelbin, O. 7
 Khujadze, G. 123
 Kirrkamm, Nils 119
 Kluwick, Alfred 85

 Larsen, Gunner C. 223, 259
 Laval, J.-P. 201, 209
 Lebrón, José 275
 Leitzl, Bernd 171, 239
 Li, L. 283
 Lo, C. 11
 Lobutova, E. 297
 Loyer, S. 227

 Maldonado, Víctor 275
 Mann, Jakob 223, 259, 263
 Marquillie, M. 209
 Mazellier, N. 17
 Mazur, O. 205
 McComb, W.D. 31
 Mellert, Volker 119
 Meneveau, Charles 275
 Meyer, K.E. 147
 Milan, Patick 167
 Morales, A. 247
 Mücke, Tanja 167, 247
 Müller, S. 111

 Nagata, Masato 129, 135

 Oberlack, Martin 7, 21, 123
 Okino, Shinya 135
 Örlü, R. 181, 213

 Paton, Jon 85
 Peinke, Joachim 41, 97, 101, 119, 151,
 167, 247
 Peters, Norbert 35
 Petersen, Graciana 171
 Petrosyan, A.S. 115
 Picano, Francesco 63, 71
 Pouransari, Zeinab 75
 Puczylowski, Jaroslaw 101

 Rehill, B. 217
 Reinartz, B. 111
 Resagk, C. 297
 Robinet, J.-C. 81
 Rosteck, Andreas M. 21
 Rubinstein, Robert 25

 Salewski, M. 31
 Sardina, Gaetano 71
 Sassa, K. 271
 Sathe, Ameya 263
 Saygin, Hasan 91
 Schaefer, Philip 35
 Schatzmann, Michael 171, 239
 Scheichl, Bernhard 85
 Schlatter, P. 213, 217
 Schneemann, J. 247
 Sedat, Tardu 45
 Segalini, A. 139
 Shiri, Abolfazl 287
 Shishkin, Andrei 41
 Shishkina, Olga 293
 Smith, Frank T. 85
 Spalart, P.R. 255
 Stanislas, M. 201
 Stoevesandt, Bernhard 41
 Stresing, Robert 41, 151

 Talamelli, A. 139
 Taniwaki, K. 271
 Tardu, S. 143
 Tatsumi, Tomomasa 49
 Tchouaké, T.F. 223
 Tevzadze, A. 123
 Torres-Nieves, Sheilla 275
 Troiani, G. 63
 Trolldborg, Niels 259

 Uruba, Vaclav 105, 205

Vallet, I. 11
Vassilicos, J.C. 17
Vigueras-Rodríguez, A. 251
Wächter, Matthias 167, 247
Wagenaar, Jan Willem 231
Wagner, Claus 41, 293
Walsh, E.J. 217
Wänström, Maja 147
Wedin, Håkan 135

Wędołowski, K. 175
Wegfrass, A. 297
Weitemeyer, Stefan 151
Wilczek, Michael 57, 67
Yılmaz, İlyas 91
Yoffe, S. 31
Younis, B.A. 11
Zaki, T.A. 217